



## Computational modeling of pharmacokinetics and tumor dynamics to guide anti-cancer treatment

Yin, A.

### Citation

Yin, A. (2024, February 1). *Computational modeling of pharmacokinetics and tumor dynamics to guide anti-cancer treatment*. Retrieved from <https://hdl.handle.net/1887/3715801>

Version: Publisher's Version

[Licence agreement concerning inclusion of doctoral thesis in the Institutional Repository of the University of Leiden](#)

License: <https://hdl.handle.net/1887/3715801>

**Note:** To cite this publication please use the final published version (if applicable).

# Computational modeling of pharmacokinetics and tumor dynamics to guide anti-cancer treatment



Anyue Yin  
尹安玥



**Computational modeling of  
pharmacokinetics and tumor dynamics  
to guide anti-cancer treatment**

**Anyue Yin**

尹安玥

The research presented in this thesis was performed at the department of Clinical Pharmacy and Toxicology of Leiden University Medical Center, Leiden, the Netherlands. Financial support for the publication of this thesis was provided by Afdelingsfonds Klinische Farmacie & Toxicologie.

|                   |                                 |
|-------------------|---------------------------------|
| <b>Cover</b>      | Anyue Yin                       |
| <b>Layout</b>     | Renate Siebes   Proefschrift.nu |
| <b>Printed by</b> | Proefschriftmaken.nl   De Bilt  |
| <b>ISBN</b>       | 978-94-6469-730-8               |

© 2023 Anyue Yin

All rights reserved. No part of this publication may be reproduced or transmitted in any form or by any means, electronically or mechanically, including photocopying, recording or in any information storage or retrieval system, without prior permission of the author.

# **Computational modeling of pharmacokinetics and tumor dynamics to guide anti-cancer treatment**

## **Proefschrift**

ter verkrijging van  
de graad van doctor aan de Universiteit Leiden,  
op gezag van rector magnificus prof. dr. ir. H. Bijl,  
volgens besluit van het college voor promoties  
te verdedigen op donderdag 1 februari 2024  
klokke 10:00 uur

door

**Anyue Yin**

geboren te Beijing, China  
in 1992

**Promotor** Prof. dr. H.-J. Guchelaar

**Copromotor** Dr. D.J.A.R. Moes

**Promotiecommissie** Prof. dr. A.J. Gelderblom  
Prof. dr. C.A.J. Knibbe  
Prof. dr. E.F. Smit  
Dr. K. Staňková, TU Delft

# Contents

|                   |  |  |
|-------------------|--|--|
| <b>Chapter 1</b>  | General introduction   | <b>7</b>                               |
| <hr/>             |  |  |
| <b>Section I</b>  | <b>Modeling tumor dynamics including treatment resistance</b>  |  |
| <b>Chapter 2</b>  | A review of mathematical models for tumor dynamics and treatment resistance evolution of solid tumors<br><i>CPT Pharmacometrics Syst Pharmacol. 2019 Oct;8(10):720-737</i>                       | <b>19</b>                              |
| <b>Chapter 3</b>  | Anti-cancer treatment schedule optimization based on tumor dynamics modelling incorporating evolving resistance<br><i>Sci Rep. 2022 Mar 10;12(1):4206</i>  | <b>65</b>                              |
| <b>Chapter 4</b>  | Quantitative modeling of tumor dynamics and development of drug resistance in non-small cell lung cancer patients treated with erlotinib<br><i>Submitted</i>                                     | <b>109</b>                             |
| <hr/>             |  |  |
| <b>Section II</b> | <b>Modeling pharmacokinetics &amp; pharmacodynamics</b>  |  |
| <b>Chapter 5</b>  | Model-informed precision dosing in oncology<br><i>In preparation</i>   | <b>143</b>                             |
| <b>Chapter 6</b>  | Population pharmacokinetic and pharmacogenetic analysis of mitotane in patients with adrenocortical carcinoma: towards individualized dosing<br><i>Clin Pharmacokinet. 2021 Jan;60(1):89-102</i> | <b>155</b>                             |
| <b>Chapter 7</b>  | Population pharmacokinetic and toxicity analysis of high-dose methotrexate in patients with central nervous system lymphoma<br><i>In preparation</i>   | <b>193</b>                             |
| <b>Chapter 8</b>  | General discussion   | <b>221</b>                             |
| <b>Chapter 9</b>  | Summary<br>Nederlands Samenvatting   | <b>247</b><br><b>251</b>               |
| <b>Appendices</b> | Curriculum Vitae<br>List of publications<br>Acknowledgement  | <b>259</b><br><b>260</b><br><b>261</b> |



# Chapter 1

## General introduction





## Importance of optimizing anti-cancer treatment

Worldwide, cancer is a leading cause of death and the incidence of cancer is rapidly increasing, reflecting both the aging of the population and the prevalence of main risk factors such as unhealthy lifestyle [1, 2]. Continuous efforts have been made to meet the medical needs of cancer patients and numerous options are currently available. A conventional treatment option for cancer patients is cytotoxic chemotherapy, which aims to inhibit tumor cell multiplication by affecting the synthesis or function of macromolecular [3]. In recent decades, targeted therapies, which act on specific oncogenic proteins that drive tumor growth or progression, have also become a standard type of anti-cancer treatment [4, 5]. Due to the increasing knowledge of molecular alterations in tumor cells, appropriate drug targets can be identified and specific targeted treatment options can be selected [6]. These targeted therapies have significantly improved the survival of cancer patients, and more than eighty targeted drugs have been brought to the market over the past decades [4, 7].

However, obstacles to accomplishing successful anti-cancer treatment still exist. First, for both conventional chemotherapies and targeted therapies, one important reason for patients experiencing treatment failure is drug resistance [8, 9]. The occurrence of drug resistance is mediated by a range of mechanisms, including physical barriers and impact of the tumor microenvironment [4, 9]. Evolutionary mechanisms are also increasingly acknowledged as key factors that contribute to the development of drug resistance. It is driven by inter- and intra-tumor heterogeneity, i.e. distinct cells exist in different or same tumors which show different susceptibility to treatments, and the evolving adaptation of tumor cells to the selection pressure of anti-cancer drug treatment, i.e. resistance subclones are acquired or are adaptively selected from pre-existing subclones during treatment [9-12]. To increase the chance to suppress the development of drug resistance, a better characterization and understanding of evolutionary tumor progression, and subsequent use of this knowledge to design new adaptive treatment regimens are desired.

Another important factor that challenges successful treatment is the substantial variability in pharmacokinetics (PK) and pharmacodynamics (PD) of anti-cancer drugs, which is especially frequently observed in real-world patients. Due to the existing correlations between drug exposure and treatment response (efficacy and toxicity) for many oncologic drugs, such variability can result in suboptimal treatment outcomes for part of the patients especially when the therapeutic window is narrow [13, 14]. Thus, the need for precision dosing in cancer therapy instead of a 'one-dose-fits-all-approach' is emerging [14]. In addition, the dosages of most oncology drugs are selected according to the maximum tolerated dose (MTD) paradigm [15]. This can lead to a demand for dose modification

in real-world patients due to the risk of toxicity [15]. Therefore, optimizing dosage of anti-cancer drugs to ensure efficacy while minimizing toxicity is essential. To achieve this goal, it would be beneficial to better understand and predict PK/PD profiles and exposure-response relationships of anti-cancer drugs, and identify factors that explain PK/PD variability (between and within patients) in real-world populations. In addition, a useful tool to support optimal and personalized dose and regimen selection based on the therapeutic target is warranted. This knowledge can also contribute to a better implementation of therapeutic drug monitoring (TDM) in cancer patients.

## **Longitudinal (bio)markers**

Monitoring longitudinal (bio)markers during anti-cancer therapies enables assessment of cancer progression and treatment response. Tumor burden is a commonly used indicator of anti-cancer treatment effect and is routinely monitored in clinical practice. In solid tumors, tumor burden is typically quantified with the sum of the longest diameters (SLD) of target lesions, which also forms several clinical endpoints defined by Response Evaluation Criteria in Solid Tumours (RECIST version 1.1) [16]. The longitudinal tumor size measurements can reflect the dynamics of treatment effect and tumor progression. SLD related metrics, such as relative or absolute changes from baseline, have also showed to be predictive to the overall survival of cancer patients [17]. In addition to tumor diameters, soluble tumor markers have also been used to measure total tumor burden in clinical practice. These include prostate-specific antigen (PSA) in prostate cancer, CA125 in ovarian cancer, M-protein in multiple myeloma, and carcinoembryonic antigen (CEA) in colorectal cancer [17, 18].

Circulating biomarkers, including soluble drug targets, inflammatory biomarkers, and circulating genetic biomarkers, can also be assessed to monitor treatment response and guide treatment modification. Circulating tumor DNA (ctDNA) is an emerging genetic biomarker which refers to cell-free DNA (cfDNA) fragments that are released into the circulation from primary tumor or metastatic cells [6]. It can be detected from liquid biopsies which allows real-time monitoring with limited patient burden. From serial ctDNA analysis, cancer-related genetic alternations can be detected and quantified, which can reveal the mechanisms of resistance to targeted therapies, and provide important insights into tumor heterogeneity and drug resistance evolution during treatment [6, 9, 19-21]. With relevant genetic alternations detected, ctDNA monitoring can potentially guide early adjustment of treatment to target newly developed actionable mutations, thereby suppressing the proliferation of tumor subclones [9, 19, 22]. In addition, the quantified

ctDNA measurements have also shown to correlate with tumor burden and stage, and ctDNA dynamics has been demonstrated to correlate with therapeutic response in various kinds of cancers [19, 20, 23-25].

Therefore, data on longitudinal (bio)markers demonstrate great value in supporting the investigation of evolutionary tumor dynamics and resistance development and PK/PD relationships of oncologic drugs. Biomarker monitoring also holds the potential to guide better treatment design aiming for improved cancer treatment outcomes.

## Pharmacometric modeling

Pharmacometric modeling has been increasingly applied in pharmaceutical research to support decision making in drug development and treatment optimization. Computational models allows quantitative characterization and prediction of the time courses of drug exposure (PK), treatment response (PD), and disease progression, as well as their relationships following drug administration [26, 27]. Mixed-effect modeling (population modeling) approach is commonly applied which allows the description of population level trends (i.e. fixed effects) and quantify random inter- and intra-individual variability (i.e. random effects) simultaneously [26, 27]. Covariates that explain the variability can also be explored.

In oncology research, the model-based approach is a helpful tool to make use of longitudinal data to gain knowledge about the interaction between drug treatment, the human body and disease. This knowledge can subsequently be used to advance treatment optimization and rationalize individualized therapy [14, 27, 28].

Models that characterize the dynamics of tumor size measurements represent one key class of PD models in cancer research. To better interpret the emergence of drug resistance, the importance of accounting for tumor heterogeneity and drug resistance evolution in tumor dynamics modeling has been pointed out before [29]. Up until now, various model structures have been proposed to characterize the tumor dynamics and drug resistance evolution in solid tumors, which can serve as references for future studies [10, 17, 30, 31]. Moreover, PK metrics and genetic biomarkers as well as their relation with tumor size dynamics can also be investigated and incorporated in the model, which would further benefit the understanding of PK/PD relationships and evolutionary tumor progression. In conjunction with simulations, the model could be used to explore optimal adaptive treatment strategies that can better prevent or delay anti-cancer treatment resistance.

Computational models that characterize the PK/PD profiles and variability of anti-cancer drugs can also guide optimal dose selection and enable individualized therapy (model-informed precision dosing (MIPD)) [14]. With the PK-PD behavior and covariates identified by the model, the optimal treatment regimen that ensures balance between efficacy and toxicity for individual patients can be identified. This can be especially helpful to guide the selection of the initial dose and schedule aiming at the target exposure. Other approaches that support precision dosing, such as pharmacogenomics, can also be integrated with MIPD [14]. Moreover, with the Bayesian framework of the developed model, individual parameters can be estimated once patient characteristics and data are known [14]. This enables more precise capture and prediction of individual PK/PD profiles, which could guide the selection of the next dose rationally. Compared with conventional TDM, MIPD provides the decision support in a quantitative manner.

## **Aim and outline of this thesis**

With the studies in this thesis, we aim to proceed toward better treatment for oncology patients with model-based approach.

In **section I**, we aim to quantitatively characterize and understand the evolutionary tumor dynamics and resistance development during treatment, and to identify treatment schedules that can better suppress the occurrence of resistance.

In **chapter 2**, we perform a systematic literature search and comprehensively summarize the mathematical models that have been used to describe and predict tumor growth (inhibition) dynamics and evolutionary resistance development. The focus of this review lies particularly on models that are applicable for clinical data.

In **chapter 3**, a mathematical model incorporating various tumor clonal populations and evolving cancer resistance is developed to characterize tumor size dynamics and resistance development under treatment, as well as ctDNA dynamics based on data from metastatic colorectal cancer (mCRC) patients. Subsequently, we evaluate adaptive and intermittent treatment schedules and demonstrate the use of ctDNA as a marker to guide adaptive treatment.

In **chapter 4**, we further characterize the tumor dynamics and development of drug resistance in NSCLC patients treated with erlotinib with a model considering tumor heterogeneity. A population PK model of erlotinib is also developed and subsequently used to facilitate the investigation on the exposure-tumor dynamics relationship of erlotinib.

Additionally, the potential correlation between ctDNA measurements and tumor dynamics in NSCLC patients is explored to further understand the value of monitoring ctDNA.

In **section II**, we aim to characterize the PK/PD profiles and variabilities of anti-cancer drugs in real-world patients to facilitate treatment optimization, and to demonstrate the use of pharmacometric models in guiding individualized treatment.

In **chapter 5**, we introduce the application and benefits of model-informed precision dosing in supporting anti-cancer treatment optimization and individualization, and discuss the challenges and future perspectives of implementing MIPD in cancer therapies.

In **chapter 6**, a population PK analysis is performed for mitotane in patients with adrenocortical carcinoma (ACC). The effect of pharmacogenetic variations on mitotane PK are investigated to better explain mitotane PK variability. Simulations are subsequently performed to investigate optimal treatment regimens and facilitate treatment individualization for patients with ACC.

In **chapter 7**, we perform a population PK analysis on high-dose methotrexate (HD-MTX) in patients with central nervous system lymphoma. Additionally, a (exposure-)toxicity analysis is performed to identify baseline and exposure-related predictive factors for the acute renal and hepatotoxicity.

Finally, in **chapter 8** we conclude this thesis with a general discussion and future perspectives in data collection, model development, and results implementation regarding the suggested regimens and developed models. English and Dutch summaries are presented in **chapter 9**.

## References

1. Sung H, Ferlay J, Siegel RL, Laversanne M, Soerjomataram I, Jemal A, et al. Global Cancer Statistics 2020: GLOBOCAN Estimates of Incidence and Mortality Worldwide for 36 Cancers in 185 Countries. *CA Cancer J Clin.* 2021;71(3):209-49. doi:10.3322/caac.21660.
2. Chen SLF, Nost TH, Botteri E, Ferrari P, Braaten T, Sandanger TM, et al. Overall lifestyle changes in adulthood are associated with cancer incidence in the Norwegian Women and Cancer Study (NOWAC) - a prospective cohort study. *BMC Public Health.* 2023;23(1):633. doi:10.1186/s12889-023-15476-3.
3. Amjad MT, Chidharla A, Kasi A. *Cancer Chemotherapy.* 2023 Feb 27 [cited 2023 May 23]; Available from: <https://www.ncbi.nlm.nih.gov/books/NBK564367/>
4. Twomey JD, Brahme NN, Zhang B. Drug-biomarker co-development in oncology - 20 years and counting. *Drug Resist Updat.* 2017;30:48-62. doi:10.1016/j.drup.2017.02.002.
5. Sawyers C. Targeted cancer therapy. *Nature.* 2004;432(7015):294-7. doi:10.1038/nature03095.
6. Oliveira KCS, Ramos IB, Silva JMC, Barra WF, Riggins GJ, Palande V, et al. Current Perspectives on Circulating Tumor DNA, Precision Medicine, and Personalized Clinical Management of Cancer. *Mol Cancer Res.* 2020;18(4):517-28. doi:10.1158/1541-7786.MCR-19-0768.
7. Smith CEP, Prasad V. Targeted Cancer Therapies. *Am Fam Physician.* 2021;103(3):155-63.
8. Sun X, Hu B. Mathematical modeling and computational prediction of cancer drug resistance. *Brief Bioinform.* 2018;19(6):1382-99. doi:10.1093/bib/bbx065.
9. Vasan N, Baselga J, Hyman DM. A view on drug resistance in cancer. *Nature.* 2019;575(7782):299-309. doi:10.1038/s41586-019-1730-1.
10. Zhao B, Hemann MT, Lauffenburger DA. Modeling Tumor Clonal Evolution for Drug Combinations Design. *Trends Cancer.* 2016;2(3):144-58. doi:10.1016/j.trecan.2016.02.001.
11. Beksac AT, Paulucci DJ, Blum KA, Yadav SS, Sfakianos JP, Badani KK. Heterogeneity in renal cell carcinoma. *Urol Oncol.* 2017;35(8):507-15. doi:10.1016/j.urolonc.2017.05.006.
12. Kim C, Gao R, Sei E, Brandt R, Hartman J, Hatschek T, et al. Chemoresistance Evolution in Triple-Negative Breast Cancer Delineated by Single-Cell Sequencing. *Cell.* 2018;173(4):879-93 e13. doi:10.1016/j.cell.2018.03.041.
13. Verheijen RB, Yu H, Schellens JHM, Beijnen JH, Steeghs N, Huitema ADR. Practical Recommendations for Therapeutic Drug Monitoring of Kinase Inhibitors in Oncology. *Clin Pharmacol Ther.* 2017;102(5):765-76. doi:10.1002/cpt.787.
14. Kluwe F, Michelet R, Mueller-Schoell A, Maier C, Klopp-Schulze L, van Dyk M, et al. Perspectives on Model-Informed Precision Dosing in the Digital Health Era: Challenges, Opportunities, and Recommendations. *Clin Pharmacol Ther.* 2021;109(1):29-36. doi:10.1002/cpt.2049.
15. Fourie Zirkelbach J, Shah M, Vallejo J, Cheng J, Ayyoub A, Liu J, et al. Improving Dose-Optimization Processes Used in Oncology Drug Development to Minimize Toxicity and Maximize Benefit to Patients. *J Clin Oncol.* 2022;40(30):3489-500. doi:10.1200/JCO.22.00371.
16. Eisenhauer EA, Therasse P, Bogaerts J, Schwartz LH, Sargent D, Ford R, et al. New response evaluation criteria in solid tumours: revised RECIST guideline (version 1.1). *Eur J Cancer.* 2009;45(2):228-47. doi:10.1016/j.ejca.2008.10.026.
17. Bender BC, Schindler E, Friberg LE. Population pharmacokinetic-pharmacodynamic modelling in oncology: a tool for predicting clinical response. *Br J Clin Pharmacol.* 2015;79(1):56-71. doi:10.1111/bcp.12258.
18. Bruno R, Chanu P, Kagedal M, Mercier F, Yoshida K, Guedj J, et al. Support to early clinical decisions in drug development and personalised medicine with checkpoint inhibitors using dynamic biomarker-overall survival models. *British journal of cancer.* 2023. doi:10.1038/s41416-023-02190-5.

19. Wan JCM, Massie C, Garcia-Corbacho J, Mouliere F, Brenton JD, Caldas C, et al. Liquid biopsies come of age: towards implementation of circulating tumour DNA. *Nat Rev Cancer*. 2017;17(4):223-38. doi:10.1038/nrc.2017.7.
20. Normanno N, Cervantes A, Ciardiello F, De Luca A, Pinto C. The liquid biopsy in the management of colorectal cancer patients: Current applications and future scenarios. *Cancer Treat Rev*. 2018;70:1-8. doi:10.1016/j.ctrv.2018.07.007.
21. Siravegna G, Mussolin B, Buscarino M, Corti G, Cassingena A, Crisafulli G, et al. Clonal evolution and resistance to EGFR blockade in the blood of colorectal cancer patients. *Nat Med*. 2015;21(7):795-801. doi:10.1038/nm.3870.
22. Nangalia J, Campbell PJ. Genome Sequencing during a Patient's Journey through Cancer. *N Engl J Med*. 2019;381(22):2145-56. doi:10.1056/NEJMra1910138.
23. Bergerot PG, Hahn AW, Bergerot CD, Jones J, Pal SK. The Role of Circulating Tumor DNA in Renal Cell Carcinoma. *Curr Treat Options Oncol*. 2018;19(2):10. doi:10.1007/s11864-018-0530-4.
24. Dawson SJ, Tsui DW, Murtaza M, Biggs H, Rueda OM, Chin SF, et al. Analysis of circulating tumor DNA to monitor metastatic breast cancer. *N Engl J Med*. 2013;368(13):1199-209. doi:10.1056/NEJMoa1213261.
25. Herbreteau G, Vallee A, Charpentier S, Normanno N, Hofman P, Denis MG. Circulating free tumor DNA in non-small cell lung cancer (NSCLC): clinical application and future perspectives. *J Thorac Dis*. 2019;11(Suppl 1):S113-S26. doi:10.21037/jtd.2018.12.18.
26. Lalonde RL, Kowalski KG, Hutmacher MM, Ewy W, Nichols DJ, Milligan PA, et al. Model-based drug development. *Clin Pharmacol Ther*. 2007;82(1):21-32. doi:10.1038/sj.cpt.6100235.
27. Buil-Bruna N, Lopez-Picazo JM, Martin-Algarra S, Troconiz IF. Bringing Model-Based Prediction to Oncology Clinical Practice: A Review of Pharmacometrics Principles and Applications. *Oncologist*. 2016;21(2):220-32. doi:10.1634/theoncologist.2015-0322.
28. Agur Z, Elishmereni M, Kheifetz Y. Personalizing oncology treatments by predicting drug efficacy, side-effects, and improved therapy: mathematics, statistics, and their integration. *Wiley interdisciplinary reviews Systems biology and medicine*. 2014;6(3):239-53. doi:10.1002/wsbm.1263.
29. Terranova N, Girard P, Klinkhardt U, Munafò A. Resistance Development: A Major Piece in the Jigsaw Puzzle of Tumor Size Modeling. *CPT Pharmacometrics Syst Pharmacol*. 2015;4(6):320-3. doi:10.1002/psp.445.
30. Zhang J, Cunningham JJ, Brown JS, Gatenby RA. Integrating evolutionary dynamics into treatment of metastatic castrate-resistant prostate cancer. *Nature Communications*. 2017;8(1). doi:10.1038/s41467-017-01968-5.
31. Ribba B, Holford NH, Magni P, Trocóniz I, Gueorguieva I, Girard P, et al. A review of mixed-effects models of tumor growth and effects of anticancer drug treatment used in population analysis. *CPT Pharmacometrics Syst Pharmacol*. 2014;3(5):e113. doi:10.1038/psp.2014.12.





# Section I

Modeling tumor dynamics including  
treatment resistance



# Chapter 2

## **A review of mathematical models for tumor dynamics and treatment resistance evolution of solid tumors**

Anyue Yin, Dirk Jan A.R. Moes, Johan G.C. van Hasselt,  
Jesse J. Swen, Henk-Jan Guchelaar



## Abstract

Increasing knowledge of intertumor heterogeneity, intratumor heterogeneity, and cancer evolution has improved the understanding of anticancer treatment resistance. A better characterization of cancer evolution and subsequent use of this knowledge for personalized treatment would increase the chance to overcome cancer treatment resistance. Model-based approaches may help achieve this goal. In this review, we comprehensively summarized mathematical models of tumor dynamics for solid tumors and of drug resistance evolution. Models displayed by ordinary differential equations, algebraic equations, and partial differential equations for characterizing tumor burden dynamics are introduced and discussed. As for tumor resistance evolution, stochastic and deterministic models are introduced and discussed. The results may facilitate a novel model-based analysis on anticancer treatment response and the occurrence of resistance, which incorporates both tumor dynamics and resistance evolution. The opportunities of a model-based approach as discussed in this review can be of great benefit for future optimizing and personalizing anticancer treatment.

## 1. Introduction

Drug resistance is one of the major reasons for patients experiencing treatment failure in the area of oncology [1]. Increasing knowledge of intertumor and intratumor heterogeneity that suggests distinct cells exist in different or the same tumors as well as cancer evolution have improved the understanding of anticancer treatment resistance [2]. It thereby pushes forward the necessity of precision medicine rather than a one-size-fits-all approach [2]. To rationalize the treatment personalization and address treatment failure, the use of modeling and simulation, which can quantitatively characterize and predict the relationships between drug exposure/pharmacokinetics (PK), drug effects/pharmacodynamics (PD), and disease progression, is widely accepted to support drug decision making [3-6].

Mathematical models that characterize the effects of anticancer drug treatment for solid tumors based on tumor size dynamics, which is typically quantified with measurements of tumor diameter and volume, represent one key class of models applied in cancer pharmacology. Various tumor growth modeling strategies have been previously reviewed, including agent-based models [7], image-based models [8], multiscale models [9], and PK/PD models [10, 11].

Currently, an increasing number of studies concerning the gene sequencing of tumor biopsies in different cancer types have demonstrated the dynamics of cancer evolution [2, 12]. Intratumor heterogeneity that results from cancer evolution and an evolving adaption of heterogeneous tumor to treatment are also increasingly acknowledged as key factors related to the development of resistance [2, 12]. To better characterize this process and to account for tumor heterogeneity, mathematical models that consider the evolution of tumors have been proposed [13-17]. Potentially, such evolution models in conjunction with tumor growth models could be of benefit to interpret both tumor size change and evolving tumor progression during treatment and thereby ultimately rationalize adaptive treatments for individual patients and overcome treatment resistance.

To identify the challenges and opportunities of characterizing tumor size change and resistance evolution simultaneously with a model-based approach that can facilitate anticancer treatment optimization and personalized medicine, an overview of the current available model structures is needed. Thus, in the current review, we comprehensively summarized mathematical models for the characterization of tumor growth (inhibition) dynamics in solid tumors and the relevant clonal evolution of drug resistance by a systematic search and study of previous literature. The focus in this review lies particularly on models that are applicable for clinical data.

## 2. Literature search

Studies that characterized tumor growth (inhibition) dynamics and clonal evolution of drug resistance with mathematical models were systematically retrieved and studied from the PubMed database to provide a comprehensive and unbiased review. In total, 274 and 85 publications were obtained, respectively, for studies of tumor dynamics and tumor resistance evolution based on established search terms. Details of the literature search are described in **Supplementary Material S2.1** and **Figure S2.1**. Ultimately, 61 and 25 papers, among which 13 and 2 papers were obtained from the publications' references, which introduced corresponding original models or demonstrated application examples of certain model structures, were included, respectively, for tumor dynamics and resistance evolution modeling. Model structures, cancer types, treatments, and the ways of reporting tumor sizes were extracted from the included papers. The identified model structures were classified by equation types in later sessions and were summarized in **Tables 2.1** and **2.2**. Data input, knowledge requirement, study type, and objectives related to different model structures were summarized in **Table 2.3** to provide a reference of the selection of different model structures. The information of software that was used to perform the corresponding modeling and simulation analysis was also obtained and are summarized in **Supplementary Material S2.1** and **Table S2.1**.

## 3. Tumor dynamics modeling

### 3.1 Ordinary differential equation

#### 3.1.1 Basic growth model

A majority of the included studies applied ordinary differential equations (ODEs) to describe tumor burden change. The natural growth of a tumor without treatment is commonly characterized with several basic functions, including linear, exponential, logistic, Gompertz, and combined exponential and linear models (**Table 2.1**). The time curves of different models were simulated and are presented in **Figure 2.1**. Differential equations were solved with the RxODE package implemented in R software (version 3.4.1; R Foundation for Statistical Computing, Vienna, Austria).

The linear tumor growth assumes a constant zero-order growth rate (Eq. 2.1; **Figure 2.1**) [10]. It has been applied to describe the natural tumor growth of metastatic renal cell carcinoma [18] based on the measurements of sum of longest diameters (SLD) of the target lesions in patients.

**Table 2.1:** Modeling frameworks for characterizing tumor dynamics

| Models/assumptions   | Equations   | Ref.              |
|--|---|-------------------|
| <b>Ordinary differential equations</b>                                       |   |                   |
| <b>Basic functions describing natural tumor growth</b>                       |   |                   |
| Linear growth  | $\frac{dT}{dt} = k_g$   | Eq. 2.1 [18]      |
|  | $\frac{dT}{dt} = k_g - d \cdot T$   | Eq. 2.2 [21]      |
| Exponential growth   | $\frac{dT}{dt} = k_g \cdot T$   | Eq. 2.3 [20]      |
|  | $\frac{dT}{dt} = k_g \cdot T - d \cdot T$   | Eq. 2.4 [22, 23]  |
| Logistic growth  | $\frac{dT}{dt} = k_g \cdot T \cdot \left(1 - \frac{T}{T_{max}}\right)$  | Eq. 2.5 [24, 25]  |
| Gompertz growth  | $\frac{dT}{dt} = k_g \cdot T \cdot \ln\left(\frac{T_{max}}{T}\right)$   | Eq. 2.6 [27, 29]  |
|  | $\frac{dlnT}{dt} = a - b lnT$   | Eq. 2.7 [28]      |
| Combination of exponential and linear growth                                 | $\frac{dT}{dt} = \frac{\lambda_0 \cdot T}{\left[1 + \left(\frac{\lambda_0}{\lambda_1} \cdot T\right)^{20}\right]^{\frac{1}{20}}}$ | Eq. 2.8 [31]      |
| <b>Model structures integrating tumor heterogeneity</b>                      |   |                   |
| Tumor burden(T)=<br>Proliferative component (P)<br>+ Quiescent component (Q) | $\begin{cases} \frac{dP}{dt} = f(P) - m_1 \cdot P \\ \frac{dQ}{dt} = m_1 \cdot P \end{cases}$                                     | Eq. 2.9 [25]      |
|  | $\begin{cases} \frac{dP}{dt} = f(P) - m_1 \cdot P + m_2 \cdot Q \\ \frac{dQ}{dt} = m_1 \cdot P - m_2 \cdot Q \end{cases}$         | Eq. 2.10 [22, 33] |
| Tumor burden (T)=<br>Sensitive component (S) +<br>Resistant component (R)    | $\begin{cases} \frac{dS}{dt} = f(S) \\ \frac{dR}{dt} = f(R) \end{cases}$  | Eq. 2.11 [24]     |

Table 2.1 continues on next page.

**Table 2.1: Continued**

| Models/assumptions  | Equations   | Ref.              |
|---|---|-------------------|
| Tumor burden (T)=<br>Sensitive component (S) +<br>Resistant component (R) | $\begin{cases} \frac{dS}{dt} = f(S) - m_1 \cdot S \\ \frac{dR}{dt} = f(R) + m_1 \cdot S \end{cases}$  | Eq. 2.12 [23, 35] |
|   | $\begin{cases} \frac{dS}{dt} = f(S) - m_1 \cdot S + m_2 \cdot R \\ \frac{dR}{dt} = f(R) + m_1 \cdot S - m_2 \cdot R \end{cases}$  | Eq. 2.13 [34, 36] |
| <b>Model structures integrating tumor biology process</b>                 |   |                   |
| Angiogenesis  | $\frac{dT}{dt} = f(T) - k \cdot \frac{BM_0 - BM_t}{BM_0} \cdot T$ $= f(T) - k \cdot \left(1 - \frac{BM_t}{BM_0}\right) \cdot T$   | Eq. 2.14 [31, 39] |
|   | $\begin{cases} \frac{dT}{dt} = k_g \cdot T \cdot \left(1 - \frac{T}{E}\right) \\ \frac{dE}{dt} = k_2 \cdot T^{\frac{1}{2}} \end{cases}$   | Eq. 2.15 [40]     |
|   | $\begin{cases} \frac{dT}{dt} = k_g \cdot V \cdot \log\left(\frac{E}{T}\right) \\ \frac{dE}{dt} = k_2 \cdot T - d \cdot T^{\frac{2}{3}} \cdot E \end{cases}$                     | Eq. 2.16 [41, 42] |
| Immune system   | $\begin{cases} \frac{dT}{dt} = f(T) - f(I) \cdot T \cdot \left(\frac{h}{T+h}\right) \\ f(I) = d \cdot I \end{cases}$  | Eq. 2.17 [44]     |
|   | $\begin{cases} \frac{dT}{dt} = f(T) - f(I) \cdot T \cdot \left(\frac{h}{T+h}\right) \\ f(I) = (d_1 \cdot I_1 + d_2 \cdot I_2) \cdot \left(\frac{I_3}{I_3+g}\right) \end{cases}$ | Eq. 2.18 [43]     |
|   | $\frac{dT}{dt} = f(T) - d_1 \cdot I \cdot T - d_2 \cdot N \cdot T$  | Eq. 2.19 [46]     |
|   | $\frac{dT}{dt} = f(T) - d \cdot I \cdot T$  | Eq. 2.20 [47]     |
| <b>Empirical model structures describing therapeutic effect</b>           |   |                   |
| First-order treatment effect<br>("log-kill" pattern)                      | $\frac{dT}{dt} = f(T) - k_d \cdot T$  | Eq. 2.21 [18]     |
| Exposure-dependent treatment effect                                       | $\frac{dT}{dt} = f(T) - k_d \cdot \text{Exposure} \cdot T$  | Eq. 2.22 [22, 25] |

Table 2.1 continues on next page.

**Table 2.1:** *Continued*

| Models/assumptions  | Equations  | Ref.                          |
|---|--|-------------------------------|
| Exposure-dependent treatment effect with resistance (TGI model) | $\frac{dT}{dt} = f(T) - k_d \cdot e^{-\lambda \cdot t} \cdot \text{Exposure} \cdot T$  | Eq. 2.23 [20, 48, 49]         |
| Introducing a damaged cell compartment                          | $\begin{cases} \frac{dS}{dt} = f(S) - k_d \cdot \text{Exposure} \cdot S \\ \frac{dD}{dt} = k_d \cdot \text{Exposure} \cdot S - d \cdot D \\ T = S + D \end{cases}$ | Eq. 2.24 [24, 25]             |
| Nonlinear drug exposure-effect relationship                     | $k_g' = k_g \cdot \left(1 - \frac{E_{max} \cdot \text{Exposure}}{IC_{50} + \text{Exposure}}\right)$  | Eq. 2.25 [21]                 |
| <b>Algebraic equations</b>                                      |  |                               |
| Two-phase model   | $T = (e^{-k_d \cdot t} + e^{k_g \cdot t} - 1) \cdot \text{BASE}$   | Eq. 2.26 [50, 51, 55]         |
|   | $T = (e^{-k_d \cdot t} + e^{k_g \cdot (t-\tau)} - 1) \cdot \text{BASE}$  | Eq. 2.27 [50]                 |
|   | $T = (\phi \cdot e^{-k_d \cdot t} + [e^{k_g \cdot t} - \phi]) \cdot \text{BASE}$   | Eq. 2.28 [55]                 |
| Model proposed by Wang et al.                                   | $T = \text{BASE} \cdot e^{-A \cdot t} + B \cdot t$   | Eq. 2.29 [52, 56]             |
| An extension of Eq. 2.30  | $T = \text{BASE} \cdot e^{-A \cdot t} + B \cdot t + C \cdot t^2$   | Eq. 2.30 [53]                 |
|   | $A = \theta_1 + \theta_2 \cdot \left(\frac{\text{Dose}}{100 \text{mg}}\right)$   | Eq. 2.31 [53]                 |
| Simplified TGI model  | $T = \text{BASE} \cdot e^{k_g \cdot t - \left(\frac{k_d}{\lambda}\right) \cdot (1 - e^{-\lambda \cdot t})}$  | Eq. 2.32 [54, 57, 58, 59, 60] |
| <b>Partial differential equations</b>                           |  |                               |
| Proliferation-invasion model                                    | $\frac{\partial c(x, t)}{\partial t} = \text{Diff} \cdot \nabla^2 c(x, t) + f(c(x, t))$  | Eq. 2.33 [61, 63, 64, 69, 70] |
|   | $v = 2\sqrt{\text{Diff} \cdot \rho}$   | Eq. 2.34                      |
|   | $\frac{\partial c(x, t)}{\partial t} = \text{Diff} \cdot \nabla^2 c(x, t) + f(c(x, t)) - k_d \cdot c(x, t)$  | Eq. 2.35 [67]                 |
|   | $\text{Surv} = e^{-(\alpha \cdot \text{Dose} + \beta \cdot \text{Dose}^2)}$  | Eq. 2.36 [64]                 |

Table 2.1 continues on next page.

**Table 2.1: Continued**

| Models/assumptions           | Equations  | Ref.          |
|------------------------------|--|---------------|
| Proliferation-invasion model | $\frac{\partial c(x, t)}{\partial t} = \text{Diff} \cdot \nabla^2 c(x, t) + f(c(x, t)) - (1 - \text{Surv}) \cdot f(c(x, t))$ | Eq. 2.37 [64] |
|                              | $\frac{\partial c(x, t)}{\partial t} = \text{Diff} \cdot \nabla^2 c(x, t) + f(c(x, t)) - G(x, t)$                            | Eq. 2.38 [74] |

$a, \beta$ , radio sensitivity parameters;  $A$ , exponential shrinkage rate constant as a result of treatment;  $a, b$ , constants;  $B$ , linear growth rate constant;  $\text{BASE}$ , baseline of tumor burden;  $BM_0$ , baseline of biomarkers;  $BM_t$ , biomarker amount at time point  $t$ , which could be assumed to remain constant and equal to baseline in the absence of treatment;  $C$ , coefficient of quadratic growth term;  $c(x, t)$ , tumor cell concentration/density at location  $x$  at time  $t$ ;  $D$ , damaged cells;  $d$ , death rate constant;  $d_1, d_2$ , rate constants;  $\text{Diff}$ , diffusion coefficient;  $E$ , vessel endothelial cells;  $E_{\max}$ , maximal fraction of inhibition;  $f(P), f(S), f(R), f(T)$ , growth function of proliferative cells (P), sensitive cells (S), resistant cells (R), and tumor tissue (T), respectively;  $G(x, t)$ , surgical term;  $h, g$ , constants;  $I, I_1, I_2, I_3$ , components in the immune system;  $IC_{50}$ , the drug exposure that produces 50% of  $E_{\max}$ ;  $k$ ,  $k_2$ , rate constants;  $k_d$ , shrinkage rate constant of tumor as a result of drug treatment;  $k_g$ , growth rate/growth rate constant;  $k_g'$ , tumor growth rate constant under treatment;  $m_1, m_2$ , conversion rate constants that can be set as 0;  $N$ , normal cells;  $\text{Surv}$ , the probability of tumor cell survival;  $T$ , tumor burden; TGI, tumor growth inhibition;  $T_{\max}$ , carrying capacity;  $\lambda$ , treatment efficacy decay rate constant;  $\lambda_0$ , exponential growth rate;  $\lambda_1$ , linear growth rate;  $\tau$ , delayed time of tumor regrowth;  $\phi$ , sensitive fraction of the tumor;  $\rho$ , growth rate constant;  $\nabla^2$ , a Laplacian operator;  $f(c(x, t))$ , tumor proliferation function.

The exponential growth assumes the growth rate of a tumor is proportional to tumor burden (first-order growth; Eq. 2.3; **Figure 2.1**) [10, 19]. It has been adopted in a widely used tumor growth inhibition (TGI) model developed by Claret et al. to describe nature tumor growth [11, 20].

The linear and exponential growth models have also been expanded by introducing a first-order shrinkage term describing natural tumor death. For example, a model with a linear growth and a first-order shrinkage (Eq. 2.2) was applied to describe the natural tumor growth in patients with advanced solid malignancies based on SLD measurements [21]. An exponential growth with a first-order shrinkage (Eq. 2.4) was also used as part of the model structure to describe the natural growth of pediatric neuroblastoma based on tumor volume measurements [22]. The same model structure was also adopted for the description of the change of prostate cancer burden reflected by the level of prostate-specific antigen (PSA) [23].

When compared with the unlimited growing pattern of linear and exponential growth models, the logistic and Gompertz growth models provide a biologically realistic change of the growth rate as the tumor burden increases [6] (**Figure 2.1**). The logistic growth model assumes that the growth is limited by a carrying capacity (Eq. 2.5) [10] whereas the Gompertz model assumes the growth rate of tumor decreases over time (Eqs. 2.6 and

2.7) [10, 11]. Many clinical studies have applied the logistic [24–26] and Gompertz models [11, 27] as well as simulation studies [28, 29].

Finally, a combination of exponential and linear growth models (Eq. 2.8) has also been introduced to describe tumor growth in patients, although it was proposed primarily for characterizing xenograft tumor dynamics [30]. This combined model structure assumes that an exponential (first-order) growth switches to a linear (zero-order) growth after reaching a threshold (Figure 2.1). It was well used to describe the natural growth of vestibular schwannoma volume in patients with neurofibromatosis type 2 [31]. Setting the power term as 20 allows the switch between two growth patterns sharply enough [30].

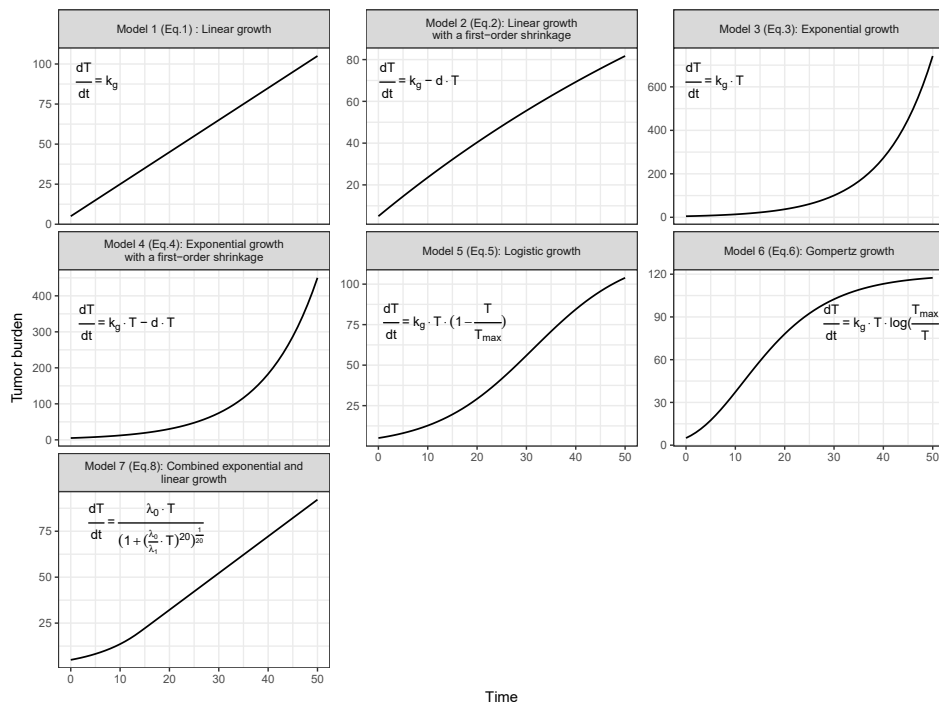


**Figure 2.1:** Simulated time curves of tumor burden ( $T$ ) with tumor natural growth models displayed by Eqs. 2.1–2.6 and 8.  $kg$  is the tumor growth rate / growth rate constant,  $d$  is the tumor death rate constant,  $T_{max}$  is the carrying capacity,  $\lambda_0$  is the exponential growth rate, and  $\lambda_1$  is the linear growth rate. The baseline of tumor burden is 5. Parameter values used for the simulations are as follows: Models 1 and 2 (Eqs. 2.1 and 2.2),  $kg = 2$ ; Model 2 (Eq. 2.2),  $d = 0.01$ ; Models 3–6 (Eqs. 2.3–2.6),  $kg = 0.1$ ; Model 4 (Eq. 2.4),  $d = 0.01$ ; Models 5 and 6 (Eqs. 2.5 and 2.6),  $T_{max} = 120$ ; Model 7 (Eq. 2.8),  $\lambda_0 = 0.1$ ,  $\lambda_1 = 2$ .

### 3.1.2 Tumor heterogeneity

As a result of the increasing awareness of the relevance of considering tumor heterogeneity, model structures displayed by ODEs that incorporate tumor heterogeneity and mutations have been developed for the characterization of tumor dynamics as was described in a simulation study [32]. The general used model structures concerning tumor heterogeneity are shown in **Table 2.1**.

#### *Proliferative and quiescent cells*

One frequently made assumption when modeling the growth of heterogeneous tumors is to separate total tumor mass into proliferative and quiescent cells [22, 25, 33]. The increase of quiescent tumor cells is assumed to result from a first-order conversion from proliferative tumor cells instead of their own proliferation (Eq. 2.9). A reversed conversion can also be assumed to be present (Eq. 2.10). The growth of proliferative cells may follow the patterns as were introduced in the Basic growth model section. Based on these assumptions, the time courses of mean tumor diameter (MTD) in patients with low-grade glioma [25] and that of tumor volume in pediatric neuroblastoma patients were successfully described [22]. A similar model structure was also used to predict the effect of different treatment regimens taking tumor cell number as a target [33]. Drug treatment effect could work on both kinds of tissues [25], only on the proliferative tissue [22], or on targeted tissues depending on the types of drug [33].

#### *Sensitive and resistant cells*

Another commonly made assumption is that tumors are composed of drug-sensitive and drug-resistant cells [24, 34]. These two cell types both proliferate, but drug treatment can only decrease the amount of drug-sensitive cells. Primary and acquired resistance can both be taken into consideration. For illustrating the acquired resistance, the resistant cells are mostly assumed to mutate from sensitive cells because of the treatment with a first-order process [23, 24, 34, 35] (Eqs. 2.12–2.13). By separating tumor mass into sensitive and resistant cells, the dynamics of low-grade glioma measured with MTD in patients was well described with models assuming that primary resistant cells or both primary and acquired resistant cells are present in the tumor [24]. In the study, the natural growth of drug-sensitive and primary-resistant cells were described separately without any conversion (Eq. 2.11). The acquired resistant cells are assumed to emerge exponentially from damaged sensitive cells as a result of treatment. Also, by assuming that resistant cells can also convert back to sensitive cells (Eq. 2.13), the dynamics of the PSA level in prostate cancer patients was well described, where the rate constants of cell proliferation, apoptosis, and conversion are expressed as functions of intracellular concentration of androgen receptors [34].

In addition, the treatment sensitivity of both proliferative and quiescent cells can also be considered when modeling tumor growth, leading to a combination of previous introduced model structures. One example can be seen from a study that assumed proliferative and quiescent cells form a tumor and the proliferative cells could mutate from drug sensitive to drug resistant, which is biologically plausible [33].

#### *Androgen-dependent cells and androgen-independent cells*

Studies regarding prostate cancer often consider prostate tumors consists of androgen-dependent (AD) and androgen-independent (AI) cells [23, 36-38]. PSA levels are commonly used to represent tumor burden in this case. Two frequently reported model structures for describing the growth of prostate cancer were proposed by Idetu et al. [23] and Hirata et al. [36].

The former model structure assumes that prostate cancer consists of AD and AI cells, and AD cells can mutate exponentially to AI cells when treatment alters the androgen level. The model structure is shown in Eq. 2.12. The natural proliferation and apoptosis rate constants of AD and AI cells were expressed as functions of the androgen level [23]. The net growth rate of AD decreases when the androgen level decreases because of treatment, whereas that of AI cells increases. When the androgen level is normal, three cases of the net growth rate of AI cells were considered: larger than 0, equal to 0, and smaller than 0. This model was recently extended by accounting for competition between two kinds of cells and the finite carrying capacity environment [35].

The latter model structure assumes that besides AD cells, reversible and irreversible AI cells exist. All types of cells are assumed to proliferate and convert to each other exponentially. It is assumed that AD cells convert to both types of AI cells during on-treatment status and reversible AI cells convert back to AD cells during off-treatment status. The model structure is expressed with Eq. 2.13. This model has been applied to adequately describe patient data [37, 38].

#### **3.1.3 Integration of biology process**

Tumor growth models displayed by ODEs that additionally incorporate biological factors and processes have also been developed [6], such as integration of angiogenesis biomarkers and the dynamics of components in the immune system (**Table 2.1**). To apply these methods, apart from tumor burden measurements, knowledge related to the biological processes is also needed.

### *Angiogenesis*

Concentration of vascular endothelial growth factor (VEGF) or soluble VEGF receptor may serve as biomarkers indicating the treatment effect for patients treated with angiogenesis inhibitors [11]. Incorporating the dynamics of angiogenesis biomarkers in tumor growth modeling enables better understanding and prediction of tumor progression. A model structure showed as Eq. 2.14, where the change of biomarkers from baseline affects the tumor decay rate, was applied in two studies [31, 39]. One study characterized the time course of SLD in patients with gastrointestinal stromal cancer undergoing sunitinib treatment. The natural growth of the tumor was described with the exponential model, and the model-predicted relative change of the biomarker's amount was incorporated to affect the shrinkage of the tumor [39]. The other study well characterized the dynamics of tumor volume measured in neurofibromatosis patients undergoing bevacizumab and everolimus. The natural tumor growth was described by the combined exponential and linear model (Eq. 2.8), and the amount of unbound VEGF was considered to affect a first-order apoptosis of the tumor [31].

Another way to account for angiogenesis effect on tumor growth is by assuming the carrying capacity of the tumor is determined by the effective tumor vascular support that is in turn affected by the tumor volume (Eqs. 2.15 and 2.16) [40, 41]. Logistic and Gompertz model structures were applied under this assumption. A model structure displayed by Eq. 2.15 was applied to well characterize the tumor growth in renal cell carcinoma (RCC) patients based on SLD measurements [40]. The carrying capacity in this study was assumed to expand because of proangiogenic factors. Another similar model structure is shown by Eq. 2.16. Although as far as we know there is no clinical study that utilized this model framework, it has been used to perform simulations to optimize the delivery of therapeutic agents for enhancing targeted therapies for liver cancer [41] and to investigate the optimization of antiangiogenic treatment [42].

### *Immune system*

Apart from angiogenesis, the effect of the immune system has also been incorporated in the tumor growth model when patients were undergoing immunotherapy [43, 44]. The proposed model structure is presented in Eqs. 2.17 and 2.18, where the rate of first-order decline of tumor burden was assumed to depend on the amount of immune component and decrease while tumor burden was increasing. This model structure was adopted to characterize the growth of prostate cancer by accounting for the dynamics of the immune system. Tumor cells were assumed to proliferate exponentially, and the amount of cytotoxic T lymphocytes affected the cell decline rate (Eq. 2.17) [44]. The applicability of this model was validated by the results of a clinical trial where PSA measurements were obtained from

prostate cancer patients treated with a vaccine. Considering the effect of more than one immune component, another study developed a model structure to simulate the growth of bladder cancer undergoing immunotherapy [43]. The growth of tumor cells was described with a logistic model, and the cell decline rate was set to be linearly or nonlinearly related to the amount of immune components (Eq. 2.18).

Another concept model structure described tumor burden dynamics by a logistic growth, a first-order damage resulting from immune cells, and a first-order competition with normal cells (Eq. 2.19) [45]. This model structure was recently adopted to obtain an optimal dosing regimen for cancer patients based on simulation [46]. A model structure that omits the competition with normal cells (Eq. 2.20) was also proposed to investigate treatment optimization [47].

### 3.1.4 Treatment effect

#### *Empirical method*

Tumor shrinkage resulting from drug treatment is typically quantified with an empirical drug-induced shrinkage term as has previously been summarized [10]. Commonly used equations identified from included papers are presented in **Table 2.1**. The time curves of these equations were simulated with R and are shown in **Figure 2.2**, assuming an exponential growth with the growth rate constant  $k_g = 0.1$ .

A log-kill pattern is commonly used for modeling treatment effect, which assumes that the shrinkage rate of the tumor as a result of drug treatment is proportional to tumor burden [6]. The simplest way to adopt this pattern is using Eq. 2.21, where  $k_d$  is the drug-induced tumor shrinkage rate constant. Such an equation has been used to well described the treatment effect of everolimus on metastatic RCC patients [18]. The estimates of  $k_d$  in that study were different between two dose groups.

The rate of drug-induced shrinkage can also be considered to depend on drug exposure, i.e., drug concentration and area under the concentration-time curve or drug dose. A linear drug exposure-effect relationship can be quantified using Eq. 2.22 [22, 25]. Meanwhile, drug resistance can also be taken into consideration by introducing a  $e^{-\lambda t}$  term on the basis of Eq. 2.22 to quantify the decline of drug effect over time (Eq. 2.23; **Figure 2.2**). This model structure has been applied to characterize the effect of pazopanib on RCC patients [40]. Setting  $f(T) = k_g \cdot T$ , an exposure-driven TGI model was developed based on SLD measurements from colorectal cancer patients receiving capecitabine and fluorouracil [20]. It has then been widely applied to various cancer types and drugs as was reviewed previ-

ously [11]. Two more recent studies also adopted this model structure to characterize the tumor SLD change in metastatic breast cancer patients treated with eribulin [48] and in metastatic ovarian cancer patients receiving carboplatin or gemcitabine plus carboplatin [49], respectively.

In addition, a damaged cell compartment ( $D$ ) has also been introduced in studies to account for the damage on cell DNA as a result of the treatment, as is displayed by Eq. 2.24, which can result in a delay on drug onset (**Figure 2.2**). This model structure was used in two studies that characterized the MTD change in low-grade glioma patients treated with chemotherapy or radiotherapy [24, 25]. In these two studies, the damaged cell compartment was used to characterize the treatment effects on drug-sensitive cells [24] and quiescent cells [25] respectively. Part of the damaged cells eventually died, and the rest were assumed to become drug-resistant cells [24] and proliferative cells [25] respectively.

Apart from the linear drug exposure-effect relationship, a nonlinear drug exposure-effect relationship can also be considered to characterize treatment effect particularly for targeted anticancer treatment [21]. An  $E_{max}$  model is commonly used in this circumstance. An example equation is showed as Eq. 2.25, which was derived from a model where the studied medicine was assumed to inhibit the zero-order growth rate of advanced solid malignancies following the nonlinear drug exposure-effect relationship [21].

### *Considering biomarkers*

When biomarkers that represent the drug-targeting system are incorporated in the tumor dynamic models, treatment effect can be added on the dynamics of biomarkers according to corresponding mechanisms.

In the study where neurofibromatosis patients were treated with bevacizumab and everolimus, the decrease of the unbound VEGF amount because of the binding with bevacizumab was considered in the model [31]. Meanwhile, the inhibition of the zero-order production rate of total VEGF because of everolimus was described with a nonlinear exposure-effect relationship:  $k' = k \cdot \left( \frac{IC_{50}}{IC_{50} + \text{Exposure}} \right)$ , where  $IC_{50}$  the drug exposure that produces 50% of the maximal inhibition effect. As a result of the quantity decrease of biomarkers, the shrinkage rate of tumor burden increased (Eq. 2.14). The delayed activation of tumor proliferation result from the continuous use of everolimus was also integrated in their model structure [31]. In the study where gastrointestinal stromal cancer patients were treated with sunitinib, the effect of sunitinib was described by a nonlinear inhibition on the zero-order production rate or first-order decline rate of biomarkers using  $k' = k \cdot \left( 1 - \frac{I_{max} \cdot \text{Exposure}}{IC_{50} + \text{Exposure}} \right)$ , where  $I_{max}$  is the maximal fraction of inhibition

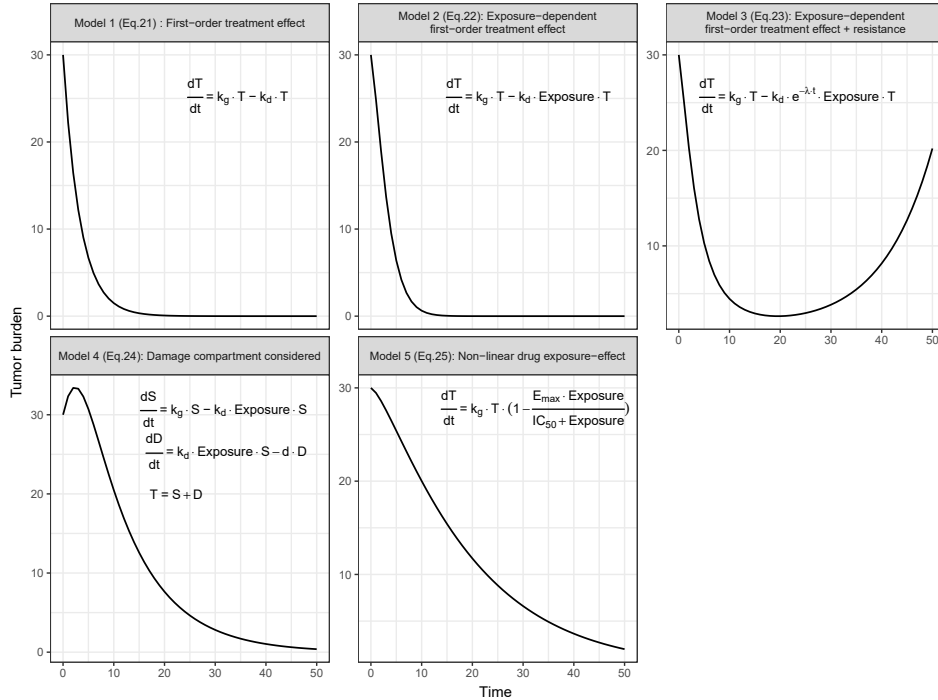


**Figure 2.2:** Simulated time curves of total tumor burden (T) with tumor dynamic models incorporating treatment effect with Eqs. 2.21–2.25 and assuming an exponential growth (growth rate constant  $k_g = 0.1$ ).  $k_d$  is the tumor shrinkage rate constant due to drug treatment,  $\lambda$  is the treatment efficacy decay rate constant,  $S$  is the drug sensitive cells,  $D$  represents the damaged cells,  $d$  is the death rate constant.  $E_{\max}$  is the maximal fraction of inhibition, and  $IC_{50}$  is the drug exposure that produces 50% of  $E_{\max}$ . The baseline of total tumor burden is 30. Parameter values used for the simulations are as follows: Model 1 (Eq. 2.21),  $k_d = 0.4$ ; Models 2–4 (Eqs. 2.22–2.24),  $k_d = 0.04$ ; Model 3 (Eq. 2.23),  $\lambda = 0.1$ ; Model 4 (Eq. 2.24),  $d = 0.1$ ; Model 5 (Eq. 2.25),  $E_{\max} = 2$ ,  $IC_{50} = 5$ .  
Drug exposure was simulated with Hill's equation:  $\text{Exposure} = E_{\max} \cdot \frac{t^{0.5}}{E_{\max} t^{0.5} + t^{0.5}} = 30 \cdot \frac{t^{0.5}}{10^{0.5} + t^{0.5}}$ , where  $E_{\max}$  represents the maximum exposure at steady state and  $E_{\max} t^{0.5}$  represents the time when the exposure reaches half maximum value.

[39]. The negative item in Eq. 2.23 was also included to quantify the treatment effect and resistance [39].

In addition, the effect of angiogenesis inhibition treatment can also be incorporated by introducing a first-order drug exposure dependent decline term (Eq. 2.22) on the dynamics of tumor vascular support [40, 41] when the vascular support was assumed to determine the carrying capacity of tumor (Eqs. 2.15 and 2.16).

Studies where patients were treated with immunotherapy have also considered drug interaction with the immune system. The presence of immunotherapeutic agents is frequently assumed to affect the dynamics of components in the immune system, and the amount of

those components can affect the decrease rate of tumor burden (Eqs. 2.17 and 2.18) [43, 44]. For example, the model structure proposed to describe PSA change in prostate cancer patients treated with a vaccine assumed that the presence of the vaccine upregulated the zero-order production rate of mature dendritic cells and therefore increased the number of cytotoxic T lymphocytes, which increased the decay of tumor tissue [44].

### 3.2 Algebraic equation

Besides using ODEs, model structures displayed by algebraic equations have also been developed to characterize the dynamics of tumor directly as is summarized in **Table 2.1** [50-54]. The simulated time curves of tumor dynamics given by these models are shown in **Figure 2.3**. Although these equations could be treated as analytical solutions of ODEs, they provided different shapes of time curves when compared with what was introduced previously.

A novel two-phase model that combines exponential tumor regrowth and regression was developed to interpret serial PSA measurements from AI prostate cancer patients [50] and metastatic castration-resistant prostate carcinoma patients undergoing combination therapy [51]. The corresponding model equation is shown in Eq. 2.26, where  $k_g$  is the tumor regrowth rate constant and  $k_d$  is the drug-dependent tumor regression rate constant. The same model structure was also utilized to assess the therapeutic efficacy of bevacizumab in patients with RCC using the sum of perpendicular diameter measurements [55]. On the bases of this model structure, an extra parameter  $\tau$  has been introduced to account for the delayed tumor regrowth as presented in **Figure 2.3** (Eq. 2.27) [50]. In addition, a parameter  $\phi$  has also been introduced on the basis of Eq. 2.26 to differentiate the sensitive and resistant part of the tumor (Eq. 2.28) [55], which results in a less degree of tumor shrinkage at the early phase (**Figure 2.3**). This model structure was found to be applicable when sufficient data points were available, and the estimation of growth rate constant was similar to what was obtained by the original equation (Eq. 2.26).

Another model structure was proposed by Wang et al. to describe the time courses of tumor SLD data of non-small cell lung cancer (NSCLC) patients from four clinical trials treated with eight treatments/placebos [11, 52], as shown by Eq. 2.29.  $A$  and  $B$  represent the rate constants of exponential shrinkage as a result of treatment and linear growth, respectively. The treatment effect was also characterized as a drug-dependent manner. This model structure has been successfully applied afterward [11] and was recently applied to analyze SLD measurements collected from NSCLC patients from three clinical studies to identify the obstacles to wider use of quantitative measures [56].

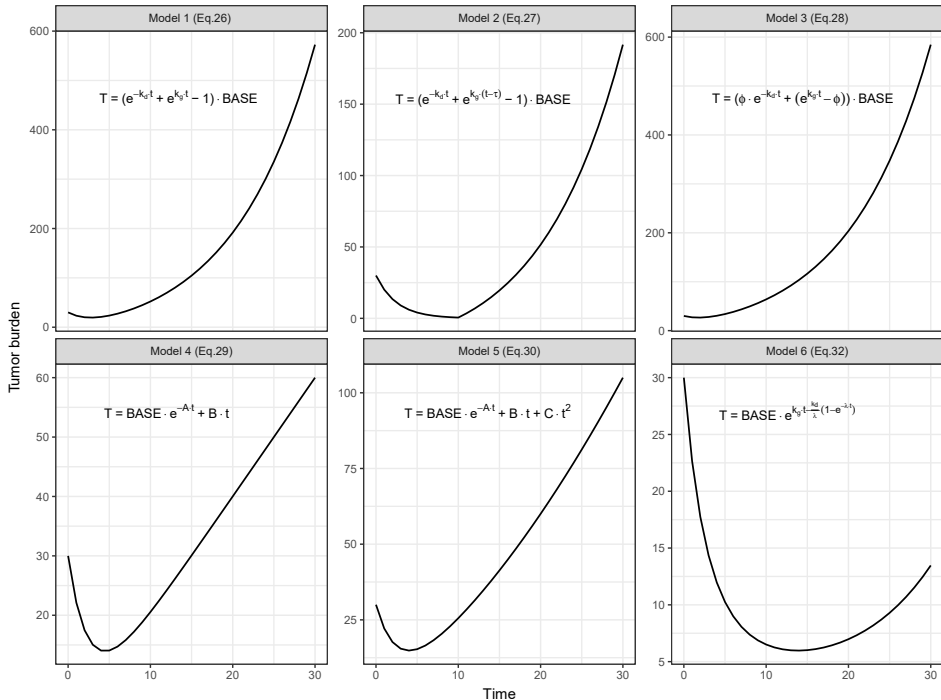


**Figure 2.3:** Simulated time curves of tumor burden ( $T$ ) with tumor dynamic models displayed by algebraic equations that describe both tumor natural growth and treatment effect (Eqs. 2.26–2.30 and 2.32).  $k_g$  is the tumor growth rate constant,  $k_d$  is the tumor shrinkage rate constant due to drug treatment,  $\tau$  is the delayed time of tumor regrowth,  $\phi$  is the sensitive fraction of the tumor,  $A$  is the exponential shrinkage rate constant due to treatment,  $B$  is the linear growth rate constant,  $C$  is the coefficient of quadratic growth term,  $BASE$  is the baseline of tumor burden, and  $\lambda$  is the treatment efficacy decay rate constant. Parameter values used for the simulations are as follows: Models 1–3 (Eqs. 2.26–2.28),  $k_g = 0.1$ ,  $k_d = 0.4$ ,  $BASE = 30$ ; Model 2 (Eq. 2.27),  $\tau = 10$ ; Model 3 (Eq. 2.28),  $\phi = 0.6$ ; Models 4 and 5 (Eqs. 2.29 and 2.30),  $A = 0.4$ ,  $B = 2$ ,  $C = 0.05$ ,  $BASE = 30$ ; Model 6 (Eq. 2.32),  $k_g = 0.1$ ,  $k_d = 0.4$ ,  $\lambda = 0.1$ .

A quadratic growth term with a coefficient  $C$  was later introduced to this model structure as is shown in Eq. 2.30 [53]. This model structure was demonstrated to have the best performance on characterizing the SLD measurements in RCC patients receiving pazopanib or placebo, and predictive patient-specific covariates were also identified [53]. Treatment effect, which is reflected by parameter  $A$ , was described in a dose-depended manner for one group of the patients in this case (Eq. 2.31).

In addition, a simplified version of the previously introduced TGI model, which was displayed by an algebraic equation, was also developed (Eq. 2.32) [54]. This model structure also assumes an exponential tumor growth with growth rate ( $k_g$ ) while the treatment effect is described in a drug-dependent manner with parameters account for tumor growth inhibition ( $k_d$ ) and drug resistance ( $\lambda$ ). By applying this model structure, the tumor size

change in metastatic colorectal cancer patient treated with bevacizumab and chemotherapy was described satisfactorily [54]. This model structure has been well applied to describe tumor size change in metastatic RCC patients treated with cytokine, mammalian target of rapamycin inhibitor, and VEGF receptor inhibitors [57]; in NSCLC patients undergoing treatment of carboplatin/paclitaxel combining motesanib or not [58]; in NSCLC patients treated with bevacizumab and erlotinib [59]; and in gastric cancer patients treated with bevacizumab and chemotherapy [60].

### 3.3 Partial differential equation

#### 3.3.1 Natural growth

Partial differential equations (PDEs), which take the change of a dependent variable in time and space into consideration, have also been adopted in the modeling of solid tumor dynamics in clinical research. One common application is known as a proliferation-invasion model or a reaction-diffusion model, which hypothesize that it is the net proliferation and invasion that contribute to the growth of cancer [61]. This model formation has been typically used in studies where imaging observations of tumor, especially brain tumors, were available to describe and predict tumor expansion [8]. The equation of this structure is shown as Eq. 2.33 in **Table 2.1**, where the dynamics of tumor cell concentration/density at location  $x$  at time  $t$  ( $c(x, t)$ ) is described [8, 61]. The tumor proliferation in this model can be expressed by exponential, logistic, or Gompertz functions [8, 61]. Moreover, this model mathematically regards the expansion of imaging detectable tumor edge as a “traveling wave,” and the velocity of tumor expansion is a constant that is determined by the diffusion coefficient ( $D_{if}$ ) and growth rate constant  $\rho$  (Eq. 2.34) [61]. This linear radius/ diameter expansion was confirmed in a group of grade II gliomas patients with magnetic resonance image (MRI) measurements before any oncological treatment [62].

Studies applying the proliferation-invasion model to characterize tumor dynamics typically have interest in estimating the rate constants of net proliferation and invasion. An application of this model structure can be found in a study where the tumor volumes obtained from the MRI imaging were available for 70 patients with previously untreated glioblastoma [61]. The tumor proliferation was described by a logistic function (Eq. 2.5) with a growth rate constant  $\rho$ . The ratio  $D_{if} / \rho$  was estimated for each patient based on MRI observations. Subsequently, setting  $\rho$  as a reported mean value and estimating  $D_{if}$ , the velocity of tumor radial expansion was estimated, and the survival time of patients underwent tumor resection were satisfactorily predicted by the estimated time of reaching a target radius. The same model structure was also applied on serial available MRI data

from 32 glioblastoma patients before treatment [63]. The net proliferation and invasion rates they quantified were significantly associated with the survival of patients. Another study characterized tumor natural growth for nine patients with glioblastoma with the same model [64]. This study demonstrated that the parameter estimated based on pretreatment MRIs had high prediction accuracy for responses after treatment for these patients. Using the same model structure, the correlation between proliferation rate and hypoxic volumes based on imaging data from newly diagnosed glioblastomas patients was demonstrated [65]. This model structure was also recently used to investigate the personalization of radiotherapy strategy for brain cancer patients [66].

Setting  $f(c(x, t)) = \rho \cdot c(x, t)$  a similar model structure was also used to simulate the growth of glioblastoma based on previous reported parameters estimated from patients and estimated the survival times of patients under different parameter settings [67].

Likewise, the proliferation-invasion model with logistic growth function was also successfully applied in breast cancer patients to characterize and predict their tumor burden. [68] The model developed based on MRI data that were available from the early treatment phase was demonstrated to be able to predict patient response at the end of treatment [69, 70]. In these studies, an apparent diffusion coefficient was estimated based on diffusion-weighted MRI data and was then transformed to an estimate of tumor cell number, which was the dependent variable in the model. Moreover, the inhibitory effect of tumor diffusivity resulting from the stress and the deformation of surrounding tissue forced by the tumor cells were also considered in these studies [69, 70], which is called “mass effect” [8]. More examples of the application of the proliferation-invasion model can be found in a previous review [8].

Apart from taking the diffusion coefficient as a constant, the difference between diffusion rates in gray and white matter can also be considered, such as setting  $Dif$  as two different constants for the cells in gray and white matter, respectively [71]. The proportions of white and gray matter (i.e.  $P_w(x)$ ,  $P_g(x)$ ) have also been taken into account when computing the diffusion coefficient with the following equation:  $Dif(x) = P_g(x) \cdot Dif_g + P_w(x) \cdot Dif_w$ . The prediction of the model was validated with clinical imaging data from one glioma patient case [72].

Recently, a threshold and a necrosis rate were also introduced into the proliferation-invasion model structure, which assumes an exponential decay will occur once the tumor cell amount exceeds the threshold [73].

### 3.3.2 Treatment effect

When using the proliferation-invasion model, the treatment effect can also be expressed by subtracting an extra term (corresponding equations are shown in **Table 2.1**). The effect of chemotherapy can be expressed with Eq. 2.35, where  $k_d$  is the drug effect rate constant [67]. For radiotherapy, a linear-quadratic equation has been used to estimate the probability of tumor cell survival (*Surv*) after the administration of radiation with dose (*Dose*) (Eq. 2.36). The effect of radiotherapy can thus be incorporated as presented by Eq. 2.37 [64]. In addition, it is also possible to incorporate the effect of resection in the proliferation-invasion model to describe tumor growth after surgery. The resection can be simulated by setting the cell concentration in the resected region as zero at the time point of surgery [61]. Subtracting a surgical term (Eq. 2.38) was also found to be applied to simulate the resection of tumor [74].

## 4. Tumor resistance evolution modelling

### 4.1 Tumor clonal evolution

Theoretically, three models of tumor evolution have been reported. One is a selective sweep model, which is also known as “linear” model [14, 75]. It holds that during cancer initiation, mutations with fitness advantage are raised and then selectively take over the whole population sequentially [14, 75]. However, because intratumor heterogeneity was identified and evidence of branching growth was found from multibiopsy and genomewide studies, a branching evolution theory where multiple subclones are considered to present and compete was developed [14, 75]. Another “big bang” model of tumor evolution was observed in colorectal tumors, which suggests that advantage mutations arise and cumulate during the early phase of cancer development and the tumor then grows as a neutral single clonal [14, 75].

Mathematical models that characterize tumor initiation and progression as an evolving process, including stochastic models and deterministic models, were sufficiently introduced in previous reviews [13, 14]. A well-mixed cell population is typically assumed [13]. Modeling strategies that focus on describing the evolution of cancer resistance have also been discussed [15, 17]. In the following sections, we will mainly give an introduction about different mathematical modeling strategies that were used to characterize cancer resistance with the tumor evolution principle.

## 4.2 Stochastic model

### 4.2.1 Probability model assuming the branching process

The branching process, which is also called the birth-death process, is a commonly adopted stochastic process that is used to characterize the evolving dynamics of cancer resistance [13, 15, 17]. The Markov property is adopted in this model. Normally, at least two cell types, i.e., sensitive cells and resistant cells, are considered. It assumes that a tumor grows exponentially and that each sensitive cell has a certain birth rate, death rate, and a mutation probability in one cell division, and each resistant cell also has a certain birth rate and death rate. The probability of cell number change from current generation to the next could therefore be expressed with these parameters, as is shown in Eq. 2.39 (**Table 2.2**).  $n$  and  $m$  the numbers of sensitive cells and resistant cells, respectively. Substantially, stochastic simulation could be performed and the probability of resistance (the probability of at least one resistant cell is present;  $P_R$ ) and the expected number of resistant cells ( $E_R$ ) could be calculated with probability-generating function.

#### *Resistance evolution before treatment*

By applying the branching process, the resistance evolution before treatment can be investigated. One study estimated the  $P_R$  and  $E_R$  of a cell population reached a certain size through the branching process starting with one sensitive cell [76]. The fitness of the resistant cells that is relative to sensitive cells was also taken into consideration [76]. The derived equations were later adopted to estimate the resistance probability of colorectal cancer prior to endothelial growth factor receptor (EGFR) antibody treatment, where the parameters were estimated based on longitudinal KRAS mutation amount measurements [77]. The results indicated that the resistant mutation was highly likely to be present prior to the initiation of treatment. The same process has also been applied to investigate the evolution of drug resistance in chronic lymphocytic leukemia before treatment [78], where the growth and death rates of cancer cells were set based on patient results. In this case, besides estimating  $P_R$  and  $E_R$  at the time of treatment start, a time needed for the resistant population to reach a detectable level after treatment was also estimated based on which disease progression was analyzed and compared with real patient data.

Another study proposed functions for estimating the expected and median cell numbers for each resistant subclone in a metastatic lesion containing a certain number of cells with the branching process starting with a single sensitive cell [79]. The predictions of relative cell numbers of resistant subclones assuming resistant cells were neutral were demonstrated to be in agreement with what was estimated based on the mutation concentrations in circulation tumor DNA (ctDNA) obtained from colorectal cancer patients treated with an EGFR blockade [79].

**Table 2.2:** Modeling frameworks for characterizing tumor resistance evolution

| Models                                       | Equations  | Ref.                  |
|--|--|-----------------------|
| <b>Stochastic models</b>                     |  |                       |
| Probability model assuming branching process | $\left\{ \begin{array}{l} P(n+1, m n, m) = b_s \cdot (1-u) \cdot n \cdot \Delta t \\ P(n-1, m n, m) = d_s \cdot n \cdot \Delta t \\ P(n, m+1 n, m) = b_r \cdot m \cdot \Delta t + b_s \cdot u \cdot n \cdot \Delta t \\ P(n, m-1 n, m) = d_r \cdot m \cdot \Delta t \\ P(n, m n, m) = 1 - ((b_s + d_s) \cdot n \cdot \Delta t + (b_r + d_r) \cdot m \cdot \Delta t) \end{array} \right.$ | Eq. 2.39 [76, 81, 83] |
| Stochastic differential equation             | $\left\{ \begin{array}{l} dS = k_g \cdot S \cdot \left(1 - \frac{(S+R)}{T_{max}}\right) \cdot dt - u \cdot S \cdot dt - k_d \cdot S \cdot dt + \sigma_1 \cdot S \cdot dW_1 - q_M \cdot K \cdot S \cdot dN_1 \\ k_d' = k_d \cdot \frac{C_D}{K_D + C_D} \end{array} \right.$   | Eq. 2.40 [90]         |
| <b>Deterministic models</b>                  |  |                       |
| Ordinary differential equation               | $\left\{ \begin{array}{l} \frac{dS}{dt} = (k_g - d - k_d) \cdot S \\ \frac{dR}{dt} = (k_g - d) \cdot R + u \cdot S \end{array} \right.$  | Eq. 2.41 [91]         |
|  | $\left\{ \begin{array}{l} \frac{dS}{dt} = (k_g \cdot (1-u) - d - k_d) \cdot S \\ \frac{dR}{dt} = (k_g - d) \cdot R + k_g \cdot u \cdot S \end{array} \right.$  | Eq. 2.42 [88]         |
|  | $\left\{ \begin{array}{l} \frac{dS}{dt} = (k_g - k_d \cdot Dose) \cdot S \\ \frac{dR}{dt} = k_g \cdot R + k_g \cdot u \cdot S \end{array} \right.$   | Eq. 2.43 [92]         |
|  | $\left\{ \begin{array}{l} \frac{dS}{dt} = (k_{g1} - u_1 - k_{d1} \cdot C_D) \cdot S + u_2 \cdot R \\ \frac{dR}{dt} = (k_{g2} - u_2) \cdot R + u_1 \cdot R \end{array} \right.$   | Eq. 2.44 [93]         |
| Game theory                                  | $W(i) = \sum p_j \cdot \text{Payoff}(ij) = 1 - r_i - d_i + (1 - p_i) \cdot X_i$  | Eq. 2.45 [94]         |
|  | $\overline{W} = \sum p_i \cdot W(i)$   | Eq. 2.46              |
|  | $\frac{dp_i}{dt} = p_i \cdot (W(i) - \overline{W})$  | Eq. 2.47              |
| Integral-differential equation               | $\left\{ \begin{array}{l} \frac{\partial n(x, t)}{\partial t} = [r(x) \cdot (1-\theta) - c(x) - G(\rho(t)) \cdot d(x)] \cdot n(x, t) + \theta \cdot \int_0^1 r(y) \cdot M(y, x) \cdot n(y, t) \cdot dy \\ \rho(t) = \int_0^1 n(x, t) dx \end{array} \right.$   | Eq. 2.48 [95, 96]     |

$n$ , numbers of sensitive cells;  $m$ , numbers of resistant cells;  $b_s$ , birth rate of sensitive cells;  $d_s$ , death rate of sensitive cells;  $u$ , mutation probability in one cell division;  $b_r$ , birth rate of resistant cells;  $d_r$ , death rate of resistant cells;  $P$ , probability of cell number changing from current generation to the next;  $S$ , sensitive cells,  $R$ , resistant cells,  $k_g$ ,  $k_g'$ ,  $k_g''$ , growth rate constant;  $d$ , death rate constant;  $k_d$ , shrinkage rate constant as a result of drug treatment;  $C_D$ , drug concentration;  $K_D$ , drug concentration that produces 50% of maximum treatment effect;  $dW$ , stochastic cell diffusion in a small time interval (Wiener process);  $dN$ , stochastic dissemination in a small time interval (Poisson process);  $\sigma_1$ , diffusion rate;  $q_M$ , dissemination rate;  $K$ , angiogenesis;  $u_1$ ,  $u_2$ , mutation rate;  $W(i)$ , fitness of type  $i$  cell;  $\text{Payoff}(ij)$ , payoff of type  $i$  cells when they meet cell type  $j$ ;  $p_i$ ,  $p_j$ , proportion of cells;  $r$ , cost of resistance;  $d$ , cost as a result of treatment;  $X$ , benefit for resistant cells when interacting with susceptible cells;  $x$ ,  $y$ , resistance levels;  $n(x, t)$ , cell density with resistance level  $x$  at time  $t$ ;  $r(x)$ ,  $r(y)$ , cell division rate;  $c(x)$ , treatment effect;  $d(x)$ , cell death rate;  $G(\rho(t))$ , a density dependence term;  $\theta$ , mutation fraction;  $M(y, x)$ , probability that cell  $y$  mutates to cell  $x$ .

### *Resistance evolution during treatment*

The branching process has also been applied to simulate the evolving resistance during treatment. Regarding treatment initiation as the starting point, the dynamics of resistance evolution has been investigated with branching stochastic processes. Starting with a group of drug-sensitive cells, Foo and Michor [80] proposed functions of  $P_R$  and  $E_R$  during treatment depending on the length of treatment on and break time for continuous and pulsed dosing strategies. Treatment effect was incorporated by setting different birth and death rates for sensitive and resistant cells, if considering partial resistance, at on-treatment and off-treatment periods, respectively. They also estimated  $P_R$ ,  $E_R$ , and variance of resistance cell number during treatment as functions of time considering with or without preexisting resistant cells [81]. Treatment effect in this study was incorporated by making the birth and death rates of both sensitive and (partial) resistant cells affected by drug concentration. The treatment schedule could therefore be optimized by minimizing resistance risk or limiting the size of resistant clones. Corresponding equations were later adopted to simulate the time curve of  $E_R$  and  $P_R$ , and thereby to identify a relatively best treatment strategy for *EGFR*-mutant NSCLC patients receiving erlotinib [82]. In that study, the birth and death rates of different types of cells were obtained from *in vitro* experiments, and the birth rates were affected by drug concentration [82]. Three cases of mutation rate change because of drug dose were also considered in the study.

Cancer progression under combination therapies has also been investigated with evolution models to predict the outcome of multiple treatment strategies in *EGFR*-mutant lung cancer patients treated with two drugs [83]. Tumor evolution after treatment initiation was modeled as a branching process with at least three types of cells considered: one type of sensitive cell and two types of preexisting resistant cells that are resistant to only one of the two drugs, respectively. The expected numbers of each type of cells were thereby estimated and the sum of which was the total expected cancer cell number (treatment outcome). The treatment effect was described by decreasing the birth rates of cells depending on drug concentration, and drug interaction was also taken into consideration [83].

Besides separating tumor cells as being sensitive and resistant to treatment, one study also separated cells (subclones) according to resistant status and the number of accumulated drivers [84]. In the stochastic branching process of tumor progression, subclones were assumed to have probabilities of raising a driver mutation and a resistant mutation during division. The accumulation of driver mutations resulted in an increase in the fitness of cells, whereas resistance was related to a fitness cost, and the fitness of nonresistant cells decreased because of treatment. By modeling the probability change of each cell type, the expected tumor size and the average frequency of resistant cells were estimated as functions

of time. Subsequently, tumor detection time was calculated and used to compare the effect of prevention and postdiagnostic interventions [84].

#### *Tumor eradication*

Considering that resistant mutations may die out as a result of stochastic drift during branching evolution, tumor eradication (treatment success) probability has also been investigated. One study modeled tumor progression as the following three phases: expansion with decreasing division rate until steady state, maintaining steady state, and treatment phase, starting with a single sensitive cell [85]. Treatment was assumed to decrease the division rate and increase the death rate of sensitive cells. A formula of the probability of resistant cells arising but becoming extinct by the end of the treatment in each phase was then proposed, and the overall probability of treatment success was estimated as the product of the three probabilities [85].

#### *Multidrug resistance*

The evolution of multidrug resistance has also been elucidated by a stochastic model where drug-sensitive and drug-resistant cells can divide, die (naturally and as a result of treatment), and mutate with certain probabilities [86, 87]. In this model, cells accumulate one mutation that leads to resistance to one drug each time, and all mutations must be accumulated to make a cell resistant to all drugs. The treatment success probability (probability of extinction) as well as the probabilities of resistance when resistant cells generated exclusively before and during treatment were estimated, respectively. Based on the derived equations, the tumor size at which a certain percentage of patients were treated successfully were investigated under various numbers of drugs, mutation rates, and the turnover rates of cancer cells [86, 87]. This model structure and the derived equation of treatment success probability were later utilized to optimize cyclic treatment scheduling [88]. Moreover, taking the contribution of quiescent tumor cells into consideration by incorporating the branching process of both cycling cells and quiescent cells, the effect of quiescent cells on the treatment outcome, such as the resistance probability, of chronic myelogenous leukemia patients has also been investigated [89].

#### **4.2.2 Stochastic differential equation**

In addition of the probability models, another stochastic modeling strategy that has been applied to characterize the development of resistance during treatment is by using stochastic differential equations. An example can be found in a study on melanoma cancer patients [90]. Three types of cancer cells, including sensitive, resistant, and metastasis cells, and angiogenetic cells were considered. The dynamics of the number of drug-sensitive cells

is described by Eq. 2.40 (**Table 2.2**). In this differential equation, cell growth, mutation, and death were described deterministically, whereas cell diffusion and dissemination were considered as stochastic processes. Logistic growth function was used to describe the growth of cells, and the mutation from sensitive to resistant cells is described with a first-order process. The death of sensitive cells was caused by drug treatment, and the nonlinear drug exposure-effect relationships was adopted (Eq. 2.40). Wiener process and Poisson process were incorporated to account for stochastic cell diffusion and dissemination, respectively. The effect of angiogenesis was also included. A drug-induced resistance factor, which depends on drug concentrations, was integrated to increase the growth and dissemination rates. The model predictions of the progression-free survival and number of metastasis cells were demonstrated to be, respectively, comparable with the observed progression-free survival and ctDNA level obtained from melanoma patients treated with B-Raf kinase and mitogen-activated protein kinase inhibitors [90].

### 4.3 Deterministic model

#### 4.3.1 ODEs

Other than stochastic models, deterministic differential equations have also been used to study the evolution toward drug resistance, especially for a population with a large size that often behaves nearly deterministically [13]. The dynamics of sensitive cells and resistant cells can be modeled with ODEs similar to what were introduced in the “Tumor Heterogeneity” section, but the transition from resistant to sensitive cells is often neglected. The model structures that have been identified are shown in **Table 2.2**.

One model of resistance evolution displayed by ODEs is shown as Eq. 2.41, where drug resistance is considered to raise due to point mutations [91]. When considering multiple drug resistance, multiresistant cells were assumed to only be mutated from single-resistant cells. Starting with a certain number of sensitive cells, the resistance amount by the time of treatment initiation and during treatment was estimated under different conditions. The authors demonstrated that the simpler ODE model provided comparable results to previous models that were derived from more complicated stochastic models [91]. Another example can be seen in Eq. 2.42. This model was used to investigate the preferable treatment by controlling the total amount of fully resistant mutants, which can be acquired from sensitive cells and single-resistant cells [88]. In addition, a model with treatment effect being proportional to drug dose has also been used to model evolving tumor resistance (Eq. 2.43) [92]. Multiresistant cells were also considered and were assumed to mutate only from single-resistant cells. Based on this model structure, the survival of patients undergoing

different treatment strategies, such as the strategy of minimizing the total cell population or minimizing the multiresistant population, was investigated [92]. Another model structure of resistance evolution that includes the transition from resistant to sensitive cells (Eq. 2.44) has also been adopted to investigate the optimization of treatment [93].

#### **4.3.2 Game theory**

Evolutionary game theory has also been used to investigate the evolution of cancer resistance, especially under combination therapy [94]. It assumes the fitness of one type of cell, which can be understood as the growth rate, changes when the cells interact with different types of other cells. This can be expressed with a payoff matrix, and the final fitness of one type of cell is their expected payoff of this “game” [13]. An example was found from a study where a well-mixed population and a deterministic dynamic of the evolving process were considered [94]. The evolutionary game theory was adopted to investigate and understand the evolving resistance for small cell lung cancer patients under a combination of chemotherapy and tumor suppressor p53 vaccine treatment [94]. Three cell populations, including cells that are sensitive to both treatments and cells that are resistant to one of the treatments but sensitive to the other, were considered to constitute the total tumor population. As presented in **Table 2.2**, the fitness of type  $i$  cell can be expressed as a sum of the product of the payoff of type  $i$  cell interacting with type  $j$  cell and the proportion of type  $j$  cell (Eq. 2.45), where a cost of resistance and a cost as a result of treatment was considered [94]. In addition, to account for the influence of cell interaction on cell sensitivity and fitness, an extra benefit for resistant cells when interacting with susceptible cells under treatment was also introduced (Eq. 2.45) [94]. The average fitness was expressed with Eq. 2.46, where  $p_i$  is the proportion of each type of cells. The dynamics of each cell type under sequencing treatment was described using a replicator equation (Eq. 2.47), and the time curve of the proportion and fitness of each cell type are two main outcomes of the simulations in this study.

#### **4.3.3 Integral-differential equation**

An integral-differential equation, where the states of cancer resistance are described in a continuous way ranging from complete sensitivity to complete resistance, has also been used to characterize the evolution of cancer resistance [95, 96]. A model structure shown as Eq. 2.48 has been used to describe the dynamics of cancer cell density with resistance level  $x$  at time  $t$  [95, 96], where cell division, cell death, treatment effect, and cell mutation were all incorporated (**Table 2.2**). Simulations were performed in these studies to illustrate the evolution of resistant level during treatment, but it has not yet been applied in clinical studies.

## 5. Model selection

Applying different model structures to characterize tumor dynamics and tumor resistance evolution may achieve different objectives and require different data input and knowledge (**Table 2.3**). The target cancer type and treatment option may also influence the selection of model structure (**Table 2.3**).

As for the tumor dynamics models displayed by ODEs and algebraic equations, most models are applicable to describe tumor size change in patients with various kinds of solid tumors and under different kinds of treatment (monotherapy or combination therapy). However, the models specifically developed for prostate cancer are mainly suitable to describe PSA level change, and the models incorporating angiogenesis biomarkers or immune components are normally considered when patients are treated with antiangiogenesis treatment or immunotherapy, respectively.

Longitudinal tumor size data, such as the SLD of target lesions, MTD, or tumor volumes, or PSA measurements are required to estimate model parameters. A mixed-effect modeling approach has been applied to most model structures that are displayed by ODEs and algebraic equations to account for interindividual variability, whereas the parameters of other structures, such as the two-phase model, were normally estimated for each subject separately. In the former case, each subject in a group is normally required to contribute at least one measurement before treatment and one thereafter. More data points are preferred to enable the better estimate of all parameters. However, the latter method may require each subject to contribute enough data points to enable parameter estimates. In addition, if a study aims at developing a model incorporating biomarkers, longitudinal biomarker observations or previously reported models for treatment-biomarkers interaction are required. If no specific biological process is considered, the selection of model structures can also depend on the model fit to the data as long as the model is physiologically or biologically plausible.

Among the functions of the natural tumor growth (Eqs. 2.1–2.8), which are always part of the tumor dynamics models, the exponential growth model has been the most frequently selected in clinical studies. The logistic growth model was normally satisfactorily applied when the maximum tumor capacity was fixed. The selection of the basic functions could also depend on the model fit to the data. More than one available pretreatment tumor size measurement would be helpful to find the best fit natural growth model and would enable a more accurate estimate of the tumor natural growth rate.

**Table 2.3:** Data input and knowledge requirement, study type, and objectives (besides characterizing treatment effect in cancer patients) for applying different model structures

| Models  | Data input and knowledge requirement   | Study types  | Study objective  |
|---|--|--|--|
| <b>Tumor growth models</b>                            |  |  |  |
| <b>Models considering tumor heterogeneity (ODEs)</b>  |  |  |  |
| Proliferative + Quiescent (Eqs. 2.9–2.10)             | <ul style="list-style-type: none"> <li>Longitudinal TS measurement</li> <li>Mechanism of treatment (cell cycle specific or not)</li> <li>Applicable for different treatments and cancer types</li> <li>Applicable for monotherapy or combination therapy</li> </ul>  | <ul style="list-style-type: none"> <li>Estimation based study and simulation study</li> <li>Mixed-effect model possible</li> </ul> | <ul style="list-style-type: none"> <li>Optimize treatment</li> </ul>   |
| Sensitive + Resistant (Eqs. 2.11–2.13)                | <ul style="list-style-type: none"> <li>Longitudinal TS measurement</li> <li>Applicable for different treatments and cancer types</li> <li>Applicable for monotherapy (or combination therapy)</li> </ul>   | <ul style="list-style-type: none"> <li>Estimation based study and simulation study</li> <li>Mixed-effect model possible</li> </ul> | <ul style="list-style-type: none"> <li>Identify resistance type (acquired or primary) and mechanism</li> </ul>   |
| Model developed by Ieta et al. (Eq. 2.12)             | <ul style="list-style-type: none"> <li>IAS and CAS</li> <li>Prostate cancer</li> </ul>   | <ul style="list-style-type: none"> <li>Simulation study</li> </ul>   | <ul style="list-style-type: none"> <li>Describe and predict PSA change under treatment</li> </ul>  |
| Model developed by Hirata et al. (Eq. 2.13)           | <ul style="list-style-type: none"> <li>Longitudinal PSA measurement</li> <li>IAS and CAS</li> <li>Prostate cancer</li> </ul>   | <ul style="list-style-type: none"> <li>Estimation based study</li> <li>Estimate parameters for each subject</li> </ul>             | <ul style="list-style-type: none"> <li>Describe and predict PSA change under treatment</li> <li>Optimize treatment</li> <li>Individualize treatment</li> </ul> |
| <b>Models incorporating biological factors (ODEs)</b> |  |  |  |
| Angiogenesis biomarkers (Eq. 2.14)                    | <ul style="list-style-type: none"> <li>Longitudinal TS measurement</li> <li>Longitudinal biomarkers measurement or previously reported models for treatment-biomarker interaction</li> <li>Mechanism of treatment</li> <li>Applied mainly for antiangiogenesis treatment, monotherapy or combination therapy</li> <li>Applicable for different cancer types</li> </ul> | <ul style="list-style-type: none"> <li>Estimation based study</li> <li>Mixed-effect model possible</li> </ul>                      | <ul style="list-style-type: none"> <li>Identify clinically relevant outcome predictors and optimal time to measure the biomarkers</li> </ul>                   |

|   |   |   |  |
|---|---|---|--|
| <b>Tumor vascular support (Eqs. 2.15–2.16)</b>              | <ul style="list-style-type: none"> <li>Longitudinal TS measurement</li> <li>Mechanism of treatment</li> <li>Applicable for different treatments and cancer types</li> <li>Applicable for monotherapy (or combination therapy)</li> </ul>  | <ul style="list-style-type: none"> <li>Estimation based study and simulation study</li> <li>Mixed-effect model possible</li> </ul>          | <ul style="list-style-type: none"> <li>Optimize treatment</li> </ul>   |
| <b>Immune system (Eqs. 2.17–2.18)</b>                       | <ul style="list-style-type: none"> <li>Longitudinal TS / PSA measurement</li> <li>Immunotherapy</li> <li>Mechanism of treatment</li> <li>Applicable for different cancer types</li> </ul>   | <ul style="list-style-type: none"> <li>Estimation based study and simulation study</li> <li>Estimate parameters for each subject</li> </ul> | <ul style="list-style-type: none"> <li>Optimize treatment</li> </ul>   |
| <b>Immune system (Eqs. 2.19–2.20)</b>                       | <ul style="list-style-type: none"> <li>General cancer</li> <li>Chemotherapy</li> </ul>  | <ul style="list-style-type: none"> <li>Simulation study</li> </ul>  | <ul style="list-style-type: none"> <li>Optimize treatment</li> </ul>   |
| <b>Treatment effect model (ODEs)</b>                        |   |   |  |
| <b>First-order treatment effect (Eq. 2.21)</b>              | <ul style="list-style-type: none"> <li>Drug dependent</li> <li>Parameter can be different for different dose group</li> </ul>   | <ul style="list-style-type: none"> <li>Estimation based study and simulation study</li> <li>Mixed-effect model possible</li> </ul>          | <ul style="list-style-type: none"> <li>Characterize treatment effect</li> </ul>  |
| <b>Exposure-dependent treatment effect (Eqs. 2.22–2.25)</b> | <ul style="list-style-type: none"> <li>Longitudinal concentration data</li> <li>Or PK model (newly developed or previously published) for simulating drug exposure, or dose (as a metric of drug exposure)</li> <li>Applicable for different treatments and cancer types</li> <li>Applicable for monotherapy or combination therapy</li> <li>A compartment for damaged cells (Eq. 2.24) applied mainly for chemotherapy and/or radio therapy</li> </ul> | <ul style="list-style-type: none"> <li>Estimation based study and simulation study</li> <li>Mixed-effect model possible</li> </ul>          | <ul style="list-style-type: none"> <li>Characterize relationship between tumor size change and treatment exposure</li> <li>Optimize treatment</li> </ul> |
| <b>Algebraic equation</b>                                   |   |   |  |
| <b>Two-phase model (Eqs. 2.26–2.28)</b>                     | <ul style="list-style-type: none"> <li>Longitudinal TS/PSA data</li> <li>PK information is not necessary</li> <li>Applicable for different treatments and cancer types</li> <li>Applicable for monotherapy or combination therapy</li> </ul>  | <ul style="list-style-type: none"> <li>Estimation based study</li> <li>Estimate parameters for each subject</li> </ul>                      | <ul style="list-style-type: none"> <li>Investigate the relationship between tumor growth rate and survival</li> </ul>                                    |

Table 2.3 continues on next page.

**Table 2.3: Continued**

| Models   | Data input and knowledge requirement  | Study types   | Study objective  |
|--|---|---|--|
| Model developed by Wang et al. (Eq. 2.29)                    | <ul style="list-style-type: none"> <li>Longitudinal TS data</li> <li>PK information is not necessary</li> <li>Applicable for different treatments, monotherapy or combination therapy</li> <li>Mainly in NSCLC patients</li> </ul>  | <ul style="list-style-type: none"> <li>Estimation based study</li> <li>Mixed-effect model possible</li> </ul>   | <ul style="list-style-type: none"> <li>Elucidate relationship between metrics of tumor size and survival</li> </ul>  |
| Extension of model developed by Wang et al. (Eqs. 2.30–2.31) | <ul style="list-style-type: none"> <li>Longitudinal TS data</li> <li>Mainly in RCC patients treated with pazopanib</li> <li>Dose–depended treatment effect can be incorporated</li> </ul>   | <ul style="list-style-type: none"> <li>Estimation based study</li> <li>Mixed-effect model possible</li> </ul>   | <ul style="list-style-type: none"> <li>–</li> </ul>  |
| Simplified TGI model (Eq. 2.32)                              | <ul style="list-style-type: none"> <li>Longitudinal TS data</li> <li>PK information is not necessary</li> <li>Applicable for different treatments and cancer types</li> <li>Applicable for monotherapy or combination therapy</li> </ul>  | <ul style="list-style-type: none"> <li>Estimation based study</li> <li>Mixed-effect model possible</li> </ul>   | <ul style="list-style-type: none"> <li>Elucidate relationship between metrics of tumor size and survival</li> </ul>  |
| <b>Partial differential equation</b>                         |   |   |  |
| Proliferation–invasion model (Eqs. 2.33–2.38)                | <ul style="list-style-type: none"> <li>Two pair of T1-Gd and T2 MRI data before treatment</li> <li>Or one pair of T1-Gd and T2 MRI data before treatment, with available parameters in previous studies</li> <li>Glioblastoma</li> <li>Resection, radiotherapy, or without treatment</li> </ul> | <ul style="list-style-type: none"> <li>Estimation based study and simulation study</li> <li>Estimate parameters for each subject</li> </ul>                             | <ul style="list-style-type: none"> <li>Predict patients' survival and tumor size after treatment</li> <li>Simulate patients' outcome under different treatment</li> <li>Personalize treatment</li> <li>Investigate the application of a novel model</li> </ul> |
|  | <ul style="list-style-type: none"> <li>DW-MRI data, one before and two after treatment, for tumor cell numbers calculation</li> <li>Breast cancer patients with neoadjuvant therapy</li> <li>Consider mass effect</li> </ul>  | <ul style="list-style-type: none"> <li>Estimate parameters for each subject (the growth rate is the net growth rate considering both tumor growth and death)</li> </ul> | <ul style="list-style-type: none"> <li>Predict tumor burden at the conclusion of treatment.</li> </ul>   |

| Tumor resistance evolution models  |  | Probability model (Eq. 2.39)  |  | Stochastic differential equation (Eq. 2.40)        |  | ODEs (Eqs. 2.41–2.44)   |   | Game theory (Eqs. 2.45–2.47)                                      |                                      | Integral-differential equation (Eq. 2.48)               |   |
|--|--|---|--|--|--|---|---|---|--------------------------------------|---|---|
| Parameter values (from previous studies or by estimating clinical or pre-clinical data)                                  | • Parameter values (from previous studies or by estimating clinical or pre-clinical data)                                  | • Simulation study  | • Simulation study   | • Simulation study                                 | • Simulation study                                 | • General cancer and treatment  | • General cancer and treatment  | • Payoff matrix   | • General cancer and treatment       | • General cancer and treatment                          | • General cancer and treatment                          |
| If available, longitudinal or static ctDNA measurement can be used to estimate parameters or evaluate simulation results | • If available, longitudinal or static ctDNA measurement can be used to estimate parameters or evaluate simulation results | • Apply proposed equations in data obtained in clinical study (mainly in lung cancer, colorectal and leukaemia treated with targeted treatment) | • No mixed-effect model applied yet  | • No mixed-effect model applied yet                | • No mixed-effect model applied yet                | • Single or multidrug resistance  | • Single or multidrug resistance  | • Combination treatment   | • Single or multidrug resistance     | • Single or multidrug resistance                        | • Single or multidrug resistance                        |
| General cancer and treatment   | • General cancer and treatment   | • Estimate the detection time   | • Predict treatment outcome and optimize treatment   | • Predict treatment outcome and optimize treatment | • Predict treatment outcome and optimize treatment | • Single or multidrug resistance  | • Mechanism of treatment  | • Mainly in melanoma patients treated with BRAF and MEK inhibitor | • General cancer and treatment       | • General cancer and treatment                          | • General cancer and treatment                          |
| Single or multidrug resistance   | • Single or multidrug resistance   | • Demonstrate if resistance exist at the start of treatment   | • Connect cellular mechanisms underlying cancer drug resistance to patients survival.              | • No mixed-effect model applied yet                | • No mixed-effect model applied yet                | • If available, longitudinal ctDNA measurement can be used to evaluate simulation results | • If available, longitudinal ctDNA measurement can be used to evaluate simulation results | • No mixed-effect model applied yet                               | • No mixed-effect model applied yet  | • No mixed-effect model applied yet                     | • No mixed-effect model applied yet                     |
| Elucidate the resistance evolution of cancer   | • Elucidate the resistance evolution of cancer   | • Propose equations for estimating $E_{R^*} P_{R^*}$ total tumor cells, and treatment success rate  | • Propose equations for estimating $E_{R^*} P_{R^*}$ total tumor cells, and treatment success rate | • Predict treatment outcome and optimize treatment | • Predict treatment outcome and optimize treatment | • To understand experimental results  | • To understand experimental results  | • To understand experimental results                              | • To understand experimental results | • Describing multidrug resistance                       | • Describing multidrug resistance                       |
| Propose equations for estimating $E_{R^*} P_{R^*}$ total tumor cells, and treatment success rate                         | • Propose equations for estimating $E_{R^*} P_{R^*}$ total tumor cells, and treatment success rate                         | • Estimate the detection time   | • Demonstrate if resistance exist at the start of treatment  | • Propose model                                    | • Propose model                                    | • Demonstrating the evolving resistance under treatment                                   | • Demonstrating the evolving resistance under treatment                                   | • Propose model   | • Propose model                      | • Demonstrating the evolving resistance under treatment | • Demonstrating the evolving resistance under treatment |

The treatment effect can be characterized in a drug-dependent manner or exposure-dependent manner. If a study does not focus on investigating the exposure-effect relationship, using a model with drug-dependent tumor shrinkage will be enough and drug-exposure information is not required. For studies aiming at characterizing the relationship between drug exposure/dose and tumor response and/or optimizing treatment regimens for patients based on simulations, the exposure-dependent (or dose-dependent) treatment effect structure should be applied. To estimate drug exposure, longitudinal concentration data for PK model development or a previously reported PK model are needed. In addition, the previous knowledge of the treatment mechanism may also be required to appropriately characterize the treatment effect, especially when applying models considering biological factors.

The proliferation-invasion model that is displayed by PDE has mainly been applied to investigate glioblastoma or breast cancer based on available MRI measurements. The required parameters can be estimated for each patient separately based on two sets of pretreatment MRI data or one before treatment and one thereafter. Simulations can then be performed to predict patient outcome with the model or with the velocity function of tumor radius expansion (Eq. 2.34). The mixed-effect modeling approach has not been found to be applied in these studies yet.

The model structures of tumor resistance evolution have been mainly applied to perform simulations to understand evolving resistance and optimize the treatment. The equations derived from the branching process can be applied to answer clinical questions. Available longitudinal or static ctDNA measurements can be utilized to determine the parameter values and to evaluate the simulation results. Although no mixed-effect modeling approach has been applied in these studies yet, the model structures displayed by ODEs, which can provide comparable results to stochastic models, are considered to be potentially able to account for interindividual variability.

## 6. Discussion

Overcoming treatment resistance with a better understanding of cancer evolution and personalizing treatment brings opportunities to treat cancer as a chronic disease and has been increasingly studied in the oncology field. Model-based approaches incorporating tumor growth and resistance evolution may help achieve this goal. By applying mathematical models, prior knowledge derived from clinical trials and routine patients care can be utilized to quantitatively understand drug PK profiles, the drug-response relationship,

and evolving resistance in cancer patients. These profiles can be predicted accordingly for future patients, which could be beneficial for identifying optimized therapeutic regimens. Furthermore, by accounting for interindividual variability with a mixed-effect modeling approach, treatment individualization can also be designed and guided rationally [97].

In the current review, feasible model structures that have been used to describe and predict tumor dynamics and resistance evolution during treatment for patients with solid tumors are discussed. Models concerning tumor evolution in leukemia were included because they provide reference value for solid tumors. Apart from what has been introduced, more extensive models have also been found in the literature search, such as agent-based models and the cellular automata approach. The agent-based models often include components from two or more spatial or temporal scales, ranging from molecular to tissue [7], and the cellular automata approach adopts a discrete dynamical system of time and space [9]. Although tumor growth can be simulated in silico realistically with these approaches, because they require infeasible information input (e.g., cell location, nutrition distribution, and/or oxygen amount) from clinical patients, they were excluded from the current review. Studies applying the proliferation-invasion model, which are expressed with PDE, were not excluded, although tumor cell location is also one of the variables. It is because two main parameters in this model structure, the diffusion coefficient  $D_{if}$  and growth rate constant  $\rho$ , can be estimated directly based on MRI results obtained from patients, and the velocity of tumor radius expansion can then be estimated and utilized for prediction.

Models displayed by ODEs, algebraic equations, and PDE are commonly reported for the modeling of tumor size change and, in the case of prostate cancer, PSA amount change. Five main basic natural tumor growth model structures were frequently reported. The diversity in model selection can be explained by the difficulties of assessing real long-term natural tumor growth pattern in patients [11]. Although setting the maximum boundaries of tumor growth is more biologically plausible, the models without such limits, especially the exponential growth models, have also been used extensively. The concept of linear growth is also reflected in the studies that applied the proliferation-invasion model, as the expansion of tumor radius has a constant velocity under such a model, and this concept has been used to predict tumor radius [63-65].

For characterizing treatment effect, empirical methods are relatively simple to apply for describing the effect of various kinds of drugs and are therefore more generally applicable. The shrinkage rate of tumor burden caused by treatment can be described to be proportional to drug exposure/dose or by utilizing drug-dependent parameters, although the latter method does not allow differentiation among different dosing regimens. In addition,

when the dynamics of biomarkers are available and are incorporated in the tumor dynamics models, the treatment effect on the production of biomarkers can be integrated according to drug mechanism [31, 39]. Furthermore, the regrowth of a tumor during treatment can be considered in several ways. Studies applying algebraic equations generally characterize the decline and regrowth of a tumor by a single equation. For studies that used ODEs, tumor regrowth was mainly characterized by separating the tumor in two parts consisting of drug-sensitive cells and drug-resistant cells or by adding the  $e^{-\lambda t}$  term.

The resistance evolution of cancer has been mainly characterized by stochastic models within which the branching process is reported most frequently. However, in studies applying the branching process, the focus was mainly on the expected outcome of tumor evolution, such as the  $P_R$  and  $E_R$ . Therefore, relatively simpler deterministic models are considered to be good alternative choices. It has already been demonstrated that ODE models can provide comparable results to those that are derived from stochastic models [91]. Given that the goal is to characterize evolving tumor resistance based on clinical data, applying deterministic models might be more suitable given clinical available data generally represents the apparent response of each patient.

Among the studies included in this review, the detailed data of resistance evolution have not yet been incorporated in tumor size-based modeling of anticancer treatment response. However, genetic biomarkers that represent tumor heterogeneity and resistance evolution become increasingly available as a result of novel technologies. For example, in a clinical setting, a feasible genetic biomarker that is also correlated with tumor burden has been identified as ctDNA [98]. Three of the included studies have already utilized the available ctDNA data to support the estimation of parameters in the tumor evolution model or to evaluate the model simulation results [77, 79, 90]. It has also been demonstrated that the mutation in ctDNA, which represents treatment resistance, is detectable before disease progression [99], suggesting the predictive value of ctDNA to the development of drug resistance. By applying longitudinal monitoring of ctDNA, an adaptive treatment for individual patients may be achieved by selecting drugs that target emerging actionable mutations [98]. Therefore, it is feasible to obtain the information of evolving cancer resistance and, to increase the chance to overcome treatment resistance, it would be helpful if such information could be incorporated in future model-based studies.

Based on what was learned from previous reported studies, as is introduced in this review, model structures displayed by ODEs are considered to be feasible for the characterization of both tumor size change and resistance evolution in cancer patients. A mathematical model can be developed based on the input data of tumor size, mutation load of ctDNA,

and treatment information over time. The emergence and dynamics of mutations in ctDNA can provide insight of the occurrence, growth, decay, and mutation for different tumor subclones. External data sets, if available, can be used to further evaluate the developed model structure. Subsequently, the effect of sequential treatment regimens with different dose levels or starting times of therapies can be explored with simulation and thereby to facilitate the identification of an optimal regimen. Moreover, because the parameter values can be estimated for each individual and the variability of which can be partially explained by patient characteristics, the treatment personalization can also be rationally guided based on the modeling and simulation results. These will be the ultimate output of the model-based study.

However, challenges remain beyond what is already stated. First, in terms of data collection, previous knowledge of the mutations that represent resistant subclones is required. Second, if sequencing data of the subclones (ctDNA) over time are available, efforts need to be made to handle the vast amount of genetic data in a quantitative manner in relation to tumor size dynamics. Third, the optimal method on how to predict a newly acquired mutation that has not yet occurred in the data needs to be further explored. Finally, because in-depth knowledge is required from multiple aspects of tumor and clone dynamics as well as complex modeling and simulation, a multidisciplinary collaboration is essential to enable the achievement of the ultimate goal of optimizing and personalizing anticancer treatment.

In conclusion, based on a systematic search of studies from the literature, mathematical models that have been used to describe and predict tumor size change, drug effect, and resistance evolution based on clinically available data were introduced in this review. The results may facilitate the model-based anticancer treatment response analysis that accounts for both tumor growth inhibition and resistance evolution, although important challenges still need to be overcome. An ultimate model structure handling all of these aspects would be of great benefit for optimizing and personalizing anticancer treatment.

## References

1. Sun X, Hu B. Mathematical modeling and computational prediction of cancer drug resistance. *Brief Bioinform.* 2018;19(6):1382-99. doi:10.1093/bib/bbx065.
2. Beksac AT, Paulucci DJ, Blum KA, Yadav SS, Sfakianos JP, Badani KK. Heterogeneity in renal cell carcinoma. *Urol Oncol.* 2017;35(8):507-15. doi:10.1016/j.urolonc.2017.05.006.
3. Buil-Bruna N, Lopez-Picazo JM, Martin-Algarra S, Troconiz IF. Bringing Model-Based Prediction to Oncology Clinical Practice: A Review of Pharmacometrics Principles and Applications. *Oncologist.* 2016;21(2):220-32. doi:10.1634/theoncologist.2015-0322.
4. Kimko H, Pinheiro J. Model-based clinical drug development in the past, present and future: a commentary. *Br J Clin Pharmacol.* 2015;79(1):108-16. doi:10.1111/bcp.12341.
5. van Hasselt JG, van der Graaf PH. Towards integrative systems pharmacology models in oncology drug development. *Drug Discov Today Technol.* 2015;15:1-8. doi:10.1016/j.ddtec.2015.06.004.
6. Barbolosi D, Ciccolini J, Lacarelle B, Barlesi F, Andre N. Computational oncology--mathematical modelling of drug regimens for precision medicine. *Nat Rev Clin Oncol.* 2016;13(4):242-54. doi:10.1038/nrclinonc.2015.204.
7. Wang Z, Butner JD, Kerketta R, Cristini V, Deisboeck TS. Simulating cancer growth with multiscale agent-based modeling. *Semin Cancer Biol.* 2015;30:70-8. doi:10.1016/j.semancer.2014.04.001.
8. Meghdadi N, Soltani M, Niroomand-Oscuui H, Ghalichi F. Image based modeling of tumor growth. *Australas Phys Eng Sci Med.* 2016;39(3):601-13. doi:10.1007/s13246-016-0475-5.
9. Masoudi-Nejad A, Bidkhori G, Hosseini Ashtiani S, Najafi A, Bozorgmehr JH, Wang E. Cancer systems biology and modeling: microscopic scale and multiscale approaches. *Semin Cancer Biol.* 2015;30:60-9. doi:10.1016/j.semancer.2014.03.003.
10. Ribba B, Holford NH, Magni P, Troconiz I, Gueorguieva I, Girard P, et al. A review of mixed-effects models of tumor growth and effects of anticancer drug treatment used in population analysis. *CPT Pharmacometrics Syst Pharmacol.* 2014;3:e113. doi:10.1038/psp.2014.12.
11. Bender BC, Schindler E, Friberg LE. Population pharmacokinetic-pharmacodynamic modelling in oncology: a tool for predicting clinical response. *Br J Clin Pharmacol.* 2015;79(1):56-71. doi:10.1111/bcp.12258.
12. Kim C, Gao R, Sei E, Brandt R, Hartman J, Hatschek T, et al. Chemoresistance Evolution in Triple-Negative Breast Cancer Delineated by Single-Cell Sequencing. *Cell.* 2018;173(4):879-93 e13. doi:10.1016/j.cell.2018.03.041.
13. Beerenwinkel N, Schwarz RF, Gerstung M, Markowetz F. Cancer evolution: mathematical models and computational inference. *Syst Biol.* 2015;64(1):e1-25. doi:10.1093/sysbio/syu081.
14. Zhao B, Hemann MT, Lauffenburger DA. Modeling Tumor Clonal Evolution for Drug Combinations Design. *Trends Cancer.* 2016;2(3):144-58. doi:10.1016/j.trecan.2016.02.001.
15. Chisholm RH, Lorenzi T, Clairambault J. Cell population heterogeneity and evolution towards drug resistance in cancer: Biological and mathematical assessment, theoretical treatment optimisation. *Biochim Biophys Acta.* 2016;1860(11 Pt B):2627-45. doi:10.1016/j.bbagen.2016.06.009.
16. Attolini CS, Michor F. Evolutionary theory of cancer. *Ann N Y Acad Sci.* 2009;1168:23-51. doi:10.1111/j.1749-6632.2009.04880.x.
17. Foo J, Michor F. Evolution of acquired resistance to anti-cancer therapy. *J Theor Biol.* 2014;355:10-20. doi:10.1016/j.jtbi.2014.02.025.
18. Stein A, Wang W, Carter AA, Chiparus O, Hollaender N, Kim H, et al. Dynamic tumor modeling of the dose-response relationship for everolimus in metastatic renal cell carcinoma using data from the phase 3 RECORD-1 trial. *BMC Cancer.* 2012;12:311.

2

19. Cameron DA, Gregory WM, Bowman A, Anderson ED, Levack P, Forouhi P, et al. Identification of long-term survivors in primary breast cancer by dynamic modelling of tumour response. *Br J Cancer*. 2000;83(1):98-103. doi:10.1054/bjoc.2000.1216.
20. Claret L, Girard P, Hoff PM, Van Cutsem E, Zuiderveld KP, Jorga K, et al. Model-based prediction of phase III overall survival in colorectal cancer on the basis of phase II tumor dynamics. *J Clin Oncol*. 2009;27(25):4103-8. doi:10.1200/jco.2008.21.0807.
21. De Buck SS, Jakab A, Boehm M, Bootle D, Juric D, Quadt C, et al. Population pharmacokinetics and pharmacodynamics of BYL719, a phosphoinositide 3-kinase antagonist, in adult patients with advanced solid malignancies. *Br J Clin Pharmacol*. 2014;78(3):543-55. doi:10.1111/bcp.12378.
22. Panetta JC, Schaiquevich P, Santana VM, Stewart CF. Using pharmacokinetic and pharmacodynamic modeling and simulation to evaluate importance of schedule in topotecan therapy for pediatric neuroblastoma. *Clin Cancer Res*. 2008;14(1):318-25. doi:10.1158/1078-0432.ccr-07-1243.
23. Ideta AM, Tanaka G, Takeuchi T, Aihara K. A Mathematical Model of Intermittent Androgen Suppression for Prostate Cancer. *Journal of Nonlinear Science*. 2008;18(6):593-614. doi:10.1007/s00332-008-9031-0.
24. Ollier E, Mazzocco P, Ricard D, Kaloshi G, Idbaih A, Alentorn A, et al. Analysis of temozolomide resistance in low-grade gliomas using a mechanistic mathematical model. *Fundam Clin Pharmacol*. 2017;31(3):347-58. doi:10.1111/fcp.12259.
25. Ribba B, Kaloshi G, Peyre M, Ricard D, Calvez V, Tod M, et al. A tumor growth inhibition model for low-grade glioma treated with chemotherapy or radiotherapy. *Clin Cancer Res*. 2012;18(18):5071-80. doi:10.1158/1078-0432.CCR-12-0084.
26. Atuegwu NC, Arlinghaus LR, Li X, Welch EB, Chakravarthy BA, Gore JC, et al. Integration of diffusion-weighted MRI data and a simple mathematical model to predict breast tumor cellularity during neoadjuvant chemotherapy. *Magn Reson Med*. 2011;66(6):1689-96. doi:10.1002/mrm.23203.
27. Belfatto A, Riboldi M, Ciardo D, Cecconi A, Lazzari R, Jereczek-Fossa BA, et al. Adaptive Mathematical Model of Tumor Response to Radiotherapy Based on CBCT Data. *IEEE journal of biomedical and health informatics*. 2016;20(3):802-9. doi:10.1109/jbhi.2015.2453437.
28. Yu RX, Holmgren E. Endpoints for agents that slow tumor growth. *Contemp Clin Trials*. 2007;28(1):18-24. doi:10.1016/j.cct.2006.05.011.
29. Bethge A, Schumacher U, Wedemann G. Simulation of metastatic progression using a computer model including chemotherapy and radiation therapy. *J Biomed Inform*. 2015;57:74-87. doi:10.1016/j.jbi.2015.07.011.
30. Simeoni M, Magni P, Cammia C, De Nicolao G, Croci V, Pesenti E, et al. Predictive pharmacokinetic-pharmacodynamic modeling of tumor growth kinetics in xenograft models after administration of anticancer agents. *Cancer Res*. 2004;64(3):1094-101.
31. Ouerdani A, Goutagny S, Kalamarides M, Troconiz IF, Ribba B. Mechanism-based modeling of the clinical effects of bevacizumab and everolimus on vestibular schwannomas of patients with neurofibromatosis type 2. *Cancer Chemother Pharmacol*. 2016;77(6):1263-73. doi:10.1007/s00280-016-3046-2.
32. Stura I, Venturino E, Guiot C. A two-clones tumor model: Spontaneous growth and response to treatment. *Math Biosci*. 2016;271:19-28. doi:10.1016/j.mbs.2015.10.014.
33. Gardner SN. Modeling multi-drug chemotherapy: tailoring treatment to individuals. *J Theor Biol*. 2002;214(2):181-207. doi:10.1006/jtbi.2001.2459.
34. Morken JD, Packer A, Everett RA, Nagy JD, Kuang Y. Mechanisms of resistance to intermittent androgen deprivation in patients with prostate cancer identified by a novel computational method. *Cancer Res*. 2014;74(14):3673-83. doi:10.1158/0008-5472.can-13-3162.

35. Yang J, Zhao TJ, Yuan CQ, Xie JH, Hao FF. A nonlinear competitive model of the prostate tumor growth under intermittent androgen suppression. *J Theor Biol.* 2016;404:66-72. doi:10.1016/j.jtbi.2016.05.033.
36. Hirata Y, Bruchovsky N, Aihara K. Development of a mathematical model that predicts the outcome of hormone therapy for prostate cancer. *J Theor Biol.* 2010;264(2):517-27. doi:10.1016/j.jtbi.2010.02.027.
37. Tanaka G, Hirata Y, Goldenberg SL, Bruchovsky N, Aihara K. Mathematical modelling of prostate cancer growth and its application to hormone therapy. *Philosophical transactions Series A, Mathematical, physical, and engineering sciences.* 2010;368(1930):5029-44. doi:10.1098/rsta.2010.0221.
38. Hirata Y, Azuma S, Aihara K. Model predictive control for optimally scheduling intermittent androgen suppression of prostate cancer. *Methods.* 2014;67(3):278-81. doi:10.1016/jymeth.2014.03.018.
39. Hansson EK, Amantea MA, Westwood P, Milligan PA, Houk BE, French J, et al. PKPD Modeling of VEGF, sVEGFR-2, sVEGFR-3, and sKIT as Predictors of Tumor Dynamics and Overall Survival Following Sunitinib Treatment in GIST. *CPT Pharmacometrics Syst Pharmacol.* 2013;2:e84. doi:10.1038/psp.2013.61.
40. Ouerdani A, Struemper H, Suttle AB, Ouellet D, Ribba B. Preclinical Modeling of Tumor Growth and Angiogenesis Inhibition to Describe Pazopanib Clinical Effects in Renal Cell Carcinoma. *CPT Pharmacometrics Syst Pharmacol.* 2015;4(11):660-8. doi:10.1002/psp.4.12001.
41. Mellal L, Folio D, Belharet K, Ferreira A. Modeling of Optimal Targeted Therapies Using Drug-Loaded Magnetic Nanoparticles for Liver Cancer. *IEEE Trans Nanobioscience.* 2016;15(3):265-74. doi:10.1109/tnb.2016.2535380.
42. Ledzewicz U, Marriott J, Maurer H, Schattler H. Realizable protocols for optimal administration of drugs in mathematical models for anti-angiogenic treatment. *Math Med Biol.* 2010;27(2):157-79. doi:10.1093/imammb/dqp012.
43. Bumimovich-Mendrazitsky S, Halachmi S, Kronik N. Improving Bacillus Calmette-Guerin (BCG) immunotherapy for bladder cancer by adding interleukin 2 (IL-2): a mathematical model. *Math Med Biol.* 2016;33(2):159-88. doi:10.1093/imammb/dqv007.
44. Kronik N, Kogan Y, Elishmereni M, Halevi-Tobias K, Vuk-Pavlovic S, Agur Z. Predicting outcomes of prostate cancer immunotherapy by personalized mathematical models. *PLoS One.* 2010;5(12):e15482. doi:10.1371/journal.pone.0015482.
45. De Pillis LG, Radunskaya A. The dynamics of an optimally controlled tumor model: A case study. *Math Comput Model.* 2003;37(11):1221-44. doi:Pii S0895-7177(03)00133-X. doi:10.1016/S0895-7177(03)00133-X.
46. Lobato FS, Machado VS, Steffen V, Jr. Determination of an optimal control strategy for drug administration in tumor treatment using multi-objective optimization differential evolution. *Comput Methods Programs Biomed.* 2016;131:51-61. doi:10.1016/j.cmpb.2016.04.004.
47. de Pillis LG, Gu W, Fister KR, Head T, Maples K, Murugan A, et al. Chemotherapy for tumors: an analysis of the dynamics and a study of quadratic and linear optimal controls. *Math Biosci.* 2007;209(1):292-315. doi:10.1016/j.mbs.2006.05.003.
48. Majid O, Gupta A, Reyderman L, Olivo M, Hussein Z. Population pharmacometric analyses of eribulin in patients with locally advanced or metastatic breast cancer previously treated with anthracyclines and taxanes. *J Clin Pharmacol.* 2014;54(10):1134-43. doi:10.1002/jcph.315.
49. Zecchin C, Gueorguieva I, Enas NH, Friberg LE. Models for change in tumour size, appearance of new lesions and survival probability in patients with advanced epithelial ovarian cancer. *Br J Clin Pharmacol.* 2016;82(3):717-27. doi:10.1111/bcp.12994.

50. Stein WD, Figg WD, Dahut W, Stein AD, Hoshen MB, Price D, et al. Tumor growth rates derived from data for patients in a clinical trial correlate strongly with patient survival: a novel strategy for evaluation of clinical trial data. *Oncologist*. 2008;13(10):1046-54. doi:10.1634/theoncologist.2008-0075.

51. Stein WD, Gulley JL, Schlom J, Madan RA, Dahut W, Figg WD, et al. Tumor regression and growth rates determined in five intramural NCI prostate cancer trials: the growth rate constant as an indicator of therapeutic efficacy. *Clin Cancer Res*. 2011;17(4):907-17. doi:10.1158/1078-0432.ccr-10-1762.

52. Wang Y, Sung C, Dartois C, Ramchandani R, Booth BP, Rock E, et al. Elucidation of relationship between tumor size and survival in non-small-cell lung cancer patients can aid early decision making in clinical drug development. *Clin Pharmacol Ther*. 2009;86(2):167-74. doi:10.1038/clpt.2009.64.

53. Bonate PL, Suttle AB. Modeling tumor growth kinetics after treatment with pazopanib or placebo in patients with renal cell carcinoma. *Cancer Chemother Pharmacol*. 2013;72(1):231-40. doi:10.1007/s00280-013-2191-0.

54. Claret L, Gupta M, Han K, Joshi A, Sarapa N, He J, et al. Evaluation of tumor-size response metrics to predict overall survival in Western and Chinese patients with first-line metastatic colorectal cancer. *J Clin Oncol*. 2013;31(17):2110-4. doi:10.1200/JCO.2012.45.0973.

55. Stein WD, Yang J, Bates SE, Fojo T. Bevacizumab reduces the growth rate constants of renal carcinomas: a novel algorithm suggests early discontinuation of bevacizumab resulted in a lack of survival advantage. *Oncologist*. 2008;13(10):1055-62. doi:10.1634/theoncologist.2008-0016.

56. Li CH, Bies RR, Wang Y, Sharma MR, Karovic S, Werk L, et al. Comparative Effects of CT Imaging Measurement on RECIST End Points and Tumor Growth Kinetics Modeling. *Clin Transl Sci*. 2016;9(1):43-50. doi:10.1111/cts.12384.

57. Claret L, Mercier F, Houk BE, Milligan PA, Bruno R. Modeling and simulations relating overall survival to tumor growth inhibition in renal cell carcinoma patients. *Cancer Chemother Pharmacol*. 2015;76(3):567-73. doi:10.1007/s00280-015-2820-x.

58. Claret L, Bruno R, Lu JF, Sun YN, Hsu CP. Exploratory modeling and simulation to support development of motesanib in Asian patients with non-small cell lung cancer based on MONET1 study results. *Clin Pharmacol Ther*. 2014;95(4):446-51. doi:10.1038/clpt.2014.11.

59. Han K, Claret L, Sandler A, Das A, Jin J, Bruno R. Modeling and simulation of maintenance treatment in first-line non-small cell lung cancer with external validation. *BMC Cancer*. 2016;16:473. doi:10.1186/s12885-016-2455-2.

60. Han K, Claret L, Piao Y, Hegde P, Joshi A, Powell JR, et al. Simulations to Predict Clinical Trial Outcome of Bevacizumab Plus Chemotherapy vs. Chemotherapy Alone in Patients With First-Line Gastric Cancer and Elevated Plasma VEGF-A. *CPT Pharmacometrics Syst Pharmacol*. 2016;5(7):352-8. doi:10.1002/psp.4.12064.

61. Swanson KR, Rostomily RC, Alvord EC, Jr. A mathematical modelling tool for predicting survival of individual patients following resection of glioblastoma: a proof of principle. *Br J Cancer*. 2008;98(1):113-9. doi:10.1038/sj.bjc.6604125.

62. Mandonnet E, Pallud J, Clatz O, Taillandier L, Konukoglu E, Duffau H, et al. Computational modeling of the WHO grade II glioma dynamics: principles and applications to management paradigm. *Neurosurg Rev*. 2008;31(3):263-9. doi:10.1007/s10143-008-0128-6.

63. Wang CH, Rockhill JK, Mrugala M, Peacock DL, Lai A, Jusenius K, et al. Prognostic significance of growth kinetics in newly diagnosed glioblastomas revealed by combining serial imaging with a novel biomathematical model. *Cancer Res*. 2009;69(23):9133-40. doi:10.1158/0008-5472.can-08-3863.

64. Rockne R, Rockhill JK, Mrugala M, Spence AM, Kalet I, Hendrickson K, et al. Predicting the efficacy of radiotherapy in individual glioblastoma patients *in vivo*: a mathematical modeling approach. *Phys Med Biol.* 2010;55(12):3271-85. doi:10.1088/0031-9155/55/12/001.
65. Szeto MD, Chakraborty G, Hadley J, Rockne R, Muzi M, Alvord EC, Jr., et al. Quantitative metrics of net proliferation and invasion link biological aggressiveness assessed by MRI with hypoxia assessed by *FMISO-PET* in newly diagnosed glioblastomas. *Cancer Res.* 2009;69(10):4502-9. doi:10.1158/0008-5472.can-08-3884.
66. Le M, Delingette H, Kalpathy-Cramer J, Gerstner ER, Batchelor T, Unkelbach J, et al. Personalized Radiotherapy Planning Based on a Computational Tumor Growth Model. *IEEE Trans Med Imaging.* 2017;36(3):815-25. doi:10.1109/tmi.2016.2626443.
67. Murray JD. Glioblastoma brain tumours: estimating the time from brain tumour initiation and resolution of a patient survival anomaly after similar treatment protocols. *J Biol Dyn.* 2012;6 Suppl 2:118-27. doi:10.1080/17513758.2012.678392.
68. Yankeelov TE, Atuegwu N, Hormuth D, Weis JA, Barnes SL, Miga MI, et al. Clinically relevant modeling of tumor growth and treatment response. *Sci Transl Med.* 2013;5(187):187ps9. doi:10.1126/scitranslmed.3005686.
69. Weis JA, Miga MI, Arlinghaus LR, Li X, Abramson V, Chakravarthy AB, et al. Predicting the Response of Breast Cancer to Neoadjuvant Therapy Using a Mechanically Coupled Reaction-Diffusion Model. *Cancer Res.* 2015;75(22):4697-707. doi:10.1158/0008-5472.can-14-2945.
70. Weis JA, Miga MI, Arlinghaus LR, Li X, Chakravarthy AB, Abramson V, et al. A mechanically coupled reaction-diffusion model for predicting the response of breast tumors to neoadjuvant chemotherapy. *Phys Med Biol.* 2013;58(17):5851-66. doi:10.1088/0031-9155/58/17/5851.
71. Harpold HL, Alvord EC, Jr., Swanson KR. The evolution of mathematical modeling of glioma proliferation and invasion. *J Neuropathol Exp Neurol.* 2007;66(1):1-9. doi:10.1097/nen.0b013e31802d9000.
72. Sakkalis V, Roniotis A, Farmaki C, Karatzanis I, Marias K. Evaluation framework for the multilevel macroscopic models of solid tumor growth in the glioma case. *Conf Proc IEEE Eng Med Biol Soc.* 2010;2010:6809-12. doi:10.1109/embc.2010.5625961.
73. Patel V, Hathout L. Image-driven modeling of the proliferation and necrosis of glioblastoma multiforme. *Theor Biol Med Model.* 2017;14(1):10. doi:10.1186/s12976-017-0056-7.
74. Hathout L, Ellingson B, Pope W. Modeling the efficacy of the extent of surgical resection in the setting of radiation therapy for glioblastoma. *Cancer Sci.* 2016;107(8):1110-6. doi:10.1111/cas.12979.
75. Cross W, Graham TA, Wright NA. New paradigms in clonal evolution: punctuated equilibrium in cancer. *J Pathol.* 2016;240(2):126-36. doi:10.1002/path.4757.
76. Iwasa Y, Nowak MA, Michor F. Evolution of resistance during clonal expansion. *Genetics.* 2006;172(4):2557-66. doi:10.1534/genetics.105.049791.
77. Diaz LA, Jr., Williams RT, Wu J, Kinde I, Hecht JR, Berlin J, et al. The molecular evolution of acquired resistance to targeted EGFR blockade in colorectal cancers. *Nature.* 2012;486(7404):537-40. doi:10.1038/nature11219.
78. Komarova NL, Burger JA, Wodarz D. Evolution of ibrutinib resistance in chronic lymphocytic leukemia (CLL). *Proc Natl Acad Sci U S A.* 2014;111(38):13906-11. doi:10.1073/pnas.1409362111.
79. Bozic I, Nowak MA. Timing and heterogeneity of mutations associated with drug resistance in metastatic cancers. *Proc Natl Acad Sci U S A.* 2014;111(45):15964-8. doi:10.1073/pnas.1412075111.
80. Foo J, Michor F. Evolution of resistance to targeted anti-cancer therapies during continuous and pulsed administration strategies. *PLoS Comput Biol.* 2009;5(11):e1000557. doi:10.1371/journal.pcbi.1000557.

2

81. Foo J, Michor F. Evolution of resistance to anti-cancer therapy during general dosing schedules. *J Theor Biol.* 2010;263(2):179-88. doi:10.1016/j.jtbi.2009.11.022.
82. Liu LL, Li F, Pao W, Michor F. Dose-Dependent Mutation Rates Determine Optimum Erlotinib Dosing Strategies for EGFR Mutant Non-Small Cell Lung Cancer Patients. *PLoS One.* 2015;10(11):e0141665. doi:10.1371/journal.pone.0141665.
83. Chakrabarti S, Michor F. Pharmacokinetics and Drug Interactions Determine Optimum Combination Strategies in Computational Models of Cancer Evolution. *Cancer Res.* 2017;77(14):3908-21. doi:10.1158/0008-5472.can-16-2871.
84. Akhmetzhanov AR, Hochberg ME. Dynamics of preventive vs post-diagnostic cancer control using low-impact measures. *eLife.* 2015;4:e06266. doi:10.7554/eLife.06266.
85. Bozic I, Allen B, Nowak MA. Dynamics of targeted cancer therapy. *Trends Mol Med.* 2012;18(6):311-6. doi:10.1016/j.molmed.2012.04.006.
86. Komarova N. Stochastic modeling of drug resistance in cancer. *J Theor Biol.* 2006;239(3):351-66. doi:10.1016/j.jtbi.2005.08.003.
87. Komarova NL, Wodarz D. Drug resistance in cancer: principles of emergence and prevention. *Proc Natl Acad Sci U S A.* 2005;102(27):9714-9. doi:10.1073/pnas.0501870102.
88. Katouli AA, Komarova NL. The worst drug rule revisited: mathematical modeling of cyclic cancer treatments. *Bull Math Biol.* 2011;73(3):549-84. doi:10.1007/s11538-010-9539-y.
89. Komarova NL, Wodarz D. Effect of cellular quiescence on the success of targeted CML therapy. *PLoS One.* 2007;2(10):e990. doi:10.1371/journal.pone.0000990.
90. Sun X, Bao J, Shao Y. Mathematical Modeling of Therapy-induced Cancer Drug Resistance: Connecting Cancer Mechanisms to Population Survival Rates. *Sci Rep.* 2016;6:22498. doi:10.1038/srep22498.
91. Tomasetti C, Levy D. An elementary approach to modeling drug resistance in cancer. *Mathematical biosciences and engineering : MBE.* 2010;7(4):905-18. doi:10.3934/mbe.2010.7.905.
92. Beckman RA, Schemmann GS, Yeang CH. Impact of genetic dynamics and single-cell heterogeneity on development of nonstandard personalized medicine strategies for cancer. *Proc Natl Acad Sci U S A.* 2012;109(36):14586-91. doi:10.1073/pnas.1203559109.
93. Ledzewicz U, Wang S, Schattler H, Andre N, Heng MA, Pasquier E. On drug resistance and metronomic chemotherapy: A mathematical modeling and optimal control approach. *Mathematical biosciences and engineering : MBE.* 2017;14(1):217-35. doi:10.3934/mbe.2017014.
94. Basanta D, Gatenby RA, Anderson AR. Exploiting evolution to treat drug resistance: combination therapy and the double bind. *Mol Pharm.* 2012;9(4):914-21. doi:10.1021/mp200458e.
95. Greene J, Lavi O, Gottesman MM, Levy D. The impact of cell density and mutations in a model of multidrug resistance in solid tumors. *Bull Math Biol.* 2014;76(3):627-53. doi:10.1007/s11538-014-9936-8.
96. Lavi O, Greene JM, Levy D, Gottesman MM. The role of cell density and intratumoral heterogeneity in multidrug resistance. *Cancer Res.* 2013;73(24):7168-75. doi:10.1158/0008-5472.can-13-1768.
97. Agur Z, Elishmereni M, Kheifetz Y. Personalizing oncology treatments by predicting drug efficacy, side-effects, and improved therapy: mathematics, statistics, and their integration. *Wiley Interdiscip Rev Syst Biol Med.* 2014;6(3):239-53. doi:10.1002/wsbm.1263.
98. Wan JCM, Massie C, Garcia-Corbacho J, Mouliere F, Brenton JD, Caldas C, et al. Liquid biopsies come of age: towards implementation of circulating tumour DNA. *Nat Rev Cancer.* 2017;17(4):223-38. doi:10.1038/nrc.2017.7.
99. Xiong L, Cui S, Ding J, Sun Y, Zhang L, Zhao Y, et al. Dynamics of EGFR mutations in plasma recapitulates the clinical response to EGFR-TKIs in NSCLC patients. *Oncotarget.* 2017;8(38):63846-56. doi:10.18632/oncotarget.19139.

## Supplementary Material S2.1

### Literature searching method

As for tumor dynamic modelling, a search term: (“Models, Theoretical” [Majr:NoExp] OR “Computer Simulation”[Mesh] OR “Models, Biological\*” [Majr:NoExp]) AND (“mathematical” [title/abstract] OR “computational”[title/abstract] OR “model-based”[title/abstract] OR “model based” [title/abstract] OR “pharmacometric\*”[title/abstract] OR model framework[title/abstract] OR modelling framework[title/abstract] OR modeling framework[title/abstract] OR PK/PD model\* [title/abstract] OR PK-PD model\* [title/abstract]) AND (pharmacody\* [title/abstract] OR tumor growth[title/abstract] OR tumour growth[title/abstract] OR tumor dynamic[title/abstract] OR tumour dynamic[title/abstract] OR tumor dynamics[title/abstract] OR tumour dynamics[title/abstract] OR tumor-growth[title/abstract] OR tumour-growth[title/abstract] OR “change in tumor size”[title/abstract] OR “change in tumour size”[title/abstract] OR “tumor growth inhibition”[title/abstract] OR “tumour growth inhibition”[title/abstract]) AND (“Neoplasms”[Majr:NoExp] OR “cancer”[title/abstract] OR “tumor\*”[title/abstract] OR “tumour\*”[title/abstract] OR malignan\*[title/abstract] OR oncolog\*[title/abstract]) AND “Humans”[Mesh] NOT “Animals”[Mesh:NoExp] NOT “Cells”[Mesh] AND English[Language] AND (Pharmacology OR oncology) was used to retrieve records from PubMed database. Papers published until the start of March 2018 were scanned based on their abstract and method part. Papers that met the following criteria were included: 1) published after 2000; 2) studies where longitudinal tumor size data obtained from patients with solid tumors was described with mathematical models; 3) studies where longitudinal PSA data from prostate cancer patients was characterized with mathematical models; 4) studies where tumor size data from patients were obtained to estimate model parameters; 5) reviews that summarized equations of different tumor growth modelling structures; 6) simulation studies where the models are potentially applicable in clinical settings, i.e. well mixed cancer cell population were considered.

Exclusion criteria include: 1) studies published before 2000; 2) studies for which the full text was not available; 3) animal studies; 4) computer aided molecular studies; 5) studies with no equation reported; 6) studies characterizing disease progression; 7) studies that focus on MRI/PET/CT utility, optimization, or kinetics; 8) studies characterizing safety and toxicity profiles; 9) studies characterizing the dynamic of biomarkers or markers related to drug activity; 10) studies where the target cancer types are not solid tumor; 11) studies that modelled cell cycle kinetics or signaling pathway; 12) computational methodology studies; 13) studies characterizing tumor evolution; 14) introductory journal article; 15)

reviews discussing the application of mathematical models and/or have no equations reported; 16) other studies that are not focus on tumor growth analysis; 17) simulation studies where the models are potentially not feasible in clinical settings, including studies considered nutrition distribution, cellular automata, multiple scales, chemical potential, and in silico illustration of tumor growth .

As for tumor resistance evolution modelling, a search term: (“Models, Theoretical” [Mesh] OR “Computer Simulation”[Mesh] OR “Models, Biological\*” [Mesh]) AND (“mathematical” [title/abstract] OR “computational”[title/abstract] OR “model-based”[title/abstract] OR “model based”[title/abstract] OR “pharmacometric\*”[title/abstract] OR model framework[title/abstract] OR modelling framework[title/abstract] OR modeling framework[title/abstract]) AND (“Neoplasms”[Majr:NoExp] OR “cancer”[title/abstract] OR “tumor\*”[title/abstract] OR “tumour\*”[title/abstract] OR malignan\*[title/abstract] OR oncolog\*[title/abstract]) AND “Humans”[Mesh] NOT “Cells”[Mesh] AND English[Language] AND (“Drug Resistance, Neoplasm”[mesh] OR “Biological Evolution”[Majr:NoExp] OR “Clonal Evolution”[Mesh]) AND (“Resistance”[title/abstract] OR “heterogeneit\*”[title/abstract] OR “evolution”[title/abstract] OR “clone”[title/abstract] OR microenvironment[title/abstract]) was used to retrieve records from PubMed database. Papers published until the start of March 2018 were scanned based on their abstract and method part. Papers that met the following criteria were included: 1) published after 2000; 2) model-based studies on the evolution of tumor resistance and tumor progression; 3) reviews that summarized equations of different model structure.

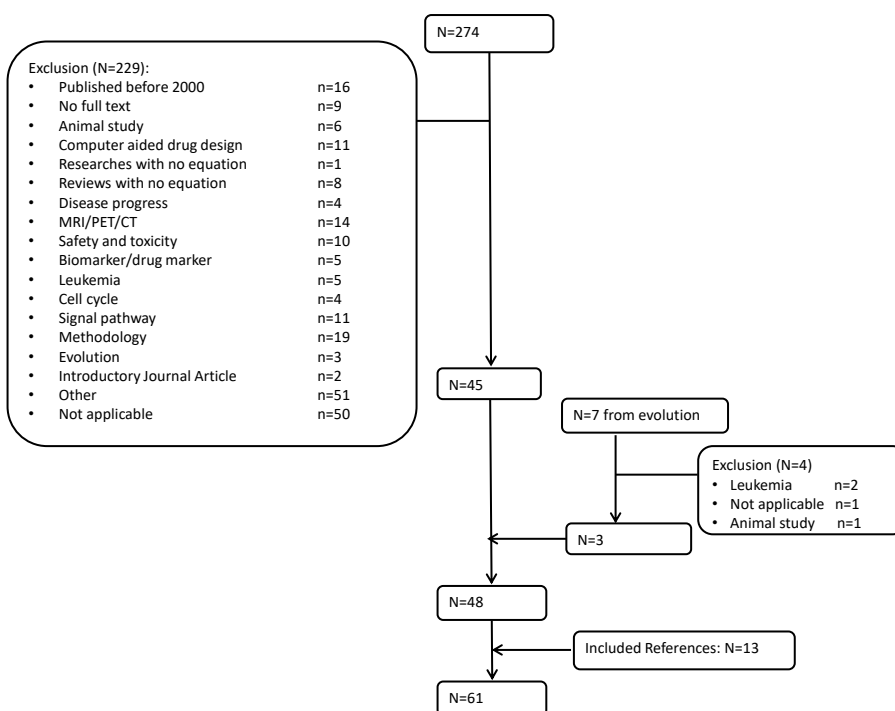
Exclusion criteria include: 1) studies published before 2000; 2) articles that overlap with what we obtained from tumor growth modelling; 3) studies for which the full text was not available; 4) computational molecular studies; 5) network studies; 6) studies concerning P-glycoprotein and resistance protein; 7) studies focus on cell cycle kinetics or signaling pathway; 8) introductory journal article; 9) studies characterizing tumor growth; 10) studies with no equation reported; 11) reviews discussing the application of models and/or have no equations reported; 12) other studies that are not focus on tumor evolution.

Studies concerning tumor dynamics and tumor resistance evolution that were retrieved by the other search term were also scanned and included according to their own corresponding inclusion and exclusion criteria respectively. Included articles’ references which introduced corresponding original models or demonstrated application examples, which were not found in the included papers, of certain model structures were included as well.

The flow diagram of scanning literature is shown in **Figure S2.1**.

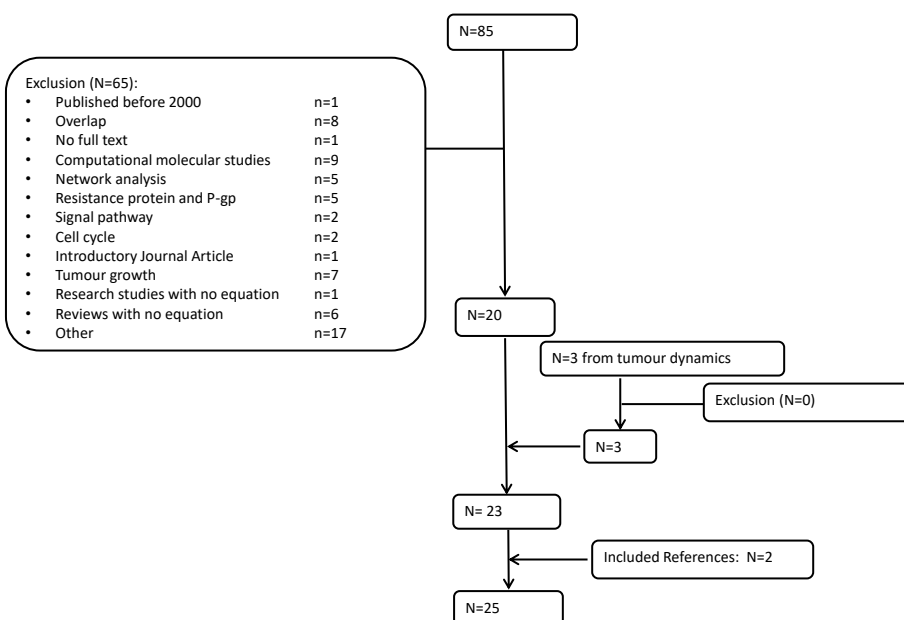
1A

## Tumour dynamics



1B

## Tumour evolution

**Figure S2.1:** Diagram of literature scanning for (A) tumor dynamics and (B) tumor resistance evolution.

## Software

Software that was applied in studies concerning tumor dynamics (TD) and tumor evolution (TE) to perform parameter estimation and data simulation is summarized in **Table S2.1**. As can be seen in the table, NONMEM and Matlab are two most frequently used software that performing model-based analysis concerning tumor dynamics. Studies applying non-linear mixed-effect models (NLMEM) mostly utilized NONMEM software to estimate parameter values, while Matlab was popular when performing simulation with partial differential equations. Three other commonly used software packages for tumor dynamics modelling are Monolix, Phoenix NLME, and Sigmplot. For studies performing tumor evolution analysis, only a few of them reported the software, namely Matlab and R.

**Table S2.1:** Software that was applied in studies concerning tumor dynamics (TD) and tumor evolution (TE) to perform parameter estimation and data simulation

| Application | Name                                | Algorithm  |
|-------------|-------------------------------------|--|
| TD          | NONMEM (ICON Development Solutions) | First-order conditional estimation with interaction (FOCE-I) algorithm |
|             |                                     | First-order conditional estimation (FOCE) algorithm                    |
|             |                                     | Laplacian algorithm  |
|             |                                     | Stochastic approximation of expectation minimization (SAEM) algorithm  |
| TE          | Matlab                              | Ordinary differential equation solver                                  |
|             |                                     | pdepe  |
|             |                                     | ODE45 subroutine   |
|             |                                     | A custom genetic algorithm   |
| TE          | Monolix                             | SAEM algorithm   |
|             | Phoenix NLME                        | FOCE algorithm   |
|             | Sigmplot (Systat Software Inc)      | Not mentioned  |
|             | SPLUS                               | Not mentioned  |
|             | C programme                         | Not mentioned  |
| TE          | Matlab                              | Not mentioned  |
|             | R; coded with C++                   | Not mentioned  |



# Chapter 3

## **Anti-cancer treatment schedule optimization based on tumor dynamics modelling incorporating evolving resistance**

Anyue Yin, Johan G.C. van Hasselt, Henk-Jan Guchelaar,  
Lena E. Friberg, Dirk Jan A.R. Moes



## Abstract

Quantitative characterization of evolving tumor resistance under targeted treatment could help identify novel treatment schedules, which may improve the outcome of anti-cancer treatment. In this study, a mathematical model which considers various clonal populations and evolving treatment resistance was developed. With parameter values fitted to the data or informed by literature data, the model could capture previously reported tumor burden dynamics and mutant KRAS levels in circulating tumor DNA (ctDNA) of patients with metastatic colorectal cancer treated with panitumumab. Treatment schedules, including a continuous schedule, intermittent schedules incorporating treatment holidays, and adaptive schedules guided by ctDNA measurements were evaluated using simulations. Compared with the continuous regimen, the simulated intermittent regimen which consisted of 8-week treatment and 4-week suspension prolonged median progression-free survival (PFS) of the simulated population from 36 weeks to 44 weeks. The median time period in which the tumor size stayed below the baseline level ( $T_{TS < TS_0}$ ) was prolonged from 52 weeks to 60 weeks. Extending the treatment holiday resulted in inferior outcomes. The simulated adaptive regimens showed to further prolong median PFS to 56–64 weeks and  $T_{TS < TS_0}$  to 114–132 weeks under different treatment designs. A prospective clinical study is required to validate the results and to confirm the added value of the suggested schedules.

## 1. Introduction

Emerging treatment resistance during anti-cancer therapy is one of the major causes of cancer patients experiencing treatment failure [1, 2]. The occurrence of treatment resistance is mediated by a range of mechanisms [1, 2]. Evolutionary mechanisms driven by intra-tumor heterogeneity and the evolving adaptation of tumor cells to the selection pressure of treatment are increasingly acknowledged as key factors related to the development of treatment resistance [3-7].

3

To improve the treatment outcome in cancer patients, it may be important to take the intra-tumor heterogeneity and evolutionary dynamics of tumors into consideration when designing treatment strategies. A clinical genetic biomarker that is useful to capture the tumor heterogeneity and to monitor the evolving treatment resistance in a quantitative way is circulating tumor DNA (ctDNA), i.e. tumor DNA fragments circulating in the bloodstream [2, 8-10]. Different from tumor size, which is commonly used as an indicator of anti-cancer treatment effect [11], ctDNA can be detected from liquid biopsies and allows real-time monitoring with limited patient burden. It has been demonstrated that mutations present in multiple biopsies of primary tumor and metastasis can be detected in ctDNA including those being missed in certain biopsies [12]. In addition, the genetic alterations captured by ctDNA can also be quantified. The relative change of genetic alterations in serial ctDNA analysis could provide important insight into the molecular evolution of the tumor and reveal the mechanisms of resistance to targeted agents [8-10]. Previous studies of ctDNA in colorectal cancer patients have demonstrated a positive selection of mutant *KRAS* clones during epidermal growth factor receptor (EGFR) blockade [10, 13], and a decline in mutant *KRAS* clones upon the withdrawal of the therapy [9]. The concentration of ctDNA has also been shown to correlate with tumor burden and stage, and is associated with therapeutic response, such as disease progression and recurrence, in different kinds of cancers [8, 9, 14-18].

Monitoring tumor-specific genetic alterations can facilitate the selection and adjustment of drugs that target newly developed actionable mutations [2, 8]. Such adaptive treatment suppresses the proliferation of resistant tumor clones and thereby overcome or at least delay treatment resistance [2, 8].

Considering evolutionary dynamics, suppressing the emergence of resistance by applying intermittent treatment has also been previously proposed [19, 20]. Intermittent treatment allows sensitive cells to utilize their fitness advantage during the withdrawal of treatment to suppress the growth of the resistant population, so that the same treatment can remain effective when it is reinitiated, which is especially relevant in the metastatic setting when

cure is not possible [19, 21]. This principle was demonstrated *in silico* with game theory models and with a pilot study of abiraterone in prostate cancer patients [19]. For colorectal cancer, it has been shown that tumor genomes adapt dynamically to intermittent drug schedules and re-challenge of EGFR blockade can be efficient [9]. This strategy is also of emerging clinical interest and has been investigated in several clinical studies [22-27].

Mathematical modelling and simulation is a widely accepted tool in pharmaceutical research to characterize and understand the interaction among drug treatment, the human body, and disease [11, 28-30]. Various mathematical model structures have been used to characterize the tumor dynamics and drug resistance evolution for solid tumors [19, 31, 32]. Tumor proliferation, regression due to treatment, heterogeneity, and treatment resistance are key elements that are commonly considered in those models [32]. The dynamics of biomarkers can also be incorporated which enables better understanding and prediction of tumor progression [32]. A non-linear mixed-effect modeling approach is commonly applied to account for inter-individual variability (IIV) [32]. Studies developing models for tumor dynamics and evolving drug resistance are mostly aimed at optimizing and individualizing current treatments. Furthermore, they are also aimed at better understanding of emerging drug resistance and identification of outcome predictors [32]. Connecting these models to patients' survival and adverse effects with time-to-event modelling is also common to support the understanding of treatment efficacy and enables the exploration of optimized dosing schedules [33]. These models could guide the interpretation and clinical decision making process based on observed tumor size dynamics and the associated evolution of tumor progression during treatment, and thereby supporting the identification of novel personalized strategies to optimize anti-cancer treatment schedules and overcome treatment resistance.

The aim of the current study was to develop a mathematical model to quantitatively characterize the dynamics of treatment response and evolving resistance, based on tumor sizes and mutant *KRAS* levels in ctDNA from metastatic colorectal cancer (mCRC) patients. We also aimed to evaluate anti-cancer treatment designs which consider cancer resistance evolution and demonstrate the use of ctDNA as a marker to guide adaptive treatment. These aspects might be beneficial to improve the treatment outcome, especially in the metastatic setting. Data identified from the literature were used for model development. Anti-cancer treatment schedules, including continuous, intermittent, and adaptive schedules guided by ctDNA measurements were designed to evaluate optimal treatment schedules.

## 2. Results

### 2.1 Data and model evaluation

A dataset containing longitudinal tumor burden measurements and mutant KRAS levels in ctDNA was identified from 28 mCRC patients treated with the anti-EGFR inhibitor panitumumab in a previous clinical study [13] (Figure 3.1). Among the 28 patients, 25 were identified to be initially KRAS wild-type and 9 of those 25 developed KRAS mutation after 5–34 weeks' (median 22 weeks') treatment. The remaining 3 patients had detectable mutant KRAS at the start of treatment. The characteristics of the patients are summarized in **Supplementary Table S3.1**.

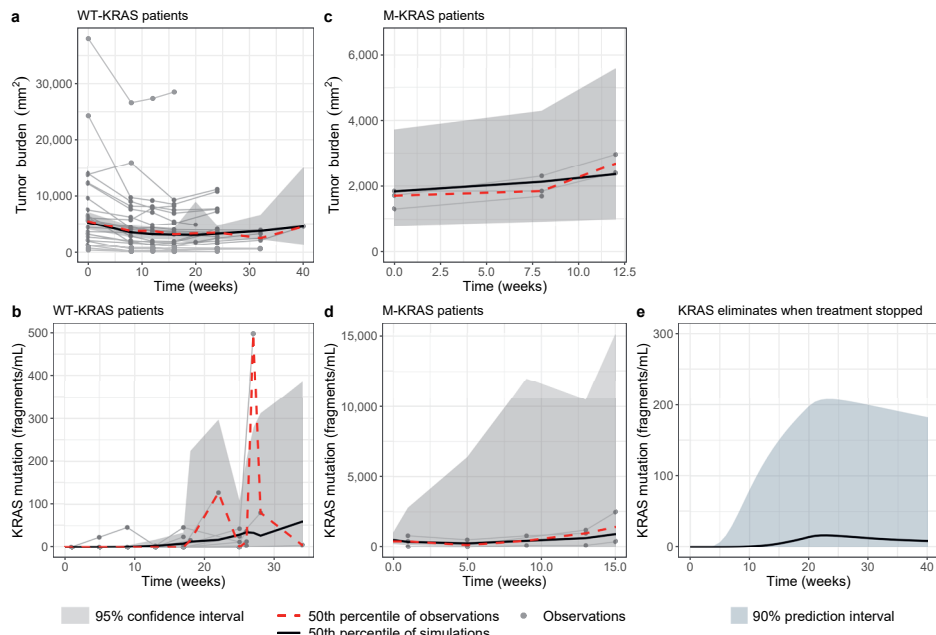


**Figure 3.1:** Model evaluations results on the data of tumor burden (a, c) and mutant KRAS (b, d) collected from a previous clinical trial on patients with metastatic colorectal cancer who were identified to be initially KRAS wild-type (a, b) or had detectable mutant KRAS at the start of treatment (c, d); Model predicted mutant KRAS concentrations under a regimen of 20-week treatment and 20-week suspension (e).

The developed model consists of three clonal tumor populations, including  $T_s$  which was sensitive to anti-EGFR inhibitor ( $D_1$ ),  $T_{R1}$  which harbored KRAS mutation and was resistant to  $D_1$ , and  $T_{R2}$  which was resistant to both  $D_1$  and a hypothetical second treatment targeting  $T_{R1}$  ( $D_2$ ), as well as two compartments for mutant KRAS ( $M_{ctDNA1}$ ) and a hypothetical second mutation ( $M_{ctDNA2}$ ) in ctDNA (Figure 3.2).  $M_{ctDNA1}$  and  $M_{ctDNA2}$  were assumed to emerge

**Table 3.1:** Parameters values of the developed model characterizing the dynamics of tumor size and mutation concentrations in metastatic colorectal cancer (mCRC) patients

| Parameters (units)                                   | Description  | Typical values   |                         | Reference  |
|--|--|------------------|-------------------------|--|
|  |  | WT-KRAS patients | M-KRAS patients         |  |
| $T_s \text{ (mm}^2\text{)}$                          | Baseline of $T_s$ (clonal population that is sensitive to anti-EGFR inhibitor ( $D_1$ ))   | 5500             | 100                     | Data/estimated value; mutation was assumed to be acquired during treatment |
| $T_{R1,0} \text{ (mm}^2\text{)}$                     | Baseline of $T_{R1}$ (clonal population that is resistance to $D_1$ but is sensitive to the second hypothetical treatment ( $D_2$ )) | 0                | 1700                    |  |
| $T_{R2,0} \text{ (mm}^2\text{)}$                     | Baseline of $T_{R2}$ (clonal population that is resistance to both treatments)   | 0                | 0                       |  |
| $M_{ctDNA1,0}$ (fragments/ml)                        | Baseline of mutant KRAS ( $M_{ctDNA1}$ ) in ctDNA  | 0                | 500                     |  |
| $M_{ctDNA2,0}$ (fragments/ml)                        | Baseline of a second hypothetical mutation ( $M_{ctDNA2}$ ) in ctDNA   | 0                | 0                       |  |
| $k_{g1}$ (/week)                                     | Growth rate constant of $T_s$  | 0.03             | 0.03                    | [40]   |
| $k_{g2}$ (/week)                                     | Growth rate constant of $T_{R1}$   | 0.021            | 0.021                   | [43, 44]   |
| $k_{g3}$ (/week)                                     | Growth rate constant of $T_{R2}$   | 0.015            | 0.015                   | [43, 44]   |
| $k_{s1}$ (/week)                                     | Tumor shrinkage rate constant due to $D_1$   | 0.1              | Estimated value         |  |
| $k_{s2}$ (/week)                                     | Tumor shrinkage rate constant due to $D_2$   | 0.1              | $k_{s1}$                | Estimated value  |
| $k_{m1}$ (/week)                                     | Mutation rate from $T_s$ to $T_{R1}$ when $D_1 = 1$  | 0.05             | Lower than $k_{m1}$ [9] |  |
| $k_{m2}$ (/week)                                     | Mutation rate from $T_{R1}$ to $T_s$ when $D_1 = 0$  | 0.03             | $k_{m1}$                |  |
| $k_{m3}$ (/week)                                     | Mutation rate from $T_{R1}$ to $T_{R2}$ when $D_2 = 1$   | 0.05             |                         |  |
| $k_{m4}$ (/week)                                     | Mutation rate from $T_{R2}$ to $T_{R1}$ when $D_2 = 0$   | 0.03             |                         |  |
| $H$  | Hill coefficient   | 5                | $k_{m2}$                | Visually matching the slope of data and the detectable time of mutant KRAS |
| $KT_{s0} \text{ (mm}^2\text{)}$                      | The size of tumor that provide half-maximal shedding rate of ctDNA   | 3500             | 1.5                     |  |
| $k_{max,1}$ ((fragments/ml)/(week*mm <sup>2</sup> )) | Maximum shedding rate of $M_{ctDNA1}$ ctDNA eliminate rate constant  | 0.015            | 0.5                     |  |
| $k_e$ (/week)  |  |                  |                         |  |
| $k_{max,2}$ ((fragments/ml)/(week*mm <sup>2</sup> )) | Maximum shedding rate of $M_{ctDNA2}$  | 0.015            | 1.5                     | $k_{max,1}$  |
| $IV_B(\omega_1)$                                     | Standard deviation of IV of baselines  | 0.6              | Data                    |  |
| $IV_K_g(\omega_2)$                                   | Standard deviation of IV of $K_g$  | 0.2              | Data                    |  |

ctDNA, circulating tumor DNA; IV, inter-individual variability; WT-KRAS patients, patients who were initially identified as KRAS wild-type in ctDNA; M-KRAS patients, patients who had detectable mutant KRAS in ctDNA pre-treatment.

during treatment. Shedding rates of ctDNA depended on the size of  $T_{R1}$  and  $T_{R2}$ , and Hill equations with tumor size as independent variable were applied to describe the delayed emergence (or ability to detect) of mutant genes in ctDNA. Values of model parameters were obtained by fitting to the data or informed by literature (Table 3.1). Parameters describing tumor dynamics under  $D_1$  therapy were estimated based on the observed raw data and the results are shown in **Supplementary Table S3.2**.

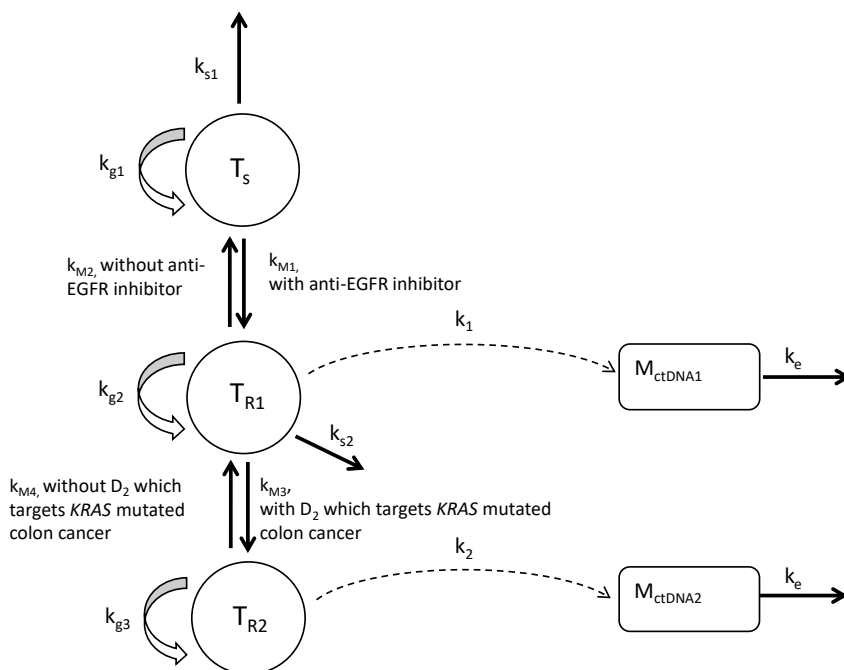


**Figure 3.2:** The model that characterizes the dynamics of tumor size and mutation concentrations in ctDNA from metastatic colorectal cancer patients.  $T_s$ ,  $T_{R1}$ , and  $T_{R2}$  represent the sizes of three tumor clonal populations, respectively.  $M_{ctDNA1}$  and  $M_{ctDNA2}$  represent the concentration of mutant KRAS and a hypothetical mutation in ctDNA.  $k_{g1}$ ,  $k_{g2}$ ,  $k_{g3}$  represent the net growth rate constants of three clonal populations.  $k_{s1}$  and  $k_{s2}$  represent the tumor shrinkage rate due to treatments.  $k_{M1}$  and  $k_{M3}$  represent the mutation rate constant from drug susceptible clonal population to drug resistant clonal population during the course of anti-EGFR treatment ( $D_1$ ) and a hypothetical treatment ( $D_2$ ), respectively.  $k_{M2}$  and  $k_{M4}$  represent the transition rate constant from drug resistant clonal population to drug susceptible clonal population upon the withdrawal of treatments.  $k_1$  and  $k_2$  represent the transition rate constant from drug resistant clonal population to drug susceptible clonal population upon the withdrawal of treatments.  $k_3$  and  $k_4$  represent the shedding rate constant of ctDNA which carries mutations.  $k_e$  represent the elimination rate constant of ctDNA.

The model evaluation results show that the 50<sup>th</sup> percentiles of the simulated time-courses of total tumor size ( $T_s$ ) and mutant KRAS ( $M_{ctDNA1}$ ) concentrations were generally in line with the 50<sup>th</sup> percentiles of corresponding observations (Figure 3.1). The 50<sup>th</sup> percentiles of observations were also adequately covered by the 95% confidence intervals (CIs) of corresponding percentile obtained from the simulations. Upon a treatment suspension

after 20 weeks of treatment, a decay of KRAS levels that was observed in previous studies [9] could also be described by the model. The median and 90% prediction interval of corresponding simulations of 100 virtual patients were shown in **Figure 3.1E**. The predicted median half-life of KRAS levels was 4.98 months.

An available dataset on 16 non-small cell lung cancer (NSCLC) patients was utilized as an evaluation cohort (**Supplementary Table S3.3**) [14]. Patients included in this study had detectable EGFR L858R mutation / exon 19 deletion at the start of treatment and developed EGFR T790M mutation during treatment. The model used in the validation cohort was adjusted according to the findings of the study, the details of which can be found in **Supplementary method** and **Supplementary Figure S3.1**. Model evaluation results show that the distribution of the model simulations was also in line with the distribution of the tumor size and concentrations of mutant EGFR obtained from NSCLC patients (**Supplementary Figure S3.2**).

## 2.2 Treatment schedule evaluation

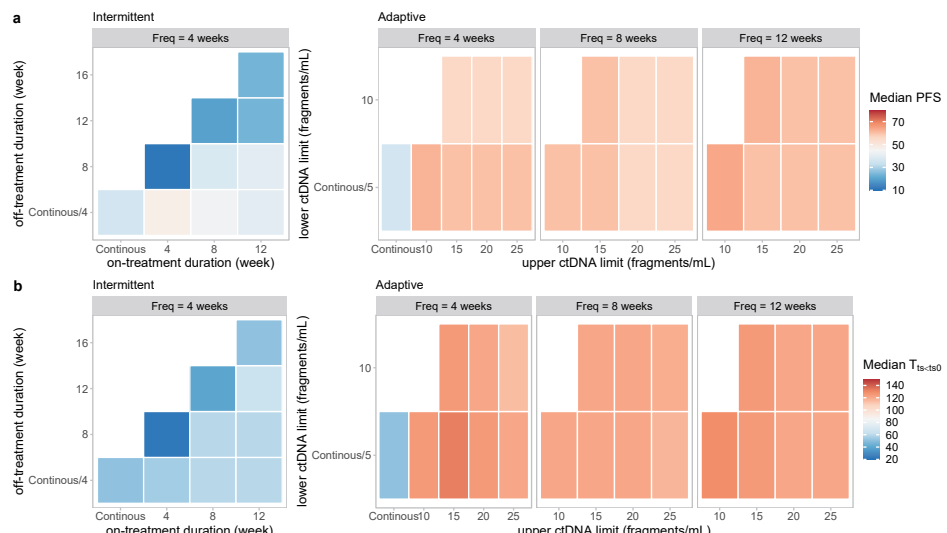
Based on the developed model, multiple dosing schedules, including a continuous  $D_1$  schedule, intermittent  $D_1$  schedules with different on- and off-dosing durations, and adaptive schedules where the use of  $D_1$  and  $D_2$  were guided by ctDNA measurements, were simulated and evaluated to identify optimal treatment designs (**Table 3.2**). For adaptive schedules, the treatment started with a continuous  $D_1$  and switched to a continuous  $D_2$  when the ctDNA measurements increased to an upper limit for drug adjustment. When the mutation concentration decreased back to a lower limit for drug adjustment, the treatment was switched back to  $D_1$  and the loop continued.

Predicted median progression-free survival (PFS) and time until the tumor size had grown back to the baseline level ( $T_{TS < TSO}$ ) of the simulated population under all evaluated regimens are shown in **Figure 3.3**, the detailed results of which can be found in **Supplementary Table S3.4**. The median predicted PFS under continuous drug exposure was 36 weeks and median  $T_{TS < TSO}$  was 52 weeks. Five out of 9 designs of intermittent schedule prolonged median PFS and median  $T_{TS < TSO}$  compared with continuous treatment (**Figure 3.3**). Four- or 8-week treatment suspension was introduced in these regimens. Extending the treatment holiday from 4 weeks to 4 weeks more than the treatment period mostly resulted in inferior results (**Figure 3.3**). A regimen consisting of 4-week treatment and 4-week suspension ( $S_{interm(4on_4off)}$ ) provided the longest median PFS (48 weeks), while a schedule consisting of 8-week treatment and 4-week suspension ( $S_{interm(8on_4off)}$ ) provided the longest  $T_{TS < TSO}$  (60 weeks). A survival prediction also illustrated a better clinical outcome provided by regimen  $S_{interm(8on_4off)}$  than continuous regimen (**Figure 3.4**).

**Table 3.2:** Evaluated treatment schedules

| Schedules   | Details   |                                       |                  |                                       |      |                |          |    |              |   |   |                |   |    |            |   |   |                |    |    |            |    |
|---|---|---------------------------------------|------------------|---------------------------------------|------|----------------|----------|----|--------------|---|---|----------------|---|----|------------|---|---|----------------|----|----|------------|----|
| Continuous schedule (standard of care)                  | $D_1$ was continuously administered resulting in continuous drug exposure for 180 weeks   |                                       |                  |                                       |      |                |          |    |              |   |   |                |   |    |            |   |   |                |    |    |            |    |
| Intermittent schedules                                  | $D_1$ was administered for N weeks and suspended for M weeks. Total treatment time was 180 weeks.   |                                       |                  |                                       |      |                |          |    |              |   |   |                |   |    |            |   |   |                |    |    |            |    |
|   | <table border="1"> <thead> <tr> <th>N (weeks)</th> <th>M (weeks)</th> </tr> </thead> <tbody> <tr> <td>4</td> <td>4, 8</td> </tr> <tr> <td>8</td> <td>4, 8, 12</td> </tr> <tr> <td>12</td> <td>4, 8, 12, 16</td> </tr> </tbody> </table>   | N (weeks)                             | M (weeks)        | 4                                     | 4, 8 | 8              | 4, 8, 12 | 12 | 4, 8, 12, 16 |   |   |                |   |    |            |   |   |                |    |    |            |    |
| N (weeks)   | M (weeks)   |                                       |                  |                                       |      |                |          |    |              |   |   |                |   |    |            |   |   |                |    |    |            |    |
| 4   | 4, 8  |                                       |                  |                                       |      |                |          |    |              |   |   |                |   |    |            |   |   |                |    |    |            |    |
| 8   | 4, 8, 12  |                                       |                  |                                       |      |                |          |    |              |   |   |                |   |    |            |   |   |                |    |    |            |    |
| 12  | 4, 8, 12, 16  |                                       |                  |                                       |      |                |          |    |              |   |   |                |   |    |            |   |   |                |    |    |            |    |
| Adaptive schedules with a hypothetical second treatment | $D_1$ was continuously given, and suspended and switched to $D_2$ when the ctDNA measurement increased to higher than UP fragment/ml. Treatment switched back to $D_1$ when ctDNA measurement decreased back to lower than LOW fragment/ml. Total treatment time was 180 weeks.   |                                       |                  |                                       |      |                |          |    |              |   |   |                |   |    |            |   |   |                |    |    |            |    |
|   | <table border="1"> <thead> <tr> <th>LOW (fragment/ml)</th> <th>UP (fragment/ml)</th> <th>Monitoring frequency of ctDNA (weeks)</th> </tr> </thead> <tbody> <tr> <td>5</td> <td>10, 15, 20, 25</td> <td>4</td> </tr> <tr> <td>10</td> <td>15, 20, 25</td> <td>4</td> </tr> <tr> <td>5</td> <td>10, 15, 20, 25</td> <td>8</td> </tr> <tr> <td>10</td> <td>15, 20, 25</td> <td>8</td> </tr> <tr> <td>5</td> <td>10, 15, 20, 25</td> <td>12</td> </tr> <tr> <td>10</td> <td>15, 20, 25</td> <td>12</td> </tr> </tbody> </table> | LOW (fragment/ml)                     | UP (fragment/ml) | Monitoring frequency of ctDNA (weeks) | 5    | 10, 15, 20, 25 | 4        | 10 | 15, 20, 25   | 4 | 5 | 10, 15, 20, 25 | 8 | 10 | 15, 20, 25 | 8 | 5 | 10, 15, 20, 25 | 12 | 10 | 15, 20, 25 | 12 |
| LOW (fragment/ml)                                       | UP (fragment/ml)  | Monitoring frequency of ctDNA (weeks) |                  |                                       |      |                |          |    |              |   |   |                |   |    |            |   |   |                |    |    |            |    |
| 5   | 10, 15, 20, 25  | 4                                     |                  |                                       |      |                |          |    |              |   |   |                |   |    |            |   |   |                |    |    |            |    |
| 10  | 15, 20, 25  | 4                                     |                  |                                       |      |                |          |    |              |   |   |                |   |    |            |   |   |                |    |    |            |    |
| 5   | 10, 15, 20, 25  | 8                                     |                  |                                       |      |                |          |    |              |   |   |                |   |    |            |   |   |                |    |    |            |    |
| 10  | 15, 20, 25  | 8                                     |                  |                                       |      |                |          |    |              |   |   |                |   |    |            |   |   |                |    |    |            |    |
| 5   | 10, 15, 20, 25  | 12                                    |                  |                                       |      |                |          |    |              |   |   |                |   |    |            |   |   |                |    |    |            |    |
| 10  | 15, 20, 25  | 12                                    |                  |                                       |      |                |          |    |              |   |   |                |   |    |            |   |   |                |    |    |            |    |

$D_1$ , anti-EGFR inhibitor;  $D_2$ , a hypothetical second treatment to which the newly acquired clone is susceptible; ctDNA, circulating tumor DNA. Drug exposure variability was not considered in this study but only the presence ( $D_n = 1$ ) or absence ( $D_n = 0$ ) of a drug were considered.

**Figure 3.3:** The predicted median progression-free survival (PFS) (a) and the time until the tumor size had grown back to the baseline level ( $T_{TS<TS0}$ ) (b) of evaluated regimens.

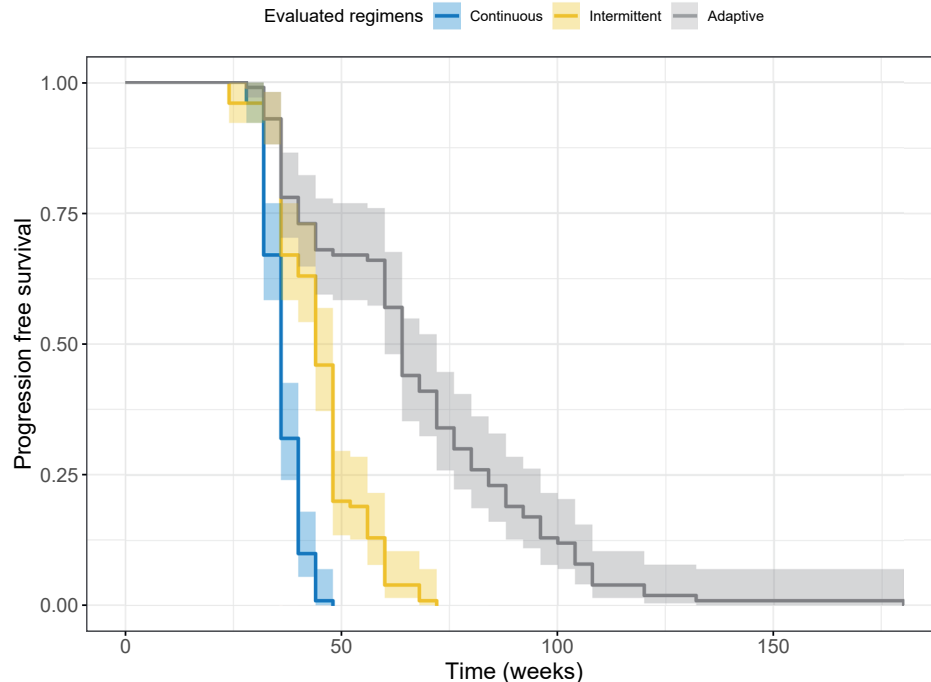


**Figure 3.4:** The survival plot of 100 virtual patients under continuous treatment, intermittent treatment (8-week treatment and 4-week suspension), and adaptive treatment with the second hypothetical drug (ctDNA limits for drug adjustment: 5 and 10 fragments/ml, monitor frequency: 12 weeks).

As for the adaptive regimen guided by ctDNA measurements, all designs further prolonged median PFS to 56–64 weeks and  $T_{TS < TS_0}$  to 114–132 weeks (Figure 3.3). Comparable results were obtained when the monitoring frequency of ctDNA altered and slightly longer median PFSs were observed when the monitoring frequency of ctDNA was once every 12 weeks. Under the same monitoring frequency, the different upper and lower ctDNA limits for drug adjustment only resulted in small changes in median PFS and  $T_{TS < TS_0}$ , especially when the ctDNA was less frequently monitored. Overall, the longest median PFS and  $T_{TS < TS_0}$  were mostly observed when the upper and lower ctDNA limits for drug adjustment were 5 fragments/ml and 10 fragments/ml, respectively (Figure 3.3). A regimen with 5 and 10 fragments/ml as ctDNA limits for drug adjustment and a monitoring frequency of once every 12 weeks ( $S_{adapt(5\_10\_Freq12)}$ ) provided the longest median PFS. The survival prediction of  $S_{adapt(5\_10\_Freq12)}$  also showed a better clinical outcome than the regimen  $S_{interm(8on\_4off)}$  and the continuous regimen (Figure 3.4).

Figure 3.5 shows the simulated time-curves of each tumor clonal population and each mutation in ctDNA over time from a typical subject under the continuous schedule, the intermittent schedule  $S_{interm(8on\_4off)}$ , and the adaptive schedule  $S_{adapt(5\_10\_Freq12)}$ . The corresponding

results of the simulated population are shown in **Supplementary Figure S3.3**. It can be seen that the schedule  $S_{\text{interm(8on_4off)}}$  and  $S_{\text{adapt(5_10_Freq12)}}$  suppressed the growth of resistant clonal population  $T_{R1}$ . In addition, predicted time until detectable mutation ( $T_{\text{mutant\_test}}$ ) under each evaluated regimen was evaluated. It was shown that  $M_{\text{ctDNA1}}$  under both continuous and intermittent regimens could become detectable before disease progression (**Figure 3.5**, **Supplementary Table S3.4**). In the setting of adaptive treatment, as the  $M_{\text{ctDNA1}}$  level was applied as a biomarker to guide the treatment switching, the median  $T_{\text{mutant\_test}}$  of  $M_{\text{ctDNA2}}$  was evaluated. The results indicate that  $M_{\text{ctDNA2}}$  would be observed after disease progression has occurred but before the tumor size grows back to baseline level (**Figure 3.5**).

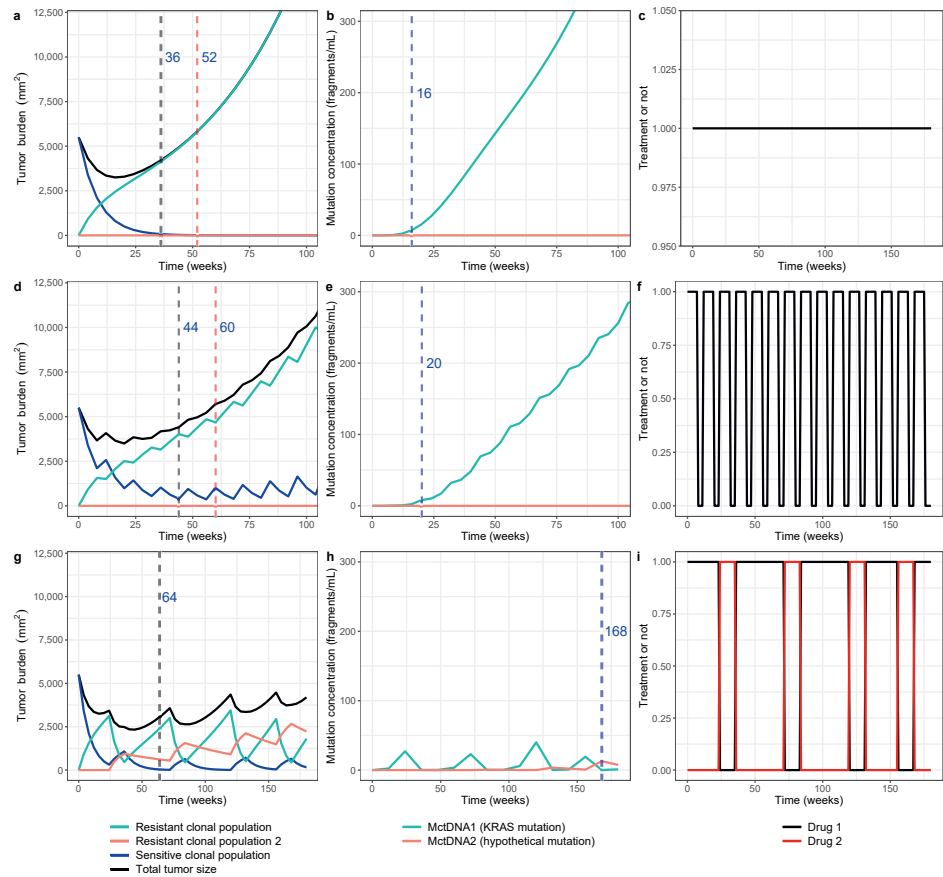


**Figure 3.5:** The simulated time-curves of total tumor burden and each clonal population (a, d, g), mutation concentrations (b, e, h), and dosing strategies (c, f, i) of a typical subject with metastatic colorectal cancer undergoing continuous treatment (a, b, c), intermittent treatment (8-week treatment and 4-week suspension) (d, e, f), and adaptive treatment with the second hypothetical drug (ctDNA limits for drug adjustment: 5 and 10 fragments/ml, monitor frequency: 12 weeks) (g, h, i). Estimated PFS (black dashed vertical line),  $T_{\text{TS} < \text{TS}0}$  (red dashed vertical line), and  $T_{\text{mutant\_test}}$  (blue dash-dot vertical line) are also shown in the figure.

## 2.3 Sensitivity analysis

While the value of the parameters describing tumor dynamics were estimated based on the data or adapted from literature, that of other parameters were set based on a visual fit to the data since the amount of data did not support estimation of parameters. These parameter values may however not be optimal, and therefore the parameter sensitivity to the simulated curves was assessed by increasing or decreasing parameters by 50% one at a time.

The predicted PFS and  $T_{\text{mutant\_test}}$  derived from each time of simulation, which represent the dynamics of tumor burden and mutation concentrations in ctDNA respectively, are shown in **Figure 3.6** and **Supplementary Table S3.5**. Both simulated tumor sizes and mutation concentrations were affected when any of the parameters characterizing the tumor burden dynamics, including net growth rate constants ( $k_g$ ), tumor shrinkage rate due to treatments ( $k_s$ ), and mutation rate constants ( $k_M$ ) varied. In contrast, the change of

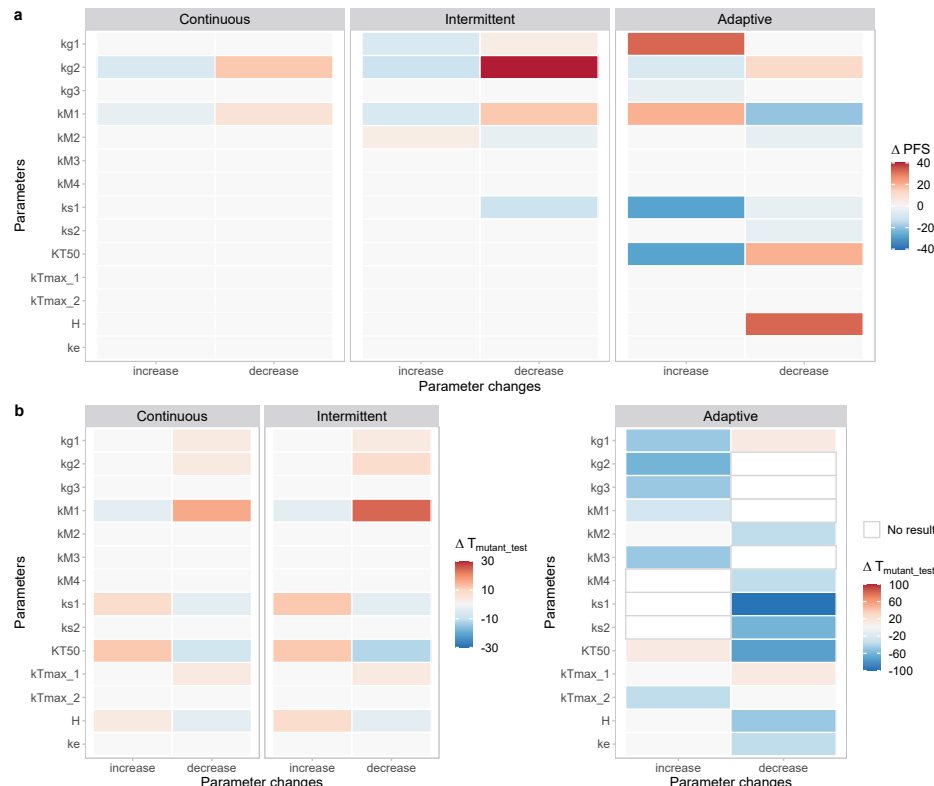


**Figure 3.6:** Relative change ( $\Delta$ ) of predicted progression-free-survival (weeks) (a) and time until detectable mutation (weeks) (b) compared with using original parameters in the sensitivity analysis. No result, the mutant gene concentrations did not reach the detectable limit (5 fragments/ml) by the end of simulation time (180 weeks).

the parameters characterizing the mutation concentrations, including the Hill coefficient ( $H$ ), max releasing rates ( $k_{max}$ ), the tumor size that provide half-maximal releasing rate ( $KT_{50}$ ), and elimination rate constant of ctDNA ( $k_e$ ), only affected the simulated mutation concentrations but not the simulated tumor size except for  $KT_{50}$  and  $H$  under an adaptive treatment design. The predicted PFS was mainly sensitive to parameters  $k_{g2}$  and  $k_{M1}$ , and the predicted  $T_{\text{mutant\_test}}$  was mainly sensitive to parameters  $k_{s1}$ ,  $k_{M1}$ ,  $H$  and  $KT_{50}$ . Nonetheless, the intermittent regimen and the adaptive regimen still resulted in better treatment outcomes (i.e. longer PFS) than the continuous regimen, no matter how the parameter values varied (**Supplementary Table S3.5**). More detailed simulated time-curves of tumor burden and  $M_{ctDNA1}$  concentrations under each setting, and the relative changes of predicted total tumor sizes and  $M_{ctDNA}$  levels compared with original results are shown in **Supplementary Figure S3.4** and **Figure S3.5**.

### 3. Discussion

In the current study, a mathematical model was developed to characterize the tumor size dynamics and tumor resistance development in response to treatment. The model was built based on findings from previously published studies and the collected raw data itself. The model well captured the reported time curves of tumor sizes and mutant KRAS levels in ctDNA from mCRC patients. A similar model could also characterize the time-curves of EGFR mutation and tumor sizes obtained from NSCLC patients.

The current model assumed that for patients who had no detectable KRAS mutation pre-treatment, there was no primary resistance, despite that the original study estimated that drug resistance is likely to be present prior to the initiation of treatment [13]. However, since the size of the resistant clonal population was estimated to only account for a small part of the total tumor cell population (2300 cells out of one billion cells) [13], the primary resistance was eventually not included in our model.

During treatment interruption, a back transfer process from drug resistant clonal population to drug sensitive clonal population was incorporated to capture the recovery of sensitivity to the treatment. This assumption was supported by in vitro observations [9]. This process could also describe the phenomenon that in the absence of the drug, susceptible tumor cells have the benefit of growing back again at the expense of resistant tumor cells. When the back transfer process was removed ( $k_{M2}$  and  $k_{M4}$  fixed to 0), prolonged predicted median PFSs under the schedule  $S_{\text{interm(4on\_4off)}}$  and  $S_{\text{adapt(5\_10\_Freq12)}}$  compared with the continuous regimen were still observed, although not for schedule  $S_{\text{interm(8on\_4off)}}$  in contrast to when the back

transfer was allowed (**Supplementary Figures S3.6, S3.7**). However, the decline of ctDNA upon withdrawal of treatment, which has been observed in mCRC patients [9, 34], could not be captured when removing the back transfer process (**Supplementary Figure S3.8**). It was also observed that under this circumstance, the remaining susceptible cells had no growth advantage over the resistant cells during the withdrawal of treatment, hence tumor would not regain susceptibility (**Supplementary Figures S3.7, S3.8**). Therefore, the back transfer process is considered to be a reasonable assumption to describe the dynamics of and the competition among different clonal populations upon treatment withdrawal based on current available data. More data under intermittent therapy would be valuable to better characterize this dynamic process, and to better estimate parameters.

A delayed emergence of a mutation indicating treatment resistance in ctDNA was observed in both original studies on mCRC patients (after in median 22 weeks' treatment) [13] and NSCLC patients (after in median 10.5 months' treatment) [14]. This phenomenon was characterized by the Hill equations with tumor size as the independent variable (Eq. 3.4 and 3.5) in the current study, assuming a delayed shedding of ctDNA from the tumor tissue. We also investigated a model where the delayed process was incorporated in the mutation from one clonal population to another by applying transit compartments. This model could also capture the delayed emergence of mutation in ctDNA.

The designs of intermittent and adaptive regimens aim to prolong the duration of suppressing treatment resistance since they considered intra-tumor heterogeneity and evolving adaptation of tumor to treatment. In addition, the evaluated adaptive schedules also enabled the personalized design of therapy since the switch of drug was guided by individual ctDNA measurements. Here we focused explicitly on the use of ctDNA and therefore the change in tumor size was not considered as a criterion to switch therapy, despite the fact that tumor size is a common marker in clinical practice for the efficacy of anti-cancer treatment [11]. In the future, the help of tumor size could be further evaluated when data regarding ctDNA and tumor size dynamics under adaptive therapy are available to facilitate a better understanding of their relationship and refining the current model.

In the current study, the intermittent and adaptive regimens, with appropriate designs, were shown to outperform the conventional continuous treatment by simulations (i.e. median PFS was prolonged) (**Figure 3.3**). This is in line with the evolutionary principle of control and the findings from clinical observations. For example, an adaptive intermittent treatment of abiraterone based on prostate-specific antigen (PSA) levels was shown to result in a better clinical outcome than the typical continuous treatment [19], although the study design may need to be refined [35]. Another recent retrospective analysis demonstrated

that intermittent use of enzalutamide in metastatic castration-resistant prostate cancer patients prolonged the time to PSA failure and improved overall survival [20]. Traditional approaches to cancer therapy have not exploited these theoretical advantages. For example, current protocols typically apply a treatment agent or agents at the maximum tolerated dose (MTD) until there is unequivocal clinical evidence of progression [21].

The intermittent therapy has also been investigated in several clinical studies. In contrast to our simulation results and the clinical observations, these studies did not show improved outcomes in patients undergoing intermittent therapy [22-27]. One study on BRAF and MET inhibitors in melanoma patients even showed an inferior result under the intermittent therapy compared to continuous therapy [22]. The underlined mechanism remains unclear. Nevertheless, in these cases, the developed mathematical model may be helpful for understanding these conflicting results. Further identification of optimal designs based on different resistance mechanisms and dynamics of cancers can be supported by the model-based approach. For example, a previous *in silico* study showed that an intermittent abiraterone followed by a lead-in period was not beneficial for prostate cancer patients, and the adaptive intermittent treatment guided by PSA was demonstrated to be the best option [19]. Moreover, the simulation results derived from the current study suggest that although introducing a treatment holiday may improve the treatment outcome, the length of the treatment holiday still needs to be controlled. Extending the treatment holiday mostly resulted in inferior results, especially when the holiday was longer than the treatment period. This is in accordance with a previous finding that chemotherapy with shorter intervals (dose-dense therapy) resulted in better treatment outcome even though the total dose amounts were the same [36].

When evaluating the adaptive treatment, a second hypothetical treatment ( $D_2$ ) targeting  $T_{R1}$  was introduced. An example of this idea can be seen from the treatments of NSCLC patients. For NSCLC patients, acquisition of T790M mutation is the main mechanism of acquired resistance upon treatment of erlotinib/gefitinib, and osimertinib can be selected for T790M-positive patients [37]. Lately, the Food and Drug Administration (FDA) also granted accelerated approval to the first KRAS-blocking drug [38]. This indicates potential feasibility of the here suggested adaptive treatment design. Due to the use of  $D_2$ , a hypothetical newly acquired mutation ( $M_{ctDNA2}$ ) was also considered in the model. Unlike  $M_{ctDNA1}$  (KRAS mutation),  $M_{ctDNA2}$  only became detectable after disease progression in the current study. This brings on a question about the predictive value of mutations in ctDNA. Most likely the dynamics of the sensitive clones are also very important to predict emerging resistance at an earlier phase. However, to answer this question, more data is required to support the understanding of the dynamics of the hypothetical mutation.

With the sensitivity analysis, we showed that the choice of parameter values can affect the simulated curves. The predicted tumor sizes were mainly sensitive to the parameters  $k_{g2}$  and  $k_{M1}$  using the developed model, and the predicted mutation concentrations were mainly sensitive to the parameters  $k_{s1}$ ,  $k_{M1}$ ,  $H$  and  $KT_{50}$  (**Figure 3.6**). This suggests that an accurate estimation of these parameters is of importance for this model. However, the intermittent and adaptive treatment still provided better treatment outcome when parameter values varied, indicating that the value of the parameters didn't affect the conclusion that the intermittent and adaptive regimens with a certain design outperform the conventional continuous treatment.

To apply the novel treatment strategy, there are still some challenges. Firstly, for patients who had detectable *KRAS* mutation pre-treatment, the intermittent treatment provided similar treatment outcome compared to continuous treatment (**Supplementary Figure S3.9**). Therefore, for these patients, a better option will be to choose another treatment from start. In fact, in clinical practice panitumumab is contraindicated for patients with *KRAS* mutation. Secondly, to be able to monitor the development of resistance with ctDNA, the mutations that are associated with the resistance to a target treatment need to be acknowledged beforehand. If multiple mutations have been reported, a selection may be required based on the capability of the applied quantification technique, such as the selection of gene panel in the assay and the number of mutations that can be detected simultaneously. Thirdly, as can be seen from the previous study, only 9 out of 25 patients developed detectable *KRAS* mutations and the median disease progression time of the 9 patients was the same as for the remaining 16 patients (23 weeks). It was also noticed when the individual results were compared, 4 out of 100 virtual patients were predicted to have longer PFS under a continuous schedule than under regimen  $S_{\text{interm(8on\_4off)}}$ . Additionally, despite that adaptive regimens provided longer median PFS than intermittent regimens, 31 out of 100 patients had longer PFS under regimen  $S_{\text{interm(8on\_4off)}}$  than under regimen  $S_{\text{adapt(5\_10\_Freq12)}}$ . These results indicate that ctDNA guided treatment may not be feasible for all patients and variability between individuals can affect the choice of regimen.

Our study has some limitations. First of all, the amount of data we obtained limited the ability to adequately estimate all parameters of the developed model. We were also not able to fully consider pre-treatment tumor heterogeneity and incorporate the eco-evolutionary dynamics in the model. Additionally, due to the lack of drug exposure records, dose- or exposure-response relationship was not incorporated in the model and was not investigated in this study. However, for panitumumab, it has been shown that with standard treatment regimens, even the trough concentrations are maintained above the 90% saturation levels, meaning almost maximum effect in all patients [39]. However, for other molecules such

as tyrosine kinase inhibitors (TKIs), drug levels are also important to be included in the analysis. In these cases, drug exposure measurements can be helpful for the understanding of exposure-response relationship under the evaluated regimens. Secondly, alternative mutations that are related to anti-EGFR treatment resistance in addition to the reported mutant genes were not considered in this study. However, *KRAS* mutation and *EGFR* mutation were the most commonly reported gene mutations that are associated with resistance to anti-EGFR treatment in mCRC and NSCLC patients respectively [18]. Therefore, we mainly considered the most representative mutations. Thirdly, the idea of individual intermittent treatment could be further investigated. Because of the above limitations, an external dataset is needed to validate the results and a clinical pilot study is required to confirm the added value of the suggested schedules.

In conclusion, a mathematical model incorporating evolving cancer resistance was developed to characterize tumor size dynamics and resistance development under treatment. The model well captured the clinical data from colorectal cancer patients as well as from NSCLC patients. Compared with a conventional continuous anti-cancer treatment schedule, intermittent and adaptive schedules were predicted to better suppress the evolving cancer resistance and suggested a potential improvement in clinical outcome. However, a prospective study is required to validate the results and to confirm the added value of the suggested approach.

## 4. Methods

### 4.1 Dataset

A dataset containing longitudinal tumor burden measurements and mutant *KRAS* levels in ctDNA was identified from a published study where patients diagnosed with mCRC were treated with the anti-EGFR inhibitor panitumumab [13]. Patient demographic information, time-courses of tumor burden that was reported as the aggregate cross-sectional diameter of all index lesions ( $\text{mm}^2$ ), and the time-courses of mutant *KRAS* concentrations (fragments/ml) of 28 patients were collected from the supplementary tables of the paper [13]. When corresponding time of a data point was not shown in the table, the time information was digitized from the corresponding supplementary figures using WebplotDigitizer (<https://apps.automeris.io/wpd/>).

All data in this study were collected from publicly available materials (i.e. supplementary material or figures) in literature from which the studies were approved by corresponding ethical committees and all informed consents were obtained. Therefore, for this study, no

additional ethical approval or written informed consent was required. All procedures in this study were performed in accordance with relevant guidelines.

## 4.2 Model structure

A mathematical model was developed to describe the obtained time-courses of tumor burden and mutant *KRAS* concentrations under anti-EGFR therapy. The model structure is shown in **Figure 3.2**.

Six assumptions were made when developing the model structure:

1. The growth of the tumor was assumed to follow an exponential growth pattern [40, 41].
2. Tumor tissue was assumed to consist of multiple clonal sub populations which are defined as sets of cancer cells that share a common genotype [5]. One clonal population ( $T_s$ ) was defined to be sensitive to the anti-EGFR inhibitor panitumumab ( $D_1$ ). Another clonal population ( $T_{R1}$ ) harbored *KRAS* mutation ( $M_{ctDNA1}$ ) and was consequently resistant to  $D_1$ . This is based on previous evidence where patients harboring *RAS* variant in pre-treatment ctDNA did not benefit from EGFR blockade [13, 42]. The emergence of *KRAS* mutation was also suggested to be a mediator of acquired resistance to EGFR blockade [13, 42].

For patients who were initially identified as *KRAS* wild-type in ctDNA (WT-*KRAS* patients),  $T_s$  was assumed to form the whole tumor at the start of treatment. While for patients who had detectable mutant *KRAS* in ctDNA pre-treatment (M-*KRAS* patients), tumor tissue was assumed to consist of both  $T_s$  and  $T_{R1}$  at the start of treatment. In addition, given that the resistant clonal population may have fitness cost [43], the proliferation rate of resistant clones was assumed to be lower than that of the sensitive clones [44].

3. A *KRAS* mutation could be acquired during the treatment of  $D_1$ , as WT-*KRAS* patients could develop detectable mutations [13].
4. A hypothetical treatment next to panitumumab ( $D_2$ ) was incorporated in the current study and assumed to target *KRAS*-mutated colorectal cancer and thereby inhibiting the growth of  $T_{R1}$ . In the meantime, a second mutation ( $M_{ctDNA2}$ ) was able to be acquired which resulted in a third clonal population ( $T_{R2}$ ) that was resistant to  $D_2$ . The mutation rate was assumed to be the same as that of the acquiring *KRAS* mutation clonal population.
5. During treatment interruption, a back transfer process from the drug resistant clonal population to drug sensitive clonal population was assumed to be present

and was incorporated in the model with a rate lower than the mutation rate. This assumption was supported by a previous *in vitro* study in colorectal cancer (CRC) cells [9], which showed that CRC cells that acquired resistance to cetuximab with amplification of KRAS gene regained partial sensitivity to cetuximab when cultured in the absence of the drug [9]. This process could also be understood as the competition between drug susceptible and resistant cells in the absence of the drug. When the pressure of the drug was gone, the susceptible cells have the benefit to grow back again at the expense of resistant cells in the tumor.

6. ctDNA which carries the target mutations was shed from resistant clonal populations and the shedding rate depends on the corresponding tumor tissue size.

In order to be able to capture the following features observed from clinical studies, two features were incorporated in the model structure:

1. The mutant KRAS concentration became detectable after 5–34 weeks' (median 22 weeks) treatment for WT-KRAS patients who developed detectable mutant KRAS [13]. Therefore, the Hill equations (Eq. 3.4 and 3.5) were applied to describe this delayed emergence (or ability to detect) of  $M_{ctDNA1}$  and  $M_{ctDNA2}$ .
2. Mutant KRAS levels in ctDNA increased when challenged with  $D_1$  and declined upon the withdrawal of treatment [9]. The elimination half-life of resistance mutations is approximately 4 months [34, 42]. Therefore, in addition to the back transfer process, a first-order ctDNA elimination was incorporated. The half-life of a typical patient was confirmed to be 4.15 months with the given parameter values.

The ordinary differential equations of the model were as follows:

$$\frac{dT_s}{dt} = k_{g1} \cdot T_s - k_{s1} \cdot D_1 \cdot T_s - k_{M1} \cdot D_1 \cdot T_s + k_{M2} \cdot (1 - D_1) \cdot T_{R1} \quad (3.1)$$

$$\frac{dT_{R1}}{dt} = k_{M1} \cdot D_1 \cdot T_s + k_{g2} \cdot T_{R1} - k_{s2} \cdot D_2 \cdot T_{R1} - k_{M2} \cdot (1 - D_1) \cdot T_{R1} - k_{M3} \cdot D_2 \cdot T_{R1} + k_{M4} \cdot (1 - D_2) \cdot T_{R2} \quad (3.2)$$

$$\frac{dT_{R2}}{dt} = k_{M3} \cdot D_2 \cdot T_{R1} + k_{g3} \cdot T_{R2} - k_{M4} \cdot (1 - D_2) \cdot T_{R2} \quad (3.3)$$

$$k_1 = k_{\max\_1} \cdot T_{R1}^H / (T_{R1}^H + KT_{50}^H) \quad (3.4)$$

$$k_2 = k_{\max\_2} \cdot T_{R2}^H / (T_{R2}^H + KT_{50}^H) \quad (3.5)$$

$$\frac{dM_{ctDNA1}}{dt} = k_1 \cdot T_{R1} - k_e \cdot M_{ctDNA1} \quad (3.6)$$

$$\frac{dM_{ctDNA2}}{dt} = k_2 \cdot T_{R2} - k_e \cdot M_{ctDNA2} \quad (3.7)$$

$$TS = T_s + T_{R1} + T_{R2} \quad (3.8)$$

TS represents the total tumor size as detected by CT scan.  $k_{g1}$ ,  $k_{g2}$ , and  $k_{g3}$  represent the net growth rate constants of three clonal populations.  $k_{s1}$  and  $k_{s2}$  represent the tumor shrinkage rate due to treatments. Drug exposure variability was not considered in this study but only the presence ( $D_n = 1$ ) or absence ( $D_n = 0$ ) of a drug were considered ( $n = 1$  and 2 represent panitumumab and the hypothetical treatment, respectively).  $k_{M1}$  and  $k_{M3}$  represent the mutation rate constants governing the transfer from the drug susceptible clonal population to the drug resistant clonal population during  $D_1$  and  $D_2$  treatment, respectively.  $k_{M2}$  and  $k_{M4}$  represent the mutation rate constants from drug resistant clonal population to drug susceptible clonal population upon the withdrawal of treatments.  $k_1$  and  $k_2$  represent the shedding rate constants of ctDNA which carries mutations. Hill equations (Eq. 3.4 and 3.5) was applied to capture the concentration change of  $M_{ctDNA}$ .  $k_{max\_1}$  and  $k_{max\_2}$  are max releasing rates,  $KT_{50}$  is the tumor size that provide half-maximal releasing rate, H is the Hill coefficient.  $k_e$  represent the elimination rate constant of ctDNA.

When performing simulations, the baseline levels of TS (Eq. 3.8) and  $M_{ctDNA1}$  were set to the median of the real observations in different patient groups (**Supplementary Table S3.1**). For WT-KRAS patients, the baseline  $T_{R1}$  ( $T_{R1\_0}$ ) and  $T_{R2}$  ( $T_{R2\_0}$ ) were both set to 0. For M-KRAS patients,  $T_{R2\_0}$  were set to 0 while  $T_{R1\_0}$  was set according to the median of observations.

### 4.3 Parameter values

The values of all model parameters used in the simulation are shown in **Table 3.1**.

To assist the setting of parameter values, the parameters describing tumor dynamics under  $D_1$  therapy ( $k_{s1}$  and  $k_{M1}$ ) were estimated by fitting the collected tumor sizes data using the first order conditional estimation method with interaction (FOCEI) implemented in the NONMEM software, version 7.4.1 (ICON Development Solutions). The detailed method on parameter estimates can be found from the Supplementary methods.

The estimated typical values of  $k_{s1}$  and  $k_{M1}$  were adopted to simulations. Assuming the tumor growth follows an exponential growth pattern,  $k_{g1}$  was fixed as 0.03/week ( $= \ln 2 / (6.8 \text{ months} \cdot 4 \text{ weeks/month})$ ) according to a previously reported median placebo tumor doubling time of colorectal carcinomas, i.e. 6.8 months (range: 3–24 months) [40]. Accordingly,  $k_{g2}$  was fixed as 0.021 /week (0.03–70%).  $k_{M2}$  was set to be lower than  $k_{M1}$  based on the 5<sup>th</sup> assumption. The parameters that are related to the emergence of mutations ( $H$ ,  $KT_{50}$ , and  $k_{max}$ ) were set by visually matching the slope of mutant KRAS time-courses and the detectable time of mutant KRAS.

Random IIV was incorporated on  $k_g$  and baselines, which was assumed to be log-normally distributed, when performing the simulations (**Table 3.1**). It was due to the fact that patients in the dataset had different baseline tumor burden and mutant KRAS levels, and different growth rates of CRC were reported in different studies [13, 40]. If data from more patients can be included, the IIV on parameters will be able to be added to more parameters and be estimated.

3

#### 4.4 Model evaluation

To evaluate the suitability of the model, five hundred times of simulations were performed for  $TS$  and  $M_{ctDNA1}$  concentrations under continuous drug exposure. The 50<sup>th</sup> percentiles and the corresponding 95% CIs of simulations derived from the model were plotted along with the real observation points and the 50<sup>th</sup> percentiles of observations. In addition, assuming  $D_1$  was administered continuously for 20 weeks (leading to a continuous drug exposure) and then stopped for 20 weeks, the time-course of  $M_{ctDNA1}$  concentrations were simulated for 100 virtual patients to demonstrate if the decay upon the withdrawal of treatment could be captured by this model.

The performance of the model was also evaluated using another dataset from a study on NSCLC patients receiving EGFR inhibitors (icotinib/gefitinib) with the same method as above [14]. The time curves of tumor size which was reported as the longest diameter (mm) and that of EGFR mutation (L858R, exon 19 deletion, and T790M) concentrations (mutation copies/ml plasma) detected from ctDNA were digitized from published figures using WebplotDigitizer (<https://apps.automeris.io/wpd/>). The model used in the evaluation cohort was adjusted according to the findings of the study. More detailed introduction of the model and parameter values is shown in **Supplementary methods**.

#### 4.5 Treatment schedule evaluation

Treatment schedules that were considered in the current study are shown in **Table 3.2**. These schedules were evaluated on WT-KRAS patients.

A continuous schedule with  $D_1$  was first considered. The continuous schedule is the conventional treatment strategy in clinical practice where a therapy is administered continuously until disease progression (i.e. in schedules leading to continuous drug exposure) [19]. Monitoring frequency, i.e. the frequency of taking blood samples for ctDNA analysis and assessing tumor sizes, was set as once every 4 weeks according to the frequency of the obtained data.

To identify an optimized anti-cancer treatment schedule that suppresses the development of treatment resistance, intermittent schedules with  $D_1$  and adaptive schedules with  $D_1$  and  $D_2$  guided by ctDNA measurements, as proposed in previous studies [2, 8, 19, 21], were considered. For the intermittent schedules, drug-exposure interruption was introduced and multiple combinations of on- and off-dosing durations were evaluated. For the adaptive schedules, the ctDNA measurements were monitored and applied as a biomarker to determine the time point of switching treatment between  $D_1$  and  $D_2$ . The treatment started with  $D_1$  and continued till the ctDNA measurements increased to an upper limit for drug adjustment. Then  $D_1$  was suspended and switched to a continuous  $D_2$ . When the mutation concentration decreased back to a lower limit for drug adjustment, the treatment was switched back to  $D_1$  and the loop continued. In this case, multiple monitoring frequencies of ctDNA and multiple threshold of mutation concentrations for treatment switching were explored for comparison. The frequency of assessing tumor sizes was set as once every 4 weeks.

Simulations were performed with the package RxODE (version 1.0.8) implemented in R (version 4.0.2). One hundred virtual patients were simulated under each regimen. PFS of each virtual patient under each schedule was derived from the simulated total tumor size at every monitoring time point. PFS was defined based on WHO criteria (i.e. 25% increase in TS) as was applied in the original study [13, 45]. The  $T_{TS < TS_0}$  was also estimated to compare the effect of different regimens. In addition,  $T_{\text{mutant\_test}}$  was estimated assuming a lower limit of quantification for target mutant genes in ctDNA of 5 fragments/ml which was set based on the observed data. This aimed to determine if detectable mutation in ctDNA can be a predictor of disease progression.

## 4.6 Sensitivity analysis

A sensitivity analysis was performed to evaluate the impact of all parameter values on the model predictions. Every parameter was set as 50% or 150% of the original typical values one at a time. The continuous schedule, one intermittent schedule  $S_{\text{interm}(8\text{on\_4off})}$ , and one adaptive schedule  $S_{\text{adapt}(5\_10\_Freq12)}$  were simulated. IIV was not incorporated here. The sensitivity to the parameters was assessed by comparing the newly simulated time-courses of total tumor size and mutation concentrations together with the original simulation results. Median PFS and  $T_{\text{mutant\_test}}$  derived from each simulation were also estimated for comparison.

## References

1. Sun X, Hu B. Mathematical modeling and computational prediction of cancer drug resistance. *Brief Bioinform.* 2018;19(6):1382-99. doi:10.1093/bib/bbx065.
2. Nangalia J, Campbell PJ. Genome Sequencing during a Patient's Journey through Cancer. *N Engl J Med.* 2019;381(22):2145-56. doi:10.1056/NEJMra1910138.
3. Zhao B, Hemann MT, Lauffenburger DA. Modeling Tumor Clonal Evolution for Drug Combinations Design. *Trends Cancer.* 2016;2(3):144-58. doi:10.1016/j.trecan.2016.02.001.
4. Gerlinger M, Swanton C. How Darwinian models inform therapeutic failure initiated by clonal heterogeneity in cancer medicine. *British journal of cancer.* 2010;103(8):1139-43. doi:10.1038/sj.bjc.6605912.
5. Beerenwinkel N, Schwarz RF, Gerstung M, Markowetz F. Cancer evolution: mathematical models and computational inference. *Syst Biol.* 2015;64(1):e1-25. doi:10.1093/sysbio/syu081.
6. Carr TH, McEwen R, Dougherty B, Johnson JH, Dry JR, Lai Z, et al. Defining actionable mutations for oncology therapeutic development. *Nat Rev Cancer.* 2016;16(5):319-29. doi:10.1038/nrc.2016.35.
7. Kim C, Gao R, Sei E, Brandt R, Hartman J, Hatschek T, et al. Chemoresistance Evolution in Triple-Negative Breast Cancer Delineated by Single-Cell Sequencing. *Cell.* 2018;173(4):879-93 e13. doi:10.1016/j.cell.2018.03.041.
8. Wan JCM, Massie C, Garcia-Corbacho J, Mouliere F, Brenton JD, Caldas C, et al. Liquid biopsies come of age: towards implementation of circulating tumour DNA. *Nat Rev Cancer.* 2017;17(4):223-38. doi:10.1038/nrc.2017.7.
9. Siravegna G, Mussolin B, Buscarino M, Corti G, Cassingena A, Crisafulli G, et al. Clonal evolution and resistance to EGFR blockade in the blood of colorectal cancer patients. *Nat Med.* 2015;21(7):795-801. doi:10.1038/nm.3870.
10. Normanno N, Cervantes A, Ciardiello F, De Luca A, Pinto C. The liquid biopsy in the management of colorectal cancer patients: Current applications and future scenarios. *Cancer Treat Rev.* 2018;70:1-8. doi:10.1016/j.ctrv.2018.07.007.
11. Buil-Bruna N, Lopez-Picazo JM, Martin-Algarra S, Troconiz IF. Bringing Model-Based Prediction to Oncology Clinical Practice: A Review of Pharmacometrics Principles and Applications. *Oncologist.* 2016;21(2):220-32. doi:10.1634/theoncologist.2015-0322.
12. De Mattos-Arruda L, Weigelt B, Cortes J, Won HH, Ng CKY, Nuciforo P, et al. Capturing intra-tumor genetic heterogeneity by de novo mutation profiling of circulating cell-free tumor DNA: a proof-of-principle. *Ann Oncol.* 2014;25(9):1729-35. doi:10.1093/annonc/mdu239.
13. Diaz LA, Jr., Williams RT, Wu J, Kinde I, Hecht JR, Berlin J, et al. The molecular evolution of acquired resistance to targeted EGFR blockade in colorectal cancers. *Nature.* 2012;486(7404):537-40. doi:10.1038/nature11219.
14. Xiong L, Cui S, Ding J, Sun Y, Zhang L, Zhao Y, et al. Dynamics of EGFR mutations in plasma recapitulates the clinical response to EGFR-TKIs in NSCLC patients. *Oncotarget.* 2017;8(38):63846-56. doi:10.18632/oncotarget.19139.
15. Herbreteau G, Vallee A, Charpentier S, Normanno N, Hofman P, Denis MG. Circulating free tumor DNA in non-small cell lung cancer (NSCLC): clinical application and future perspectives. *J Thorac Dis.* 2019;11(Suppl 1):S113-S26. doi:10.21037/jtd.2018.12.18.
16. Bergerot PG, Hahn AW, Bergerot CD, Jones J, Pal SK. The Role of Circulating Tumor DNA in Renal Cell Carcinoma. *Curr Treat Options Oncol.* 2018;19(2):10. doi:10.1007/s11864-018-0530-4.
17. Dawson SJ, Tsui DW, Murtaza M, Biggs H, Rueda OM, Chin SF, et al. Analysis of circulating tumor DNA to monitor metastatic breast cancer. *N Engl J Med.* 2013;368(13):1199-209. doi:10.1056/NEJMoa1213261.

18. Oliveira KCS, Ramos IB, Silva JMC, Barra WF, Riggins GJ, Palande V, et al. Current Perspectives on Circulating Tumor DNA, Precision Medicine, and Personalized Clinical Management of Cancer. *Mol Cancer Res.* 2020;18(4):517-28. doi:10.1158/1541-7786.MCR-19-0768.
19. Zhang J, Cunningham JJ, Brown JS, Gatenby RA. Integrating evolutionary dynamics into treatment of metastatic castrate-resistant prostate cancer. *Nature Communications.* 2017;8(1). doi:10.1038/s41467-017-01968-5.
20. Rowe M, Hidayat A, Walter S, Pollard A, Norris T, Victor D, et al. The use of intermittent enzalutamide dosing in the treatment of metastatic castrate-resistant prostate cancer. *Journal of Clinical Oncology.* 2020;38(6\_suppl):81-. doi:10.1200/JCO.2020.38.6\_suppl.81.
21. Gatenby RA, Brown JS. Integrating evolutionary dynamics into cancer therapy. *Nature Reviews Clinical Oncology.* 2020;17(11):675-86. doi:10.1038/s41571-020-0411-1.
22. Algazi AP, Othus M, Daud AI, Lo RS, Mehnert JM, Truong TG, et al. Continuous versus intermittent BRAF and MEK inhibition in patients with BRAF-mutated melanoma: a randomized phase 2 trial. *Nat Med.* 2020;26(10):1564-8. doi:10.1038/s41591-020-1060-8.
23. Alva A, Hussain M. Optimal pharmacotherapeutic management of hormone-sensitive metastatic prostate cancer. *Drugs.* 2013;73(14):1517-24. doi:10.1007/s40265-013-0106-3.
24. Celli D, Jensen SE, Hahn EA, Beaumont JL, Korytowsky B, Bhattacharyya H, et al. Fatigue in patients with advanced renal cell carcinoma receiving sunitinib on an intermittent versus continuous dosing schedule in a randomized phase II trial. *Cancer Med.* 2014;3(5):1353-8. doi:10.1002/cam4.286.
25. Colleoni M, Luo W, Karlsson P, Chirgwin J, Aebi S, Jerusalem G, et al. Extended adjuvant intermittent letrozole versus continuous letrozole in postmenopausal women with breast cancer (SOLE): a multicentre, open-label, randomised, phase 3 trial. *Lancet Oncol.* 2018;19(1):127-38. doi:10.1016/s1470-2045(17)30715-5.
26. Jerusalem G, Farah S, Courtois A, Chirgwin J, Aebi S, Karlsson P, et al. Continuous versus intermittent extended adjuvant letrozole for breast cancer: final results of randomized phase III SOLE (Study of Letrozole Extension) and SOLE Estrogen Substudy. *Ann Oncol.* 2021;32(10):1256-66. doi:10.1016/j.annonc.2021.07.017.
27. Sofen H, Gross KG, Goldberg LH, Sharata H, Hamilton TK, Egbert B, et al. A phase II, multicenter, open-label, 3-cohort trial evaluating the efficacy and safety of vismodegib in operable basal cell carcinoma. *J Am Acad Dermatol.* 2015;73(1):99-105.e1. doi:10.1016/j.jaad.2015.03.013.
28. Kimko H, Pinheiro J. Model-based clinical drug development in the past, present and future: a commentary. *Br J Clin Pharmacol.* 2015;79(1):108-16. doi:10.1111/bcp.12341.
29. van Hasselt JG, van der Graaf PH. Towards integrative systems pharmacology models in oncology drug development. *Drug Discov Today Technol.* 2015;15:1-8. doi:10.1016/j.ddtec.2015.06.004.
30. Barbolosi D, Ciccolini J, Lacarelle B, Barlesi F, Andre N. Computational oncology--mathematical modelling of drug regimens for precision medicine. *Nature Reviews Clinical Oncology.* 2016;13(4):242-54. doi:10.1038/nrclinonc.2015.204.
31. Terranova N, Girard P, Klinkhardt U, Munafo A. Resistance Development: A Major Piece in the Jigsaw Puzzle of Tumor Size Modeling. *CPT Pharmacometrics Syst Pharmacol.* 2015;4(6):320-3. doi:10.1002/psp4.45.
32. Yin A, Moes D, van Hasselt JGC, Swen JJ, Guchelaar HJ. A Review of Mathematical Models for Tumor Dynamics and Treatment Resistance Evolution of Solid Tumors. *CPT Pharmacometrics Syst Pharmacol.* 2019;8(10):720-37. doi:10.1002/psp4.12450.
33. Bender BC, Schindler E, Friberg LE. Population pharmacokinetic-pharmacodynamic modelling in oncology: a tool for predicting clinical response. *Br J Clin Pharmacol.* 2015;79(1):56-71. doi:10.1111/bcp.12258.

3

34. Parseghian CM, Loree JM, Morris VK, Liu X, Clifton KK, Napolitano S, et al. Anti-EGFR-resistant clones decay exponentially after progression: implications for anti-EGFR re-challenge. *Ann Oncol.* 2019;30(2):243-9. doi:10.1093/annonc/mdy509.
35. Mistry HB. On the reporting and analysis of a cancer evolutionary adaptive dosing trial. *Nat Commun.* 2021;12(1):316. doi:10.1038/s41467-020-20174-4.
36. Gray R, Bradley R, Braybrooke J, Liu Z, Peto R, Davies L, et al. Increasing the dose intensity of chemotherapy by more frequent administration or sequential scheduling: a patient-level meta-analysis of 37 298 women with early breast cancer in 26 randomised trials. *The Lancet.* 2019;393(10179):1440-52. doi:10.1016/s0140-6736(18)33137-4.
37. Nagano T, Tachihara M, Nishimura Y. Mechanism of Resistance to Epidermal Growth Factor Receptor-Tyrosine Kinase Inhibitors and a Potential Treatment Strategy. *Cells.* 2018;7(11):212. doi:10.3390/cells7110212.
38. FDA Approval of KRAS Inhibitor Sotorasib for Lung Cancer Hailed as Milestone. 2021 June 25 [cited 2021 July12th]; Available from: <https://www.cancer.gov/news-events/cancer-currents-blog/2021/fda-sotorasib-lung-cancer-kras>
39. Yang BB, Lum P, Chen A, Arends R, Roskos L, Smith B, et al. Pharmacokinetic and pharmacodynamic perspectives on the clinical drug development of panitumumab. *Clin Pharmacokinet.* 2010;49(11):729-40. doi:10.2165/11535970-000000000-00000.
40. Blagoev KB, Wilkerson J, Burotto M, Kim C, Espinal-Dominguez E, Garcia-Alfonso P, et al. Neutral evolution of drug resistant colorectal cancer cell populations is independent of their KRAS status. *PLoS One.* 2017;12(10):e0175484. doi:10.1371/journal.pone.0175484.
41. Claret L, Gupta M, Han K, Joshi A, Sarapa N, He J, et al. Evaluation of tumor-size response metrics to predict overall survival in Western and Chinese patients with first-line metastatic colorectal cancer. *J Clin Oncol.* 2013;31(17):2110-4. doi:10.1200/JCO.2012.45.0973.
42. Xie H, Kim RD. The Application of Circulating Tumor DNA in the Screening, Surveillance, and Treatment Monitoring of Colorectal Cancer. *Ann Surg Oncol.* 2020. doi:10.1245/s10434-020-09002-7.
43. Basanta D, Gatenby RA, Anderson AR. Exploiting evolution to treat drug resistance: combination therapy and the double bind. *Molecular pharmaceutics.* 2012;9(4):914-21. doi:10.1021/mp200458e.
44. Zhou J, Liu Y, Zhang Y, Li Q, Cao Y. Modeling Tumor Evolutionary Dynamics to Predict Clinical Outcomes for Patients with Metastatic Colorectal Cancer: A Retrospective Analysis. *Cancer Res.* 2020;80(3):591-601. doi:10.1158/0008-5472.CAN-19-1940.
45. Choi JH, Ahn MJ, Rhim HC, Kim JW, Lee GH, Lee YY, et al. Comparison of WHO and RECIST criteria for response in metastatic colorectal carcinoma. *Cancer Res Treat.* 2005;37(5):290-3. doi:10.4143/crt.2005.37.5.290.

## Supplementary Methods

### Parameter estimate

To assist the setting of parameter values, the values of parameter describing tumor dynamics under anti-EGFR inhibitor ( $D_1$ ) therapy were estimated by fitting the collected tumor sizes data [1] using the first order conditional estimation method with interaction (FOCEI) implemented in NONMEM software, version 7.4.1 (ICON Development Solutions).

A non-linear mixed-effect model was developed. Parameters were assumed to be log-normally distributed and were expressed using Eq. S3.1.  $P_i$  represents the parameter of  $i$ th individual,  $P_{pop}$  represents typical value of the parameter, and  $\eta_i$  represents the random inter-individual variability (IIV) which was normally distributed with mean of 0 and variance of  $\omega^2$ . The residual error was characterized with a proportional error model as is shown in Eq. S3.2, where  $Obs$  represents observations,  $IPRED$  represents individual predictions, and  $\varepsilon_i$  represents the proportional residual error which was assumed to be normally distributed with mean of 0 and variance of  $\sigma^2_i$ .

$$P_i = P_{pop} \cdot e^{\eta_i} \quad \text{Eq. S3.1}$$

$$Obs = IPRED \cdot (1 + \varepsilon_i) \quad \text{Eq. S3.2}$$

Assuming the tumor growth follows an exponential growth pattern,  $k_{g1}$  was fixed as 0.03/week ( $= \ln 2 / (6.8 \text{ months} \cdot 4 \text{ weeks/month})$ ) according to a previously reported median placebo tumor doubling time colorectal carcinomas, i.e. 6.8 months (range: 3–24 months) [2].  $k_{g2}$ , as was assumed, was fixed as 0.021 /week (0.03–70%). The baseline levels of  $TS$  and mutant  $KRAS$  ( $M_{ctDNA1}$ ) were fixed according to real observations of each patient. For WT-KRAS patients, the baseline of  $T_{R1}$  were set to 0. For M-KRAS patients, the baseline of  $T_{R1}$  was estimated and the baseline of  $T_s$  equals the difference between the observed baseline and estimated baseline  $T_{R1}$ .

### Model in an evaluation cohort

The model used in the evaluation cohort was adjusted according to the findings of the study:

1. The detectable  $EGFR$  L858R mutation or exon 19 deletion in ctDNA at the start of treatment indicates the tumor is sensitive to anti-EGFR inhibitor. Therefore, the sensitive clonal population ( $T_s$ ) was assumed to carry one of these two mutations ( $M_{ctDNA1}$ );

3

2. L858R mutation or exon 19 deletion became undetectable when EGFR inhibitor ( $D_1$ ) started and raised back again together with the newly developed EGFR T790M mutation ( $M_{ctDNA2}$ ) during treatment [3], which indicates the emergence of treatment resistance. Therefore the acquired resistant clonal population under  $D_1$  ( $T_{R1}$ ) was assumed to carry both  $M_{ctDNA1}$  and  $M_{ctDNA2}$ ;
3. A hypothetical treatment next to anti-EGFR inhibitor ( $D_2$ ) was incorporated and assumed to target T790M positive NSCLC cancer ( $T_{R1}$ ). In the meantime, a third mutation ( $M_{ctDNA3}$ ) was able to be acquired which resulted in a third clonal population ( $T_{R2}$ ) that were resistant to  $D_2$ .

More details of the model and the parameters are shown in **Supplementary Figure S3.1** and **Supplementary Table S3.6**.

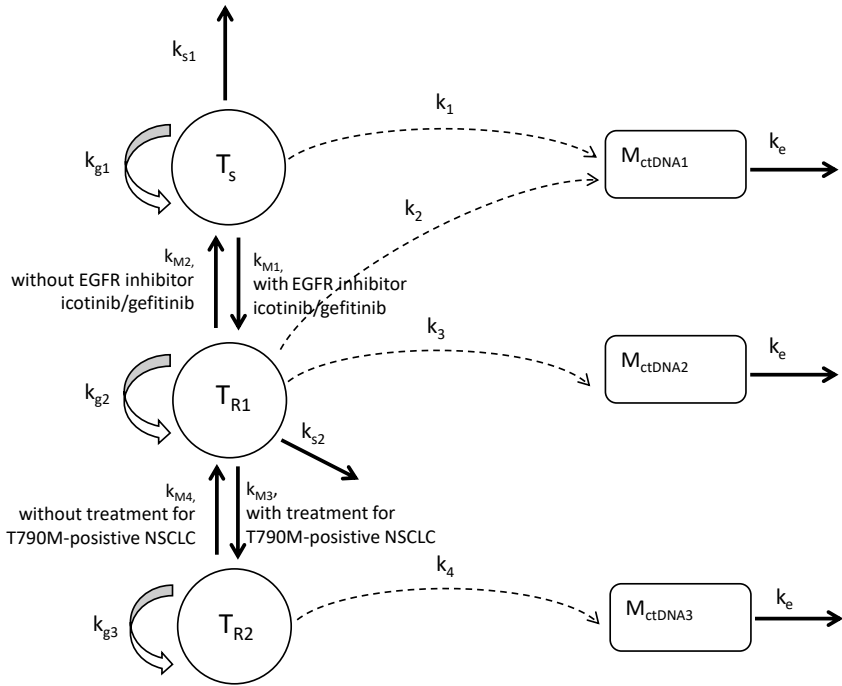
The values of parameters regarding tumor dynamics were estimated using the collected time curves of tumor sizes as described above. The residual error was characterized with an additive error model as is shown in Eq. S3.3, where  $Obs$  represents observations,  $IPRED$  represents individual predictions, and  $\varepsilon_2$  represents the additive residual error which was assumed to be normally distributed with mean of 0 and variance of  $\sigma_2^2$ . The parameter estimate results can be found in **Supplementary Table S3.7**.

$$Obs = IPRED + \varepsilon_2 \quad \text{Eq. S3.3}$$

### Supplementary References

1. Diaz LA, Jr., Williams RT, Wu J, Kinde I, Hecht JR, Berlin J, et al. The molecular evolution of acquired resistance to targeted EGFR blockade in colorectal cancers. *Nature*. 2012;486(7404):537-40. doi:10.1038/nature11219.
2. Blagoev KB, Wilkerson J, Burotto M, Kim C, Espinal-Dominguez E, Garcia-Alfonso P, et al. Neutral evolution of drug resistant colorectal cancer cell populations is independent of their KRAS status. *PLoS One*. 2017;12(10):e0175484. doi:10.1371/journal.pone.0175484.
3. Xiong L, Cui S, Ding J, Sun Y, Zhang L, Zhao Y, et al. Dynamics of EGFR mutations in plasma recapitulates the clinical response to EGFR-TKIs in NSCLC patients. *Oncotarget*. 2017;8(38):63846-56. doi:10.18632/oncotarget.19139.

## Supplementary Figures



$$\frac{dT_s}{dt} = k_{g1} \cdot T_s - k_{s1} \cdot T_s - k_{M1} \cdot D_1 \cdot T_s + k_{M2} \cdot (1 - D_1) \cdot T_{R1} \quad \text{Eq. S3.4}$$

$$\frac{dT_{R1}}{dt} = k_{M1} \cdot D_1 \cdot T_s + k_{g2} \cdot T_{R1} - k_{s2} \cdot D_2 \cdot T_{R1} - k_{M2} \cdot (1 - D_1) \cdot T_{R1} - k_{M3} \cdot D_2 \cdot T_{R1} + k_{M4} \cdot (1 - D_2) \cdot T_{R2} \quad \text{Eq. S3.5}$$

$$\frac{dT_{R2}}{dt} = k_{M3} \cdot D_2 \cdot T_{R1} + k_{g3} \cdot T_{R2} - k_{M4} \cdot (1 - D_2) \cdot T_{R2} \quad \text{Eq. S3.6}$$

$$k_1 = k_{\max,1} \cdot T_s^H / (T_s^H + KT_{50}^H) \quad \text{Eq. S3.7}$$

$$k_2 = k_{\max,1} \cdot T_{R1}^H / (T_{R1}^H + KT_{50}^H) \quad \text{Eq. S3.8}$$

$$k_3 = k_{\max,2} \cdot T_{R1}^H / (T_{R1}^H + KT_{50}^H) \quad \text{Eq. S3.9}$$

$$k_4 = k_{\max,3} \cdot T_{R2}^H / (T_{R2}^H + KT_{50}^H) \quad \text{Eq. S3.10}$$

$$\frac{dM_{ctDNA1}}{dt} = k_1 \cdot T_s + k_2 \cdot T_{R1} - k_e \cdot M_{ctDNA1} \quad \text{Eq. S3.11}$$

$$\frac{dM_{ctDNA2}}{dt} = k_3 \cdot T_{R1} - k_e \cdot M_{ctDNA2} \quad \text{Eq. S3.12}$$

$$\frac{dM_{ctDNA3}}{dt} = k_4 \cdot T_{R2} - k_e \cdot M_{ctDNA3} \quad \text{Eq. S3.13}$$

$$TS = T_s + T_{R1} + T_{R2} \quad \text{Eq. S3.14}$$

**Figure S3.1:** The model structure that characterize the dynamics of tumor size and mutation concentrations in ctDNA from NSCLC patients.  $T_s$ ,  $T_{R1}$ , and  $T_{R2}$  represent the sizes of the three tumor clonal populations, respectively.  $k_{g1}$ ,  $k_{g2}$ ,  $k_{g3}$  represent the net growth rates of three clonal populations.  $k_{s1}$  and  $k_{s2}$  represent the tumor decay rate due to treatments.  $k_{M1}$  and  $k_{M3}$  represent the mutation rate constant from drug susceptible clonal population to drug resistant clonal population during the course of anti-EGFR inhibitor ( $D_1$ ) and the hypothetical treatment ( $D_2$ ), respectively.  $k_{M2}$  and  $k_{M4}$  represent the transition rate constant from drug resistant clonal population to drug susceptible clonal population upon the withdrawal of treatments.  $k_1$ ,  $k_2$ ,  $k_3$ , and  $k_4$  represent the shedding rate constant of ctDNA which carries mutations.

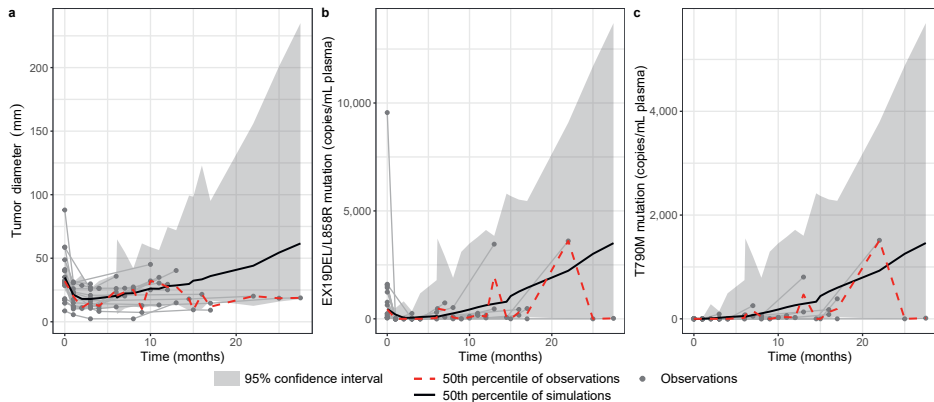


**Figure S3.2:** Model evaluation results on the time-courses of tumor diameters (a) and EGFR mutation concentrations including L858R mutation/ exon 19 deletion (b) and T790M mutation (c) collected from a previous clinical study where patients with non-small cell lung cancer were treated with anti-EGFR inhibitor icotinib/gefitinib.

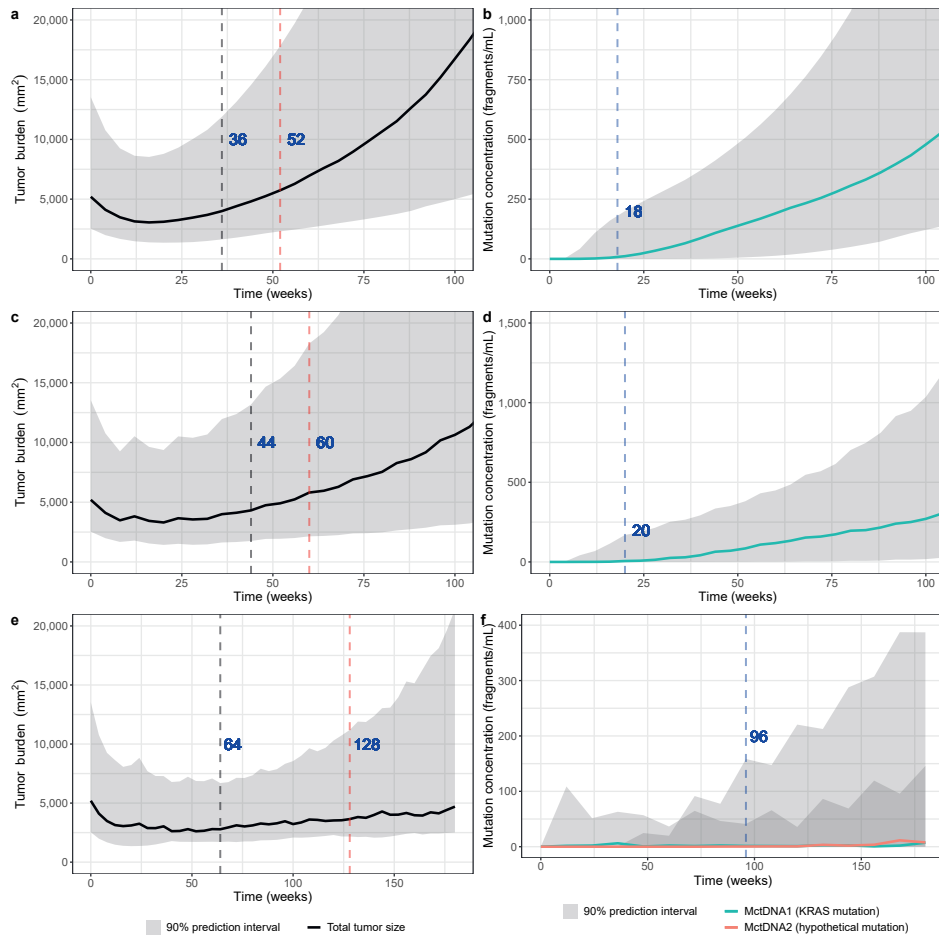


**Figure S3.3:** The simulated total tumor burden (a, c, e) and mutation concentrations (b, d, f) under continuous treatment (a, b), intermittent treatment (8-week treatment and 4-week suspension) (c, d), and adaptive treatment with the second hypothetical drug (ctDNA limits for drug adjustment: 5 and 10 fragments/ml, monitor frequency: 12 weeks) (e, f) for 100 colorectal cancer patients. Median total tumor sizes (black lines),  $M_{ctDNA1}$  (light sea green lines), and  $M_{ctDNA2}$  (salmon lines) were plotted together with corresponding 90% prediction intervals. Median PFS (black dashed vertical line),  $T_{TS<TS0}$  (red dashed vertical line), and  $T_{\text{mutant\_test}}$  (blue dash vertical line) were also shown in the figure.

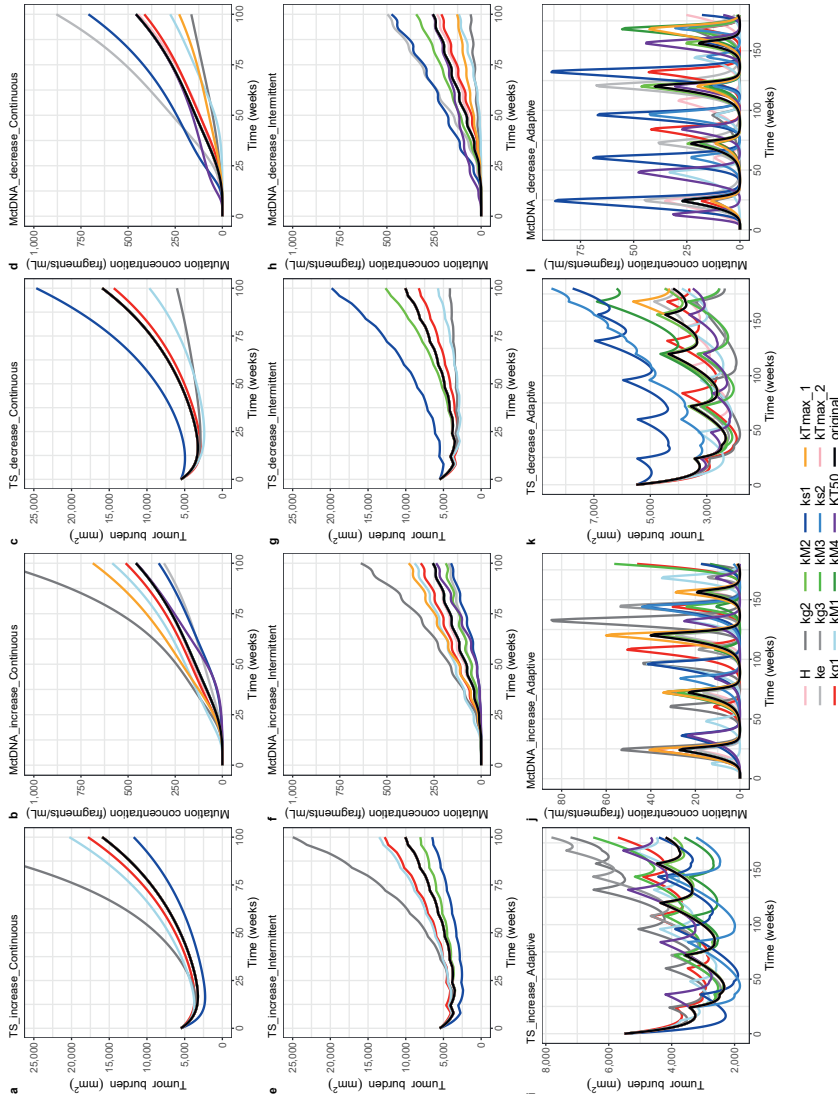


**Figure S3:4:** Simulated time-curves from sensitivity analysis. Simulated time-curves of tumor burden (a, c, e, g, i, k) and  $M_{\text{ctDNA}}$  concentrations (b, d, f, h, j, l) based on each parameter setting under continuous treatment (a-d), intermittent treatment (8-week treatment and 4-week suspension) (e-h), and adaptive treatment (ctDNA limits for drug adjustment: 5 and 10 fragments/ml; monitor frequency: 12 weeks) (i-k). Every parameter increased by 50% (a, b, e, f, i, j) or decreased by 50% one at a time (c, d, g, h, k, l).

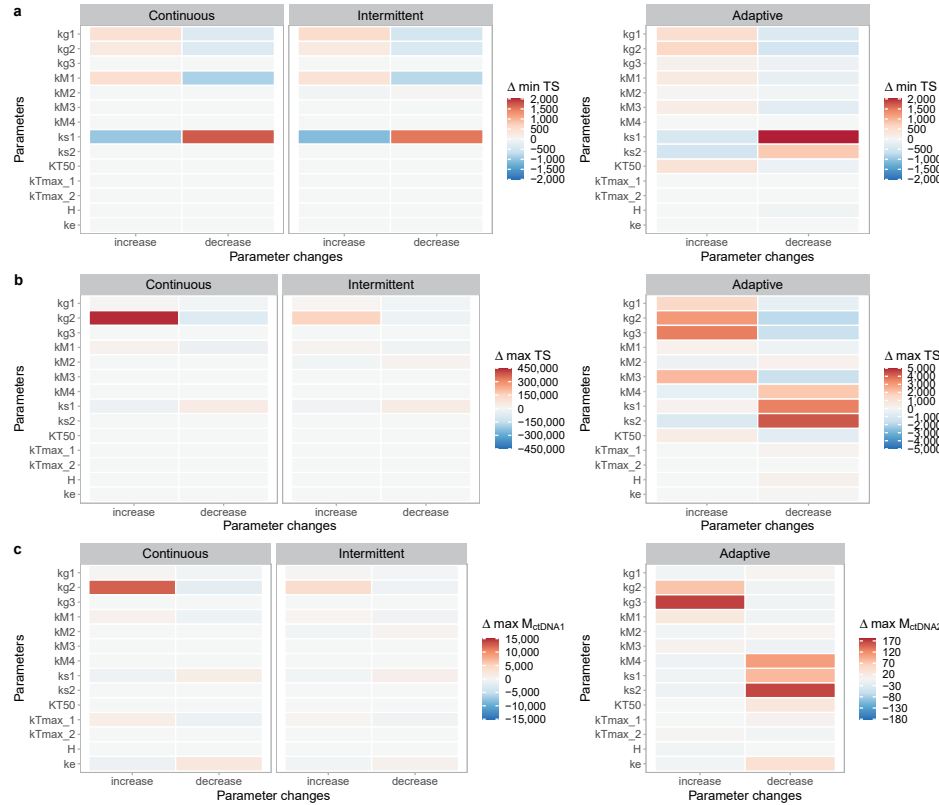


**Figure S3.5:** Relative change ( $\Delta$ ) of predicted minimum total tumor size (a), of total tumor size at the last simulated time point (180 weeks) (b), and of  $M_{ctDNA1}$  or  $M_{ctDNA2}$  concentrations at the last simulated time point (180 weeks) (c) compared with using original parameters in the sensitivity analysis.

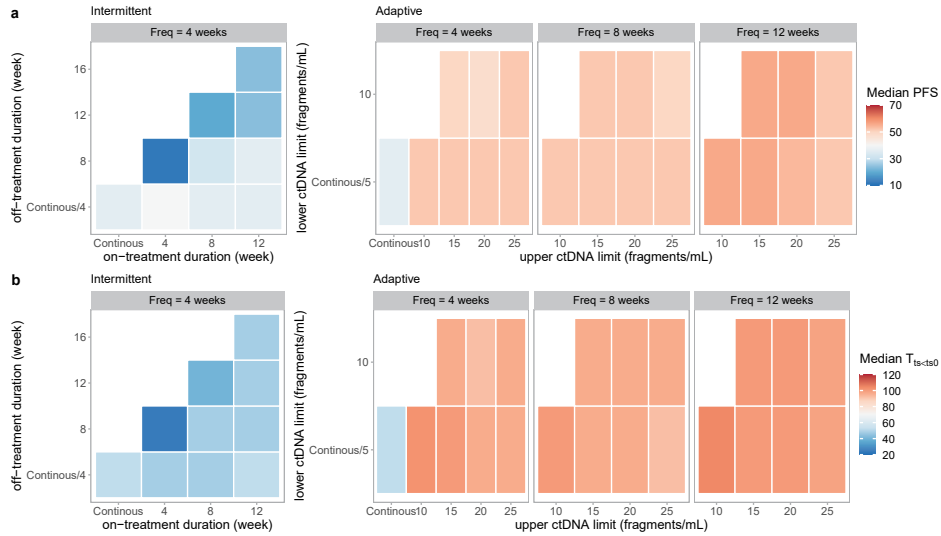


**Figure S3.6:** When fixing  $k_{M2}$  and  $k_{M4}$  to zero, the predicted median progression-free survival (PFS) (a) and the time until the tumor size had grown back to the baseline level ( $T_{TS<TS0}$ ) (b) of evaluated regimens.

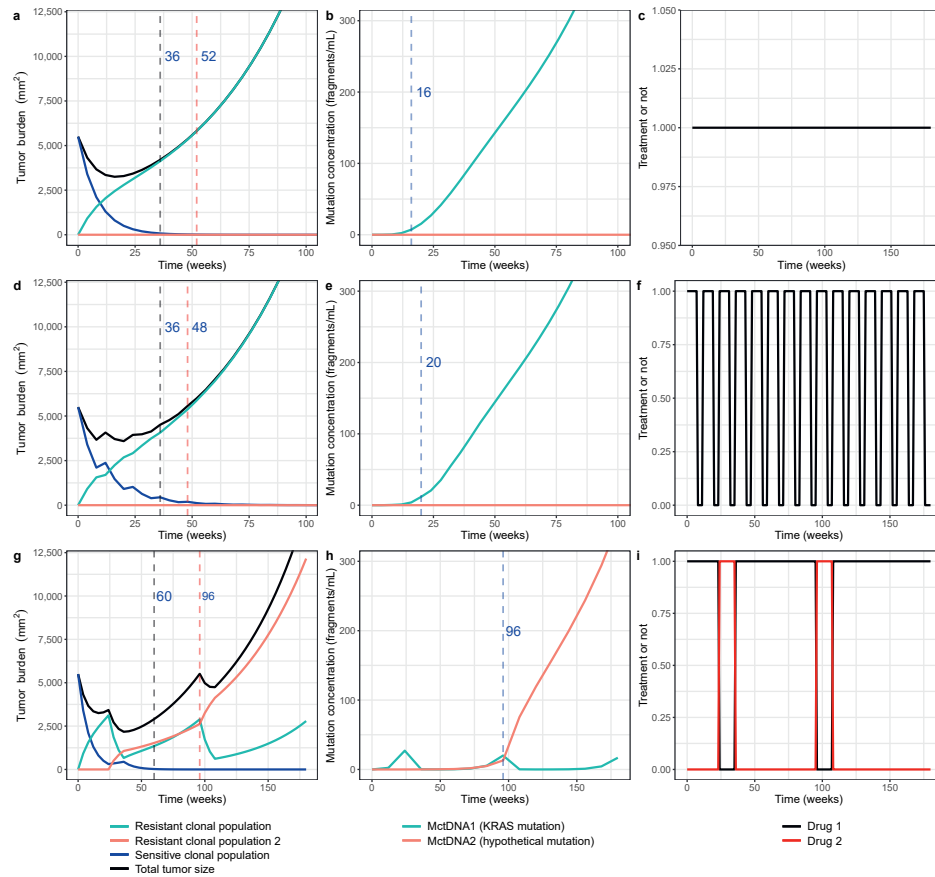


**Figure S3.7:** When fixing  $k_{M2}$  and  $k_{M4}$  to zero, the simulated time-curves of total tumor burden and each clonal population (a, d, g), mutation concentrations (b, e, h), and dosing strategies (c, f, i) of a typical subject with metastatic colorectal cancer undergoing continuous treatment (a, b, c), intermittent treatment (8-week treatment and 4-week suspension) (d, e, f), and adaptive treatment with the second hypothetical drug (ctDNA limits for drug adjustment: 5 and 10 fragments/ml, monitor frequency: 12 weeks) (g, h, i). Estimated PFS (black dashed vertical line),  $T_{TS < TS0}$  (red dashed vertical line), and  $T_{mutant\_test}$  (blue dash vertical line) are also shown in the figure.

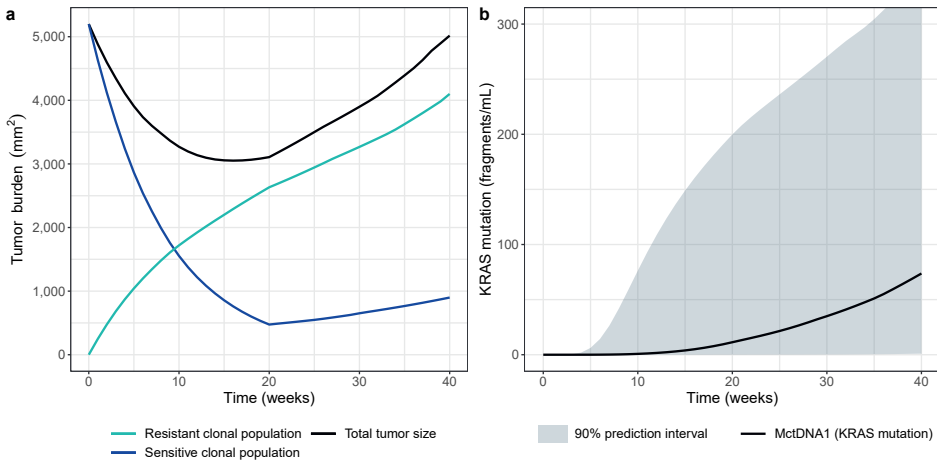


**Figure S3.8:** When fixing  $k_{M2}$  and  $k_{M4}$  to zero, model predicted total tumor burden and each clonal population (a) and mutant KRAS concentrations (b) under a regimen of 20-week treatment and 20-week suspension.

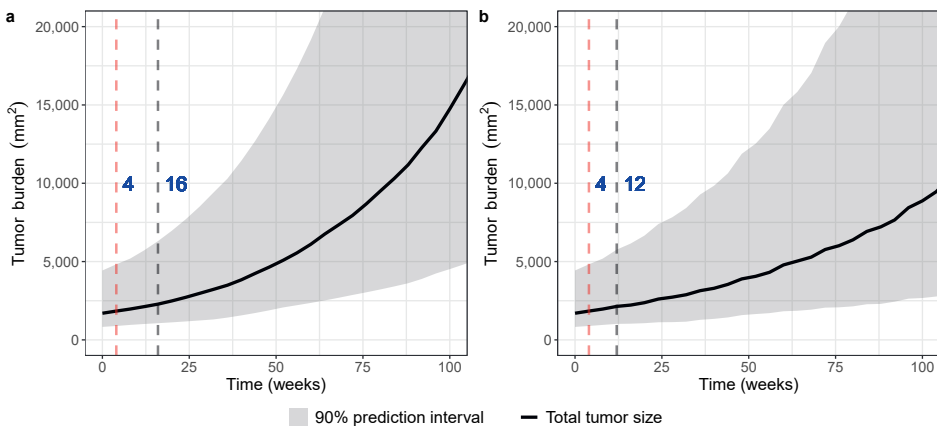


**Figure S3.9:** The simulated total tumor burden under continuous treatment (a) and intermittent treatment (8-week treatment and 4-week suspension) (b) for 100 colorectal cancer patients with detectable KRAS mutation pre-treatment. Median total tumor sizes (black lines) were plotted along with 90% prediction intervals. Median PFS (black dashed vertical line) and  $T_{TS < TS0}$  (red dashed vertical line) were also shown in the figure.

## Supplementary Tables

**Table S3.1:** Characteristics of the dataset collected from patients with metastatic colorectal cancer

|  | WT-KRAS patients  | M-KRAS patients  |
|--|-------------------|------------------|
| Number of patients                                   | 25                | 3                |
| Gender (Male (%))                                    | 15 (60%)          | 0 (0%)           |
| Age (years) (median (range))                         | 59 (42–78)        | 56 (48–78)       |
| TS <sub>0</sub> (mm <sup>2</sup> ) (median (range))  | 5649 (396–38006)  | 1714 (1312–1849) |
| Baseline mutant KRAS (fragments/ml) (median (range)) | 0                 | 411 (23–810)     |
| PFS (week) (median (range))                          | 23 (7–52)         | 7 (7–11)         |
| Mutant KRAS detectable time (week) (median (range))  | 22 (5–34) (N = 9) | 0                |

TS<sub>0</sub>, baseline tumor size; PFS, progression-free survival; WT-KRAS patients, patients who were identified to be initially KRAS wild-type; M-KRAS patients, patients who had detectable mutant KRAS pre-treatment.

**Table S3.2:** Parameter estimates of the tumor dynamics model based on the dataset collected from patients with metastatic colorectal cancer

| Parameters                           | Estimate (RSE)                            | IIV (CV%) [shrinkage] |
|--------------------------------------|---|-----------------------|
| WT-KRAS patients                     |   | -                     |
| T <sub>S,0</sub> (mm <sup>2</sup> )  | TS <sub>Obs</sub> (fixed)                 | -                     |
| T <sub>R1,0</sub> (mm <sup>2</sup> ) | 0 (fixed)                                 | -                     |
| M-KRAS patients                      |   |                       |
| T <sub>S,0</sub> (mm <sup>2</sup> )  | TS <sub>Obs</sub> – T <sub>R1,0_Est</sub> | -                     |
| T <sub>R1,0</sub> (mm <sup>2</sup> ) | 1830 (17%)                                | 0 (fixed)             |
| k <sub>g1</sub> (/week)              | 0.03 (fixed)                              | 68.6% [14%]           |
| k <sub>g2</sub> (/week)              | 0.7 · k <sub>g1</sub> (fixed)             | -                     |
| k <sub>s1</sub> (/week)              | 0.127 (5%)                                | -                     |
| k <sub>M1</sub> (/week)              | 0.0459 (18%)                              | -                     |
| Residual error                       |   | -                     |
| Prop (CV%)                           | 21.7% (11%)                               |                       |

TS<sub>Obs</sub>, observed total tumor size, T<sub>R1,0\_Est</sub>, estimated baseline of T<sub>R1</sub>, WT-KRAS patients, patients who were identified to be initially KRAS wild-type; M-KRAS patients, patients who had detectable mutant KRAS pre-treatment. RSE, relative standard error, CV, coefficient of variation, IIV, inter-individual variability, Prop, proportional residual error. Relative standard errors (RSEs) of parameter estimates were all within an acceptable range (< 30%).

**Table S3.3:** Characteristics of the dataset collected from patients with non-small cell lung cancer (NSCLC)

|  | Values              |
|--|---------------------|
| Number of patients   | 16                  |
| TS <sub>0</sub> (mm) (median (range))  | 33.92 (16.97–87.96) |
| Baseline EGFR L858R mutation /exosome 19 deletion concentration (copies/ml) (median (range)) | 438.75 (42–9555.56) |
| PFS (months) (median (range))  | 12 (4–25)           |
| EGFR T790M mutation detectable time (months) (median (range))                                | 10.5 (3–27.5)       |

TS<sub>0</sub>, baseline tumor size; PFS, progression-free survival.

**Table S3.4:** The results of each evaluated schedule in patients who were identified to be initially KRAS wild-type

| Schedules   | Median PFS*<br>(90% interval)<br>(weeks) | Median T <sub>TS&lt;TS0</sub><br>(90% interval)<br>(weeks) | Median T <sub>mutant_test</sub><br>(90% interval)<br>(weeks) |
|---|--|--|--|
| Continuous schedule (standard of care)  | 36 (32–44)                               | 52 (36–72)   | 18 (8–52.6)  |
| Intermittent schedules  |  |  |  |
| $D_1$ was administered for N weeks and suspended for M weeks. Total treatment time was 180 weeks.   |  |  |  |
| N (weeks)   | M (weeks)                                |  |  |
| 4   | 4  | 48 (24–80)   | 56 (24–112.8)  |
| 4   | 8  | 12 (12–72.6)   | 24 (12–96)   |
| 8   | 4  | 44 (32–60)   | 60 (36–104.2)  |
| 8   | 8  | 38 (16–64)   | 60 (32–113.2)  |
| 8   | 12                                       | 20 (16–20)   | 40 (20–116.4)  |
| 12  | 4  | 40 (32–56)   | 60 (36–92.2)   |
| 12  | 8  | 40 (20–60)   | 60 (36–112.2)  |
| 12  | 12                                       | 24 (20–49.0)   | 64 (24–116.2)  |
| 12  | 16                                       | 24 (20–28)   | 52 (24–108.4)  |
| Adaptive schedules with a hypothetical second treatment   |  |  |  |
| $D_1$ was continuously given, and suspended and switched to $D_2$ when the ctDNA measurement increased to higher than UP fragment/ml. Treatment switched back to $D_2$ when ctDNA measurement decreased back to lower than LOW fragment/ml. Total treatment time was 180 weeks. |  |  |  |

| LOW<br>(fragment/<br>ml) | UP<br>(fragment/<br>ml) | Monitoring<br>frequency of<br>ctDNA (weeks) |               |                  |                  |
|--------------------------|-------------------------|---|---------------|------------------|------------------|
| 5                        | 10                      | 4   | 62 (36–118.4) | 124 (45.2–170.8) | 100 (36–169.2)   |
| 5                        | 15                      | 4   | 60 (32–116.4) | 132 (45.8–176)   | 108 (36–172)     |
| 5                        | 20                      | 4   | 60 (32–112.4) | 124 (46.8–180)   | 102 (36–168)     |
| 5                        | 25                      | 4   | 60 (32–112.4) | 120 (44–172.4)   | 102 (36–168.2)   |
| 10                       | 15                      | 4   | 56 (32–124)   | 124 (47.2–172.8) | 108 (42.4–172.8) |
| 10                       | 20                      | 4   | 56 (32–108.4) | 120 (47.8–172.2) | 108 (44–176)     |
| 10                       | 25                      | 4   | 56 (32–108.8) | 114 (44–172.2)   | 110 (44–175.8)   |
| 5                        | 10                      | 8   | 60 (32–112.4) | 120 (44.8–163.2) | 96 (40–163.2)    |
| 5                        | 15                      | 8   | 60 (32–104.8) | 120 (44–169)     | 96 (40–170.4)    |
| 5                        | 20                      | 8   | 56 (32–100.4) | 120 (44–168)     | 96 (40–168)      |
| 5                        | 25                      | 8   | 56 (32–104.4) | 116 (44.8–168)   | 96 (40–168)      |
| 10                       | 15                      | 8   | 60 (32–104.4) | 120 (44–168)     | 96 (45.61–70.4)  |
| 10                       | 20                      | 8   | 56 (32–108.4) | 120 (44–164.4)   | 96 (45.6–168)    |

*Table S3.4 continues on next page.*

**Table S3.4:** *Continued*

| LOW<br>(fragment/<br>ml) | UP<br>(fragment/<br>ml) | Monitoring<br>frequency of<br>ctDNA (weeks) | 56 (32–104.8) | 118 (44.2–160) | 104 (47.2–168) |
|--------------------------|-------------------------|---|---------------|----------------|----------------|
| 10                       | 25                      | 8   | 56 (32–104.8) | 118 (44.2–160) | 104 (47.2–168) |
| 5                        | 10                      | 12  | 64 (32–108)   | 128 (44–164)   | 96 (48–180)    |
| 5                        | 15                      | 12  | 60 (36–120)   | 124 (44–176)   | 102 (48–168)   |
| 5                        | 20                      | 12  | 60 (32–104.2) | 120 (44–157.6) | 108 (48–180)   |
| 5                        | 25                      | 12  | 60 (32–104)   | 120 (44–156)   | 108 (48–168)   |
| 10                       | 15                      | 12  | 62 (32–108.2) | 124 (44–176)   | 102 (48–168)   |
| 10                       | 20                      | 12  | 60 (32–108)   | 120 (44–157.6) | 108 (48–168)   |
| 10                       | 25                      | 12  | 60 (36–104.2) | 120 (44–156)   | 108 (48–168)   |

\*Disease progression was defined by WHO criteria.

$D_1$ , anti-EGFR inhibitor;  $D_2$ , a hypothetical second treatment to which the newly acquired clone is susceptible; PFS, Progression-free survival;  $T_{\text{mutant\_test}}$ , time until detectable mutation;  $T_{\text{TS} < \text{TS}_0}$ , the time until the tumor size had grown back to the baseline level; ctDNA, circulating tumor DNA.

**Table S3.5:** Predicted progression-free-survival and time until detectable mutation in the sensitivity analysis

|  |                 | Intermittent schedule<br>(8-week treatment and<br>4-week suspension) |                 | Adaptive schedule<br>(ctDNA limits for drug<br>adjustment: 5 and 10<br>fragments/ml, monitor<br>frequency 12 weeks) |                 |                 |
|--|-----------------|--|-----------------|---|-----------------|-----------------|
| Continuous schedule  |                 | PFS (weeks) (Relative change*)                                       |                 |   |                 |                 |
| Parameters   | Increase<br>50% | Decrease<br>50%  | Increase<br>50% | Decrease<br>50%   | Increase<br>50% | Decrease<br>50% |
| $k_{g1}$   | -               | -  | 36 (-8)         | 48 (+4)   | 96 (+32)        | -               |
| $k_{g2}$   | 28 (-8)         | 52 (+16)   | 32 (-12)        | 84 (+40)  | 56 (-8)         | 76 (+12)        |
| $k_{g3}$   | -               | -  | -               | -   | 60 (-4)         | -               |
| $k_{s1}$   | -               | -  | -               | 32 (-12)  | 36 (-28)        | 60 (-4)         |
| $k_{s2}$   | -               | -  | -               | -   | -               | 60 (-4)         |
| $k_{M1}$   | 32 (-4)         | 44 (+8)  | 36 (-8)         | 60 (+16)  | 84 (+20)        | 44 (-20)        |
| $k_{M2}$   | -               | -  | 48 (+4)         | 40 (-4)   | -               | 60 (-4)         |
| $k_{M3}, k_{M4}$   | -               | -  | -               | -   | -               | -               |
| $k_e$  | -               | -  | -               | -   | -               | -               |
| $H$  | -               | -  | -               | -   | -               | 96 (+32)        |
| $KT_{50}$  | -               | -  | -               | -   | 36 (-28)        | 84 (+20)        |
| $k_{\max\_1}$  | -               | -  | -               | -   | -               | -               |
| $k_{\max\_2}$  | -               | -  | -               | -   | -               | -               |
| T <sub>mutant_test</sub> of $M_{ctDNA1}$ (weeks)<br>(Relative change*) |                 |  |                 | T <sub>mutant_test</sub> of $M_{ctDNA2}$ (weeks)<br>(Relative change*)  |                 |                 |
| Parameters   | Increase<br>50% | Decrease<br>50%  | Increase<br>50% | Decrease<br>50%   | Increase<br>50% | Decrease<br>50% |
| $k_{g1}$   | -               | 20 (+4)  | -               | 24 (+4)   | 120 (-48)       | 180 (+12)       |
| $k_{g2}$   | -               | 20 (+4)  | -               | 28 (+8)   | 108 (-60)       | No result       |
| $k_{g3}$   | -               | -  | -               | -   | 120 (-48)       | No result       |
| $k_{s1}$   | 24 (+8)         | 12 (-4)  | 32 (+12)        | 16 (-4)   | No result       | 72 (-96)        |
| $k_{s2}$   | -               | -  | -               | -   | No result       | 108 (-60)       |
| $k_{M1}$   | 12 (-4)         | 32 (+16)   | 16 (-4)         | 44 (+24)  | 144 (-24)       | No result       |
| $k_{M2}$   | -               | -  | -               | -   | -               | 132 (-36)       |
| $k_{M3}$   | -               | -  | -               | -   | 120 (-48)       | No result       |
| $k_{M4}$   | -               | -  | -               | -   | No result       | 132 (-36)       |
| $k_e$  | -               | -  | -               | -   | -               | 132 (-36)       |
| $H$  | 20 (+4)         | 12 (-4)  | 28 (+8)         | 16 (-4)   | -               | 120 (-48)       |
| $KT_{50}$  | 28 (+12)        | 8 (-8)   | 32 (+12)        | 8 (-12)   | 180 (+12)       | 96 (-72)        |
| $k_{\max\_1}$  | -               | 20 (+4)  | -               | 24 (+4)   | -               | 180 (+12)       |
| $k_{\max\_2}$  | -               | -  | -               | -   | 132 (-36)       | -               |

PFS, Progression-free survival;  $T_{\text{mutant\_test}}$ , time when mutation concentration became detectable;  $M_{ctDNA1}$ , KRAS mutation;  $M_{ctDNA2}$ , the second hypothesis mutation; -, result same as that under the original parameter setting; No result, the mutant gene concentrations did not reach the detectable limit (5 fragments/ml) by the end of simulation time (180 week).

\*With original parameters, the predicted PFS were 36, 44, and 64 weeks under continuous, intermittent, and adaptive schedule, respectively, and the predicted  $T_{\text{mutant\_test}}$  were 16, 20, and 168 weeks, respectively.

**Table S3.6:** Parameters values of the developed model characterizing the dynamics of tumor size and mutation concentrations in NSCLC patients

| Parameters                           | Description  | Typical values | Ref.   |
|--------------------------------------|--|----------------|--|
| $T_{s,0}$ (mm)                       | Baseline of $T_s$  | 35             | Data   |
| $T_{R1,0}$ (mm)                      | Baseline of $T_{R1}$   | 0              | Mutation was assumed to be acquired during treatment       |
| $T_{R2,0}$ (mm)                      | Baseline of $T_{R2}$   | 0              |  |
| $M_{ctDNA1,0}$ (copies/ml)           | Baseline of EGFR L858R mutation or exon 19 deletion ( $M_{ctDNA1}$ )           | 450            |  |
| $M_{ctDNA2,0}$ (copies/ml)           | Baseline of EGFR T790M mutation ( $M_{ctDNA2}$ )                               | 0              |  |
| $M_{ctDNA3,0}$ (copies/ml)           | Baseline of a third hypothetical mutation ( $M_{ctDNA3}$ )                     | 0              |  |
| $k_{g1}$ (/month)                    | Growth rate constant of $T_s$  | 0.07           | Estimated  |
| $k_{g2}$ (/month)                    | Growth rate constant of $T_{R1}$   | 0.049          |  |
| $k_{g3}$ (/month)                    | Growth rate constant of $T_{R2}$   | 0.035          |  |
| $k_{s1}$ (/month)                    | Tumor shrinkage rate constant due to $D_1$ (anti-EGFR inhibitor)               | 0.8            | Estimated  |
| $k_{s2}$ (/month)                    | Tumor shrinkage rate constant due to $D_2$ (the second hypothetical treatment) | 0.8            | $k_{s1}$   |
| $k_{M1}$ (/month)                    | Mutation rate from $T_s$ to $T_{R1}$ when $D_1 = 1$                            | 0.6            | Estimated  |
| $k_{M2}$ (/month)                    | Mutation rate from $T_{R1}$ to $T_s$ when $D_1 = 0$                            | 0.4            | Lower than $k_{M1}$  |
| $k_{M3}$ (/month)                    | Mutation rate from $T_{R1}$ to $T_{R2}$ when $D_2 = 1$                         | 0.6            | $k_{M1}$   |
| $k_{M4}$ (/month)                    | Mutation rate from $T_{R2}$ to $T_{R1}$ when $D_2 = 0$                         | 0.4            | $k_{M2}$   |
| $H$                                  | Hills coefficient  | 5              | Visually matching the slope of T790M mutation time-courses |
| $KT_{50}$ (mm)                       | The size of tumor that provide half-maximal shedding rate of ctDNA             | 30             |  |
| $k_{max,1}$ (copies /ml/ (month*mm)) | Maximum shedding rate of $M_{ctDNA1}$  | 120            |  |
| $k_{max,2}$ (copies /ml/ (month*mm)) | Maximum shedding rate of $M_{ctDNA2}$  | 50             |  |
| $k_{max,3}$ (copies /ml/ (month*mm)) | Maximum shedding rate of $M_{ctDNA3}$  | 50             |  |
| $k_e$ (/month)                       | ctDNA eliminate rate constant  | 2              |  |
| $IV_B(\omega_1)$                     | Standard deviation of IIV of baselines   | 0.6            |  |
| $IV_k_g(\omega_2)$                   | Standard deviation of IIV of $k_g$   | 0.2            |  |

ctDNA, circulating tumor DNA; IIV, inter-individual variability.

**Table S3.7:** Parameter estimates of the tumor dynamics model based on the dataset collected from patients with NSCLC

| Parameters        | Estimate (RSE%)            | IIV (CV%) [shrinkage] |
|-------------------|----------------------------|-----------------------|
| $T_{s,0}$ (mm)    | $TS_{0,Obs}$ (fixed)       |                       |
| $T_{R1,0}$ (mm)   | 0 (fixed)                  |                       |
| $k_{g1}$ (/month) | 0.0675 (45%)               | 105.4% [6%]           |
| $k_{g2}$ (/month) | $0.7 \cdot k_{g1}$ (fixed) | -                     |
| $k_{s1}$ (/month) | 0.835 (23%)                | 74% [3%]              |
| $k_{M1}$ (/month) | 0.553 (28%)                | -                     |
| Residual error    |                            | -                     |
| Add (mm)          | 2.67 (34%)                 |                       |

RSE, relative standard error; CV, coefficient of variation; IIV, inter-individual variability; Add, additive residual error.





# Chapter 4

## **Quantitative modeling of tumor dynamics and development of drug resistance in non-small cell lung cancer patients treated with erlotinib**

Anyue Yin, G.D. Marijn Veerman, Johan G.C. van Hasselt, Christi M.J. Steendam,  
Hendrikus Jan Dubbink, Henk-Jan Guchelaar, Lena E. Friberg,  
Anne-Marie C. Dingemans, Ron H.J. Mathijssen, Dirk Jan A.R. Moes



*Submitted*

## Abstract

Insight into the development of treatment resistance can support the optimization of anti-cancer treatments. This study aims to characterize the tumor dynamics and development of drug resistance in non-small cell lung cancer (NSCLC) patients treated with erlotinib, and investigate the relationship between baseline circulating tumor DNA (ctDNA) data and tumor dynamics. Data obtained for the analysis included 1) intensively sampled erlotinib concentrations from 29 patients from two previous pharmacokinetic (PK) studies, and 2) tumor sizes, ctDNA measurements, and sparsely sampled erlotinib concentrations from 18 patients from the START-TKI study. A two-compartment population PK model was first developed which well described the PK data. The PK model was subsequently applied to investigate the exposure-tumor dynamics relationship. To characterize the tumor dynamics, models accounting for intra-tumor heterogeneity and acquired resistance with or without primary resistance were investigated. Eventually, the model assumed acquired resistance only resulted in an adequate fit. Additionally, models with or without exposure-dependent treatment effect were explored, and no significant exposure-response relationship for erlotinib was identified within the observed exposure range. Subsequently, the correlation of baseline ctDNA data on *EGFR* and *TP53* variants with tumor dynamics parameters was explored. The analysis indicated that higher baseline plasma *EGFR* mutation levels correlated with increased tumor growth rates, and the inclusion of ctDNA measurements improved model fit. This result suggests that quantitative ctDNA measurements at baseline have the potential to be a predictor of anti-cancer treatment response. The developed model can potentially be applied to design optimal treatment regimens that better overcome resistance.

**Keywords:** oncology, quantitative modeling, intra-tumor heterogeneity, tumor dynamics, resistance development, non-small cell lung cancer, circulating tumor DNA

## 1. Introduction

The occurrence of anticancer treatment resistance due to intra-tumor heterogeneity and evolving adaptation of tumor cells to the treatment can limit the long-lasting efficacy of targeted anticancer treatment [1, 2]. In order to improve the anti-cancer treatment outcome, it is important to have detailed insight into the tumor progression during treatment since it enables designing of alternative treatment strategies.

In patients with non-small cell lung cancer (NSCLC), erlotinib, a tyrosine kinase inhibitor (TKI), is one of the effective treatment options especially for patients with *EGFR* exon 19 deletions or exon 21 mutations [3-5]. However, the occurrence of acquired drug resistance, which is most frequently due to the acquisition of the *EGFR* p.T790M mutation, and the possible presence of drug-resistant component pre-treatment (primary resistance) can limit its efficacy and result in relapse [3-6]. Thus, understanding the evolving progression of NSCLC during the treatment and identifying predictive biomarkers would be beneficial to optimize the treatment of NSCLC.

Pharmacometric modeling allows quantitative characterization and prediction of pharmacokinetic (PK) – pharmacodynamic (PD) profiles of drugs and thus facilitates treatment design [7-9]. With the help of a model-based approach, studies on evolving tumor progression can be conducted based on available data on tumor sizes and genetic biomarkers, and optimal treatment designs can be evaluated. Our previous study has proven such a concept based on data from metastatic colorectal cancer patients as well as from NSCLC patients [10]. Further incorporating the exposure of therapeutic agents in the model can support the investigation and understanding of exposure-tumor inhibition relationship and the evolutionary tumor dynamics in relation to drug exposure during anti-cancer treatment.

Circulating tumor DNA (ctDNA), which are DNA fragments in the circulation (circulating free DNA (cfDNA)) that are of tumor origin, is a clinically available and emerging genetic biomarker [11]. It has shown to be able to provide detailed insight into the molecular alterations and evolving progression of tumor under treatment [4, 5, 11]. In patients with NSCLC, numerous studies have shown that a decrease in mutant gene levels in ctDNA correlates to the therapeutic response of TKIs [5]. In another model-based study, the relative change of concentrations of driver mutation in ctDNA from the estimated baseline was shown to be predictive to disease progression of NSCLC patients [12]. Further research on the correlation between ctDNA measurements and tumor size dynamics would be beneficial to understanding the evolutionary development of treatment resistance and the value of ctDNA.

In the current study, we aimed to develop a model to understand and characterize tumor dynamics and the development of drug resistance in NSCLC patients treated with erlotinib. First, a population PK model of erlotinib was developed and thereafter applied to investigate the exposure-tumor inhibition relationship of erlotinib. Tumor dynamics models accounting for tumor heterogeneity, with or without a pre-existing resistance component, and drug exposure-dependent treatment effects, were evaluated. Subsequently, we aimed to explore the correlation of the extent of somatic driver mutation in ctDNA at baseline with the tumor dynamics in NSCLC patients.

## 2. Method

### 2.1 Patients and data

#### 2.1.1 *Intensively sampled PK data*

The study included intensively sampled erlotinib concentration-time curves from two previous PK studies in patients with NSCLC who were treated with erlotinib for an activating EGFR mutation [13, 14]. Erlotinib was administrated orally once daily with a dosage of 50–150 mg. PK samples were collected before drug intake and at 0.5, 1, 1.5, 2, 2.5, 3, 3.5, 4, 6, 8, 12, and 24 hours after drug administration at steady state. The studies were performed at the Erasmus MC Cancer Institute in Rotterdam, the Netherlands, and the details of the studies' design can be found in previous publications [13, 14]. For the current study, only the data in the control arms that were sampled after receiving erlotinib with water and without concomitant esomeprazole were included, which aimed to be consistent with real world patients.

Patients' demographic information, including age, sex, weight, height, and additional laboratory test results, including creatinine, estimated glomerular filtration rate (eGFR), albumin, total bilirubin, aspartate aminotransferase (AST), alanine aminotransferase (ALT), and alkaline phosphatase (ALP) were collected for covariate analysis.

#### 2.1.2 *PK-PD data*

Longitudinal measured tumor sizes under standard clinical care conditions as well as sparsely sampled intended trough erlotinib concentrations from real-world NSCLC patients who participated in the START-TKI study (NCT05221372), which is a prospective, observational multicenter study [6], were also included in this analysis. Erlotinib was administrated orally once daily with a dosage of 75–150 mg. The tumor size measurements,

i.e. the sum of the longest diameters (SLD, mm) of target lesions, were assessed by Response Evaluation Criteria In Solid Tumors (RECIST version 1.1 [15]). Additional data of dosing information, ctDNA data on variant allele frequency (VAF) of mutant genes over time, and concentrations of cfDNA over time from these patients were also collected. The detailed methods of cfDNA isolation and next-generation sequencing process have earlier been described [6]. Patients demographic information and lab test results as above mentioned were also collected for potential covariate analysis.

The studies from which the data were obtained were previously approved by local ethics committee and were registered in the Dutch Trial Registry. Written informed consent was obtained from all patients prior to these studies, including the use of data for further studies. For the current study, the data were shared anonymously and all procedures were performed in accordance with relevant guidelines and the Declaration of Helsinki, so no additional informed consent had to be obtained.

## 2.2 Population PK model

Based on the collected PK data, a population PK model was developed to characterize the erlotinib PK profiles of included patients. The intensively sampled PK data and the sparsely sampled PK data from patients involved in the START-TKI study were combined for the model development.

One- and two-compartment models with first-order absorption, with or without lag time, and first-order elimination were explored as the structural model. A combined proportional and additive model was applied to characterize the residual error. Parameters were assumed to be log-normally distributed. To account for the inter-individual variability (IIV) in bioavailability (F) which is shared by the estimated apparent PK parameters, the IIV on F was estimated while the typical value of F was fixed to 1. The structural model was selected based on biological plausibility and the objective function value (OFV).

Patients' demographic information and lab test results were then investigated as covariates using the stepwise covariate modeling (SCM) function of Perl-speaks NONMEM (version 4.9). The effect of all covariates on erlotinib clearance and that of weight, height, and albumin on apparent distribution volume of the central compartment were investigated. The relationship between F and dose level was not explored since the majority of patients received the same dose level. Model selection was based on the reduction in OFV (a likelihood ratio test) assuming a  $\chi^2$  distribution, a reduction in IIV, and physiological plausibility. The p values were set as 0.05 and 0.01 for the forward selection and backward

elimination process, respectively. A more detailed description of the covariates analysis can be found in **Supplementary Material S4.1**.

The final model was evaluated with goodness-of-fit (GOF) plots, visual predictive checks (VPC) based on 1000 simulations, and bootstrap with 1000 resampled datasets. In addition, the percentage where the predicted area under the curve (AUC) falls within 80–120% of the corresponding observed AUC (estimated with trapezoidal rules method) was calculated for the full concentration-time curves to evaluate the model. The percentage where the predicted trough concentrations fall within 80–120% of the corresponding observations was also estimated for the data from the START-TKI study.

### 2.3 Tumor dynamics model

The dynamics of tumor sizes during erlotinib treatment, which was represented by sum of longest diameters (SLD, mm) of target lesions, was characterized accounting for tumor heterogeneity. Tumor tissue was assumed to consist of a sensitive clonal population ( $T_s$ ) and a resistant clonal population ( $T_r$ ). Models considering 1) only acquired resistance and no primary resistance (i.e. baseline  $T_r (T_{r,0}) = 0$ ), and 2) both primary and acquired resistance (i.e.  $T_{r,0} \neq 0$  and was estimated), with or without a drug exposure-dependent decay, were explored. Considering the amount of the available data, the baseline tumor sizes were fixed to the observed values to ensure the stability of the model. The model structure is shown in **Figure 4.1** and Eqs. 4.1–4.4, where  $k_g$  represents the growth rates of  $T_s$  and  $T_r$ ,  $k_m$  represents mutation rate, and  $k_d$  represents tumor decay rate due to treatment. For the models exploring the exposure-dependent treatment effect, the tumor decay rate was assumed to depend on drug exposure and a simple linear relationship was assumed (Eq. 4.2). A non-linear relationship with Emax model was also explored. The drug exposure was defined as the trough concentration, which is the exposure metrics of interest for erlotinib exposure-response analysis and is relatively easy to measure in clinical practice. The trough concentrations were predicted by the individual PK parameters obtained from the PK model. The IIV of parameters were evaluated and parameters were assumed to be log-normally distributed. The combined proportional and additive model was applied to

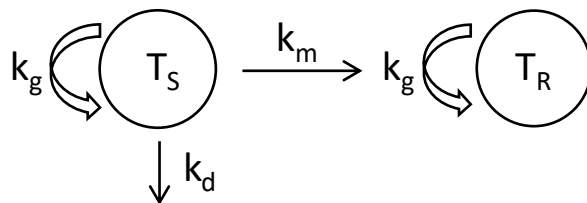


**Figure 4.1:** Graphical structure of the tumor dynamics model.

characterize the residual error. The model fit was evaluated by OFV and Akaike information criterion (AIC). The best fitted model was evaluated with GOF plots and VPC considering the censoring of data due to progression defined by RECIST version 1.1 [15].

$$\frac{dT_S}{dt} = k_g \cdot T_S - k_d \cdot T_S - k_m \cdot T_S \quad \text{Eq. 4.1}$$

$$k_d = \begin{cases} k_d, & \text{for the model without exposure-dependent decay} \\ k_d \cdot \text{Exposure}, & \text{for the model with exposure-dependent decay} \end{cases} \quad \text{Eq. 4.2}$$

$$\frac{dT_R}{dt} = k_m \cdot T_S + k_g \cdot T_R \quad \text{Eq. 4.3}$$

$$TS = T_S + T_R \quad \text{Eq. 4.4}$$

4

## 2.4 Genetic biomarkers and tumor dynamics

The correlation of baseline ctDNA measurements, including *EGFR* mutation levels and the presence of *TP53* mutations, with tumor dynamics parameters ( $k_g$ ,  $k_m$ , and  $k_d$ ) were explored graphically. Patients were separated into groups based on 1) whether their baseline mutant *EGFR* VAF was  $<$  or  $\geq$  the median value, or the measurements were unavailable, or 2) whether patients had a *TP53* mutation at baseline or not, or the results were unavailable. The correlation between baseline cfDNA concentrations and tumor dynamics parameters was also explored by separating patients into groups based on the median value to investigate informativeness of cfDNA compared to ctDNA.

Furthermore, the influence of baseline ctDNA measurements and cfDNA concentrations on  $k_g$ ,  $k_m$ , and  $k_d$  were evaluated as categorical covariates in the tumor dynamics model. The *EGFR* mutation levels and the cfDNA concentrations were categorized based on the corresponding median values as is described above. When a sample is missing, it was assigned to the third category and a sensitivity analysis was performed by evaluating models with and without the covariate for a dataset where the data from patients with missing covariates were removed. A significant correlation was defined as a decrease in OFV by more than 3.84 ( $p < 0.05$ , degree of freedom = 1, assuming  $\chi^2$  distribution).

## 2.5 Software and estimation methods

The population modeling analysis in this study was performed with NONMEM (version 7.4.4, ICON Development Solutions, Ellicott City, MD, USA). Parameters were estimated using the first order conditional estimation method with interaction (FOCEI). Data management and plots generation were performed with R statistics software (version 4.2.1, R Foundation for Statistical Computing, Vienna, Austria).

### 3. Results

#### 3.1 Patients and data

The intensively sampled erlotinib concentration-time curves were obtained from 29 patients (N = 377, 13 samples per patient). The SLD measurements (N = 155) as well as additionally sampled erlotinib concentrations (N = 146), ctDNA measurements (N = 50), and cfDNA concentrations (N = 50) were collected from 18 real-world NSCLC patients from the START-TKI study. For these 18 patients, the median time period when the SLD measurements were available is 264 days since the start of the treatment (range from 20–1168 days), and all patients had an event of disease progression or death where data were censored afterwards.

The obtained erlotinib concentration data over time are presented in **Figure S4.1**. None of the collected data was below the lower limit of quantification. The median baseline tumor size (SLD) of the included patients was 76.6 mm (range 29–116 mm). Out of the 146 obtained concentrations, 125 were measured at  $\geq$  20 hours after last drug intake (trough concentrations) with a median of 842 ng/mL and range of 318–1834 ng/mL. Activating *EGFR* variants (including exon 19 deletions (N = 11) and *EGFR* p.L858R (N = 6) and p.K852R (N = 1) mutations) were detected in the tumor biopsies of all 18 patients [6]. The plasma cfDNA samples at the start of treatment were available from 12 out of 18 patients. The median baseline cfDNA concentration was 1.44 ng/ $\mu$ L (range from 0.77–3.65 ng/ $\mu$ L). The primary *EGFR* variants were detected from baseline cfDNA samples from 8 out of 12 patients, which include exon 19 deletions (N = 6) and *EGFR* p.L858R (N = 1) and p.K852R (N = 1) mutations. The median baseline *EGFR* VAF was 1.74% (range from 0–62.74%). The obtained VAF of primary *EGFR* variants over time are shown in **Figure S4.2**. Furthermore, a *TP53* mutation was detected in 4 patients at baseline and the *EGFR* p.T790M mutation was detected in 3 patients during erlotinib treatment. The baseline characteristics and the data contributed by each patient are summarized in **Table 4.1**.

#### 3.2 Population PK model

A two-compartment population PK model with first-order absorption with lag time and first-order elimination was developed and showed to best fit the obtained PK data. Compared to the one-compartment model, the OFV of the selected model decreased by 27.5 ( $p < 0.01$ , degree of freedom = 3), indicating an improvement in the model fit. None of the tested covariates was identified to have significant effect on the PK parameters. The parameter estimates of the PK model are presented in **Table 4.2**. The relative standard errors (RSEs) were  $\leq 25\%$  for all parameters except for apparent distribution clearance

**Table 4.1:** Baseline characteristics of patients and the collected data

|                                      | Intensively sampled PK data<br>(N = 29) |         | PK/PD data<br>(N = 18) |          |
|--------------------------------------|---|---------|------------------------|----------|
|                                      | Median                                  | Range   | Median                 | Range    |
| Age (years)                          | 63                                      | 35–78   | 66                     | 48–78    |
| Sex (N (%))                          |   |         |                        |          |
| Male                                 | 13 (44.8%)                              |         | 5 (27.8%)              |          |
| Female                               | 16 (55.2%)                              |         | 13 (72.2%)             |          |
| Weight (kg)                          | 74                                      | 50–102  | 69.5                   | 46.1–109 |
| Height (cm)                          | 173                                     | 152–202 | 169                    | 154–180  |
| Serum creatinine (μmol/L)            | 82                                      | 47–138  | 66                     | 59–192   |
| eGFR (ml/(min.1.73 m <sup>2</sup> )) | 71                                      | 46–100  | 84.5                   | 23–103   |
| AST (IU/L)                           | 29                                      | 13–40   | 21.5                   | 14–37    |
| ALT (IU/L)                           | 25                                      | 10–83   | 18                     | 6–43     |
| Albumin (g/L)                        | 41                                      | 32–48   | 42.5                   | 34–51    |
| ALP (U/L)                            | 85                                      | 53–157  | 87.5                   | 3–798    |
| Bilirubin (μmol/L)                   | 8                                       | 3–58    | 6.5                    | 3–14     |
| Erlotinib starting dose (N (%))      |   |         |                        |          |
| 150 mg                               | 25 (86.2%)                              |         | 18 (100%)              |          |
| 100 mg                               | 3 (10.3%)                               |         | 0                      |          |
| 50 mg                                | 1 (3.4%)                                |         | 0                      |          |
| N of concentration per patient       | 13                                      | 13–13   | 8 (N = 2 no data )     | 1–20     |
| N of SLD per patient                 | -                                       | -       | 7                      | 2–18     |
| N of ctDNA or cfDNA data per patient | -                                       | -       | 3                      | 1–4      |

eGFR, estimated glomerular filtration rate; AST, aspartate aminotransferase; ALT, alanine aminotransferase; ALP, alkaline phosphatase; ctDNA, circulating tumor DNA; cfDNA, circulating free DNA; SLD, sum of longest diameters.

(Q/F) (40%), indicating acceptable estimation precision. High estimates for IIV on Q/F and absorption rate constant (Ka) were observed (coefficient of variation (CV%) > 100 %), with shrinkages < 30%. The parameter estimates were also in good agreement with the bootstrap results (**Table 4.2**).

The GOF plots of the final PK model demonstrated a good concordance between the model predictions and observations (**Figure S4.3**). The conditional weighted residual errors (CWRES) randomly distributed around zero without obvious trends over population predictions, but with a slight trend over time between 6–8h after last drug intake. The VPC plot (**Figure 4.2**) shows that the observed data can be adequately predicted by the developed model. Additionally, 100% of the model predicted AUC and 82.4% of the model predicted trough concentrations were within 80–120% of their corresponding observations.

**Table 4.2:** Parameter estimates of the population pharmacokinetic model

| Parameters            | Explanation  | Estimate<br>(RSE%) | IIV (CV%) (RSE%)<br>[shrinkage%] | Bootstrap |              |
|-----------------------|--|--------------------|----------------------------------|-----------|--------------|
|                       |  |                    |                                  | Median    | 95% CI       |
| CL/F (L/h)            | Apparent clearance   | 4.10 (5%)          | 15.7% (31%) [48%]                | 4.09      | 3.68– 4.47   |
| Vc/F (L)              | Apparent distribution volume of the central compartment    | 142 (7%)           | 20.3% (31%) [43%]                | 142       | 125– 162     |
| Vp/F (L)              | Apparent distribution volume of the peripheral compartment | 2420 (12%)         | -                                | 2462      | 1768– 8043   |
| Q/F (L/h)             | Apparent distribution clearance                            | 0.548 (40%)        | 194.4% (15%) [28%]               | 0.542     | 0.188–1.24   |
| Ka (/h)               | Absorption rate constant                                   | 1.61 (23%)         | 124.5% (15%) [18%]               | 1.68      | 1.03–2.65    |
| T <sub>lag</sub> (h)  | Absorption lag time  | 0.400 (5%)         | -                                | 0.400     | 0.358– 0.428 |
| F                     | Bioavailability  | 1 fixed            | 16.3% (31%) [37%]                | 1 fixed   | -            |
| Residual errors       |  |                    |                                  |           |              |
| Prop. Err. (CV%)      | proportional residual error                                | 15.4 (6%)          | [10%] <sup>*</sup>               | 15.3      | -            |
| Add. Err. (SD, ng/ml) | additive residual error                                    | 44.5 (25%)         | [10%] <sup>*</sup>               |           | -            |
|                       |  |                    |                                  | 43.4      |              |

RSE, relative standard error; IIV, inter-individual variability; CI, confidence interval; CV, coefficient of variation; SD, standard deviation.

<sup>\*</sup> Epsilon shrinkage.

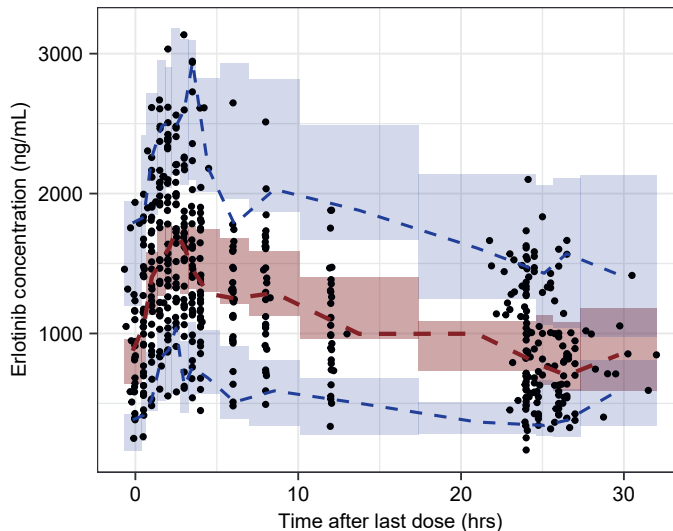


**Figure 4.2:** Visual predictive check (VPC) of the developed population PK model. Blue dashed lines represent 95<sup>th</sup> and 5<sup>th</sup> percentiles of the observations, red dashed line represents the 50<sup>th</sup> percentile of the observations, blue shaded areas represent 95% confidence interval of the 95<sup>th</sup> and 5<sup>th</sup> percentiles based on the simulations respectively, and red shaded area represents 95% confidence interval of the 50<sup>th</sup> percentile based on the simulations.

### 3.3 Tumor dynamics model

The tumor dynamics modeling results showed that the model accounting for acquired resistance only could adequately fit the data. The model that assumed the presence of primary resistance did not show an improved fit to the available data ( $p > 0.05$ , OFV decreased by 0.731 and AIC increased by 1.269, degree of freedom = 1). The typical estimate of  $T_{R_0}$  in this model was 4.51 mm which account for a small proportion (5.9%) of the median baseline tumor size (**Table S4.1**). Therefore, the pre-existing resistance component was ultimately not included in the model. Furthermore, the OFV and AIC of the model incorporating an exposure-dependent decay increased by 1.441 compared with the base model, indicating no improvement in the model fit. Therefore, the exposure-dependent drug effect was not included in the final model.

The parameter estimates of the final tumor dynamics model are shown in **Table 4.3** (model code in **Supplementary Material S4.2**). The RSEs of the parameter estimates were all  $< 30\%$ , indicating acceptable estimation precision. High estimates for IIV of the estimated tumor dynamics parameters were observed ( $CV\% > 60\%$ ). The GOF plots demonstrated a sufficient fit of the developed model to the data (**Figure S4.4**). The VPC considering the censoring of data due to progression showed that the model predicted intervals adequately captured the distribution of observations (**Figure 4.3**).

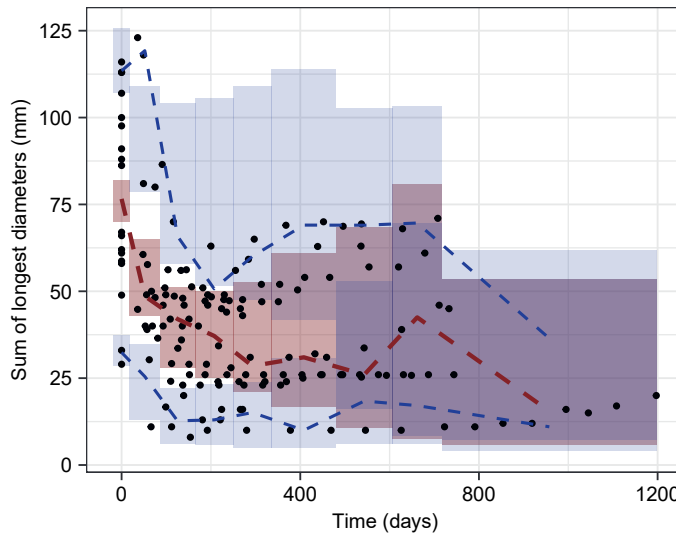


**Figure 4.3:** Visual predictive check (VPC) considering drop out of the developed tumor dynamics model. Blue dashed lines represent 95<sup>th</sup> and 5<sup>th</sup> percentiles of the observations, red dashed line represents the 50<sup>th</sup> percentile of the observations, blue shaded areas represent 95% confidence interval of the 95<sup>th</sup> and 5<sup>th</sup> percentiles based on the simulations respectively, and red shaded area represents 95% confidence interval of the 50<sup>th</sup> percentile based on the simulations.

**Table 4.3:** Parameter estimates of the tumor dynamics models without or with baseline ctDNA data incorporated

| Parameters         | Description  | Model without covariate |                               | Model with baseline ctDNA data as a covariate |                               |
|--------------------|--|-------------------------|-------------------------------|---|-------------------------------|
|                    |  | Estimate (RSE%)         | IIV (CV%) (RSE%) [shrinkage%] | Estimate (RSE%)                               | IIV (CV%) (RSE%) [shrinkage%] |
| $k_g$ (/day)       | Tumor growth rate constant                                     | 0.000799 (13%)          | 60.3% (27%) [26%]             | 0.00204 (25%)                                 | 16.6% (152%) [57%]            |
| $f_1$              | $k_g$ change fraction when mutant EGFR VAF < 1.74%             | -                       | -                             | 0.334 (28%)                                   | -                             |
| $f_2$              | $k_g$ change fraction when baseline ctDNA data was unavailable | -                       | -                             | 0.281 (28%)                                   | -                             |
| $k_d$ (/day)       | Tumor decay rate constant                                      | 0.0121 (19%)            | 68.4% (26%) [8%]              | 0.0123 (18%)                                  | 66.2% (22%) [7%]              |
| $k_m$ (/day)       | Mutation rate constant   | 0.00911 (2%)            | 56.5% (25%) [19%]             | 0.00824 (18%)                                 | 57.9% (32%) [15%]             |
| $T_{s,0}$ (mm)     | Baseline size of sensitive clonal population                   | Observed baseline       | -                             | Observed baseline                             | -                             |
| $T_{r,0}$ (mm)     | Baseline size of resistant clonal population                   | 0 fixed                 | -                             | 0 fixed                                       | -                             |
| Residual errors    |  |                         |                               |   |                               |
| Prop. Err. (CV%)   | Proportional residual error                                    | 7.54% (13%)             | [12%]*                        | 7.67% (14%)                                   | [12%]*                        |
| Add. Err. (SD, mm) | Additive residual error  | 1.17 (38%)              | [12%]*                        | 1.13 (9%)                                     | [12%]*                        |

RSE, relative standard error; IIV, inter-individual variability; CV, coefficient of variation; SD, standard deviation, VAF, variant allele frequency.

\* Epsilon shrinkage.

### 3.4 Genetic biomarkers and tumor dynamics

The baseline results regarding ctDNA measurements and cfDNA concentrations were available from 12 out of 18 patients and missing for 6 patients. No correlation was observed between baseline mutant *EGFR* VAF and cfDNA concentrations. According to the exploratory plots, patients with baseline mutant *EGFR* VAF  $\geq 1.74\%$  had relatively high  $k_g$  and  $k_m$  estimates, and slightly higher  $k_d$  estimates than patients with mutant *EGFR* VAF < 1.74% (Figure 4.4). In addition, for patients with a *TP53* mutation at baseline, the  $k_g$  and  $k_m$  estimates were relatively high compared to patients without *TP53* mutations, and comparable  $k_d$  estimates were observed (Figure 4.4). The association between baseline cfDNA concentrations and tumor dynamics parameters is shown in Figure S4.5. Patients with baseline cfDNA concentration  $\geq 1.44$  ng/ $\mu$ L showed to have higher  $k_g$  and lower  $k_d$

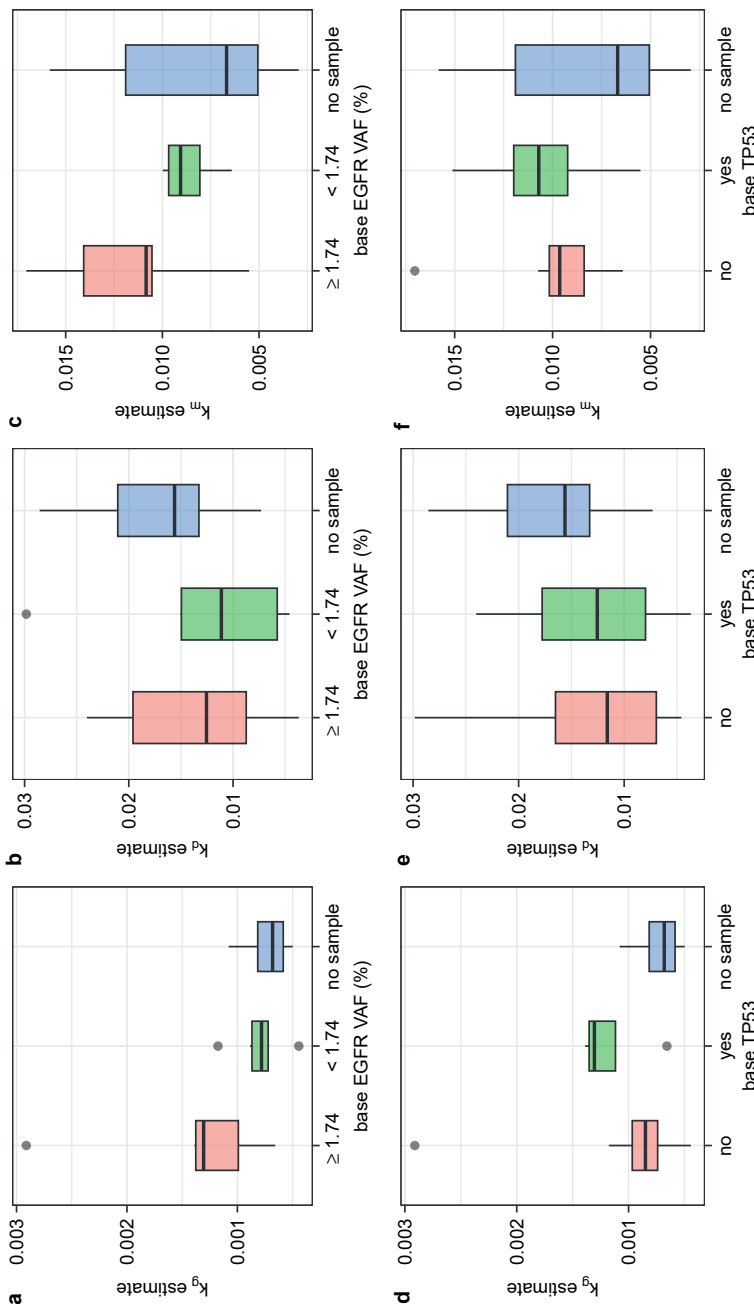


**Figure 4.4:** Parameter estimates from the tumor dynamics model versus baseline plasma circulating tumor DNA (ctDNA) measurements on primary mutant EGFR variant allele frequency and TP53 mutation.

estimate than patients with baseline cfDNA concentration  $< 1.44 \text{ ng}/\mu\text{L}$ , and comparable  $k_m$  estimates were observed.

When exploring the covariate effect of the baseline genetic biomarkers in the tumor dynamics model, the correlation between baseline mutant *EGFR* VAF and  $k_g$  was identified to be most significant when assigning the missing values as a separate category (OFV decreased by 11.6,  $p < 0.01$ , degree of freedom = 2). This correlation remained to be significant when removing the data of patients with missing covariate from the dataset (OFV decreased by 4.6,  $p < 0.05$  degree of freedom = 1). The differences in  $k_m$  or  $k_d$  among patient groups with different baseline mutant *EGFR* VAF levels were shown to be not significant. Additionally, the correlations between the presence of a *TP53* mutation and tumor dynamics parameters were also not significant in the covariate analysis. The parameter estimates of the model with baseline mutant *EGFR* VAF as the covariate are shown in **Table 4.3**. The typical  $k_g$  estimate in patients with baseline *EGFR* VAF  $\geq 1.74\%$  was 0.00204 day $^{-1}$ , which is higher than the estimate for the whole population (0.000799 day $^{-1}$ ). The typical  $k_g$  estimate in patients with baseline *EGFR* VAF  $< 1.74\%$  was 33.4% of that in patients with baseline *EGFR* VAF  $\geq 1.74\%$ , while the difference between patients with baseline *EGFR* VAF  $< 1.74\%$  and with unknown mutant *EGFR* level was not significant. The inclusion of mutant *EGFR* VAF in the model decreased the CV% of IIV in  $k_g$  from 60.3% to 16.6%, while the corresponding RSE increased. The population predictions of the model also improved according to the GOF plots (**Figure S4.6**).

## 4. Discussion

In this study, the tumor dynamics and the development of drug resistance in NSCLC patients undergoing erlotinib treatment was characterized with a mathematical model accounting for tumor heterogeneity. Incorporating the erlotinib exposure into the model was also explored. The potential correlation between baseline genetic biomarkers and parameters that characterize tumor dynamics was identified with exploratory plots and confirmed with the model.

To facilitate the investigation on the exposure-tumor inhibition relationship, a population PK model of erlotinib was first developed. The estimated clearance is comparable to what has been reported previously (4.10 L/h vs 3.64–4.71 L/h) [16-19]. Due to lack of data, previously reported covariates on erlotinib PK, including the smoking status, co-medications, and alpha-1-acid glycoprotein, could not be investigated in our analysis [16, 19]. The CV% of IIV in  $K_a$  and Q/F was estimated to exceed 100%. For  $K_a$ , this high IIV estimate might

because it covers the variability in the lag time of absorption. Considering the amount of available data, these IIV estimates may not be precise. However, this does not affect the predictive ability of the PK model for the intended use in this study. The performance of the model were confirmed by the model evaluation results. However, a trend in CWRES over time between 6–8h after last drug intake was observed. This is considered to be due to the double peaks that were observed in the obtained data: data from 18 out of 29 patients who provided intensively sampled PK data demonstrate increased drug concentrations at 6–8 hours. The possible explanation could be the delayed disintegration of the tablets, food intake [20, 21], or possible enterohepatic circulation, although the latter has not been reported in literature before. This observed double peaks could not be captured by the current PK model, nor by a model considering dual first-order absorption with different lag times. Nevertheless, the model showed to be able to adequately predict the AUC of individual concentration-time curves as well as the trough concentrations which are of interest to be linked to the tumor dynamics. Therefore, the developed PK model was considered to be valid to support our study.

For the tumor size dynamics, a model accounting for intra-tumor heterogeneity and acquired resistance showed to adequately fit the obtained data, and considering primary resistance was not favored based on the available data. This may indicate that for patients with NSCLC with an activating *EGFR* mutation, it is mainly the acquired resistance, which may be due to the acquisition of *EGFR* p.T790M mutation or other mechanisms, that limits the treatment response. Among previously reported model-based studies on tumor size dynamics in NSCLC patients undergoing erlotinib treatment, one study also considered tumor heterogeneity [22]. Their results also showed that the models with and without primary resistance could describe the data equally well even though erlotinib was used as a second-line treatment in their study [22]. However, it is worth noting that the model presented in the current study is empirical and simplifies the complex process of the emergence of treatment resistance. Previously, several mechanistic models have been proposed to provide quantitative insight into this process [23, 24]. The relatively limited amount of data in the current analysis prohibits the implementation of more mechanistic models and therefore may limit the mechanistic interpretation. In fact, the presence of *TP53* mutations may indicate the presence of primary resistance [25, 26]. However, *TP53* mutations were only detected in 4 out of 18 patients which may be unable to provide significant impact to our model. Nonetheless, this more empirical approach does take into account the existence and interaction among multiple clonal populations which are crucial for understanding resistance development [24]. We do consider this approach relevant for exploring optimal guided drug treatment in real world clinical oncology practice where

extensive data is normally sparse. Furthermore the current approach can serve as a basis for building more mechanistic-based models when more extensive data is available [24]. The growth rates of treatment sensitive and resistant clonal populations were assumed to be the same in the model. This was because of the lack of identifiability of separate growth rates due to the limited amount of data.

The current study did not identify a clear exposure-tumor inhibition relationship within the current concentration range (the median predicted drug concentrations at the tumor size monitoring time points was 992 ng/ml (range of 284–1554 ng/mL)), neither when assuming a non-linear relationship with the Emax model. A dose-tumor inhibition relationship was also explored but no clear relationship was identified. This might be because the treatment effect has already been saturated. The dose level selected for erlotinib (i.e. 150 mg daily) is the maximum tolerated dose, under which the average trough concentration at steady state is well above what is required for the required erlotinib activity and considered to be sufficient to provide a high anti-neoplastic effect [27]. This lack of relationship is in line with previous clinical studies where no significant correlation between erlotinib exposure and response has been identified [28-30]. One study also showed that increased erlotinib exposure had less impact on the antitumor effects in EGFR mutation-positive patients [31]. As an exposure-response relationship was not identified, we could not investigate the influence of drug exposure on the evolving tumor progression in this case. However, this result suggests that there is a potential option to decrease the dose of erlotinib to target for a lower concentration range that still ensures sufficient efficacy but can be better tolerated, especially since a significant proportion of erlotinib-treated patients can have severe toxicity [6]. The U.S. Food and Drug Administration (FDA) has recently proposed the Project Optimus which also encourages to improve dose selection and optimization for oncology drugs by accounting for both efficacy and tolerability rather than automatically selecting the maximum tolerated dose [32, 33]. A recent study has already suggested an optimized starting dose of 50–60 mg/day for erlotinib and a concentration range of 150–310 ng/mL for personalized erlotinib treatment in NSCLC patients considering both efficacy and tolerability [34].

The correlation between baseline genetic biomarkers and parameters in tumor dynamics model was investigated in this study. The VAF's of mutant *EGFR* and the presence of *TP53* mutations in ctDNA at baseline showed to have potential correlation with the estimated parameters in the tumor dynamics model (mainly  $k_g$  and  $k_m$ ), especially that higher baseline *EGFR* VAF was significantly correlated with increased growth rate constant  $k_g$ . This indicates that patients with higher *EGFR* VAF at baseline may have a worse response to the treatment, which is in line with the clinical findings from a *EGFR* cohort in the

START-TKI study, i.e. patients without detectable ctDNA at baseline had a lower rate of radiological progression [6]. An explanation could be the association between ctDNA levels and tumor burden [11, 35]. Our result is also in line with previous findings that baseline concomitant *TP53* mutations may relate to worse clinical outcome in patients with NSCLC [6]. After incorporating baseline ctDNA measurements, the developed tumor dynamics model could better predict the tumor sizes dynamics in response to erlotinib treatment in NSCLC patients. This finding also demonstrates the potential to use baseline ctDNA as an early biomarker to support decision making for the treatment of NSCLC patients [36].

This study also has some limitations. The results found in the current study are based on limited data from a limited number of patients, especially for genetic biomarkers. The unavailability of baseline cfDNA samples in 6 out of 18 patients could also impact the interpretation of the results, as well as the determination of the threshold value of EGFR VAF which was associated with increased growth rates. However, this study is one of the first that investigated the relationships among PK, tumor dynamics, and ctDNA measurements. Furthermore, since the data on detectable mutation levels in ctDNA are limited, development of a model for describing longitudinal ctDNA data was not feasible and only the baseline ctDNA measurements were included in the analysis, which however explored the value of ctDNA as an early biomarker. Additionally, the mutant *EGFR* VAF was only investigated as a categorical covariate while the data range from 0% to 62.74% and correspond to multiple variants. Therefore, further analysis with more extensive data is warranted to validate the current results and to explore the correlation between the longitudinal ctDNA measurements and tumor size dynamics with models.

In conclusion, our study demonstrated that the model accounting for intra-tumor heterogeneity and acquired resistance can well characterize the tumor size dynamics in NSCLC patients during erlotinib treatment. No clear exposure-tumor inhibition relationship was identified within the current concentration range. A correlation between baseline ctDNA measurements and tumor growth rates was however identified which suggests that quantitative ctDNA measurements at baseline have potential to be predictive of anti-cancer treatment response, and further study on more extensive longitudinal data is warranted. The developed model can potentially be further applied to design optimal treatment regimens that better overcome resistance.

## Study highlights

### ***What is the current knowledge on the topic?***

Insight into the evolutionary development of treatment resistance can support optimization of anti-cancer treatments. This is also the case in non-small cell lung cancer (NSCLC) patients. A model-based approach can support such study based on data on pharmacokinetics, tumor sizes and genetic biomarkers

### ***What question did this study address?***

We aimed to quantitatively characterize the tumor dynamics and evolving resistance development in NSCLC patients treated with erlotinib, and investigate the relationship between baseline circulating tumor DNA (ctDNA) measurements and tumor dynamics.

### ***What does this study add to our knowledge?***

A model accounting for intra-tumor heterogeneity and acquired resistance well characterized the tumor size dynamics in NSCLC patients during erlotinib treatment. No exposure-tumor inhibition relationship was identified in the identified exposure range. Baseline ctDNA data on mutant *EGFR* levels correlate with tumor growth rate and the inclusion of ctDNA data improved model prediction.

### ***How might this change drug discovery, development, and/or therapeutics?***

Our findings suggest that baseline ctDNA measurements have the potential to be a predictor of anti-cancer treatment response, which encouraged to use ctDNA as an early biomarker. The developed model can further be applied to design optimal treatment regimens to better overcome resistance.

## References

1. Zhao B, Hemann MT, Lauffenburger DA. Modeling Tumor Clonal Evolution for Drug Combinations Design. *Trends Cancer*. 2016;2(3):144-58. doi:10.1016/j.trecan.2016.02.001.
2. Sun X, Hu B. Mathematical modeling and computational prediction of cancer drug resistance. *Brief Bioinform*. 2018;19(6):1382-99. doi:10.1093/bib/bbx065.
3. Nagano T, Tachihara M, Nishimura Y. Mechanism of Resistance to Epidermal Growth Factor Receptor-Tyrosine Kinase Inhibitors and a Potential Treatment Strategy. *Cells*. 2018;7(11):212. doi:10.3390/cells7110212.
4. Oliveira KCS, Ramos IB, Silva JMC, Barra WF, Riggins GJ, Palande V, et al. Current Perspectives on Circulating Tumor DNA, Precision Medicine, and Personalized Clinical Management of Cancer. *Mol Cancer Res*. 2020;18(4):517-28. doi:10.1158/1541-7786.MCR-19-0768.
5. Herbreteau G, Vallee A, Charpentier S, Normanno N, Hofman P, Denis MG. Circulating free tumor DNA in non-small cell lung cancer (NSCLC): clinical application and future perspectives. *J Thorac Dis*. 2019;11(Suppl 1):S113-S26. doi:10.21037/jtd.2018.12.18.
6. Steendam CMJ, Veerman GDM, Pruis MA, Atmodimedjo P, Paats MS, van der Leest C, et al. Plasma Predictive Features in Treating EGFR-Mutated Non-Small Cell Lung Cancer. *Cancers (Basel)*. 2020;12(11):3179. doi:10.3390/cancers12113179.
7. Barbolosi D, Ciccolini J, Lacarelle B, Barlesi F, Andre N. Computational oncology--mathematical modelling of drug regimens for precision medicine. *Nature Reviews Clinical Oncology*. 2016;13(4):242-54. doi:10.1038/nrclinonc.2015.204.
8. Buil-Bruna N, Lopez-Picazo JM, Martin-Algarra S, Troconiz IF. Bringing Model-Based Prediction to Oncology Clinical Practice: A Review of Pharmacometrics Principles and Applications. *Oncologist*. 2016;21(2):220-32. doi:10.1634/theoncologist.2015-0322.
9. Kimko H, Pinheiro J. Model-based clinical drug development in the past, present and future: a commentary. *Br J Clin Pharmacol*. 2015;79(1):108-16. doi:10.1111/bcp.12341.
10. Yin A, van Hasselt JGC, Guchelaar HJ, Friberg LE, Moes D. Anti-cancer treatment schedule optimization based on tumor dynamics modelling incorporating evolving resistance. *Sci Rep*. 2022;12(1):4206. doi:10.1038/s41598-022-08012-7.
11. Wan JCM, Massie C, Garcia-Corbacho J, Mouliere F, Brenton JD, Caldas C, et al. Liquid biopsies come of age: towards implementation of circulating tumour DNA. *Nat Rev Cancer*. 2017;17(4):223-38. doi:10.1038/nrc.2017.7.
12. Janssen JM, Verheijen RB, van Duijl TT, Lin L, van den Heuvel MM, Beijnen JH, et al. Longitudinal nonlinear mixed effects modeling of EGFR mutations in ctDNA as predictor of disease progression in treatment of EGFR-mutant non-small cell lung cancer. *Clin Transl Sci*. 2022;15(8):1916-25. doi:10.1111/cts.13300.
13. van Leeuwen RW, Peric R, Hussaarts KG, Kienhuis E, NS IJ, de Brujin P, et al. Influence of the Acidic Beverage Cola on the Absorption of Erlotinib in Patients With Non-Small-Cell Lung Cancer. *J Clin Oncol*. 2016;34(12):1309-14. doi:10.1200/JCO.2015.65.2560.
14. Veerman GDM, Hussaarts K, Peric R, Oomen-de Hoop E, Landa KD, van der Leest CH, et al. Influence of Cow's Milk and Esomeprazole on the Absorption of Erlotinib: A Randomized, Crossover Pharmacokinetic Study in Lung Cancer Patients. *Clin Pharmacokinet*. 2021;60(1):69-77. doi:10.1007/s40262-020-00910-1.
15. Eisenhauer EA, Therasse P, Bogaerts J, Schwartz LH, Sargent D, Ford R, et al. New response evaluation criteria in solid tumours: revised RECIST guideline (version 1.1). *Eur J Cancer*. 2009;45(2):228-47. doi:10.1016/j.ejca.2008.10.026.
16. Emoto-Yamamoto Y, Iida S, Kawanishi T, Fukuoka M. Population pharmacokinetics of erlotinib in Japanese patients with advanced non-small cell lung cancer. *J Clin Pharm Ther*. 2015;40(2):232-9. doi:10.1111/jcpt.12232.

17. Parra-Guillen ZP, Berger PB, Haschke M, Donzelli M, Winogradova D, Pfister B, et al. Role of Cytochrome P450 3A4 and 1A2 Phenotyping in Patients with Advanced Non-small-Cell Lung Cancer Receiving Erlotinib Treatment. *Basic Clin Pharmacol Toxicol.* 2017;121(4):309-15. doi:10.1111/bcpt.12801.
18. Endo-Tsukude C, Sasaki JI, Saeki S, Iwamoto N, Inaba M, Ushijima S, et al. Population Pharmacokinetics and Adverse Events of Erlotinib in Japanese Patients with Non-small-cell Lung Cancer: Impact of Genetic Polymorphisms in Metabolizing Enzymes and Transporters. *Biol Pharm Bull.* 2018;41(1):47-56. doi:10.1248/bpb.b17-00521.
19. Evelina C, Guidi M, Khoudour N, Pascaline B-R, Fabre E, Tlemsani C, et al. Population Pharmacokinetics of Erlotinib in Patients With Non-small Cell Lung Cancer: Its Application for Individualized Dosing Regimens in Older Patients. *Clin Ther.* 2020;42(7):1302-16. doi:10.1016/j.clinthera.2020.05.008.
20. Rampaka R, Ommi K, Chella N. Role of solid lipid nanoparticles as drug delivery vehicles on the pharmacokinetic variability of Erlotinib HCl. *Journal of Drug Delivery Science and Technology.* 2021;66:102886. doi:<https://doi.org/10.1016/j.jddst.2021.102886>.
21. Veerman GDM, Hussaarts K, Jansman FGA, Koolen SWL, van Leeuwen RWF, Mathijssen RHJ. Clinical implications of food-drug interactions with small-molecule kinase inhibitors. *Lancet Oncol.* 2020;21(5):e265-e79. doi:10.1016/S1470-2045(20)30069-3.
22. Mistry HB, Helmlinger G, Al-Huniti N, Vishwanathan K, Yates J. Resistance models to EGFR inhibition and chemotherapy in non-small cell lung cancer via analysis of tumour size dynamics. *Cancer Chemother Pharmacol.* 2019;84(1):51-60. doi:10.1007/s00280-019-03840-3.
23. Foo J, Michor F. Evolution of acquired resistance to anti-cancer therapy. *Journal of theoretical biology.* 2014;355:10-20. doi:10.1016/j.jtbi.2014.02.025.
24. Terranova N, Girard P, Klinkhardt U, Munafò A. Resistance Development: A Major Piece in the Jigsaw Puzzle of Tumor Size Modeling. *CPT Pharmacometrics Syst Pharmacol.* 2015;4(6):320-3. doi:10.1002/psp4.45.
25. Canale M, Petracci E, Delmonte A, Chiadini E, Dazzi C, Papi M, et al. Impact of TP53 Mutations on Outcome in EGFR-Mutated Patients Treated with First-Line Tyrosine Kinase Inhibitors. *Clin Cancer Res.* 2017;23(9):2195-202. doi:10.1158/1078-0432.Ccr-16-0966.
26. Ulivi P, Delmonte A, Chiadini E, Calistri D, Papi M, Mariotti M, et al. Gene mutation analysis in EGFR wild type NSCLC responsive to erlotinib: are there features to guide patient selection? *Int J Mol Sci.* 2014;16(1):747-57. doi:10.3390/ijms16010747.
27. US Food and Drug Administration. Drug approval package: Tarceva (Erlotinib) Tablets (Application No.: 021743). [https://www.accessdata.fda.gov/drugsatfda\\_docs/nda/2004/21-743\\_Tarceva.cfm](https://www.accessdata.fda.gov/drugsatfda_docs/nda/2004/21-743_Tarceva.cfm).
28. Yu H, Steeghs N, Nijenhuis CM, Schellens JH, Beijnen JH, Huitema AD. Practical guidelines for therapeutic drug monitoring of anticancer tyrosine kinase inhibitors: focus on the pharmacokinetic targets. *Clin Pharmacokinet.* 2014;53(4):305-25. doi:10.1007/s40262-014-0137-2.
29. Verheijen RB, Yu H, Schellens JHM, Beijnen JH, Steeghs N, Huitema ADR. Practical Recommendations for Therapeutic Drug Monitoring of Kinase Inhibitors in Oncology. *Clin Pharmacol Ther.* 2017;102(5):765-76. doi:10.1002/cpt.787.
30. Kenmotsu H, Imamura CK, Kawamura T, Oyakawa T, Omori S, Nakashima K, et al. Prospective evaluation of the relationship between response and exposure of total and unbound erlotinib in non-small cell lung cancer patients. *Cancer Chemother Pharmacol.* 2022;90(2):115-23. doi:10.1007/s00280-022-04452-0.

31. Fukudo M, Ikemi Y, Togashi Y, Masago K, Kim YH, Mio T, et al. Population pharmacokinetics/pharmacodynamics of erlotinib and pharmacogenomic analysis of plasma and cerebrospinal fluid drug concentrations in Japanese patients with non-small cell lung cancer. *Clin Pharmacokinet*. 2013;52(7):593-609. doi:10.1007/s40262-013-0058-5.
32. Fourie Zirkelbach J, Shah M, Vallejo J, Cheng J, Ayyoub A, Liu J, et al. Improving Dose-Optimization Processes Used in Oncology Drug Development to Minimize Toxicity and Maximize Benefit to Patients. *J Clin Oncol*. 2022;40(30):3489-500. doi:10.1200/JCO.22.00371.
33. Shah M, Rahman A, Theoret MR, Pazdur R. The Drug-Dosing Conundrum in Oncology - When Less Is More. *N Engl J Med*. 2021;385(16):1445-7. doi:10.1056/NEJMp2109826.
34. Takeda Y, Ishizuka N, Sano K, Hirano S, Suzuki M, Naka G, et al. Phase I/II Study of Erlotinib to Determine the Optimal Dose in Patients With Non-Small Cell Lung Cancer Harboring Only EGFR Mutations. *Clin Transl Sci*. 2020;13(6):1150-60. doi:10.1111/cts.12796.
35. Sanz-Garcia E, Zhao E, Bratman SV, Siu LL. Monitoring and adapting cancer treatment using circulating tumor DNA kinetics: Current research, opportunities, and challenges. *Sci Adv*. 2022;8(4):eabi8618. doi:10.1126/sciadv.abi8618.
36. Bruno R, Chanu P, Kagedal M, Mercier F, Yoshida K, Guedj J, et al. Support to early clinical decisions in drug development and personalised medicine with checkpoint inhibitors using dynamic biomarker-overall survival models. *British journal of cancer*. 2023. doi:10.1038/s41416-023-02190-5.

## Supplementary Material S4.1

### Population PK analysis - covariate analysis methods

In the population PK analysis, patients' demographic information, including age, sex, weight, height, and laboratory test results, including creatinine, estimated glomerular filtration rate (eGFR), albumin, total bilirubin, aspartate aminotransferase (AST), alanine aminotransferase (ALT), and alkaline phosphatase (ALP) were investigated as covariates. The stepwise covariate modeling (SCM) function of Perl-speaks NONMEM (version 4.9) was applied to perform the covariate analysis. The effect of all covariates on erlotinib clearance and that of weight, height, and albumin on apparent distribution volume of the central compartment were investigated. Model selection was based on the reduction in objective function value (OFV) (a likelihood ratio test) assuming a  $\chi^2$  distribution, a reduction in IIV, and physiological plausibility. The  $p$  values were set as 0.05 and 0.01 for the forward selection and backward elimination process, respectively.

The effects of continuous covariates were investigated with both linear relation (Eq. S4.1) and power relation (Eq. S4.2), where  $P_i$  represents the parameter of  $i$ th individual,  $P_t$  represents typical value of the parameter, and  $\eta_i$  represents the individual variability,  $\theta_{cov}$  represents the estimate of covariate effect,  $COV_i$  represents the covariate value of  $i$ th individual,  $COV_m$  is the median value of the covariate. Categorical covariates (e.g. sex) were analyzed with Eq. S4.3, where  $\theta_{cov}$  was set as 1 for reference category (e.g. males) and was estimated for other categories (e.g. females).

$$P_i = P_t \cdot (1 \pm \theta_{cov} \cdot (COV_i - COV_m)) \cdot e^{\eta_i} \quad \text{Eq. S4.1}$$

$$P_i = P_t \cdot \left(\frac{COV_i}{COV_m}\right)^{\theta_{cov}} \cdot e^{\eta_i} \quad \text{Eq. S4.2}$$

$$P_i = P_t \cdot \theta_{cov} \cdot e^{\eta_i} \quad \text{Eq. S4.3}$$

## Supplementary Material S4.2

### NONMEM code for the tumor dynamics model

```

$INPUT
C CID DROP TIME TAD AMT ADDL II CMT EVID DV
UNDERTREAT; if treatment started: 1, yes
DROP DROP Dose; dose
DROP AGE SEX HT WT DROP BMI
baseTS; baseline tumor size
T790M; T790M: 1, yes
TP53_base; presence of TP53: 1, yes
basecfDNA; baseline cfDNA concentration
baseVAF; baseline EGFR mutant levels
DROP DROP DROP DROP DROP DROP DROP
ICL IV2 IV3 IQ IKA ILAG1 IF1; individual PK parameters

$DATA START_all6.csv IGNORE=C IGNORE=(CMT.GT.4) IGNORE=(CMT.EQ.2); only
data of tumor sizes

$SUBROUTINES ADVAN13 TOL=4

$MODEL
COMP = (DEPOT)
COMP = (CENTRAL,DEFOBS)
COMP = (PRIPH)
COMP = (TUMOR)
COMP = (TUMOR2)

$PK
KG1 = THETA(1)* EXP(ETA(1))/100
KD1 = THETA(2)* EXP(ETA(2))/100
KM1 = THETA(5)* EXP(ETA(3))/100
;IF(baseVAF.GE.0.AND.baseVAF.LT.1.74) KG1=THETA(6)*KG1
;IF(baseVAF.LT.0) KG1=THETA(7)*KG1; no sample group

CL = ICL*24; change unit from L/h to L/day
V2 = IV2
V3 = IV3

```

Q = IQ \*24

ALAG1 = IALAG1 /24

KA = IKA\*24

F1 = IF1

K=CL/V2

K23=Q/V2

K32=Q/V3

BASES = baseTS

A\_0(4)=BASES

A\_0(5)=0

\$DES

DADT(1) = -KA\*A(1); can simulate drug concentrations, if needed

DADT(2)= KA\*A(1) - K\*A(2) -K23\*A(2) +K32\*A(3); can simulate drug concentrations, if needed

DADT(3) = K23\*A(2)- K32\*A(3); can simulate drug concentrations, if needed

DADT(4) = KG1\*A(4)-KD1\* UNDERTREAT \*A(4) - KM1\* UNDERTREAT \*A(4)

DADT(5) = KM1\* UNDERTREAT \*A(4)+ KG1\* UNDERTREAT \*A(5)

\$ERROR

TS=A(4)+A(5)

IPRED = TS

W = SQRT(THETA(3)\*\*2\*IPRED\*\*2 + THETA(4)\*\*2)

Y = IPRED + W\*EPS(1)

IRES = DV-IPRED

IWRES = IRES/W

\$THETA

(0.001,0.1,1); KG1

(0.1,1,5); KD

(0.01,0.1,1); Prop err

(0.1,1,10); Add err

(0.01,1, 5); KM1

;(0.05,0.5,2); VAF < 1.74

;(0.05,0.5,2); VAF not available

\$OMEGA

0.1; IIV KG

0.1; IIV KD

0.1; IIV KM1

\$SIGMA 1 FIX;

\$ESTIMATION METHOD=1 INTER MAXEVAL=9999 NOABORT SIG=3 PRINT=10

POSTHOC

\$COV print=E

\$TABLE ID TIME TAD MDV EVID UNDERTREAT Dose baseTS T790M TP53\_base  
basecfDNA baseVAF baseTS KG1 KD1 KM1 TS IPRED IW

## Supplementary figures and table

### Supplementary Figures

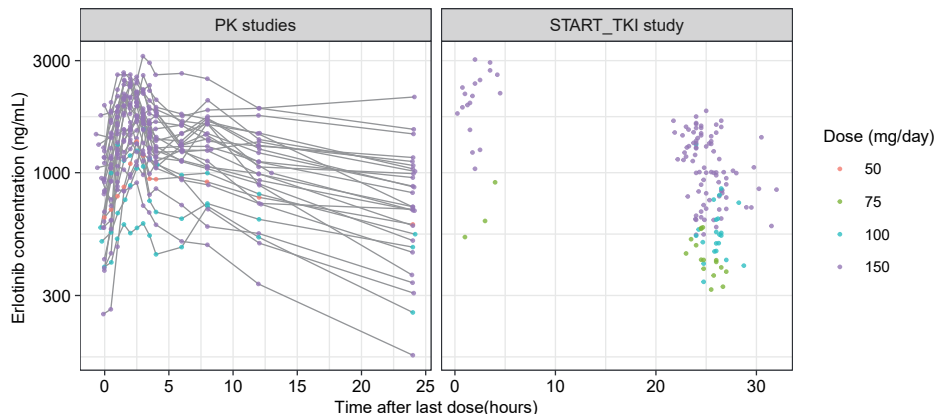


**Figure S4.1:** The collected data on erlotinib concentrations over time.

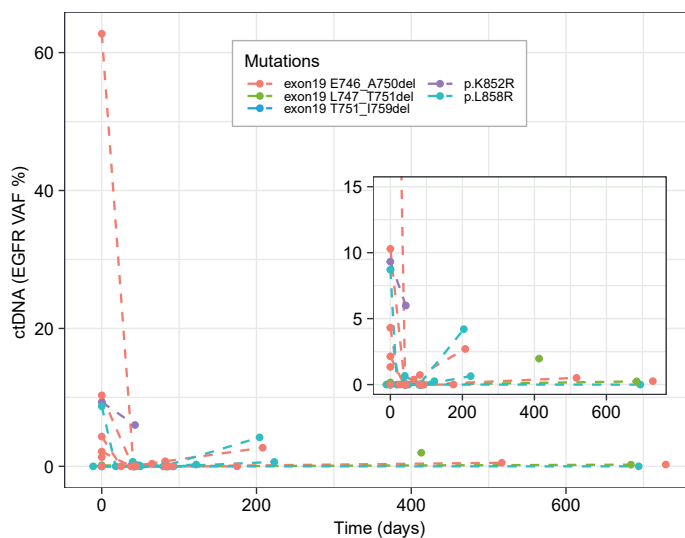


**Figure S4.2:** The collected variant allele frequency of primary EGFR variants detected from circulating free DNA (cfDNA) (ctDNA data) over time.

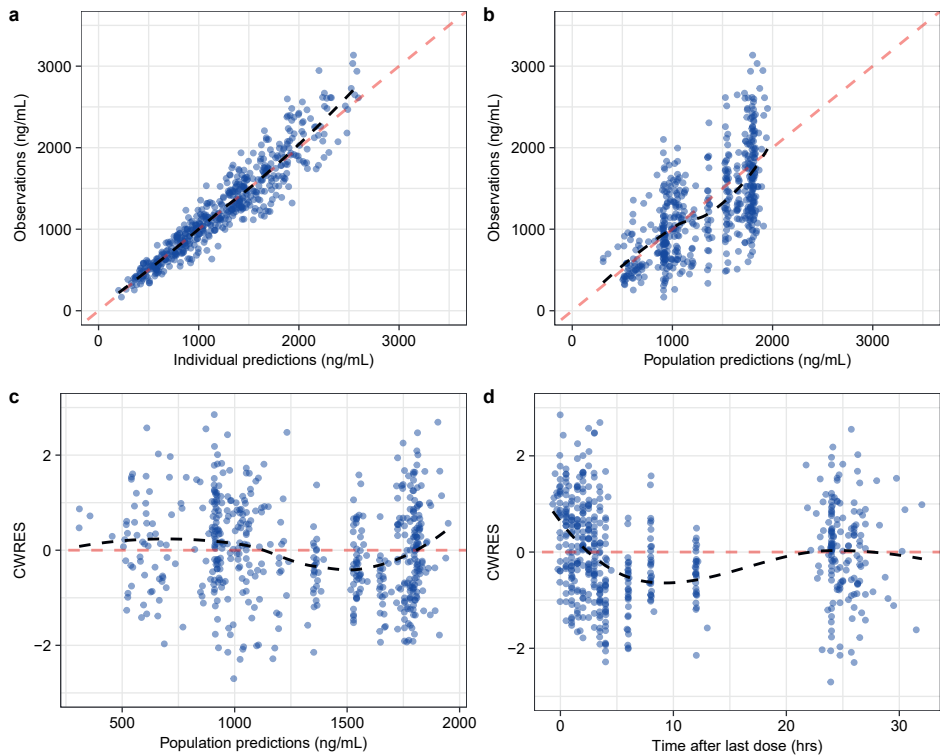


**Figure S4.3:** Goodness-of-fit plots of the developed population PK model, including observations versus individual predictions (a) and population predictions (b), and conditional weighted residual errors (CWRES) versus populations predictions (c) and versus time after last dose (d). The red dashed lines represent  $y = x$  (a, b) and  $y = 0$  (c, d). Black dashed lines represent corresponding loess regressions.

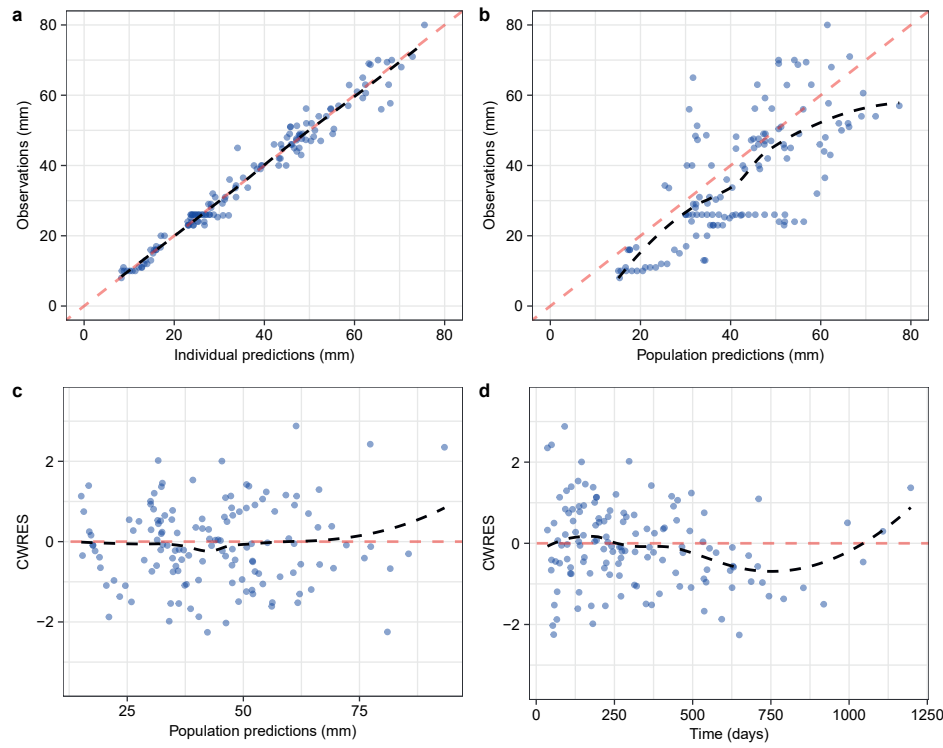


**Figure S4.4:** Goodness-of-fit plots of the developed tumor dynamics model, including observations versus individual predictions (a) and population predictions (b), and conditional weighted residual errors (CWRES) versus populations predictions (c) and versus time (d). The red dashed lines represent  $y = x$  (a, b) and  $y = 0$  (c, d). Black dashed lines represent corresponding loess regressions.

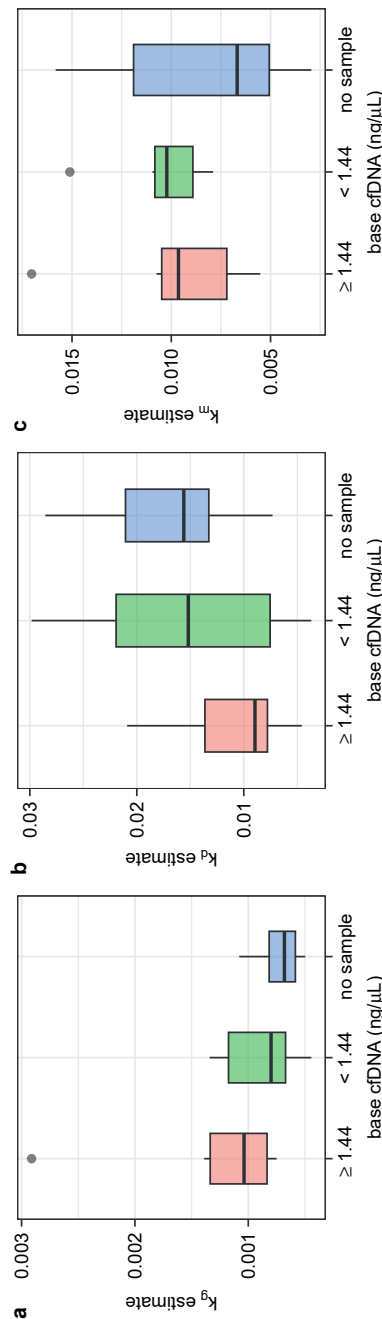
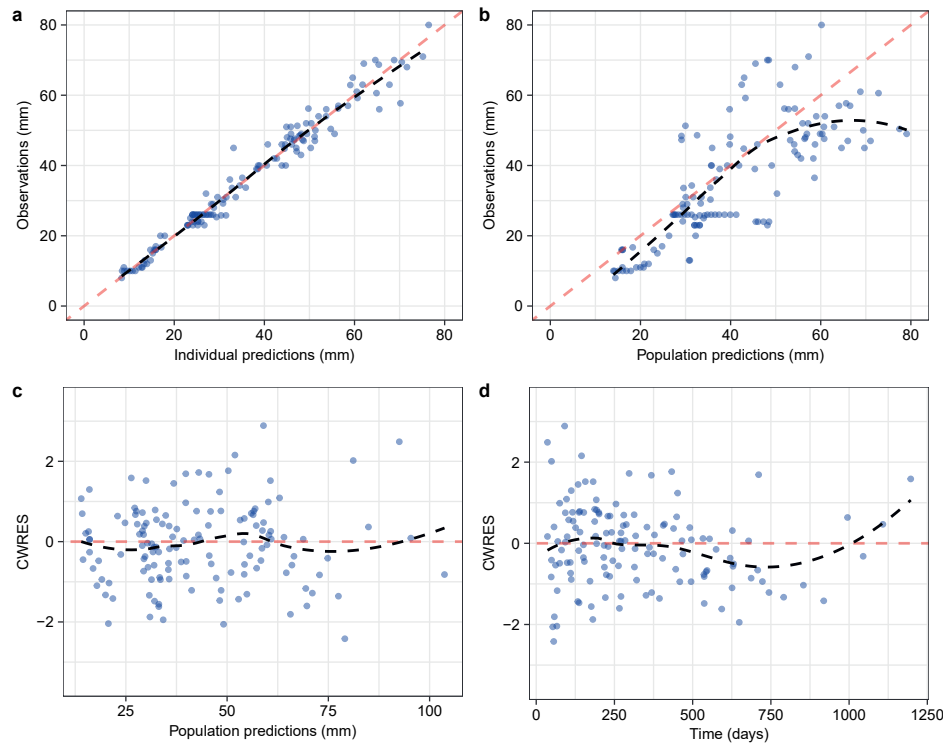


Figure S4.5: Parameter estimates from the tumor dynamics model versus baseline circulating free DNA (cfDNA) concentrations.



**Figure S4.6:** Goodness-of-fit plots of the tumor dynamics model with ctDNA as a covariate, including observations versus individual predictions (a) and population predictions (b), and conditional weighted residual errors (CWRES) versus populations predictions (c) and versus time (d). The red dashed lines represent  $y = x$  (a, b) and  $y = 0$  (c, d). Black dashed lines represent corresponding loess regressions.

**Supplementary Table****Table S4.1:** Parameter estimates of the tumor dynamics model considering pre-existing resistance component (primary resistance)

| Parameters         | Description                                  | Estimate (RSE%)               | IIV (CV%) (RSE%)<br>[shrinkage%] |
|--------------------|--|-------------------------------|----------------------------------|
| $k_g$ (/day)       | Tumor growth rate constant                   | 0.000801 (22%)                | 60.4% (29%) [26%]                |
| $k_d$ (/day)       | Tumor decay rate constant                    | 0.0129 (21%)                  | 73.6% (27%) [8%]                 |
| $k_m$ (/day)       | Mutation rate constant                       | 0.00756 (28%)                 | 66.6% (34%) [19%]                |
| $T_{S_0}$ (mm)     | Baseline size of sensitive clonal population | Observed baseline - $T_{R_0}$ | -                                |
| $T_{R_0}$ (mm)     | Baseline size of resistant clonal population | 4.51 (39%)                    | 0 fixed                          |
| Residual errors    |  |                               |                                  |
| Prop. Err. (CV%)   | Proportional residual error                  | 7.44% (18%)                   | [12%]*                           |
| Add. Err. (SD, mm) | Additive residual error                      | 1.19 (21%)                    | [12%]*                           |





## Section II

Modeling pharmacokinetics & pharmacodynamics



# Chapter 5

## Model-informed precision dosing in oncology

Anyue Yin, Henk-Jan Guchelaar, Dirk Jan A.R. Moes



*In preparation*

## Abstract

In real-world patients, anti-cancer drugs frequently show substantial variability in pharmacokinetics (PK) and pharmacodynamics (PD). Especially for anti-cancer drugs that exhibit a narrow therapeutic window, these characteristics lead to an increased risk of suboptimal therapy and toxicity. This highlights the need for more individualized dosing in cancer patients. Model-informed precision dosing (MIPD) is an advanced quantitative approach which applies pharmacometric models to guide optimal dose selection and enables individualized therapy. This expert opinion article introduces the current application of MIPD in supporting optimal anti-cancer treatment, and discusses the challenges and future perspectives of implementing MIPD in this field.

## 1. Introduction

Pharmacokinetic (PK) and pharmacodynamic (PD) characteristics of anti-cancer drugs can be highly variable in real-world patients [1, 2]. Due to the correlations between drug exposure and treatment response (efficacy and toxicity), such variability can result in suboptimal treatment outcomes for a considerable part of the patients especially when the therapeutic window is narrow [1, 2]. Moreover, since the dose selection for most oncology drugs is based on the maximum tolerated dose (MTD) or maximal administered dose (MAD) paradigm, the use of standard dosing according to the drug label can result in negative consequences for real-world patients. This leads to a demand for dose modification processes [3]. Therefore, the necessity for dose individualization and optimization in anti-cancer therapies is highlighted, and a useful tool to support the decision making is warranted.

Model-informed precision dosing (MIPD) is a promising tool which adopts pharmacometric models to guide optimal and individualized dose selection, the goal of which is to improve efficacy and reduce the risk of toxicity [2, 4]. Pharmacometric models enable quantitative characterization and prediction of drug PK and PD in target populations under certain dosing regimens [5, 6]. With a mixed-effect modeling (population modeling) approach, variability between and within patients can be quantified and predictive covariates can be identified [5, 6]. Once data of patients are known, the Bayesian framework of the population model would enable more precise description and prediction of individual PK/PD characteristics with individual parameters [2]. Combined with simulations, treatment strategies that are likely to achieve the therapeutic targets and desired clinical outcome can therefore be derived with the model. The value of MIPD in supporting cancer treatment optimization has gained increasing interest in oncology research and clinical practice. However, challenges still remain in the implementation of MIPD.

The current article aims to introduce the application and benefits of MIPD in supporting anti-cancer treatment optimization and individualization, and discuss the challenges and future perspectives of implementing MIPD in cancer therapies.

## 2. MIPD application

Insight into the correlation between drug or surrogate biomarker concentration and the clinical effect in real-world patients can facilitate determining a therapeutic target or range that is associated with sufficient efficacy and less risk of toxicity. This pre-defined target can then be incorporated in the algorithm of MIPD to derive optimal dosing regimens.

## 2.1 Starting dose selection

The benefits of MIPD in anti-cancer treatment have been demonstrated in many studies [2, 7]. First of all, MIPD can be applied to guide (starting) dose selection based on identified covariates [7]. Population modeling allows the identification of covariates that influence model parameters and explain the inter- and intra-patient variability in drug PK/PD profiles. Data from various studies can also be pooled in one analysis to facilitate a more in-depth exploration on relevant covariates. Before any data on PK or PD biomarkers are available to inform the individual parameters, the model can guide dose tailoring considering the value of relevant covariates for each individual patient, which would increase the chance to achieve the therapeutic target and reduce inter-individual variability. This can be especially helpful for determining the optimal starting dose.

The current standard practice to individualize the dose of anti-cancer drugs (normally for cytotoxic chemotherapy) is based on body surface area (BSA) [7, 8]. However, BSA may not be a relevant covariate that correlates with the PK variability of these drugs [7, 8]. Dosing based on BSA can thus still lead to substantial PK variability and cause under or over drug exposure, which may lead to less efficacy or a higher risk of toxicity. The model-informed approach allows investigating the impact of a wide range of factors, including patients' characteristics, renal or kidney function, disease related indicators, and co-medications, identifying real covariates that should be accounted for dose adjustment [7]. It also allows taking multiple influential factors into consideration at the same time. The impact of pharmacogenetic variants on drug PK profile can also be investigated and incorporated in MIPD to further refine the dose selection [7].

A clinical trial on busulfan in pediatric hematopoietic cell transplantation (HCT) patients has confirmed the advantage of model-informed dosing in guiding starting dose selection [9]. This trial compared conventional strategies for determining initial busulfan dose (based on weight), calculating AUC following TDM (trapezoidal rule), and determining the following dose (proportional scaling) with the model-informed approach. Their results show that receiving initial doses that were calculated by the PK model enabled more patients to achieve the exposure target at the time of first PK collection, especially in the cohort where the initial dose was guided with an updated PK model (75% vs. 25% in conventional group).

## 2.2 Adaptive dose selection during treatment

Secondly, MIPD also presents a potential to guide dose selection and adaptation during anti-cancer treatment, which has shown to outperform the conventional therapy in terms of

target attainment and clinical outcome. Such dose selection is typically guided by population PK models that possess sufficient predictive ability. Once measured drug concentrations and individual characteristics of the patient are available, individual parameters can be estimated (empirical Bayesian estimates) which could capture the current and forecast future individual PK time curves, given the applied dosage [2, 10]. Thus, with the aim to achieve the defined exposure target, the optimal dosage for the following treatment can be determined rationally. A recent perspective on MIPD has listed several motivating examples [2]. One study in breast cancer patients performed simulations to compare different dosing strategies of tamoxifen [11]. The results demonstrated that compared with standard dosing (20 mg QD) or CYP2D6-guided dosing, the MIPD strategy (individual maintenance dose was derived with MIPD using three monitored drug concentrations) could reduce the proportion of patients failing to reach the predefined target endoxifen (active metabolite) exposure (22.2% (standard dosing) to 7.19%) and the inter-individual variability.

In addition to drug concentrations, monitoring other biomarkers to inform dose selection can potentially also be accomplished with a model-informed approach.

The benefit of MIPD in guiding anti-cancer treatment dose adaptation has also been confirmed in clinical trials. For instance, Joerger et al. have performed a randomized study in advance non-small cell lung cancer (NSCLC) patients to compare standard paclitaxel dosing (per BSA) and PK-guided paclitaxel dosing which was proposed from their previous simulation-based study (initial paclitaxel dose was adjusted according to patients characteristics and subsequent doses were guided considering previous-cycle paclitaxel exposure estimated with a PK model) [12]. The study demonstrated that that PK-guided dosing can significantly reduce paclitaxel-associated neuropathy while having the similar response rate as standard dosing, thus suggesting an improved benefit-risk profile [12].

### 2.3 Model-informed TDM

Therapeutic drug monitoring (TDM) is a clinical practice of adjusting drug dosing regimen for an individual patient based on measured drug concentrations in biological fluid (typically plasma, serum, urine, or whole blood) [10]. For anti-cancer therapies, TDM-based dosing has been partially implemented for a small number of agents, including carboplatin, methotrexate, busulfan, and mitotane [13]. The benefits and feasibility of TDM for many other drugs have also been demonstrated in clinical studies, including imatinib, sunitinib, pazopanib, 5-fluorouracil, and tamoxifen [8, 13]. Implementing TDM for other kinase inhibitors, which are typically administrated at fixed doses, has also been recommended due to the high PK variability and clear relationships between exposure and treatment outcomes [1].

MIPD, which is able to guide dose adaptation with population PK models and Bayesian forecasting, can be combined with TDM to ensure optimal dose adjustment. This model-informed TDM has already been implemented in clinical practice, although not yet widely adopted [4]. The exposure metrics that were of interest included trough concentrations, area under the concentration-time curve (AUC), or concentrations at a certain time point. Compared with conventional TDM, the model-informed approach provides the decision support in a quantitative manner and the advantage is multifaceted [2, 8]. First, the individual parameters estimated based on the monitored concentrations (Bayesian estimates) would enable the prediction of whole drug concentration-time curves for each individual patient following the current or subsequent doses. In this way, the concentrations at any time point of interest can be obtained based on the monitored sample. This approach has proved to be able to provide more precise prediction on trough concentrations than normal log extrapolation as is used in conventional TDM [14]. In addition, this approach also allows more accurate estimation of AUC, and flexible limited sampling strategies can be applied. Second, MIPD provides the ability to account for non-linear PK behavior and guide dose adjustment when steady state is not yet reached. This is because MIPD supports the dose adaptation based on the forecasting of drug exposure after dose adjustment. In conventional TDM, the decision on dose adjustment is simply made by scaling the previous dose with the ratio of the observed and target exposures, assuming a linear PK profile [7, 10]. This requires the concentration profile to be at steady state [10]. Finally, with the help of the pharmacometric models and simulations, different TDM strategies can be explored and the most optimal strategy can be identified for further exploration and/or clinical implementation [8].

The clinical trial on busulfan in pediatric HCT patients has strengthened the clinical utility of model-informed dosing and TDM for supporting personalized busulfan dosing and target exposure attainment [9]. In addition to the benefit of selecting the initial dose using the PK model, in the cohort where busulfan AUC and subsequent doses were estimated with the MIPD platform during TDM, the achievement of the goal exposure (cumulated AUC) has shown to be significantly improved (100% vs. 66% in conventional group) and the variability among patients was reduced (from 14.8% to 4.1%), which is expected to improve clinical outcomes [9].

### **3. Challenges and perspectives**

Challenges still have to be overcome to implement MIPD of cancer therapies in clinical practice. A previous perspective has provided a comprehensive overview on the chal-

lenges that hinder the implementation of MIPD in clinical practice in general, as well as corresponding recommendations and future opportunities, from multiple aspects [2]. Here, we highlight a few challenges and provide future perspectives specifically for anti-cancer therapies.

### 3.1 Therapeutic target identification

A pre-defined therapeutic target of drug or biomarker exposure that is associated with optimal treatment outcome is fundamental for MIPD to estimate optimal dosing regimens. A therapeutic target can be determined based on the PK/PD study outcomes in registration files or clinical studies. Developing a PK-PD model on exposure-response relationship based on retrospective data can also facilitate the identification of an optimal therapeutic target for real-world cancer patients. The therapeutic target can be an exposure range, as is traditionally aimed at during drug TDM, or a specific exposure value which can relate to a specific PD target [10]. For anti-cancer drugs, the potential PD target of interest can relate to the change in tumor burden or PD biomarkers. Typically, one therapeutic target is being used for one whole patient population. For future studies and practices, personalizing dosage based on an individual target determined with the help of population PK/PD modeling and Bayesian forecasting would be of interest.

### 3.2 Model selection

In order to implement MIPD, selecting a suitable model that presents sufficient predictive ability to the target patient population is essential. Whether a model matches the target patient population, regarding e.g. age (adult or pediatric), body composition (normal or obese), indications (cancer types and drugs), or dose levels, need to be considered when selecting the model [15]. The intention to use the model should also be taken into account. For example, if a population PK model was developed based on trough concentrations, it may not be able to adequately capture the drug absorption and distribution phase, thus may be suboptimal to support AUC estimation [8].

At times, identifying one model that already has sufficient predictive ability to the target population is difficult. This can be due to the sample size of the study population, or the lack of ability to cover all potential influential factors (e.g. different genotypes or the use of co-medications) in one study [8, 10]. In this case, pooling data of the same drug and cancer type to develop a model, or updating the model (structure or parameters) with newly collected data during TDM allows to derive a model that can better fit the target population [2, 15]. The clinical study on MIPD application in busulfan treatment has proved

that a model updated with additional patient data can improve the performance of MIPD on therapeutic target attainment [9]. A recent study also proposed a continued learning framework which uses a sequential hierarchical Bayesian framework to update the model during MIPD. With this method, the prior model used within MIPD is improved as new data from the target patient population are integrated [16].

Nowadays advanced approaches such as machine learning (ML) approaches have also shown to be able to assist with model selection for MIPD [17].

Model evaluation is also essential for selecting a model that is most suitable. This can be done using the historical data considering the intention to use the model (TDM or starting dose) [15]. In the case where inter-occasion variability (IOV, which represents intra-patient variability) is considered, the predictive value of the historical data (covariate value, data points from much earlier) to subsequent treatment courses needs to be evaluated [15].

### **3.3 User-friendly MIPD program**

To motivate clinicians and clinical pharmacists to implement MIPD and remove the barrier due to the lack of knowledge in quantitative pharmacology, translating the research findings into user-friendly MIPD software would be beneficial and can also be challenging [2]. Luckily, there are already multiple programs available and some are already integrated with local electronic health records [2, 18]. The user-friendliness of 3 Bayesian forecasting programs (TDMx, InsightRx and DoseMe) in a clinical setting has also been evaluated and confirmed [19]. Moreover, many of the available programs also allow including new PK models and adjust PK/PD targets [18]. In order to guide anti-cancer treatment, a program that already has a validated model available for the intention drugs in the intention patient population, or allows including such a new model would be ideal to be selected. Developing a program for local use could also be an option, which can be facilitated by the increasingly available program packages. In addition, training and education are still needed to increase the uptake of MIPD into routine clinical practice [2].

### **3.4 Prospective clinical trials**

To promote the implementation of MIPD in clinical practice, a necessity for prospective clinical trials comparing standard dosing strategies versus MIPD has been highlighted [4]. It is pointed out that the clinical evidence supporting the benefit of the MIPD tools in improving patient outcomes is crucial for the integration of MIPD into clinical care [4]. Although clinical trials will continue to take an important role, given the repeatedly occurring evidence on the advantage of MIPD tools in cancer treatment from clinical trials

and the ability of pharmacometric methods to provide the most likely beneficial strategy, the requirement for largescale trials can decrease [8].

#### 4. Conclusion

Substantial PK/PD variability and suboptimal dosing of anti-cancer drugs highlight the need for precision dosing in real-world cancer patients. MIPD is a promising tool which adopts pharmacometric models to guide precision dose selection aiming for improved therapeutic target attainment and optimal treatment outcome. Many research and clinical trials have demonstrated the benefits of applying MIPD in anti-cancer treatment, including guiding dose selection and adaptation, as well as TDM. To promote the implementation of MIPD in clinal cancer treatment, challenges regarding optimal target identification, suitable model selection, available programs, and the necessity of prospective clinical trials need to be addressed.

## References

1. Verheijen RB, Yu H, Schellens JHM, Beijnen JH, Steeghs N, Huitema ADR. Practical Recommendations for Therapeutic Drug Monitoring of Kinase Inhibitors in Oncology. *Clin Pharmacol Ther.* 2017;102(5):765-76. doi:10.1002/cpt.787.
2. Kluwe F, Michelet R, Mueller-Schoell A, Maier C, Klopp-Schulze L, van Dyk M, et al. Perspectives on Model-Informed Precision Dosing in the Digital Health Era: Challenges, Opportunities, and Recommendations. *Clin Pharmacol Ther.* 2021;109(1):29-36. doi:10.1002/cpt.2049.
3. Fourie Zirkelbach J, Shah M, Vallejo J, Cheng J, Ayyoub A, Liu J, et al. Improving Dose-Optimization Processes Used in Oncology Drug Development to Minimize Toxicity and Maximize Benefit to Patients. *J Clin Oncol.* 2022;40(30):3489-500. doi:10.1200/JCO.22.00371.
4. Wright DFB, Martin JH, Cremers S. Spotlight Commentary: Model-informed precision dosing must demonstrate improved patient outcomes. *Br J Clin Pharmacol.* 2019;85(10):2238-40. doi:10.1111/bcp.14050.
5. Lalonde RL, Kowalski KG, Hutmacher MM, Ewy W, Nichols DJ, Milligan PA, et al. Model-based drug development. *Clin Pharmacol Ther.* 2007;82(1):21-32. doi:10.1038/sj.cpt.6100235.
6. Buil-Bruna N, Lopez-Picazo JM, Martin-Algarra S, Troconiz IF. Bringing Model-Based Prediction to Oncology Clinical Practice: A Review of Pharmacometrics Principles and Applications. *Oncologist.* 2016;21(2):220-32. doi:10.1634/theoncologist.2015-0322.
7. Barbolosi D, Ciccolini J, Lacarelle B, Barlesi F, Andre N. Computational oncology--mathematical modelling of drug regimens for precision medicine. *Nature Reviews Clinical Oncology.* 2016;13(4):242-54. doi:10.1038/nrclinonc.2015.204.
8. Menz BD, Stocker SL, Verougstraete N, Kocic D, Galettis P, Stove CP, et al. Barriers and opportunities for the clinical implementation of therapeutic drug monitoring in oncology. *Br J Clin Pharmacol.* 2021;87(2):227-36. doi:10.1111/bcp.14372.
9. Shukla P, Goswami S, Keizer RJ, Winger BA, Kharbanda S, Dvorak CC, et al. Assessment of a Model-Informed Precision Dosing Platform Use in Routine Clinical Care for Personalized Busulfan Therapy in the Pediatric Hematopoietic Cell Transplantation (HCT) Population. *Front Pharmacol.* 2020;11:888. doi:10.3389/fphar.2020.00888.
10. Briki M, Andre P, Thoma Y, Widmer N, Wagner AD, Decosterd LA, et al. Precision Oncology by Point-of-Care Therapeutic Drug Monitoring and Dosage Adjustment of Conventional Cytotoxic Chemotherapies: A Perspective. *Pharmaceutics.* 2023;15(4). doi:10.3390/pharmaceutics15041283.
11. Klopp-Schulze L, Mueller-Schoell A, Neven P, Koolen SLW, Mathijssen RHJ, Joerger M, et al. Integrated Data Analysis of Six Clinical Studies Points Toward Model-Informed Precision Dosing of Tamoxifen. *Front Pharmacol.* 2020;11:283. doi:10.3389/fphar.2020.00283.
12. Joerger M, von Pawel J, Kraff S, Fischer JR, Eberhardt W, Gauler TC, et al. Open-label, randomized study of individualized, pharmacokinetically (PK)-guided dosing of paclitaxel combined with carboplatin or cisplatin in patients with advanced non-small-cell lung cancer (NSCLC). *Ann Oncol.* 2016;27(10):1895-902. doi:10.1093/annonc/mdw290.
13. Shafiei M, Mahmood A, Beale P, Galettis P, Martin J, McLachlan AJ, et al. Dried Blood Spot Sampling in the Monitoring of Anticancer Therapy for Solid Tumors: A Systematic Review. *Ther Drug Monit.* 2023;45(3):293-305. doi:10.1097/FTD.0000000000001082.
14. Janssen JM, Dorlo TPC, Beijnen JH, Huitema ADR. Evaluation of Extrapolation Methods to Predict Trough Concentrations to Guide Therapeutic Drug Monitoring of Oral Anticancer Drugs. *Ther Drug Monit.* 2020;42(4):532-9. doi:10.1097/ftd.0000000000000767.
15. Keizer RJ, Ter Heine R, Frymoyer A, Lesko LJ, Mangat R, Goswami S. Model-Informed Precision Dosing at the Bedside: Scientific Challenges and Opportunities. *CPT Pharmacometrics Syst Pharmacol.* 2018;7(12):785-7. doi:10.1002/psp4.12353.

16. Maier C, de Wiljes J, Hartung N, Kloft C, Huisenga W. A continued learning approach for model-informed precision dosing: Updating models in clinical practice. *CPT Pharmacometrics Syst Pharmacol.* 2022;11(2):185-98. doi:10.1002/psp4.12745.
17. Powelet EA, Vinks AA, Mizuno T. Artificial Intelligence and Machine Learning Approaches to Facilitate Therapeutic Drug Management and Model-Informed Precision Dosing. *Ther Drug Monit.* 2023;45(2):143-50. doi:10.1097/FTD.0000000000001078.
18. Jager NGL, Chai MG, van Hest RM, Lipman J, Roberts JA, Cotta MO. Precision dosing software to optimize antimicrobial dosing: a systematic search and follow-up survey of available programs. *Clin Microbiol Infect.* 2022;28(9):1211-24. doi:10.1016/j.cmi.2022.03.041.
19. Kumar AA, Burgard M, Stacey S, Sandaradura I, Lai T, Coorey C, et al. An evaluation of the user-friendliness of Bayesian forecasting programs in a clinical setting. *Br J Clin Pharmacol.* 2019;85(10):2436-41. doi:10.1111/bcp.14066.



# Chapter 6

## **Population pharmacokinetic and pharmacogenetic analysis of mitotane in patients with adrenocortical carcinoma: towards individualized dosing**

Anyue Yin, Madeleine H.T. Ettaieb, Jesse J. Swen, Liselotte van Deun, Thomas M.A. Kerkhofs, Robert J.H.M. van der Straaten, Eleonora P.M. Corssmit, Hans Gelderblom, Michiel N. Kerstens, Richard A. Feelders, Mareliese Eekhoff, Henri J.L.M. Timmers, Antonio D'Avolio, Jessica Cusato, Henk-Jan Guchelaar, Harm R. Haak, Dirk Jan A.R. Moes



## Abstract

**Background:** Mitotane is the only approved treatment for patients with adrenocortical carcinoma (ACC). A better explanation for the variability in the pharmacokinetics (PK) of mitotane, and the optimization and individualization of mitotane treatment, is desirable for patients.

**Objectives:** This study aims to develop a population PK (PopPK) model to characterize and predict the PK profiles of mitotane in patients with ACC, as well as to explore the effect of genetic variation on mitotane clearance. Ultimately, we aimed to facilitate mitotane dose optimization and individualization for patients with ACC.

**Methods:** Mitotane concentration and dosing data were collected retrospectively from the medical records of patients with ACC taking mitotane orally and participating in the Dutch Adrenal Network. PopPK modelling analysis was performed using NONMEM (version 7.4.1). Genotypes of drug enzymes and transporters, patient demographic information, and clinical characteristics were investigated as covariates. Subsequently, simulations were performed for optimizing treatment regimens.

**Results:** A two-compartment model with first-order absorption and elimination best described the PK data of mitotane collected from 48 patients. Lean body weight (LBW) and genotypes of *CYP2C19\*2* (rs4244285), *SLCO1B3* 699A>G (rs7311358), and *SLCO1B1* 571T>C (rs4149057) were found to significantly affect mitotane clearance (CL/F), which decreased the coefficient of variation (CV%) of the random inter-individual variability of CL/F from 67.0 to 43.0%. Fat amount (i.e. body weight - LBW) was found to significantly affect the central distribution volume. Simulation results indicated that determining the starting dose using the developed model is beneficial in terms of shortening the period to reach the therapeutic target and limit the risk of toxicity. A regimen that can effectively maintain mitotane concentration within 14–20 mg/L was established.

**Conclusions:** A two-compartment PopPK model well-characterized mitotane PK profiles in patients with ACC. The CYP2C19 enzyme and SLCO1B1 and SLCO1B3 transporters may play roles in mitotane disposition. The developed model is beneficial in terms of optimizing mitotane treatment schedules and individualizing the initial dose for patients with ACC. Further validation of these findings is still required.

## 1. Introduction

Adrenocortical carcinoma (ACC) is a rare endocrine malignancy (1 per million per year) with a poor prognosis and limited treatment options [1]. Mitotane, a highly lipophilic compound, is the only treatment approved by the US FDA and the European Medicines Agency for ACC [1]. Mitotane is developed as an orally administered treatment and its absorption is improved by concomitant intake of fat-rich food [2]. The bioavailability of mitotane is around 35–40% [3]. Mitotane has a high volume of distribution and the primary distribution site is fat [3, 4]. The half-life of mitotane elimination ranges from 18 to 159 days, with a median of 53 days [2, 3].

The efficacy and toxicity of mitotane are related to the plasma concentration [1, 3]. In order to ensure efficacy and avoid increased toxicity, the mitotane plasma concentration should be between the therapeutic range of 14 and 20 mg/L, which requires therapeutic drug monitoring (TDM) [1].

However, due to the large distribution volume and long half-life of mitotane, a long-time interval (around 3–5 months [1]) is usually required for patients to reach the effective concentration [3], which limits the clinical utility of mitotane. The inability to reliably predict mitotane plasma concentrations may result in a prolonged time to reach the target value, hence causing a significant delay in tumour treatment, or may give rise to drug toxicity. In addition, it has been demonstrated that only half of the patients who received a high-dose regimen for 3 months achieved the target [5], suggesting a demand for individualized treatment and a presence of high inter-individual variability (IIV) in the pharmacokinetics (PK) of mitotane. Currently, the dosage titration is largely expert-based, making it prone to errors. Therefore, a tool enabling mitotane concentration prediction and an optimized treatment regimen for individual patients, which shortens the period required to reach the target concentration while limiting the toxicity, would be desirable for patients with ACC.

A population PK (PopPK) modelling approach with mixed-effect models enables quantitative characterization and prediction of drug PK profiles for both the study population and individuals [6]. The development of a PopPK model of mitotane would be beneficial for the characterization and understanding of mitotane PK, as well as for the optimization and personalization of mitotane treatment. Until now, two studies have performed PopPK modelling analysis on mitotane in patients with ACC [3, 7]; one-compartment models were developed in these two studies. One study assuming a self-induced clearance and a body mass index (BMI) was found to be a covariate of mitotane distribution volume [3], while the other study identified the effects of triglyceride and high-density lipoprotein on mitotane clearance [7]. Another model-based PK study of mitotane developed a three-

compartment model and showed weak correlations of age, sex, body weight, height, and body surface area with model parameters [8].

In order to further elucidate the variability of mitotane PK, it would be beneficial to explore the effect of pharmacogenetic polymorphisms [8]. Although the exact PK pathway of mitotane and the enzymes involved in mitotane metabolism remain unknown [9], two studies suggested possible roles for cytochrome P450 (CYP) 2B6 and CYP2C9 [10, 11]. One study demonstrated that the genotype of *CYP2B6\*6* (rs3745274) was significantly correlated with mitotane plasma concentrations at 3 and 6 months after the initiation of treatment [10]. The other study showed that one patient with high mitotane concentration was a CYP2C9 intermediate metabolizer [11]. Further analysis of the relationship between genes encoding for PK enzymes and transporters and mitotane PK profiles, and incorporating these variables into a PopPK model, may allow better explanation of mitotane PK variability.

In the current study, a PopPK analysis was performed for mitotane in patients with ACC utilizing the retrospectively collected PK data. The effect of genes encoding drug absorption, distribution, metabolism, and elimination (ADME), patient demographic information, and clinical characteristics on mitotane PK were investigated as covariates. We aimed to develop a PopPK model to describe and predict the PK of mitotane in patients with ACC, as well as to explore the effect of genetic variation on mitotane clearance. Moreover, we intended to better explain mitotane PK variability using the developed model and to facilitate treatment optimization and individualization for patients with ACC.

## 2. Methods

### 2.1 Patients

Forty-nine adult patients diagnosed with ACC ( $\geq 18$  years old), who were enrolled in the Dutch Adrenal Network Registry, had been treated with mitotane, had provided consent, and had available mitotane dosing information as well as concentration data were included in this PopPK analysis. One patient was eventually excluded because of missing information regarding starting dose.

The study was approved by the Medical Ethical Committee of the Máxima Medical Center, Veldhoven (2015), and approval for the inclusion of patients in other institutes was obtained from the local boards. The required informed consents were obtained from all patients. All procedures performed in this study were in accordance with the ethical standards of the institutional Medical Ethical Committee and the 1964 Helsinki Declaration.

## 2.2 Pharmacokinetic (PK) data

Data on mitotane plasma concentrations, including concentrations from routine TDM, data sampled during one treatment interval, and data collected after treatment discontinuation, as well as all mitotane dosing data, were collected retrospectively from patients' medical records. Patients administrated mitotane orally were advised to take mitotane with fat-rich food. Concomitant medication information was not included in the current analysis since the data were not complete. The mitotane plasma concentrations were determined by a validated gas-chromatography/ mass spectrometry assay at the Department of Clinical Pharmacy and Toxicology, Leiden University Medical Center (LUMC) [12]. The lower limit of quantification (LLOQ) was 2 mg/L. In addition, patients' demographic information, including age, sex, and body weight (WT) and height (HT) at the start of treatment, were collected. Furthermore, levels of serum aspartate transaminase (ASAT), alanine transaminase (ALAT), gamma-glutamyltransferase ( $\gamma$ GT), total cholesterol, and estimated glomerular filtration rate (GFR; recorded as 0 if the result was  $\geq 60$  mL/min/1.73  $m^2$ , otherwise 1) were also collected in our analysis.

Lean body weight (LBW) and fat amount (FAT) were also calculated for each patient. LBW was estimated using the *Boer* formula [13] and FAT was obtained by subtracting LBW from WT.

## 2.3 Genotyping method

The DNA of included patients was isolated from EDTA blood samples using Maxwell (Promega, Leiden, The Netherlands) or MagNAPure compact (Roche, Almere, The Netherlands). Genotyping of patients was performed using the Drug Metabolizing Enzymes and Transporters (DMET™) Plus array (Affymetrix UK Ltd, High Wycombe, UK), which contains 1936 genetic variants (1931 single nucleotide polymorphisms [SNPs] and 5 copy number variations [CNVs]) of ADME-related enzymes and transporters [14], according to the manufacturers' protocol. The method has been previously described in detail [15, 16].

A preset selection was performed using the DMET™ console software that generates fully annotated marker reports based on a translation file as recommended by Affymetrix® [17]. The reports include commonly recognized, haplotype-based allele calls commonly cited in Medline reference studies [18-20]. The DMET™ Plus allele translation software produces a comprehensive genotyping report containing pharmacogenomic reference data on all probes. This step leads to the selection of 959 SNPs from the total of 1931 SNPs present on the DMET™ platform. Subsequently, the SNPs that deviated from Hardy-Weinberg equilibrium ( $p < 0.0001$ ), with a call rate below 97% or with a minor allele frequency

(MAF) < 0.1, as well as tri-allelic SNPs and SNPs of genes located on the X chromosome, were excluded from further analysis.

## 2.4 Population PK model development

Based on the obtained mitotane concentration data, a non-linear mixed-effects model was developed. Parameters were estimated using the first-order conditional estimation method with interaction (FOCEI) implemented in NONMEM software version 7.4.1 (ICON Development Solutions, Ellicott City, MD, USA). One-, two- and three-compartment models with first-order absorption and first-order elimination were explored as the structural model. Data points below the LLOQ were omitted since they only contributed to 3.6% of the observations [21, 22].

Since the majority of collected data were trough concentrations, and data regarding the absorption phase were limited, the absorption rate constant (KA) was first estimated based on a sub-dataset containing data of the patients who contributed multiple data points during one treatment interval at steady state. The KA estimate was then fixed to analyze the full dataset. Inter-occasion variability (IOV) was incorporated on apparent systemic clearance (CL/F) and every 200 days of treatment was defined as an occasion. In addition, to simplify the situation, all patients were assumed to receive a single dose once daily at 8:00 am, with the dose amount being equal to the total daily dose.

A further detailed description of the PopPK modelling methods is shown in **Online Resource 6.1**.

## 2.5 Identify potential correlated single nucleotide polymorphisms and covariate analysis

Since knowledge regarding the relationship between mitotane clearance and pharmacogenetic polymorphisms is limited, an exploratory analysis was first performed to find potential SNPs that were correlated with mitotane clearance. The estimates of random IIV of CL/F ( $\eta_{IIVi\_CL}$ ) from the basic model and the genotyping results were utilized. For each SNP, when the number of patients in a minor homozygous group was < 4, the results of these patients were combined with the corresponding heterozygote group for the association analysis assuming a dominant allele effect. Additionally, when the number of patients with genotype results of 'zero copy number' or 'possible rare allele' was less than four, or when patients had 'NoCall' results, the results were not included for statistical analysis. A one-way analysis of variance (ANOVA) test and a two-sided *t* test were performed

using R version 3.6.1 (The R Foundation for Statistical Computing Vienna, Austria) to evaluate the difference in  $\eta_{IVI\_CL}$  across genotype groups for each SNP. Selection of the test method depended on the number of genotype groups of each SNP after the combination. The SNPs were considered to correlate with mitotane clearance if the *p*-value was < 0.05. Correction for multiple testing was not performed due to the exploratory characteristics of the current analysis.

The identified SNPs, as well as patient demographic information and clinical characteristics, were considered in the covariate analysis. The stepwise covariate modelling (SCM) function implemented with Perl-Speaks-NONMEM (version 4.7.0) [23] was applied. Both forward inclusion (*p* < 0.05) and backward elimination processes (*p* < 0.01) were performed to identify significant covariates. A more detailed description of the covariates analysis is shown in **Online Resource 6.1**.

## 2.6 Model evaluation

The predictability and stability of the final model was evaluated using goodness-of-fit (GOF) plots, prediction-corrected visual predictive checks (pcVPC) [24], and non-parametric bootstrap. Normalized prediction distribution errors (NPDEs) were also applied for evaluation. All figures were created using R (The R Foundation for Statistical Computing). A detailed description of the evaluation methods is shown in **Online Resource 6.1**.

## 2.7 Simulations for treatment optimization

Based on the final model, simulations were performed to optimize mitotane dosing regimen and starting dose determination, in order to shorten the target-reaching time while limiting the risk of toxicity. The simulation was performed for patients included in this study, as they are considered to be able to represent the corresponding adult patient population. The individual parameters of each patient were used to simulate the 'real' mitotane concentrations ( $C_{sim\_real}$ ) under each regimen. The residual errors were not considered. Different strategies of adjusting the dose according to  $C_{sim\_real}$  are shown in **Figure 6.1**. All simulations were performed using R (The R Foundation for Statistical Computing) and the differential equations were solved using the RxODE package (version 0.6-1) [25]. A detailed description of the regimens and simulation methods are shown in **Online Resource 6.1**.

On the basis of the simulated PK curves, for patients who originally reached the target, the mean and maximum time needed to reach the target ( $T_{target}$ , the first day when  $C_{sim\_real} \geq 14$  mg/L), the mean percentage of days when  $C_{sim\_real}$  was higher than 20 mg/L in the first 200 days ( $P_{toxicity}$ ), and the mean percentages of  $C_{sim\_real}$  located outside the ther-

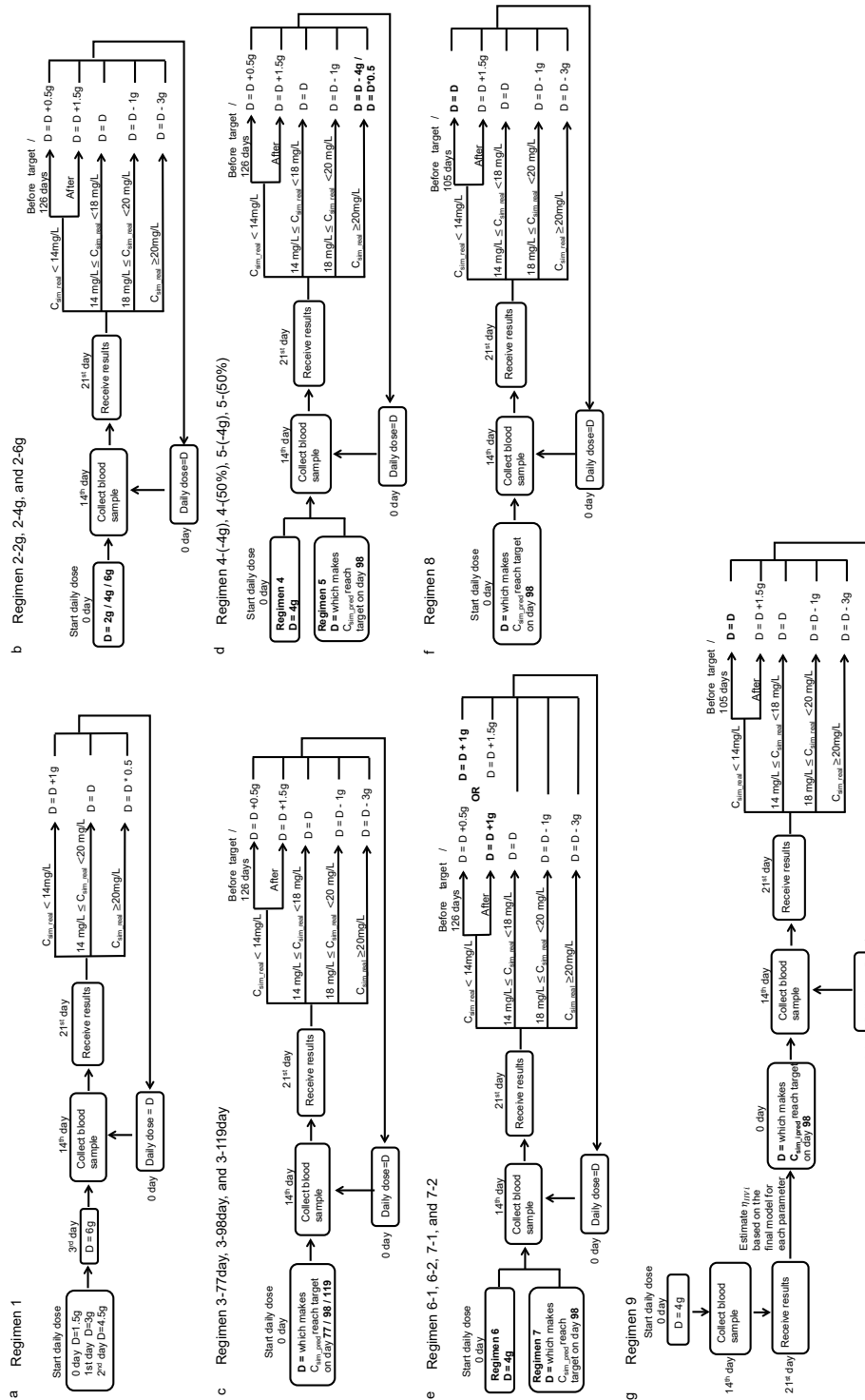


**Figure 6.1:** Designed treatment regimens that were evaluated by simulation. **(a)** A previously reported dosing regimen (Regimen 1), where the dose started as 1.5 g/day and increased up to 6 g/day in 4 days and continued until the next dose adjustment. The dosage was adjusted each time according to the monitored mitotane concentration level. **(b)** Regimens where all patients started with 2 g (Regimen 2–2 g), 4 g (Regimen 2–4 g) or 6 g (Regimen 2–6 g) per day. Dosage increased by 0.5 g every 21 days till the target was reached or 126 days if  $C_{sim\_real} < 14 \text{ mg/L}$ . Thereafter, the dosage increased by 1.5 g if  $C_{sim\_real} < 14 \text{ mg/L}$ , remained unchanged if  $14 \text{ mg/L} \leq C_{sim\_real} < 18 \text{ mg/L}$ , decreased by 1 g if  $18 \text{ mg/L} \leq C_{sim\_real} < 20 \text{ mg/L}$ , and decreased by 3 g if  $C_{sim\_real} \geq 20 \text{ mg/L}$ . **(c)** Regimens where patients started with an individualized dose that allowed  $C_{sim\_pred}$  on day 77 (Regimen 3–77 day), 98 (Regimen 3–98 day), or 119 (Regimen 3–119 day) reach the target. The remaining dose-adjustment strategies were the same as Regimen 2. **(d)** Regimens where patients started with 4 g/day (Regimen 4) or an individualized dose (Regimen 5) and the dosage decreased by 4 g, or 50%, if  $C_{sim\_real} \geq 20 \text{ mg/L}$ . The remaining dose-adjustment strategies were the same as Regimen 2. **(e)** Regimens where patients started with 4 g/day (Regimen 6) or an individualized dose (Regimen 7) and the dosage increased by 1 g after reaching target or 126 days if  $C_{sim\_real} < 14 \text{ mg/L}$  (Regimen 6–1 and 7–1), or increased by 1 g until reaching target or 126 days if  $C_{sim\_real} < 14 \text{ mg/L}$  (Regimen 6–2 and 7–2). The remaining dose-adjustment strategies were the same as Regimen 2. **(f)** A regimen where patients started with an individualized dose that remained unchanged until reaching target or 105 days if  $C_{sim\_real} < 14 \text{ mg/L}$ . The remaining dose-adjustment strategies were the same as Regimen 2. **(g)** A regimen where patients started with 4 g/day for the first 21 days and the next dosage was determined that allowed  $C_{sim\_ipred}$  on day 98 to reach the target (Regimen 9). The remaining dose-adjustment strategies were the same as Regimen 8.  $C_{sim\_real}$  simulated 'real' mitotane concentrations based on individual parameters,  $C_{sim\_pred}$  model predictions based on patient characteristics,  $C_{sim\_ipred}$  model predictions using individual parameters, i.e. incorporating the inter-individual variability ( $\eta_{IVI}$ ) estimated based on the first monitored concentration.

peutic window after reaching the target ( $P_{o>window}$ ), were calculated and compared across different strategies.  $P_{toxicity}$  represents the probability of causing toxicity in the early phase of treatment, and  $P_{o>window}$  represents the ability to maintain the concentration within the therapeutic window. Meanwhile, the median maximum and minimum  $C_{sim\_real}$ , as well as the range of determined starting doses, were also collected and evaluated. As an optimized regimen is expected to be able to ensure a shorter target-reaching time and well-maintain the concentration within the therapeutic window while not causing much toxicity, the optimization target was defined as the mean  $T_{target} \leq 90 \text{ days}$  (3 months), the mean  $P_{toxicity} \leq 10\%$ , and the mean  $P_{o>window} \leq 15\%$ .

Using the optimized regimen, a Shiny application was created based on the Shiny package (version 1.4.0) and the RxODE package in R (The R Foundation for Statistical Computing) in order to perform simulation for a random patient and to elucidate an option of providing treatment advice for a new patient based on the model. A detailed description is shown in **Online Resource 6.2**.

### 3. Results

#### 3.1 Patients and data

Data from 48 patients with ACC (21 males and 27 females) were included in the PopPK analysis. The characteristics of patients are summarized in **Table 6.1**. Patients received mitotane treatment between 2002 and 2017, and the median duration of treatment was 713.5 days (range 90–2856). The total daily dosage ranged from 0.5 to 16 g/day and was divided into one to four doses. Five (two patients), six (one patient), and eight (one patient) daily dosages were also applied occasionally. Forty-one patients reached the concentration target during treatment, among whom 16 patients reached the target after 150 days. In total, 914 concentration data points were collected from patients' electronic hospital records,

**Table 6.1:** Patient characteristics (n = 48)

| Characteristic   | Value/mean | SD    | Range     |
|--|------------|-------|-----------|
| Patient characteristics                                    |            |       |           |
| No. of patients  | 48         |       |           |
| Sex, male [n (%)]  | 21 (43.8)  |       |           |
| Age, years <sup>a</sup>                                    | 52.0       | 12.1  | 22.6–76.8 |
| Weight, kg <sup>a</sup> (n = 2 no record)                  | 80.0       | 15.9  | 52.5–120  |
| Height, cm <sup>a</sup> (n = 5 no record)                  | 172        | 10.0  | 154–193   |
| BMI, kg/m <sup>2a</sup> (n = 5 no record)                  | 27.1       | 4.48  | 18.2–38.3 |
| LBW, kg <sup>a</sup> (n = 5 no record)                     | 55.8       | 10.0  | 39.7–78.5 |
| ASAT, IU/L <sup>b</sup> (n = 1 no record)                  | 45.15      | 35.3  | 16–185    |
| ALAT, IU/L <sup>b</sup> (n = 1 no record)                  | 42.68      | 35.6  | 9–197     |
| γGT, IU/L <sup>b</sup> (n = 1 no record)                   | 278.70     | 215.9 | 55–898    |
| GFR, >50% of records were normal [n (%)] (n = 7 no record) | 39 (95.1)  |       |           |
| Cholesterol, mmol/L <sup>b</sup> (n = 11 no record)        | 6.54       | 1.56  | 3.6–11.6  |
| Disease characteristics [n (%)]                            |            |       |           |
| ENSAT I, patients  | 2 (4.2)    |       |           |
| ENSAT II, patients   | 19 (39.6)  |       |           |
| ENSAT III, patients  | 10 (20.8)  |       |           |
| ENSAT IV, patients   | 17 (35.4)  |       |           |
| Target-reaching characteristics                            |            |       |           |
| No. of patients who reached the target                     | 41         |       |           |
| 150 days [n (%)]   | 16 (39.0)  |       |           |
| ≤ 90 days [n (%)]  | 19 (46.3)  |       |           |
| Target-reaching time, days                                 | 142        | 113.9 | 24–579    |
| Duration of treatment, days                                | 742        | 553.2 | 90–2856   |

SD, standard deviation; BMI, body mass index; LBW, lean body weight; ASAT, aspartate transaminase; ALAT, alanine transaminase; γGT, gamma-glutamyl transferase; GFR, glomerular filtration rate; ENSAT, European Network for the Study of Adrenal Tumors.

<sup>a</sup> At the start of treatment.

<sup>b</sup> Mean record of each patient.

33 of which were below the LLOQ. The time-course of collected mitotane concentrations is shown in **Figure 6.2**. Nine patients contributed multiple sampling data within one treatment interval and 13 patients had more than one data point collected after treatment discontinuation. The median number of data points contributed by each patient was 16.5, ranging from 2 to 47.

Data from 48 patients with ACC (21 males and 27 females) were included in the PopPK analysis. The characteristics of patients are summarized in **Table 6.1**. Patients received mitotane treatment between 2002–2017 and the median duration of treatment was 713.5 days (range from 90–2856 days). The total daily dosage ranged from 0.5–16 g per day and was divided into one to four doses. Five (2 patients), six (1 patient), and eight (1 patient) daily dosages were also applied occasionally. Forty-one patients reached the concentration target during treatment, among whom 16 patients reached the target after 150 days. In total, 914 concentration data points were collected from patients' electronic hospital records, 33 of which were below the LLOQ. The time-course of collected mitotane concentrations was shown in **Figure 6.2**. Nine patients contributed multiple sampling data within one treatment interval and 13 patients have more than one data point collected after treatment discontinuation. The median number of data points contributed by each patient was 16.5, ranging from 2 to 47.

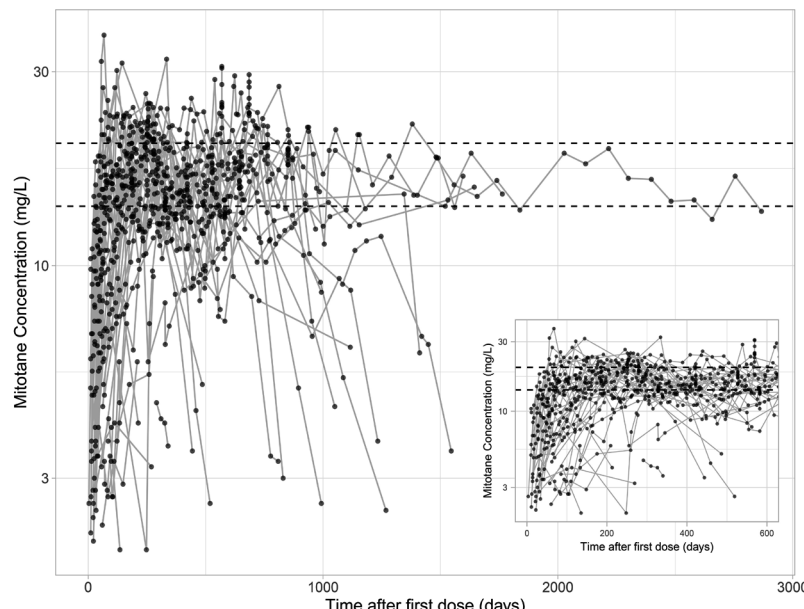


**Figure 6.2:** Mitotane concentration-time curve collected from patients on logarithmic scale. Inserts show the data during the first 600 days of treatment.

### 3.2 The basic model

Based on the sub-dataset containing data from the nine patients with multiple sampling data within one treatment interval, the KA was estimated as 22.1 (/day) and 15.0 (/day) under a one-compartment and a two-compartment model structure, respectively. A three-compartment model could not be identified, since (1) the time-course of mitotane concentration did not meet the characteristics of a three-compartment model; and (2) when running the three-compartment model, the parameters were shown to be unidentifiable. The basic models were then developed by fitting the full dataset with fixed KA and incorporating IOV on CL/F. The relative standard error (RSE) parameter estimates of both two-model structures were all within the acceptable range (< 30%). The objective function value (OFV) of the two-compartment model was reduced by 92.13 compared with that of the one-compartment model ( $p < 0.001$ , degree of freedom = 4), suggesting an improvement on the model fitness. Therefore, the two-compartment model was ultimately selected for describing mitotane PK profiles in patients with ACC in this study. The model structure is shown in **Online Resource 6.1, Figure S6.1**. The parameter estimates of the basic model are shown in **Table 6.2**. The high percentage coefficient of variation (CV%) of IIV for all parameters was identified, and the CV% of IIV for the apparent distribution rate constant (Q/F) was even higher than 100%.

### 3.3 Pharmacogenetic analysis

For each patient, the genotyping results of the 959 SNPs from the DMET<sup>TM</sup> platform were obtained. A list of these SNPs can be found in **Online Resource 6.3**. All SNPs were in Hardy–Weinberg equilibrium ( $p \geq 0.0001$ ). A flow diagram of the selection of genetic variants is shown in **Figure 6.3**. Eventually, 172 SNPs were included for further investigation. Among these 172 SNPs, 55 had less than four patients belonging to the minor homozygous group. The ‘NoCall’ result was reported in one patient in 19 SNPs and the ‘Possible Rare Allele’ result was reported in one patient in one SNP. The results of these patients were thus not included in the association analysis of corresponding SNPs. In contrast, the ‘Zero Copy Number’ result occurred in three SNPs in 8, 24, and 24 patients, respectively. Thus, patients with a ‘Zero Copy Number’ were treated as a different genotype group in the association analysis of these three SNPs.

Finally, the result of the association test showed that 11 SNPs, as shown in **Online Resource 6.1, Table S6.1**, were potentially related to mitotane clearance ( $p \leq 0.05$ ). Among these 11 SNPs, the genotyping results of *CYP2C18* 1154C>T (rs2281891) and *CYP2C19*\*2 (rs4244285) were shown to be 100% in linkage disequilibrium in our dataset, which was the same as the genotyping results of *SLCO1B3* 334G>T (rs4149117), 699A>G (rs7311358),

**Table 6.2:** Parameter estimates of both the basic and final models

| Parameters                         | Basic model        |                            |              | Final model        |                            |              | Bootstrap |             |  |
|------------------------------------|--------------------|----------------------------|--------------|--------------------|----------------------------|--------------|-----------|-------------|--|
|                                    | Estimate<br>(RSE%) | IV (CV%)<br>[shrinkage, %] | IOV<br>(CV%) | Estimate<br>(RSE%) | IV (CV%)<br>[shrinkage, %] | IOV<br>(CV%) | Median    | 95% CI      |  |
| KA (/day)                          | 15.0 fixed         | -                          | -            | 15.0 fixed         | -                          | -            | 15        | -           |  |
| CL/F (L/day) <sup>a</sup>          | 217 (11)           | 67.0 [8]                   | 30.5         | 298 (13)           | 43.0 [16]                  | 31.6         | 281.6     | 200.5–398.4 |  |
| CL_SNP1 (GA/AA)                    | -                  | -                          | -            | 0.551 (15)         | -                          | -            | 0.573     | 0.385–0.881 |  |
| CL_SNP2 (AG/GG)                    | -                  | -                          | -            | 0.601 (19)         | -                          | -            | 0.613     | 0.419–0.949 |  |
| CL_SNP3 (CC)                       | -                  | -                          | -            | 0.753 (10)         | -                          | -            | 0.784     | 0.550–1.07  |  |
| CL_SNP3 (TT)                       | -                  | -                          | -            | -                  | 2.49 (29)                  | -            | -         | -           |  |
| CL_LBW (power)                     | -                  | -                          | -            | -                  | 1.10 (16)                  | -            | 1.07      | 0.205–2.13  |  |
| V <sub>c</sub> /F (L) <sup>b</sup> | 4790 (20)          | 68.1 [53]                  | -            | 6210 (18)          | 47.2 [55]                  | -            | 6795      | 3281–10752  |  |
| V <sub>c</sub> /FAT (power)        | -                  | -                          | -            | -                  | 1.22 (19)                  | -            | -         | 0.450–2.18  |  |
| V <sub>p</sub> /F (L)              | 19300 (13)         | 76.9 [17]                  | -            | 18100 (12)         | 88.8 [15]                  | -            | 17882     | 11341–25709 |  |
| Q/F (L/day)                        | 1100 (21)          | 102 [34]                   | -            | 883 (20)           | 97.3 [34]                  | -            | 785.4     | 337.4–1502  |  |
| Residual errors                    |                    |                            |              |                    |                            |              |           |             |  |
| PRO (CV%)                          | 16.6 (7)           | -                          | -            | 16.6 (6)           | -                          | -            | 16.8      | 14.2–18.9   |  |
| ADD (mg/L)                         | 0.931 (28)         | -                          | -            | 0.920 (17)         | -                          | -            | 0.871     | 0.373–1.384 |  |

SNP1: CYP2C19\*2 (rs4244285); SNP2: SLC01B3 699A>G (rs7311358); SNP3: SLC01B1 571T>C (rs4149057); LBW, lean body weight; FAT, fat amount; RSE, relative standard error; CV, coefficient of variation; IV, interindividual variability; IOV, interoccasion variability; PRO, proportional residual error; ADD, additive residual error; CL/F, apparent system clearance; KA, absorption rate constant; V<sub>c</sub>/F, apparent distribution volume of central compartment; V<sub>p</sub>/F, apparent distribution volume of peripheral compartment; Q/F, apparent distribution rate constant; CI, confidence interval

<sup>a</sup>  $CL/F = CL/F_t * CL\_SNP1 * CL\_SNP2 * CL\_SNP3 * \frac{LBW}{CL\_LBW}$

<sup>b</sup>  $V_c/F = V_c/F_t * \frac{FAT}{(23.6)^{Vc\_FAT}}$

<sup>c</sup> Every 200 days of dosing was defined as an occasion.

and 1557G>A (rs2053098) and that of the three SNPs located on *VKORC1* (283+124G>C, 174-136C>T, and -1639G>A). The results of the 11 identified SNPs were subsequently combined into the full dataset for stepwise covariate analysis.

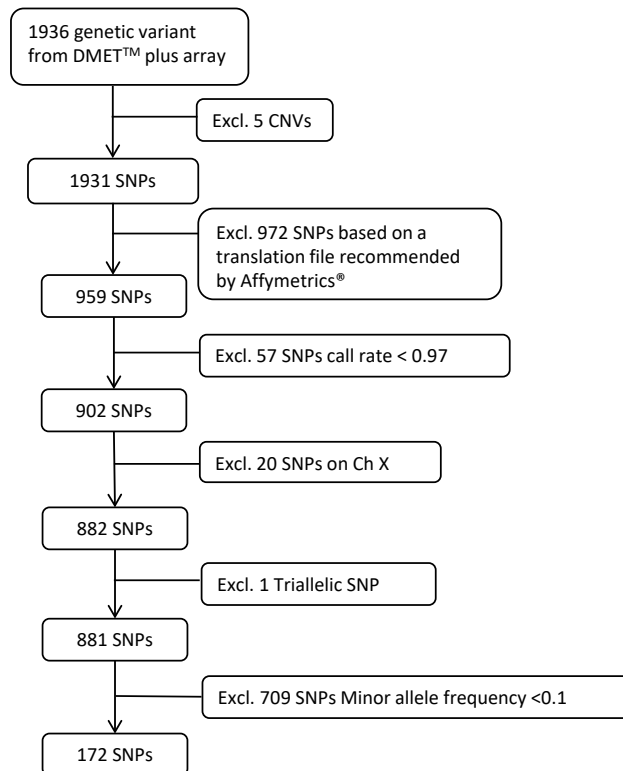


**Figure 6.3:** Selection of the genetic variants. Excl. excluding, Ch X chromosome X, DMET™ Drug Metabolizing Enzymes and Transporters, CNVs copy number variations, SNPs single nucleotide polymorphisms.

### 3.4 The final model

The parameter estimates of the final model are shown in **Table 6.2**. The *CYP2C19*\*2 (rs4244285), *SLCO1B3* 699A>G (rs7311358), and *SLCO1B1* 571T>C (rs4149057) genotypes, and LBW at the start of treatment, with power relation, were found to have a significant effect on the CL/F of mitotane (**Table 6.2**). Carrying the 'A' variant in *CYP2C19*\*2 reduced the CL/F by 44.9%, and carrying 'G' variant in *SLCO1B3* 699A>G resulted in a 39.9% reduction in CL/F (**Table 6.2**). As for *SLCO1B1* 571T>C, the CL/F of patients carrying one 'C' variant decreased to 40.2% that of wild-type patients, while the CL/F of patients carrying two 'C' variants decreased to 30.2%. The distribution of  $\eta_{IIVi\_CL}$  derived from the basic model in each genotype group of the above three SNPs is shown in **Online Resource**

**6.1, Figure S6.2.** In addition, FAT at the start of treatment with power relation was found to significantly influence the apparent distribution volume of the central compartment ( $V_c/F$ ). The inclusion of these covariates decreased the CV% of  $CL/F$  and  $V_c/F$  from 67.0% and 68.1% to 43.0% and 47.2%, respectively. Overall, the parameter estimates were shown to be in good agreement with the bootstrap results (Table 6.2).

The GOF plots (Figure 6.4) show that the individual predictions of the final model are in good accordance with the observations, while the population predictions are slightly deviated from the observations. The conditional weighted residual errors (CWRES) randomly distributed around zero, without obvious trends over time or across population predictions. The pcVPC plot (Figure 6.5) shows that the 5<sup>th</sup>, 50<sup>th</sup>, and 95<sup>th</sup> percentiles of

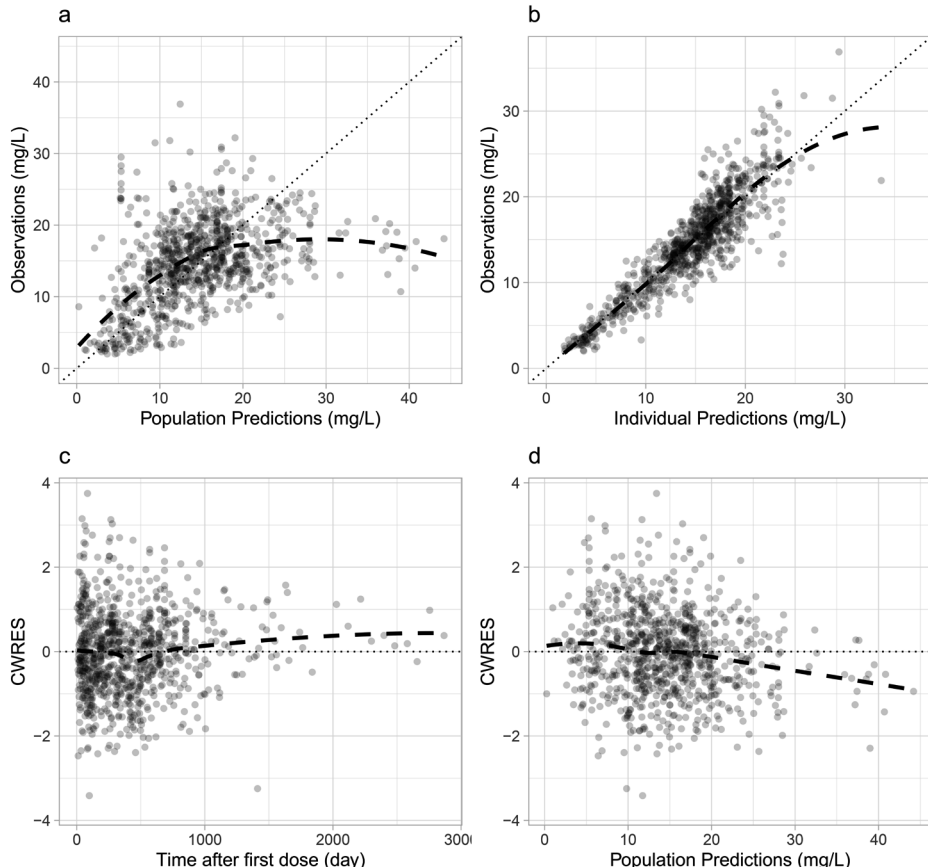


**Figure 6.4:** Goodness-of-fit plots of the final population pharmacokinetic model of mitotane in patients with adrenocortical carcinoma, including observations versus (a) population predictions and (b) individual predictions, and CWRES versus (c) time and (d) populations predictions. The black dotted lines represent  $y = x$  (a, b) and  $y = 0$  (c, d), and the black dashed lines represent the corresponding LOESS regressions. CWRES; conditional weighted residual errors; LOESS, locally estimated scatterplot smoothing.

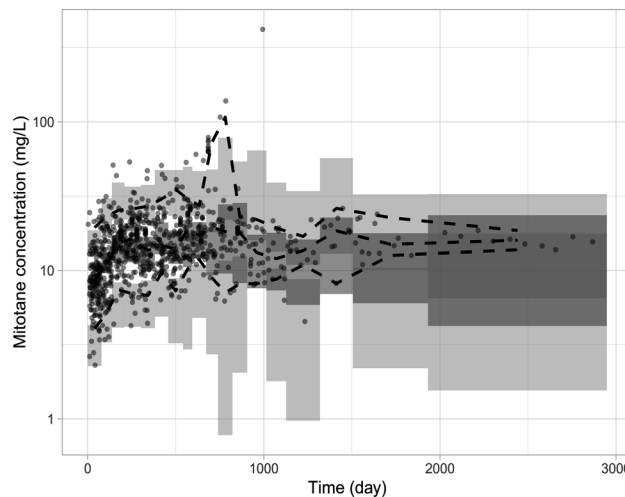


**Figure 6.5:** Prediction-corrected visual predictive check plot of the final model on the logarithmic scale. Black dashed lines represent the 50<sup>th</sup>, 95<sup>th</sup> and 5<sup>th</sup> percentiles of the prediction-corrected observations; light-grey shading represents the 95% confidence interval of the 95<sup>th</sup> and 5<sup>th</sup> percentiles of the simulations; and dark-grey shading represents the 95% confidence interval of the 50<sup>th</sup> percentiles of the simulations.

prediction-corrected concentrations can be mostly adequately covered by the 95% confidence interval (CI) of the corresponding percentiles of simulations, although a few large prediction-corrected concentrations are present. The NPDE results are shown in **Online Resource 6.1, Figure S6.3**.

### 3.5 Simulation results

The simulation results of different regimens in included patients who originally reached the target ( $n = 41$ ) are summarized in **Table 6.3**.

The previously suggested high-dose regimen (Regimen 1) resulted in the lowest  $T_{target}$  but the highest  $P_{toxicity}$ . The  $C_{sim\_real}$  can also not be well-maintained within the therapeutic range.

As for the newly designed strategies, if all patients started with the same dosage (Regimen 2–2 g, 2–4 g and 2–6 g), the increase in the starting dosage reduced the  $T_{target}$  but increased  $P_{toxicity}$  and weakened the ability of maintaining  $C_{sim\_real}$  within the therapeutic range. When determining the starting dose individually (Regimen 3–77 day, 3–98 day and 3–119 day), Regimen 3–98 day fulfilled the optimization target and resulted in a lower  $T_{target}$  but higher  $P_{toxicity}$  and  $P_{o>window}$  compared with Regimen 2–4 g. The range of determined starting dose was in accordance with what is currently recommended [26] (**Table 6.3**).

**Table 6.3:** Simulation results of different treatment regimens for included patients who originally reached the target (n = 41)

| Regimen<br>(Figure 6.1) | Mean<br>$T_{target}$ (day) | Max<br>$T_{target}$ (day) | Mean<br>$P_{toxicity}$<br>(%) | Mean<br>$P_{o>window}$<br>(%) | Median<br>max / min<br>$C_{sim\_real}$ (mg/L) | Starting<br>dose range<br>(g) |
|-------------------------|----------------------------|---------------------------|-------------------------------|-------------------------------|---|-------------------------------|
| 1                       | 54.22                      | 125                       | 23.6                          | 18.35                         | 22.3 / 13.11                                  | -                             |
| 2-2 g                   | 133.98                     | 236                       | 4.16                          | 12.6                          | 20.65 / 13.14                                 | 2                             |
| 2-4 g                   | 89.8                       | 182                       | 7.01                          | 13.15                         | 20.90 / 13.20                                 | 4                             |
| 2-6 g                   | 60.61                      | 149                       | 13.85                         | 15.13                         | 21.13 / 13.09                                 | 6                             |
| 3-77 day                | 73                         | 173                       | 10.63                         | 12.7                          | 21.07 / 13.29                                 | 3.5-7                         |
| 3-98 day                | 85.07                      | 182                       | 9.26                          | 14.35                         | 21.03 / 13.16                                 | 3-6                           |
| 3-119 day               | 97.9                       | 191                       | 6.44                          | 12.22                         | 20.96 / 13.21                                 | 2.5-5                         |
| 4-(-4 g)                | 89.8                       | 182                       | 5.96                          | 12.66                         | 20.91 / 13.22                                 | 4                             |
| 4-50%                   | 89.8                       | 182                       | 8.82                          | 12.37                         | 20.91 / 13.22                                 | 4                             |
| 5-(-4 g)                | 85.07                      | 182                       | 7.92                          | 13.01                         | 20.84 / 13.14                                 | 3-6                           |
| 5-50%                   | 85.07                      | 182                       | 11.13                         | 12.21                         | 20.84 / 13.22                                 | 3-6                           |
| 6-1                     | 91.12                      | 194                       | 6.61                          | 13.37                         | 20.84 / 12.91                                 | 4                             |
| 6-2                     | 74.32                      | 151                       | 14.34                         | 16.26                         | 21.57 / 13.02                                 | 4                             |
| 7-1                     | 86.12                      | 194                       | 8.52                          | 14.69                         | 21.03 / 12.96                                 | 3-6                           |
| 7-2                     | 80.27                      | 160                       | 14                            | 15.53                         | 21.46 / 12.87                                 | 2.5-5                         |
| 8                       | 87.85                      | 191                       | 5.05                          | 11.26                         | 20.34 / 13.30                                 | 3.5-7                         |
| 9                       | 87.8                       | 161                       | 5.56                          | 10.72                         | 20.33 / 13.09                                 | 3-10                          |

$T_{target}$ , target reaching time (the day when simulated mitotane concentration  $\geq 14$  mg/L),  $P_{toxicity}$ , percentage of days when simulated mitotane concentrations were higher than the upper limit of mitotane therapeutic window (20 mg/L) in the first 200 days,  $P_{o>window}$ , percentage of simulated mitotane concentrations located outside the therapeutic window after reaching the target, max maximum, min minimum, \* indicates the regimen fulfills the optimization target,  $C_{sim\_real}$  simulated 'real' mitotane concentrations based on individual parameters.

Compared with Regimens 2-4 g and 3-98 day, increasing the dose reduction amount to 4 g when  $C_{sim\_real} > 20$  mg/L reduced the  $P_{toxicity}$  and  $P_{o>window}$ , whereas setting a 50% deduction when  $C_{sim\_real} > 20$  mg/L reduced the  $P_{o>window}$  but increased the  $P_{toxicity}$  (Regimen 4 and 5). Both of these changes did not affect  $T_{target}$ . In contrast, when adjusting the dose change amount when  $C_{sim\_real} < 14$  mg/L, the evaluated regimens did not provide better results (Regimens 6 and 7).

Regimen 8, where a constant starting dose determined by the model was applied, provided generally better results compared with starting with 4 g/day for all patients (Regimen 2-4 g) in terms of  $T_{target}$ ,  $P_{toxicity}$ , and the ability to maintain concentration within the therapeutic range. The suggested starting dose range (3-7 g, median 5 g) was slightly beyond the current recommended range but was considered to be acceptable. In comparison, when determining a constant dose using individual PK parameters (incorporating IIV estimates) [Regimen 9], the  $P_{o>window}$  and maximum  $T_{target}$  decreased. Although  $P_{toxicity}$  increased, it was

still low enough. The suggested doses under Regimen 9 were relatively higher (3–10 g) since IIV was taken into account.

Overall, Regimens 2–4 g, 3–98 day, 4–(-4 g), 4–(-50%), 5–(-4 g), 7–1, 8, and 9 fulfilled the optimization target. The individualized starting dose resulted in a lower  $T_{target}$  but higher  $P_{toxicity}$  compared with the fixed starting dose. Regimens 3–98 day and 5–(-4 g) provided the lowest mean  $T_{target}$ , while regimen 5–(-4 g) resulted in lower  $P_{toxicity}$ . Regimen 8 provided the lowest  $P_{toxicity}$  and Regimen 9 provided the lowest maximum  $T_{target}$  and mean  $P_{o>window}$ . Based on these results, Regimen 5–(-4 g) and Regimen 8 were considered to be more beneficial, while Regimen 9 could also be applied, considering the patients' tolerance to the level of dose increase.

The Shiny app was established based on the final model, and the treatment strategy 5–(-4 g) was applied since this regimen provided the lowest mean  $T_{target}$ . A reduced model where the effect of pharmacogenetic variation was not included was also built in to serve as an alternative option for patients when genotyping results were not available. The results are shown in **Online Resource 6.2**.

## 4. Discussion

In the current study, a two-compartment PopPK model was developed that adequately described the PK profile of mitotane in patients with ACC. The covariates identified explained 24% and 20.9% of random variability in mitotane clearance and distribution volume, respectively. As mitotane distributes in most body tissues, predominantly in the fat [1], the two-compartment model structure is considered to also be in line with the PK characteristics of mitotane, although the wide 95% CI of the Q/F parameter still indicates uncertainty in the estimation. A three-compartment model structure, which has been previously applied on mitotane [8], could not be identified in this study as the time-course of mitotane concentration did not meet the characteristics of a three-compartment model and parameter estimates for the three-compartment model were found to be unidentifiable.

Because of the limited data in the absorption phase, KA was first estimated based on a sub-dataset and then fixed to analyze the full dataset. Precise KA estimation was unidentifiable if estimating based on the full dataset. The estimates of  $V_c/F$  and  $V_p/F$  were relatively large, which is in accordance with previous reports and the fact that mitotane distributes in many body tissues [1, 3]. The separate effects of LBW and FAT on mitotane distribution volumes were of interest in this study as they are more realistic covariates physiologically [3, 4]. As a result, FAT was found to be a significant covariate on the  $V_c/F$ . The estimated

half-life of mitotane in the included patients ranged from 16.4 to 700.6 days, with a median of 101.5 days. This range is wider than what has been previously reported [1, 2], which may be explained by the larger number of patients included in the current study than in the original study [2]. Incorporating IOV on CL/F in the current study explained the intrasubject variability. The estimates of IOV indicate an overall increasing clearance during the first 500 days, followed by a decrease thereafter (**Online Resource 6.1, Figure S6.4**). This dynamic indicates that a self-induction in mitotane clearance, which has been suggested previously [3], may exist temporarily.

For the first time, the current study explored and quantified the potential effect of pharmacogenetic variation on mitotane clearance in patients with ACC. Due to the lack of knowledge regarding the PK pathway of mitotane, a wide range of SNPs from the DMET™ Plus array were considered. However, because of the limited number of patients, it was decided to focus on the SNPs with known functionality by adopting a preset selection [17], although an exploratory analysis based on all genetic variants from the DMET™ Plus array was also performed. The flow diagram of the SNP selection and the nine additional SNPs that are potentially correlated to mitotane clearance if the preset selection was not considered are shown in **Online Resource 6.1, Table S6.2** and **Figure S6.5**. Genes located on the X chromosome were excluded since only the general influence of sex on mitotane PK was considered.

Eventually, three SNPs, i.e. *CYP2C19\*2* (rs4244285), *SLCO1B3* 699A>G (rs7311358), and *SLCO1B1* 571T>C (rs4149057), were included in the final model and were considered as the pharmacogenetic polymorphisms that should be considered for mitotane dose selection. This result also suggests that the CYP2C19 enzyme and SLCO1B3 and SLCO1B1 transporters for drug uptake in the liver might be involved in the mitotane PK pathways, but further confirmation is required.

In fact, in our dataset, *CYP2C19\*2* was in 100% linkage disequilibrium with *CYP2C18* 1154C>T (rs2281891), which was the same as *SLCO1B3* 699A>G with *SLCO1B3* 334G>T (rs4149117) and *SLCO1B3* 1557G>A (rs2053098). Comparable high linkage disequilibrium was also found in 1000 Genomes CEU population (Utah residents with Northern and Western European ancestry). Compared with *CYP2C18* 1154C>T, for which no sufficient evidence has been found regarding the effect on the drug PK, the 'A' variant of *CYP2C19\** is known to be a nonfunctioning variant and has been demonstrated to decrease the activity of CYP2C19 [27, 28]. Similarly, the variants of *SLCO1B3* 699A>G with *SLCO1B3* 334G>T have been reported to be associated with a decrease in drug clearance, and *SLCO1B3* 699A>G has a stronger level of clinical annotations [29, 30]. Therefore, *CYP2C19\*2* and *SLCO1B3* 699A>G were included in the final model.

*CYP2B6\*6*, which has been reported to be related to mitotane plasma concentrations detected at 3 and 6 months [10], was not found to have a significant effect on mitotane clearance in the current study. Among the five SNPs located on *CYP2B6* that were included in the association analysis, none were significantly related to mitotane clearance ( $p > 0.05$ ). This discrepancy may be due to the much longer observation period in the present study. One SNP located on *CYP2C9*, *CYP2C9\*2* (rs1799853), was also not found to be significant; however, the evidence of the involvement of *CYP2C9* is in fact insufficient.

The predictability and stability of the final model were confirmed to be acceptable. In the pcVPC plot, a few prediction-corrected concentrations are inadequately covered by the simulations. A possible explanation is that the observations at corresponding time points are from a single patient and the population prediction of this patient is much smaller than real observations. The deviation of population predictions from observations can also be seen in the GOF plots. Patients' adherence and other unknown factors may also introduce additional bias. Identification of additional covariates, such as the effect of co-medication and food intake, might improve the population predictions.

Based on the final PopPK model, several mitotane treatment strategies were designed and evaluated by simulations. A regimen with a bolus dose followed by a maintenance dose was not considered as this regimen requires a high dosage, which is not tolerable for some patients. Among the regimens that fulfilled the optimization target, applying the individual starting dose determined by the model was demonstrated to shorten the time to achieve the therapeutic window compared with starting with a fixed dose for all patients. Under the setting of individualized starting dose, the regimens with a stepwise increasing dose at start required less time to reach the therapeutic target, while the regimen with a constant starting dose demonstrated the lowest risk of having toxicity. The determined individual starting dose was also acceptable. In addition, the newly designed dose-adjustment strategies were able to satisfactorily keep the mitotane concentrations within the therapeutic range. Therefore, determining the starting dose using the developed model is considered to be most beneficial in terms of shortening the time to reach the therapeutic target and limit the risk of toxicity. However, due to the fact that a shorter  $T_{target}$  is normally paired with a higher  $P_{toxicity}$ , it is suggested to consider, based on a patient's condition, whether the increased risk of having toxicity can be tolerated in order to gain the benefit of a shorter time to reach the therapeutic target when selecting a dosing regimen.

Obtaining individual parameters based on one (or more) TDM result with the PopPK model, and determining the dose amount accordingly, can also decrease the risk of toxicity while providing a satisfactory target reaching time; thus, this is also a promising strategy.

However, patients' tolerance to the high level of dose increase needs to be considered when applying this strategy. This method can also be useful to estimate an adequate dose for the drug concentration level maintenance after reaching the therapeutic window, thereby decreasing the frequency of dose adjustment.

Simulation results also indicate that in order to reduce the risk of having toxicity and to effectively maintain mitotane concentration within the therapeutic range, a better strategy is to set the concentration boundary of dose decreases at 18 mg/L instead of 20 mg/L. This early dose adjustment takes into consideration the 7-day period when the monitoring result is unknown and the dose is not adjusted. The concentration boundary of dose increases needs to be 14 mg/L since it affects the adequacy of maintaining the plasma concentration above 14 mg/L. The frequency of TDM was set at once every 21 days, as suggested by the guideline in the simulation. If TDM is performed less frequently, a larger dose change step will be required.

The current study has some limitations. First, the small number of patients included in this study and the exploratory characteristics of this analysis may influence the power of covariate analysis, especially for pharmacogenetic analysis. However, as the dataset consisted of concentrations on different occasions for each patient, which enabled differentiation between IIV and intrasubject variability (i.e. IOV) in clearance, the certainty of the possible genotype effect on clearance, which is more likely to be covered by IIV since genotype is a constant factor in patients, was increased. Nonetheless, further validation with an external dataset to replicate the findings is warranted to confirm the identified associations and to translate the findings into a clinical recommendation. However, since ACC is a very rare disease (1 per million per year), the collection of another comparable or even larger dataset will be challenging. Therefore, an in vitro assay might be more feasible in future studies to substantiate the activity of the suggested enzymes in mitotane PK. Second, the model lacks a strong ability to accurately predict high concentrations (e.g., peak concentrations) due to the limited data input in the absorption and distribution phase. Furthermore, the accuracy of parameter estimates may be affected by our simplification of multiple daily dosing to a single dose. However, the prediction of mitotane trough concentrations and the suggestion of daily dose based on the model will not be significantly affected. Therefore, we believe this model is still fit for the current application. Third, the impact of coadministered drugs and food intake on mitotane PK was not taken into account in this study due to the lack of data.

## 5. Conclusions

The current study presents a two-compartment PopPK model that well-characterizes mitotane PK profiles in patients with ACC. The polymorphisms of *CYP2C19\*2* (rs4244285), *SLCO1B3* 699G>A (rs7311358), and *SLCO1B1* 571T>C (rs4149057) were found to be correlated to mitotane PK. Further external or in vitro evaluation is suggested to confirm the results. Moreover, optimized mitotane treatment schedules for patients with ACC were identified by simulation and the developed model can be of help to individualize the initial dose. These strategies should be confirmed in a prospective study

## Key points

- A two-compartment population pharmacokinetic (PK) model with first-order absorption and elimination was developed for mitotane based on PK data collected from 48 adrenocortical carcinoma patients.
- The pharmacogenetic variation of *CYP2C19\*2* (rs4244285), *SLCO1B3* 699A>G (rs7311358), and *SLCO1B1* 571T>C (rs4149057) was found to have a significant effect on mitotane clearance. Fat amount, which was defined as the difference between total body weight and lean body weight, had a significant effect on the central distribution volume.
- With the help of the model, mitotane treatment can be guided and optimized for individual patients. Further validation of the findings is warranted to confirm the results.

## Code availability

PopPK analysis was performed using the FOCEI method implemented in NONMEM software version 7.4.1 (ICONDevelopment Solutions). Statistical analysis, plot generation, and simulations were performed using R version 3.6.1 (The R Foundation for Statistical Computing). The R script of the Shiny application established in this study for simulation can be found at <https://github.com/AnyueYin/Shiny-app-script-for-model-simulation--Population-PK-and-PG-analysis-of-mitotane>.

## References

- Paraglioli RM, Torino F, Papi G, Locantore P, Pontecorvi A, Corsello SM. Role of Mitotane in Adrenocortical Carcinoma - Review and State of the art. *Eur Endocrinol*. 2018;142:62-6. doi:10.17925/EE.2018.14.2.62.
- Moolenaar AJ, van Slooten H, van Seters AP, Smeenk D. Blood levels of o,p'-DDD following administration in various vehicles after a single dose and during long-term treatment. *Cancer Chemother Pharmacol*. 1981;7(1):51-4. doi:10.1007/bf00258213.
- Arshad U, Taubert M, Kurlbaum M, Frechen S, Herterich S, Megerle F, et al. Enzyme autoinduction by mitotane supported by population pharmacokinetic modelling in a large cohort of adrenocortical carcinoma patients. *Eur J Endocrinol*. 2018;179(5):287-97. doi:10.1530/EJE-18-0342.
- Vanslooten H, Vanseters AP, Smeenk D, Moolenaar AJ. O,P'-Ddd (Mitotane) Levels in Plasma and Tissues during Chemotherapy and at Autopsy. *Cancer Chemoth Pharm*. 1982;9(2):85-8. doi:10.1007/bf00265384.
- Kerkhofs TM, Baudin E, Terzolo M, Allolio B, Chadarevian R, Mueller HH, et al. Comparison of two mitotane starting dose regimens in patients with advanced adrenocortical carcinoma. *J Clin Endocrinol Metab*. 2013;98(12):4759-67. doi:10.1210/jc.2013-2281.
- Buil-Bruna N, Lopez-Picazo JM, Martin-Algarra S, Troconiz IF. Bringing Model-Based Prediction to Oncology Clinical Practice: A Review of Pharmacometrics Principles and Applications. *Oncologist*. 2016;21(2):220-32. doi:10.1634/theoncologist.2015-0322.
- Cazaubon Y, Talineau Y, Feliu C, Konecki C, Russello J, Mathieu O, et al. Population Pharmacokinetics Modelling and Simulation of Mitotane in Patients with Adrenocortical Carcinoma: An Individualized Dose Regimen to Target All Patients at Three Months? *Pharmaceutics*. 2019;11(11). doi:10.3390/pharmaceutics11110566.
- Kerkhofs TM, Derijks LJ, Ettaieb H, den Hartigh J, Neef K, Gelderblom H, et al. Development of a pharmacokinetic model of mitotane: toward personalized dosing in adrenocortical carcinoma. *Ther Drug Monit*. 2015;37(1):58-65. doi:10.1097/FTD.0000000000000102.
- Scripture CD, Sparreboom A, Figg WD. Modulation of cytochrome P450 activity: implications for cancer therapy. *Lancet Oncol*. 2005;6(10):780-9. doi:10.1016/S1470-2045(05)70388-0.
- D'Avolio A, De Francia S, Basile V, Cusato J, De Martino F, Pirro E, et al. Influence of the CYP2B6 polymorphism on the pharmacokinetics of mitotane. *Pharmacogenet Genomics*. 2013;23(6):293-300. doi:10.1097/FPC.0b013e3283606cb2.
- Mornar A, Sertic M, Turk N, Nigovic B, Korsic M. Simultaneous analysis of mitotane and its main metabolites in human blood and urine samples by SPE-HPLC technique. *Biomed Chromatogr*. 2012;26(11):1308-14. doi:10.1002/bmc.2696.
- Hermsen IG, den Hartigh J, Haak HR. Mitotane serum level analysis; good agreement between two different assays. *Clin Endocrinol (Oxf)*. 2010;73(2):271-2. doi:10.1111/j.1365-2265.2010.03787.x.
- Boer P. Estimated lean body mass as an index for normalization of body fluid volumes in humans. *American Journal of Physiology-Endocrinology and Metabolism*. 1984;247(4):F632-6. doi:10.1152/ajprenal.1984.247.4.F632.
- Arbitrio M, Di Martino MT, Scionti F, Agapito G, Guzzi PH, Cannataro M, et al. DMET (Drug Metabolism Enzymes and Transporters): a pharmacogenomic platform for precision medicine. *Oncotarget*. 2016;7(33):54028-50. doi:10.18632/oncotarget.9927.
- Caldwell MD, Awad T, Johnson JA, Gage BF, Falkowski M, Gardina P, et al. CYP4F2 genetic variant alters required warfarin dose. *Blood*. 2008;111(8):4106-12. doi:10.1182/blood-2007-11-122010.

16. Dumaual C, Miao X, Daly TM, Bruckner C, Njau R, Fu DJ, et al. Comprehensive assessment of metabolic enzyme and transporter genes using the Affymetrix Targeted Genotyping System. *Pharmacogenomics*. 2007;8(3):293-305. doi:10.2217/14622416.8.3.293.
17. Affymetrix®. White Paper: DMET™ Plus allele translation reports: Summary of comprehensive drug disposition genotyping into commonly recognized allele names 2012 [cited 2020 06 Jan]; Available from: [http://tools.thermofisher.com/content/sfs/brochures/dmet\\_plus\\_translation.pdf](http://tools.thermofisher.com/content/sfs/brochures/dmet_plus_translation.pdf)
18. Burmester JK, Sedova M, Shapero MH, Mansfield E. DMET microarray technology for pharmacogenomics-based personalized medicine. *Methods Mol Biol*. 2010;632:99-124. doi:10.1007/978-1-60761-663-4\_7.
19. Sissung TM, English BC, Venzon D, Figg WD, Deeken JF. Clinical pharmacology and pharmacogenetics in a genomics era: the DMET platform. *Pharmacogenomics*. 2010;11(1):89-103. doi:10.2217/pgs.09.154.
20. Deeken J. The Affymetrix DMET platform and pharmacogenetics in drug development. *Curr Opin Mol Ther*. 2009;11(3):260-8.
21. Keizer RJ, Jansen RS, Rosing H, Thijssen B, Beijnen JH, Schellens JH, et al. Incorporation of concentration data below the limit of quantification in population pharmacokinetic analyses. *Pharmacol Res Perspect*. 2015;3(2):e00131. doi:10.1002/prp2.131.
22. Hecht M, Veigure R, Couchman L, CI SB, Standing JF, Takkis K, et al. Utilization of data below the analytical limit of quantitation in pharmacokinetic analysis and modeling: promoting interdisciplinary debate. *Bioanalysis*. 2018;10(15):1229-48. doi:10.4155/bio-2018-0078.
23. Jonsson EN, Karlsson MO. Automated covariate model building within NONMEM. *Pharm Res*. 1998;15(9):1463-8. doi:10.1023/a:1011970125687.
24. Bergstrand M, Hooker AC, Wallin JE, Karlsson MO. Prediction-corrected visual predictive checks for diagnosing nonlinear mixed-effects models. *AAPS J*. 2011;13(2):143-51. doi:10.1208/s12248-011-9255-z.
25. Wang W, Hallow KM, James DA. A Tutorial on RxODE: Simulating Differential Equation Pharmacometric Models in R. *CPT Pharmacometrics Syst Pharmacol*. 2016;5(1):3-10. doi:10.1002/psp4.12052.
26. Koninklijke Nederlandse Maatschappij ter bevordering der Pharmacie. Mitotaan. 2019 [cited 2019 28 Aug]; Available from: [https://kennisbank.knmp.nl/article/Informatiorium\\_Medicamentorum/S1853.html](https://kennisbank.knmp.nl/article/Informatiorium_Medicamentorum/S1853.html)
27. Whirl-Carrillo M, McDonagh EM, Hebert JM, Gong L, Sangkuhl K, Thorn CF, et al. Pharmacogenomics knowledge for personalized medicine. *Clin Pharmacol Ther*. 2012;92(4):414-7. doi:10.1038/clpt.2012.96.
28. PharmGKB. rs4244285, Variant annotation. [cited 2019 28 Aug]; Available from: <https://www.pharmgkb.org/variant/PA166154053/variantAnnotation>
29. PharmGKB. rs7311358, Clinical annotation. [cited 2019 28 Aug]; Available from: <https://www.pharmgkb.org/variant/PA166154602/clinicalAnnotation>
30. PharmGKB. rs4149117, Clinical annotation. [cited 2019 28 Aug]; Available from: <https://www.pharmgkb.org/variant/PA166154583/clinicalAnnotation>

## Online Resource 6.1: Supplementary methods, figures and tables

### Supplementary population PK analysis methods

One-, two- and three-compartment models, with first-order absorption and first-order elimination, were explored as the structural model. Relative standard error (RSE) of parameters, which represent the precision of parameter estimates, and the objective function value (OFV) were considered when evaluating the structural models. The one with acceptable RSE and lower OFV was selected as the final basic model structure.

Inter-individual variability (IIV) of parameters were estimated with Eq. 6.1, where  $P_i$  represents the parameter of  $i$ th individual and was assumed to be log-normally distributed,  $P_t$  represents typical value of the parameter, and  $\eta_{IIV}$  represents the random IIV which was assumed to be normally distributed with mean of 0 and variance of  $\omega_i^2$ . In addition, inter-occasion variability (IOV), which reflects the intra-individual variability, of apparent systematic clearance (CL/F) was also included when analyzing the full dataset. As is shown in Eq. S6.1,  $\eta_{IOV}$  represents the random IOV. The distribution of  $\eta_{IOV}$  in each occasion was assumed to be similar and normally distributed with mean of 0 and variance of  $\omega_2^2$ . In this study, every 200 days of treatment was defined as an occasion as the total observation periods of the patients were long.

The residual error was characterized with a combined proportional and additive model as is shown in Eq. S6.2, where  $Obs$  represents observations,  $IPRED$  represents individual predictions, and  $\varepsilon_1$  and  $\varepsilon_2$  represent the proportional residual error and additive residual error respectively which were assumed to be normally distributed with mean of 0 and variance of  $\sigma_1^2$  and  $\sigma_2^2$ , respectively.

$$P_i = P_t \cdot e^{\eta_{IIVi} + \eta_{IOV}} \quad \text{Eq. S6.1}$$

$$Obs = IPRED \cdot (1 + \varepsilon_1) + \varepsilon_2 \quad \text{Eq. S6.2}$$

As for the covariate analysis, the identified SNPs, as well as patients' demographic information and clinical characteristics were considered. For continuous covariates, for each patient the mean values of all measurements during the monitoring period were taken. In case of missing continuous covariates, the corresponding median value of all patients was assigned. For patients who only missed HT but not WT, LBW was calculated using real WT and imputed HT. For GFR, 0 (normal) was assigned if  $\geq 50\%$  of the collected patient's records were 0 otherwise 1 was assigned. Patients who missed GFR measurements, 0 was assigned.

The effect of all above covariates on mitotane CL/F and the effect of WT, LBW, FAT, and gender on apparent distribution volumes (V/F) were investigated using stepwise covariate modelling (SCM) function implemented with Perl-Speaks-NONMEM (version 4.7.0) [1]. Both a forward inclusion ( $p < 0.05$ ) and a backward elimination process ( $p < 0.01$ ) were performed to identify significant covariates. For SNPs that were in 100% linkage disequilibrium, if they were included during the SCM analysis, the more clinically relevant ones would be selected in the final model. The effects of continuous covariates were investigated with both linear relation (Eq. S6.3) and power relation (Eq. S6.4), where  $P_i$  represents the parameter of  $i$ th individual,  $P_t$  represents typical value of the parameter, and  $\eta_i$  represents the individual variability,  $\theta_{cov}$  represents the estimate of covariate effect,  $COV_i$  represents the covariate value of  $i$ th individual,  $COV_m$  is the median value of the covariate. Categorical covariates were analyzed with Eq. S6.5, where  $\theta_{cov}$  was set as 1 for reference category and was estimated for other categories.

$$P_i = P_t \cdot (1 \pm \theta_{cov} \cdot (COV_i - COV_m)) \cdot e^{\eta_i} \quad \text{Eq. S6.3}$$

$$P_i = P_t \cdot \left(\frac{COV_i}{COV_m}\right)^{\theta_{cov}} \cdot e^{\eta_i} \quad \text{Eq. S6.4}$$

$$P_i = P_t \cdot \theta_{cov} \cdot e^{\eta_i} \quad \text{Eq. S6.5}$$

### **Supplementary model evaluation methods**

pcVPC was performed by 1000 times of simulation and the data points, 5<sup>th</sup>, 50<sup>th</sup>, and 95<sup>th</sup> percentiles of prediction-corrected observations were plotted together with 95% confidence intervals (CI) of 5<sup>th</sup>, 50<sup>th</sup>, and 95<sup>th</sup> percentiles of simulations. NPDE evaluation was performed with npde package (version 2.0) implemented in R statistics software based on 1000 times of simulations. The bootstrap was conducted by 1000 runs of bootstrap replicates sampled from original dataset with replacement, which was stratified on whether the subject contributed more than two data points after the end of treatment. The median as well as 95% CI of parameters were derived and compared with original parameter estimates.

### **Supplementary simulation method**

Based on the final model structure, simulations were performed to evaluate different designed treatment strategies and approaches of starting dose determination. Patients were assumed to receive treatment as long as their last mitotane concentration monitoring time. The blood samples were assumed to be collected once every 2 weeks after knowing the result of the last sample, and the concentration of mitotane was assumed to be known 7 days after blood collection, which is in accordance with the optimal scenario in the clinical practice. The dose amount was subsequently adjusted accordingly.

As a comparison, a previous recommended 'high-dose' starting regimens, where the mitotane dose starts with 1.5 g per day and increases up to 6 g per day in 4 days, were simulated (**Regimen 1**) [2].

As for the newly designed regimens, the starting dose was 1) set as 2 g, 4 g, or 6 g for all patients according to the guideline [3] (**Regimen 2, 4, and 6**) or 2) set individually considering patients' characteristics with the help of the model (**Regimen 3, 5, 7, and 8**). As the expected time to reach the therapeutic target of mitotane is 3 to 5 months, the individually starting daily mitotane dose was estimated as the dose that allows the predicted mitotane concentrations on day 98 ( $C_{\text{sim\_pred98}}$ ) reach the therapeutic target. The  $C_{\text{sim\_pred98}}$  was obtained by performing simulation under a regimen of 6 g per day increasing by 0 g (**Regimen 8**), 0.5 g (**Regimen 2, 3, 4, 5, 6–1, and 7–1**), or 1 g (**Regimen 6–2 and 7–2**) once every 21 days till the 98<sup>th</sup> day of treatment, with only typical parameter values and covariate effects considered. Given the linear PK feature of mitotane, the suggested starting daily dose (*Dose*) was therefore determined by Eqs. S6.6 and S6.7, where  $[X]$  represents the least integer greater than or equal to  $X$ ,  $[X]$  represents the greatest integer less than or equal to  $X$ . Determining the starting dose based on the  $C_{\text{sim\_pred}}$  on day 77 and 119 were also used for comparison.

$$X = \frac{14 \text{ mg/L}}{C_{\text{sim\_pred}}} \cdot 6\text{g} \quad \text{Eq. S6.6}$$

$$Dose = \begin{cases} [X], & X - [X] > 0.650 \\ [X] + 0.5, & 0.350 \leq X - [X] \leq 0.650 \\ [X], & X - [X] < 0.350 \end{cases} \quad \text{Eq. S6.7}$$

Besides the above regimens, since individual parameters could be estimated after knowing one TDM result, **Regimen 9** was also designed and evaluated. In this strategy, patients were assumed to start with 4 g per day until the first TDM result was obtained.  $C_{\text{sim\_real}}$  of each patient on day 14 was simulated, based on which the  $\eta_{\text{HVi}}$  and  $\eta_{\text{IOVi}}$  were estimated for each patient using NONMEM with the POSTHOC function. Subsequently, the next daily dose of each patient was determined with Eqs. S6.6–S6.7 according to the individual  $C_{\text{sim\_pred98}}$  ( $C_{\text{sim\_pred98}}$ ) under the daily dosing of 6 g, based on the model incorporating  $\eta_{\text{HVi}}$  as was suggested in a previous study [4]. The constant starting regimen was applied in this regimen.

In **Regimen 2 to 8**, the dose increasing amount when  $C_{\text{sim\_real}} < 14 \text{ mg/L}$  was set differently before and after the target was reached (starting and maintenance regimen), in order to limit the toxicity at start and maintain the mitotane trough concentration within the therapeutic range at a later phase. The combination of 0 g/1.5 g, 0.5 g/1.5 g, 0.5 g/1 g, and 1 g/1.5 g were simulated and evaluated. **Regimen 2 to 7** applied stepwise increasing starting regimen and **Regimen 8** applied constant starting regimen. A maximum number of days

that follows the starting regimen was set as 126 (around 4 months) and 105 (98+7 days) for the stepwise increasing or constant starting regimens, respectively.

When  $C_{\text{sim\_real}}$  reached 20 mg/L, a 50% dose reduction was suggested in **Regimen 1**. In comparison, both fixed dose amount reduction (3 g or 4 g) and 50% reduction were evaluated in the newly designed regimens (**Regimen 2 to 9**). If a reduction resulted in a dose level lower than 0 g, then 0 g was applied. Besides, an additional concentration threshold of dose reduction, 18 mg/L, with 1 g dose reduction was introduced in **Regimen 2 to 9**, since a 7-day period of no dose adjustment presented.

## Supplementary References

1. Jonsson EN, Karlsson MO. Automated covariate model building within NONMEM. *Pharm Res*. 1998;15(9):1463-8. doi:10.1023/a:1011970125687.
2. Kerkhofs TM, Baudin E, Terzolo M, Allolio B, Chadarevian R, Mueller HH, et al. Comparison of two mitotane starting dose regimens in patients with advanced adrenocortical carcinoma. *J Clin Endocrinol Metab*. 2013;98(12):4759-67. doi:10.1210/jc.2013-2281
3. Koninklijke Nederlandse Maatschappij ter bevordering der Pharmacie. Mitotaan. 2019 [cited 2019 28 Aug]; Available from: [https://kennisbank.knmp.nl/article/Informatorium\\_Medicamentorum/S1853.html](https://kennisbank.knmp.nl/article/Informatorium_Medicamentorum/S1853.html).
4. Abrantes JA, Jonsson S, Karlsson MO, Nielsen EI. Handling interoccasion variability in model-based dose individualization using therapeutic drug monitoring data. *British journal of clinical pharmacology*. 2019;85(6):1326-36. doi:10.1111/bcp.13901.

## Supplementary Tables

**Table S6.1:** Potential SNPs out of the 959 SNPs that are correlated to mitotane clearance based on the association analysis

|    | Gene           | Common name                           | dbSNPRs.ID | P value |
|----|----------------|---------------------------------------|------------|---------|
| 1  | <i>CYP2C18</i> | <i>CYP2C18_c.1154C&gt;T(T385M)</i>    | rs2281891  | 0.020   |
| 2  | <i>CYP2C19</i> | <i>CYP2C19*2_19154G&gt;A(P227P)</i>   | rs4244285  | 0.020   |
| 3  | <i>SLCO1B3</i> | <i>SLCO1B3_c.334G&gt;T(A112S)</i>     | rs4149117  | 0.027   |
| 4  | <i>SLCO1B3</i> | <i>SLCO1B3_c.699A&gt;G(I233M)</i>     | rs7311358  | 0.027   |
| 5  | <i>SLCO1B3</i> | <i>SLCO1B3_c.1557G&gt;A(A519A)</i>    | rs2053098  | 0.027   |
| 6  | <i>SLCO1B1</i> | <i>SLCO1B1_c.571T&gt;C(L191L)</i>     | rs4149057  | 0.020   |
| 7  | <i>VKORC1</i>  | <i>VKORC1_c.*134G&gt;A(3'UTR)</i>     | rs7294     | 0.050   |
| 8  | <i>VKORC1</i>  | <i>VKORC1_c.283+124G&gt;C</i>         | rs8050894  | 0.030   |
| 9  | <i>VKORC1</i>  | <i>VKORC1_c.174-136C&gt;T</i>         | rs9934438  | 0.030   |
| 10 | <i>VKORC1</i>  | <i>VKORC1_c.-1639G&gt;A(Promoter)</i> | rs9923231  | 0.030   |
| 11 | <i>UGT1A6</i>  | <i>UGT1A6_c.315A&gt;G(L105L)</i>      | rs1105880  | 0.042   |

**Table S6.2:** Additional potential SNPs that are correlated to mitotane clearance based on the association analysis, if the pre-set selection based on a translation file as recommended by Affymetrics® was not considered

|   | Gene            | Common name                       | dbSNPRs.ID | P value |
|---|-----------------|-----------------------------------|------------|---------|
| 1 | <i>CA5P</i>     | <i>CA5P_A&gt;G(rs11859842)</i>    | rs11859842 | 0.029   |
| 2 | <i>SLC16A1</i>  | <i>SLC16A1_c.*1942T&gt;C</i>      | rs9429505  | 0.0067  |
| 3 | <i>CHST10</i>   | <i>CHST10_c.*381G&gt;A</i>        | rs1530031  | 0.040   |
| 4 | <i>CYP20A1</i>  | <i>CYP20A1_50767C&gt;T(L346F)</i> | rs1048013  | 0.014   |
| 5 | <i>SLC22A13</i> | <i>SLC22A13_c.*8336G&gt;A</i>     | rs4679028  | 0.032   |
| 6 | <i>UGT2A1</i>   | <i>UGT2A1_c.1305-109A&gt;C</i>    | rs2288741  | 0.042   |
| 7 | <i>ADH6</i>     | <i>ADH6_c.-930T&gt;C</i>          | rs10002894 | 0.012   |
| 8 | <i>ADH6</i>     | <i>ADH6_c.-2874T&gt;C</i>         | rs6830685  | 0.012   |
| 9 | <i>SLCO5A1</i>  | <i>SLCO5A1_c.97C&gt;T(L33F)</i>   | rs3750266  | 0.015   |

## Supplementary Figures

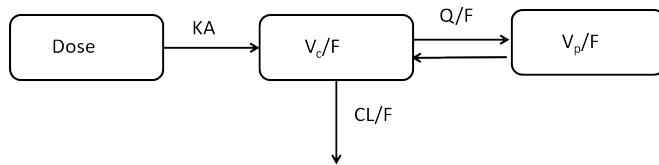


**Figure S6.1:** The population PK model structure of mitotane. CL/F represents apparent system clearance, KA represents absorption rate constant,  $V_c/F$  represents apparent distribution volume of central compartment,  $V_p/F$  represents apparent distribution volume of peripheral compartment, Q/F represents apparent distribution rate constant.

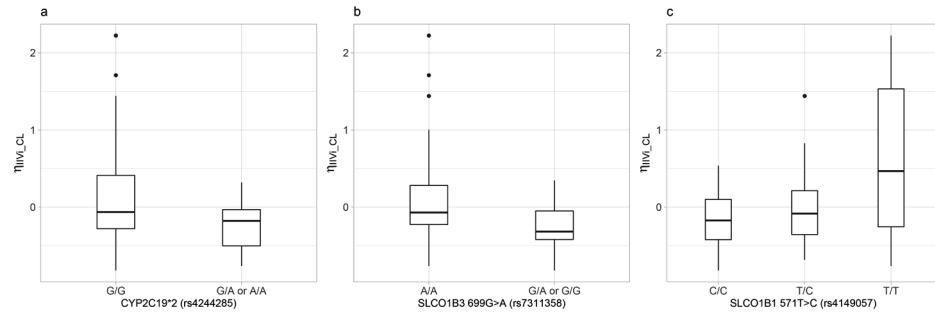


**Figure S6.2:** The boxplots of estimated  $\eta_{INV_{CL}}$  in each genotype group of SNP **(a)** CYP2C19\*2 (rs4244285), **(b)** SLCO1B3 699A>G (rs7311358), and **(c)** SLCO1B1 571T>C (rs4149057).

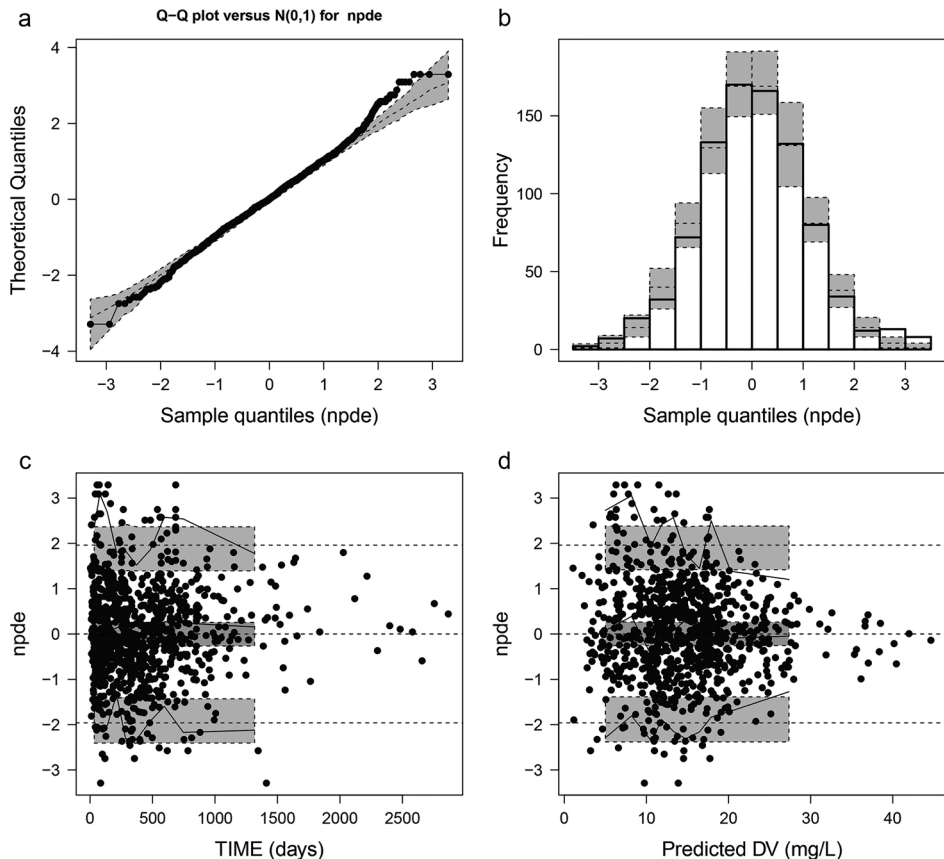


**Figure S6.3:** Normalized prediction distribution error (NPDE) results of the final population PK model of mitotane in patients with ACC, including the quantile–quantile plot (a), the distribution histogram of NPDE (b), and the NPDE versus time (c) and population predictions (d). The NPDE results are shown to distribute around a mean of 0.03616 with a variance of 1.134.

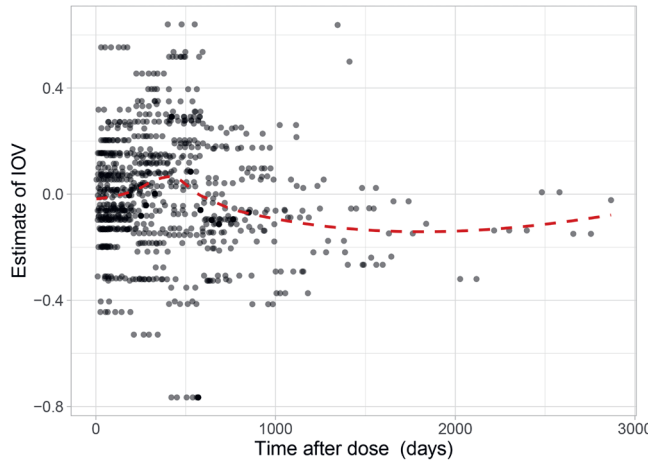


**Figure S6.4:** The estimates of inter-occasion variability (IOV) over time. Red dashed lines represent loess regression result.

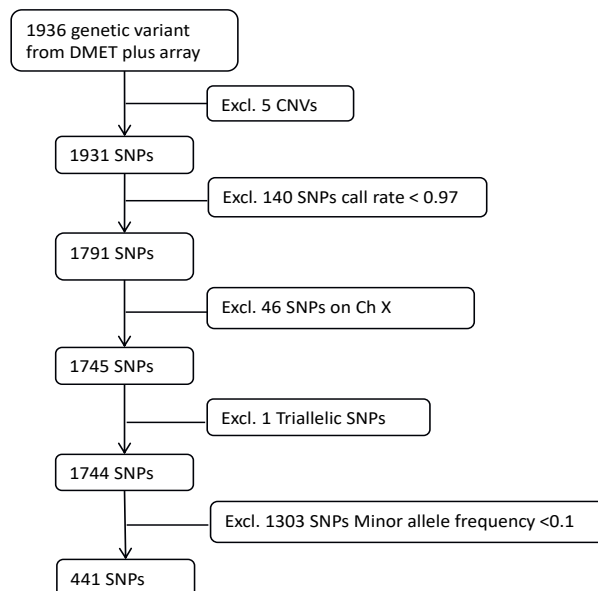


**Figure S6.5:** Flow diagram of the genetic variants selection if the pre-set selection based on a translation file as recommended by Affymetrics® was not considered. Excl. represents excluding, Ch X represents chromosome X, DMET™ represent Drug Metabolizing Enzymes and Transporters, CNVs represents copy number variations.

## Online Resource 6.2: Shiny app establishing method and results

### Shiny app establishment

Based on the final mitotane population pharmacokinetic model, a Shiny app was established for the simulation for a random patient and to elucidate an example of the model application on guiding treatment for a new patient. Package shiny (version 1.4.0) and RxODE (version 0.6-1) in R statistics software (version 3.4.2; R Foundation for Statistical Computing, Vienna, Austria) were utilized. The R script can be found through: <https://github.com/AnyueYin/Shiny-app-script-for-model-simulation---Population-PK-and-PG-analysis-of-mitotane>. Patient gender, weight, and height, which were used to estimate lean body weight (LBW) and fat amount (FAT), as well as the results of three SNPs were in the input panel, based on which the starting dose was suggested. One hundred times of simulation under an optimized mitotane treatment regimen, Regimen 5-(– 4 g), were performed given the input information. The 90% prediction interval, 50<sup>th</sup> percentile of the predictions, target reaching time, and suggested starting dose were plotted in the output figure. The residual errors were not considered in the simulation.

Screen shots of the developed shiny app is shown in **Figure S6.6**. The result shows that for a male patient with 85 kg weight and 180 cm height who carries G/G, A/A, and T/C for *CYP2C19\*2* (rs4244285), *SLCO1B3* 699A>G (rs7311358), and *SLCO1B1* 571T>C (rs4149057), respectively, the 90% prediction interval can nicely locate within the therapeutic window of mitotane. The starting dose was suggested as 5.5 g per day and the 50<sup>th</sup> percentile of the predictions reached the target on day 92. If the genotype result of *CYP2C19\*2* (rs4244285) changed to G/A, the suggested starting dose became 4 g per day and the 50<sup>th</sup> percentile of the predictions reached the target on day 94.

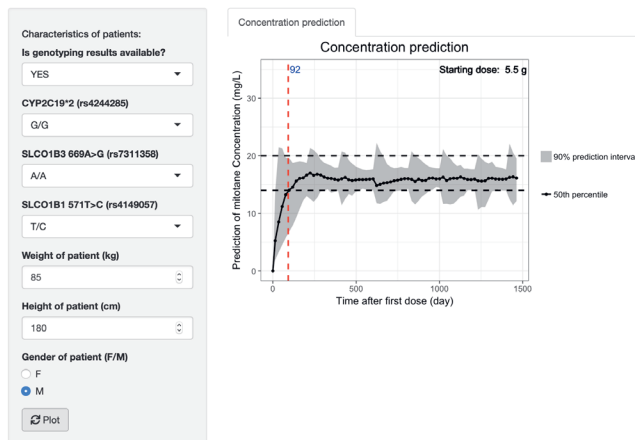
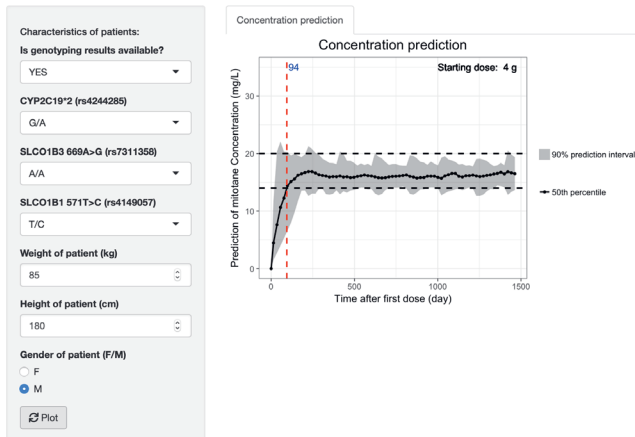
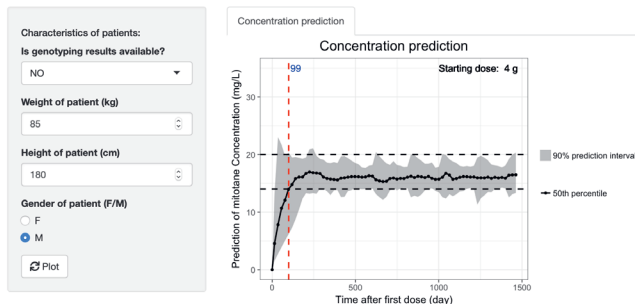
In addition, a model with FAT effect on central distribution volume as the only covariate (**Table S6.3**) was also built in the Shiny app as an alternative option to allow dosing advice and concentration prediction for patients when genotyping results are not available (**Figure S6.6c**).

**Table S6.3:** Parameter estimates of the final model without genotyping results as covariates

| Parameters         | Final model     |                          |                        |
|--------------------|-----------------|--------------------------|------------------------|
|                    | Estimate (RSE%) | IIV (CV%) [shrinkage, %] | IOV <sup>a</sup> (CV%) |
| KA (/day)          | 15.0 fixed      | -                        | -                      |
| CL/F (L/day)       | 217 (9)         | 66.3 [7]                 | 31.2                   |
| $V_c/F$ (L)        | 8450 (16)       | 63.5 [37]                | -                      |
| $V_c$ -FAT (power) | 1.12 (18)       | -                        | -                      |
| $V_p/F$ (L)        | 15500 (15)      | 80.4 [36]                | -                      |
| Q/F (/day)         | 609 (28)        | 100.5 [38]               | -                      |
| Residual errors    |                 |                          |                        |
| PRO (CV%)          | 16.7 (6)        | -                        | -                      |
| ADD (mg/L)         | 0.907 (16)      | -                        | -                      |

FAT, fat amount; RSE, relative standard error; CV, coefficient of variation; IIV, inter-individual variability; IOV, inter-occasion variability; PRO, proportional residual error; ADD, additive residual error; CL/F, apparent system clearance; KA, absorption rate constant;  $V_c/F$ , apparent distribution volume of central compartment;  $V_p/F$ , apparent distribution volume of peripheral compartment; Q/F, apparent distribution rate constant.

<sup>a</sup> Every 200 days of dosing was defined as an occasion.

**a Mitotane****b Mitotane****c Mitotane**

**Figure S6.6:** Screen shot of the shiny app established based on the final model. **(a)** A male patient with 85 kg weight and 180 cm height who carries G/G, A/A, and T/C for *CYP2C19\*2* (rs4244285), *SLCO1B3 699A>G* (rs7311358), and *SLCO1B1 571T>C* (rs4149057), respectively. **(b)** A male patient with 85 kg weight and 180 cm height who carries G/A, A/A, and T/C for *CYP2C19\*2* (rs4244285), *SLCO1B3 699A>G* (rs7311358), and *SLCO1B1 571T>C* (rs4149057), respectively. **(c)** A male patient with 85 kg weight and 180 cm height whose genotyping results are unknown.

**Online Resource 6.3: List of 959 SNPs from DMET™ array of which the genotyping results were obtained for each patient**

The online version of this article (<https://doi.org/10.1007/s40262-020-00913-y>) contains this supplementary material, which is available to authorized users.





# Chapter 7

## **Population pharmacokinetic and toxicity analysis of high-dose methotrexate in patients with central nervous system lymphoma**

Anyue Yin, Fleur A. de Groot, Henk-Jan Guchelaar, Marcel Nijland,  
Jeanette K. Doorduijn, Daan J. Touw, Thijs Oude Munnink, Brenda C.M. de Winter,  
Lena E. Friberg, Joost S.P. Vermaat, Dirk Jan A.R. Moes



*In preparation*

## Abstract

**Background:** High-dose methotrexate (HD-MTX) based polychemotherapy is widely used for patients with central nervous system (CNS) lymphoma. The pharmacokinetic (PK) variability and unpredictable occurrence of toxicity remain major concerns in HD-MTX treatment.

**Objectives:** This study aimed to characterize the population PK of HD-MTX in patients with CNS lymphoma and to identify baseline predictors and exposure thresholds that predict a high risk of renal and hepatotoxicity.

**Methods:** Routinely monitored serum MTX concentrations after intravenous infusion of HD-MTX and MTX dosing information were collected retrospectively. Acute event of toxicity was defined according to the Common Terminology Criteria for Adverse Events (CTCAE) version 5.0. A population PK model was developed in NONMEM. Toxicity data were analyzed using a logistic regression model and potential baseline and exposure-related predictors were investigated.

**Results:** In total 1584 MTX concentrations from 110 patients were available for the analysis. A two-compartment population PK model adequately described the data. Estimated glomerular filtration rate (eGFR), treatment regimen, albumin, alkaline phosphatase, and body weight were identified as significant covariates that explain PK variability of HD-MTX. Baseline eGFR and sex were identified as significant predictors for renal toxicity, and MTX dose ( $\text{mg}/\text{m}^2$ ) was the strongest predictor for hepatotoxicity. The MTX area under the concentration-time curve ( $\text{AUC}_{24\text{-}\infty}$ ) and concentration at 24 hours ( $C_{24\text{h}}$ ) showed to correlate with renal toxicity only, and  $\text{AUC}_{24\text{-}\infty} > 109.5 \mu\text{mol}/\text{L}\cdot\text{h}$  and  $C_{24\text{h}} > 8.64 \mu\text{mol}/\text{L}$  were potential exposure thresholds predicting a high risk.

**Conclusion:** A population PK model was developed for HD-MTX in patients with CNS lymphoma. The toxicity analysis showed that low baseline eGFR and male sex, and high MTX dose are associated with increased risk of acute renal and hepatotoxicity, respectively.  $\text{AUC}_{24\text{-}\infty} > 109.5 \mu\text{mol}/\text{L}\cdot\text{h}$  and  $C_{24\text{h}} > 8.64 \mu\text{mol}/\text{L}$  were potential exposure thresholds predicting a high risk of renal toxicity. The models hold the potential to guide HD-MTX dosage individualization and better prevent acute toxicity.

## 1. Introduction

High-dose methotrexate (HD-MTX)-based polychemotherapy is the standard therapy for patients with primary central nervous system (CNS) lymphoma [1, 2]. It is also widely used for patients with secondary CNS involvement of diffuse large B-cell lymphoma (DLBCL), mainly for those who are naive for HD-MTX [3].

The standard dose of HD-MTX for patients with CNS lymphoma is 3 g/m<sup>2</sup> and is administered by intravenous infusion. Methotrexate (MTX) has approximately 50% protein binding and is eliminated primarily unchanged by renal excretion (> 80%) while a small fraction is eliminated as an metabolite 7-hydroxymethotrexate [4, 5].

In routine HD-MTX treatment, MTX concentrations are monitored after each administration until they reach a safe target (< 0.2  $\mu$ M). Although HD-MTX dose is based on patients' body surface area (BSA), significant inter- and intra-individual variability in its pharmacokinetics (PK) is observed [6-8]. Delayed elimination of MTX due to impaired renal function or extravascular fluid collections can occur which will result in a prolonged period of MTX exposure and a higher risk of toxicity [4, 7, 8]. Furthermore, the unpredictable occurrence of acute toxicity during HD-MTX treatment, including kidney dysfunction and hepatotoxicity, may result in treatment interruption or delay which could cause unfavorable treatment outcome [6, 7]. To improve the outcomes of HD-MTX therapy, further individualizing HD-MTX dosage and identifying factors that predict a high risk of HD-MTX induced toxicity are desired.

The risk factors that have been identified for HD-MTX induced renal toxicity in patients with lymphoid or hematological malignancy are mostly dose- or exposure-related: doses  $\geq$  6 g/m<sup>2</sup>, area under the concentration-time curve (AUC) in the first administration cycle, and dose-normalized concentration at 24 and 48 hours [9-11]. For HD-MTX induced hepatotoxicity, studies on risk factors are limited but one study suggested that AUC of HD-MTX is associated with hepatotoxicity [12]. Yet, an exposure threshold for toxicity which would facilitate better supportive care and treatment individualization for HD-MTX is still missing. Moreover, the predictors at baseline for HD-MTX induced toxicities are less studied. One study showed that baseline lactate dehydrogenase and albumin correlated with the risk of acute kidney injury [13]. Further exploration of potential risk factors at baseline for both renal and hepatotoxicity would therefore be beneficial to guide HD-MTX therapy.

Population PK-pharmacodynamic (PD) modeling with mixed-effect models enables to quantitatively characterize as well as predict drug PK, response, or toxicity profiles and their relationships in both population and individual levels. This approach also enables

identification of covariates that explain the observed inter- and intra-individual variabilities [14]. Combined with simulations, the developed model can be applied to guide treatment rationally [15]. Until now, several population PK models of HD-MTX in patients with lymphoid malignancy have been published but many were not specifically focused on patients with CNS lymphoma [8, 10, 12, 16-21]. Subsequent toxicity analysis of HD-MTX for patients with CNS lymphoma with a model-based approach is still lacking.

In the current study, based on retrospectively collected data, we performed a population PK analysis to characterize HD-MTX PK in patients with CNS lymphoma who received various treatment regimens, and explored covariates that explain the variability. Subsequently, the occurrence of acute renal and hepatotoxicity were analyzed with a model-based approach which aims to identify baseline predictors and exposure threshold that predict a high risk of toxicity for each HD-MTX administration cycle.

## 2. Method

### 2.1 Patients and data

Patients who were diagnosed with CNS lymphoma, treated with HD-MTX based polychemotherapy with available dosing information and MTX concentrations in the period ranging from 2010 to March 2021 from the Leiden University Medical Center (LUMC), Erasmus Medical Center (EMC), and University Medical Center Groningen (UMCG) were included. Patients received HD-MTX by intravenous infusion and were dosed per body surface area (BSA). All medications that have potential drug-drug interaction with MTX (e.g. benzimidazoles and nonsteroidal anti-inflammatory drugs (NSAIDs)) were stopped 72 hours prior to the use of HD-MTX.

The routinely monitored MTX concentrations were retrospectively collected from the laboratory information system (LIS). MTX concentrations were analyzed with ARK™ assay [22] with a lower limit of quantification (LLOQ) of 18.2 µg/L (0.04 µmol/L) in the LUMC and the EMC and 15 µg/L in the UMCG. If the detected MTX was above 50 µmol/L at 24 hours, or above 5 µmol/L at 48 hours, or above 0.2 µmol/L at 72 hours after administration of HD-MTX, it was defined as delayed elimination [4]. Patients' demographic characteristics, drug dosing information (i.e. treatment regimen, infusion hours, and dose), and laboratory results (i.e. serum creatinine (SCr), alkaline phosphatase (ALP), aspartate aminotransferase (ASAT), alanine aminotransferase (ALAT), albumin, bilirubin) were collected from patients' electronic health care records. Based on the available data, estimated glomerular filtration rate (eGFR) was also estimated with the CKD-EPI creatinine equation and included in the analysis [23].

This study is approved by the local Ethical Committee of each institute (number G20.126), and did not fall within the scope of the WMO (Medical Scientific Research Act). A waiver for informed consent was granted. All performed procedures were in accordance with the ethical standards of the institutional medical ethical committee and the 1964 Declaration of Helsinki and its later amendments.

## 2.2 Population PK modeling

A population PK model was developed based on the available MTX PK data. The unit of MTX concentrations was unified to  $\mu\text{g/L}$  by multiplying the data reported in  $\mu\text{mol/L}$  by the molar mass of MTX (454.44 g/mol). The data that were below LLOQ were omitted from the analysis due to the small proportion (< 10%) [24].

One-, two- and three-compartment models with first-order elimination were explored as the structural model. Parameters were assumed to be log-normally distributed and inter-individual variability (IIV) was quantified. Inter-occasion variability (IOV) was incorporated on the PK parameter clearance (CL) to account for the intra-individual variability, and each administration cycle was defined as an occasion. A combined proportional and additive error model was applied to characterize the residual errors. The residual errors of data from different medical centers were set to follow the same distribution. The structural model was selected based on goodness-of-fit (GOF), objective function value (OFV) and the stability of the model.

Subsequently, the covariate effects of patients' demographic information, treatment regimen, time-varying laboratory results on CL, and body size related characteristics on volumes of distribution were investigated. The stepwise covariate modelling (SCM) function was applied with assistance of Perl-speaks NONMEM (version 4.9) [25]. Model selection was based on a reduction in OFV assuming a  $\chi^2$  distribution, a reduction in IIV or IOV, and physiological plausibility. Both a forward inclusion ( $p < 0.05$ ,  $\Delta\text{OFV} < -3.84$ , degrees freedom = 1) and a backward elimination process ( $p < 0.01$ ,  $\Delta\text{OFV} > 6.64$ , degrees freedom = 1) were performed to identify significant covariates.

## 2.3 Toxicity analysis

At each HD-MTX administration cycle, the renal and hepatotoxicity were graded based on monitored SCr and ALAT results according to the NCI Common Terminology Criteria for Adverse Events (CTCAE) version 5.0, respectively [26]. The  $\geq$  grade 1 toxicity was defined as a toxicity event. The data were analyzed with a logistic regression model where the probability of having toxicity was estimated. The logit function is shown in Eqs. 7.1–7.3,

where  $base$  represents baseline logit score,  $\theta$  is the typical population probability operator,  $\eta_i$  represents the random IIV which was assumed to be normally distributed with mean of 0 and variance of  $\omega^2$ .

Individual PK parameters obtained from the final PK model were applied to simulate and estimate the MTX exposure metrics of interest: AUC between 24 hours after drug administration to infinity ( $AUC_{24-\infty}$ ) and MTX concentration at 24 hours ( $C_{24h}$ ). The  $AUC_{24-\infty}$  were estimated by integrating the individual concentration-time curves from 24 hours to last sample time plus AUC from the last sample time to infinity which was approximated as last concentration divided by terminal elimination rate constant ( $\beta$ ).

The baseline predictors and exposure-related predictors were investigated by being included linearly into the logit function (Eq. 7.4). The evaluated baseline factors include patients' demographic information, baseline eGFR, ALAT, ASAT, and albumin of each administration cycle, dose amount, treatment regimen, dose divided by baseline CL as an AUC approximation ( $AUC_{base}$ ) of each administration cycle,  $AUC_{24-\infty}$  from previous administration course ( $pAUC_{24-\infty}$ ), and  $C_{24h}$  from previous administration course ( $pC_{24h}$ ). The toxicity status in the previous administration course was also evaluated as a potential predictive factor. The inclusion of covariates was based on the reduction in OFV and physiological plausibility. A forward inclusion process was performed when investigating baseline predictors. Factors that result in a  $\Delta OFV < -3.84$  were considered to be significant ( $p < 0.05$ , degrees freedom = 1).

$$base = \ln \left( \frac{\theta}{1 - \theta} \right) \quad \text{Eq. 7.1}$$

$$logit_i = base + \sum_{k=1}^n E_{cov,k} + \eta_i \quad \text{Eq. 7.2}$$

$$P_i = \frac{e^{logit_i}}{1 - e^{logit_i}} \quad \text{Eq. 7.3}$$

$$E_{cov,k} = \begin{cases} \text{categorical: } \theta_{cov} \\ \text{continuous: } \left( \frac{COV}{median(COV)} \right)^{\theta_{cov}} \end{cases} \quad \text{Eq. 7.4}$$

## 2.4 Model evaluation

The final PK model was evaluated with GOF plots, prediction-corrected visual predictive check (pcVPC), and a bootstrap based on 1000 runs of replicated datasets sampled from original dataset with replacement.

The pcVPC plot was generated based on 1000 times of simulation. MTX concentrations were commonly monitored at 24 hours, 48 hours, and 72 hours, and thereafter every 24 hours after the start of infusion until the concentration was below a threshold. Consequently, patients with delayed elimination had a longer follow-up and more samples per patient. The same sampling strategy was applied when performing simulations for the pcVPC plot, i.e., if the simulated concentration after day 3 fell below 0.1  $\mu\text{mol/L}$ , the next data point would not be sampled. The set threshold of 0.1  $\mu\text{mol/L}$  is the median of the second last monitored concentration of the collected data after day 3.

The adequacy of the toxicity model was evaluated with a visual predictive check (VPC). The original dataset was simulated 500 times to derive the 90% prediction interval of the proportion of patients having toxicity at each administration cycle and over a range of covariate values. The prediction interval was compared with the observed results.

## 2.5 Software and estimation method

The population modelling analysis was performed with NONMEM (version 7.4.4, ICON Development Solutions, Ellicott City, MD, USA) aided with Perl-speaks-NONMEM (PsN) (version 4.9, Uppsala University, Uppsala, Sweden) [27]. Parameters of the population PK model were estimated using the first order conditional estimation method with interaction (FOCEI). Conditional Laplacian method was used to approximate the marginal likelihood in the toxicity analysis. Data management and plots generation were performed with R statistics software (version 4.2.1, R Foundation for Statistical Computing, Vienna, Austria).

# 3. Results

7

## 3.1 Patients and PK data

In total 110 patients with CNS lymphoma (56 males and 54 females) were included from the LUMC ( $n = 75$ ), the UMCG ( $n = 17$ ), and the EMC ( $n = 18$ ). Among the included patients, 80 patients (73%) were diagnosed with primary CNS lymphoma, 11 patients (10%) were diagnosed with secondary CNS lymphoma, and 11 patients (10%) had secondary CNS involvement of systemic DLBCL. The baseline characteristics of the included patients from 3 medical centers are shown in **Table 7.1**.

In total, 1584 monitored MTX concentrations from 412 administration cycles were collected, of which 124 (7.8%) were below the LLOQ and were omitted from the analysis.

**Table 7.1:** Baseline characteristics of the patients included in the current study

| Item  | N (%) / Median (Range) |                  |                  |
|---|------------------------|------------------|------------------|
| Center  | LUMC                   | UMCG             | EMC              |
| Number of patients                                | 75                     | 17               | 18               |
| Age (year)  | 66 (22–83)             | 66 (52–73)       | 67 (51–76)       |
| Sex   |                        |                  |                  |
| Male  | 42 (56%)               | 6 (35%)          | 8 (44%)          |
| Female  | 33 (44%)               | 11 (65%)         | 10 (56%)         |
| Body weight (kg)                                  | 78 (53.4–115)          | 76.5 (46.4–108)  | 70.1 (49.5–96.3) |
| Height (cm)                                       | 176 (155–195)          | 169 (158–192)    | 168 (148–186)    |
| Body mass index (kg/m <sup>2</sup> )              | 25.0 (17.6–38.0)       | 25.0 (17.9–35.4) | 23.7 (18.9–34.5) |
| Body surface area (m <sup>2</sup> )               | 1.94 (1.58–2.34)       | 1.94 (1.44–2.40) | 1.8 (1.41–2.05)  |
| ASAT (IU/L)                                       | 20 (9–100)             | 20.3 (10–53)     | 22.5 (14–58)     |
| ALAT (IU/L)                                       | 30.5 (9–286)           | 43 (16–213)      | 41 (13–215)      |
| SCr (μmol/L)                                      | 64 (37–125)            | 66 (43–94)       | 65 (45–98)       |
| eGFR (ml/(min*1.73 m <sup>2</sup> )) <sup>a</sup> | 93.8 (52.9–159)        | 89.3 (54–113)    | 90.3 (66.9–115)  |
| Albumin (g/L)                                     | 38.5 (28–49)           | 37.5 (32.5–45.4) | 40 (34–49)       |
| ALP (U/L)   | 67 (25–297)            | 60 (44–82)       | 62.5 (28–118)    |
| Bilirubin (μmol/L)                                | 8 (3–23)               | 7.7 (3–25.3)     | 8 (4–19)         |
| Disease type                                      |                        |                  |                  |
| PCNSL   | 45 (60%)               | 17 (100%)        | 18 (100%)        |
| SCNSL   | 11 (14.7%)             | 0                | 0                |
| Stage IV DLBCL with CNS involvement               | 11 (14.7%)             | 0                | 0                |
| Other lymphoma with CNS involvement <sup>b</sup>  | 8 (10.7%)              | 0                | 0                |
| Number of administration cycles per patient       | 4 (1–8)                | 4 (3–4)          | 4 (1–8)          |
| Dose of MTX (mg/m <sup>2</sup> )                  | 3000 (1500–8000)       | 3000 (1950–3000) | 3000 (1500–3200) |
| Treatment regimens <sup>c</sup>                   |                        |                  |                  |
| RMP   | 35 (46.7%)             | 0                | 0                |
| MATRIX  | 40 (53.3%)             | 0                | 0                |
| MBVP  | 0                      | 17 (100%)        | 18 (100%)        |

ALAT, alanine aminotransferase; ALP, alkaline phosphatase; ASAT, aspartate aminotransferase; CNS, central nervous system; DLBCL, diffuse large B-cell lymphoma; eGFR, estimated glomerular filtration rate; MTX, methotrexate; PCNSL, primary CNS lymphoma; SCNSL, secondary CNS lymphoma; SCr, serum creatinine.

<sup>a</sup> eGFR was estimated with the CKD-EPI creatinine equation.

<sup>b</sup> Including T cell lymphoma, Follicular lymphoma, and Burkitt lymphoma

<sup>c</sup> RMP, contains high-dose MTX (HD-MTX), rituximab and procarbazine; MATRIX, contains HD-MTX, high-dose cytarabine (HD-AraC), thiotapec, and rituximab; MBVP, contains HD-MTX, teniposide, carmustine, prednisolone, with or without rituximab or HD-AraC. Details can be found in Online Resource, Table S7.1.

The concentrations were monitored daily after the start of MTX infusion until the concentrations fell to a level below 0.2 μmol/L or the LLOQ. The median number of concentrations contributed by each patient to the analysis was 12, ranging from 2 to 35. The delayed elimination was observed in 47 (31.3%) patients and the longest follow-up time during one administration cycle was 454 hours. Five patients had a treatment interruption of more

than 2.5 months and their data before and after the interruption were treated as data from two separate subjects. This resulted in 115 subjects in the dataset eventually. The time-course of all collected MTX concentrations is shown in **Online Resource 7.1, Figure S7.1**.

The treatment regimen differs among medical centers (**Table 7.1, Online Resource 7.1, Table S7.1**). The LUMC patients were separated into 2 treatment groups. Older and/or less fit patients received HD-MTX with rituximab and procarbazine (RMP). For younger and fit patients (< 70 years old), HD-MTX was given with high-dose cytarabine (HD-AraC), thiotepa, and rituximab (MATRIX). As for the UMCG and the EMC patients, HD-MTX was administered with teniposide, carmustine, prednisolone, with or without rituximab or HD-AraC (MBVP). Details about the treatment regimens including infusion durations can be found in **Online Resource 7.1, Table S7.1**.

### 3.2 Population PK model

A two-compartment population PK model with first-order elimination provided the best fit to the obtained data in HD-MTX in patients with CNS lymphoma. Compared with the one-compartment model, the objective function value (OFV) of the two-compartment model was 1843.772 units lower ( $p < 0.01$ , degree of freedom = 4). Although the three-compartment model showed to further improve the model fit, the estimated relative standard errors (RSEs) of parameters indicated unreliable parameter estimates. Therefore, the two-compartment model was selected as the structural model.

The covariate analysis identified eGFR, treatment regimen, albumin, and ALP are significant covariates on CL of MTX ( $p < 0.01$ ). Body weight was a significant covariate on the volume of distribution of the central compartment (V1). The RSEs indicate an acceptable precision (< 40%) of most parameters except for the coefficient of ALP effect (**Table 7.2**). The typical MTX CL in patients in the RMP group was estimated to be 16.0 % lower than that in the MATRIX group, while the CL differences between the MATRIX and MBVP groups were not significant (**Table 7.2, Online Resource 7.1, Figure S7.2**). The coefficient of variation (CV%) of random IIV and IOV for CL decreased from 29.2% and 23.1% to 15.5% and 12.3%, respectively, after covariate inclusions. The inclusion of IIV on V<sub>1</sub> became insignificant after covariate inclusions and was therefore fixed to zero (OFV increased by 2.265). The estimated standard deviation (SD) of the additive residual error approached zero and was therefore fixed to 0.0001 µg/L.

The GOF plots in both normal and logarithmic scale showed that the model predictions were generally in good accordance with the observations, while the population predictions underpredicted the observations at lower concentrations (**Figure 7.1**). The deviations

between model predictions and observations were also observed when the concentrations were above 20,000 µg/L. However, when it was explored to remove these data points, the new parameter estimates were still within the estimated 95% confidence interval (CI) of the current parameter estimates. The conditional weighted residual errors (CWRES) were distributed around zero without obvious trends over time, but trends over population predictions at lower concentrations can be observed (Figure 7.1). The pcVPC plot demonstrated an adequate predictability of the model (Figure 7.2). The final parameter estimates were in good agreement with the bootstrap results (Table 7.2).

**Table 7.2:** Parameter estimates of the final population PK model of HD-MTX in patients with CNS lymphoma

|                  | Estimate (RSE) | IIV (CV%) (RSE%)<br>[shrinkage] | IOV (CV%)<br>(RSE%) | Bootstrap  |                    |
|------------------|----------------|---------------------------------|---------------------|------------|--------------------|
|                  |                |                                 |                     | Median     | 95% CI             |
| CL (L/h)         | 21.2 (13%)     | 15.5 (8%) [10%]                 | 12.3 (6%)           | 21.4       | [17.2, 27.2]       |
| $\theta_{eGFR}$  | 0.0104 (5%)    | -                               |                     | 0.0104     | [0.0093, 0.011]    |
| $\theta_{TREAT}$ |                |                                 |                     |            |                    |
| MATRIX           | 1              | -                               |                     | -          | -                  |
| RMP              | 0.840 (4%)     | -                               |                     | 0.839      | [0.772, 0.913]     |
| MBVP             | 1.03 (3%)      | -                               |                     | 1.03       | [0.952, 1.11]      |
| $\theta_{ALB}$   | 0.225 (28%)    | -                               |                     | 0.225      | [0.0715, 0.369]    |
| $\theta_{ALP}$   | -0.0624 (41%)  | -                               |                     | -0.0656    | [-0.115, -0.0186]  |
| $V_1$ (L)        | 125 (16%)      | 0 FIX                           |                     | 126.4      | [98.1, 172]        |
| $\theta_{WT}$    | 0.00370 (34%)  | -                               |                     | 0.00369    | [0.00127, 0.00629] |
| $V_2$ (L)        | 36.7 (27%)     | 55.7 (11%) [13%]                |                     | 38.1       | [23.9, 62.4]       |
| Q (L/h)          | 0.593 (21%)    | 30.2 (15%) [15%]                |                     | 0.605      | [0.418 0.920]      |
| Residual errors  |                |                                 |                     |            |                    |
| Prop. (CV%)      | 25.2% (4%)     | [18%] <sup>a</sup>              |                     | 25.0%      | [23.0%, 26.9%]     |
| Add. (SD, µg/L)  | 0.0001 FIX     | -                               |                     | 0.0001 FIX | -                  |

Add., additive residual error; ALB, albumin; ALP, alkaline phosphatase; CI, confidence interval; CL, clearance; CV, coefficient of variation; eGFR, estimated glomerular filtration rate; IIV, inter-individual variability; IOV, inter-occasion variability; Prop., proportional residual error; Q, distribution clearance; RSE, relative standard error; SD, standard deviation; V1, distribution volume of the central compartment; V2, distribution volume of the peripheral compartment; WT, weight; MATRIX, RMP, and MBVP, three different treatment regimens.

<sup>a</sup> Epsilon shrinkage.

$$V_{1i} = 125 * (1 + \theta_{WT} * (WT - 75.8)) * e^{\eta_i}$$

$$CL_i = 21.2 * (1 + \theta_{eGFR} * (eGFR - 82.93)) * \left(\frac{ALB}{37.31}\right)^{\theta_{ALB}} * \left(\frac{ALP}{73.81}\right)^{\theta_{ALP}} * \theta_{TREAT} * e^{\eta_i}$$

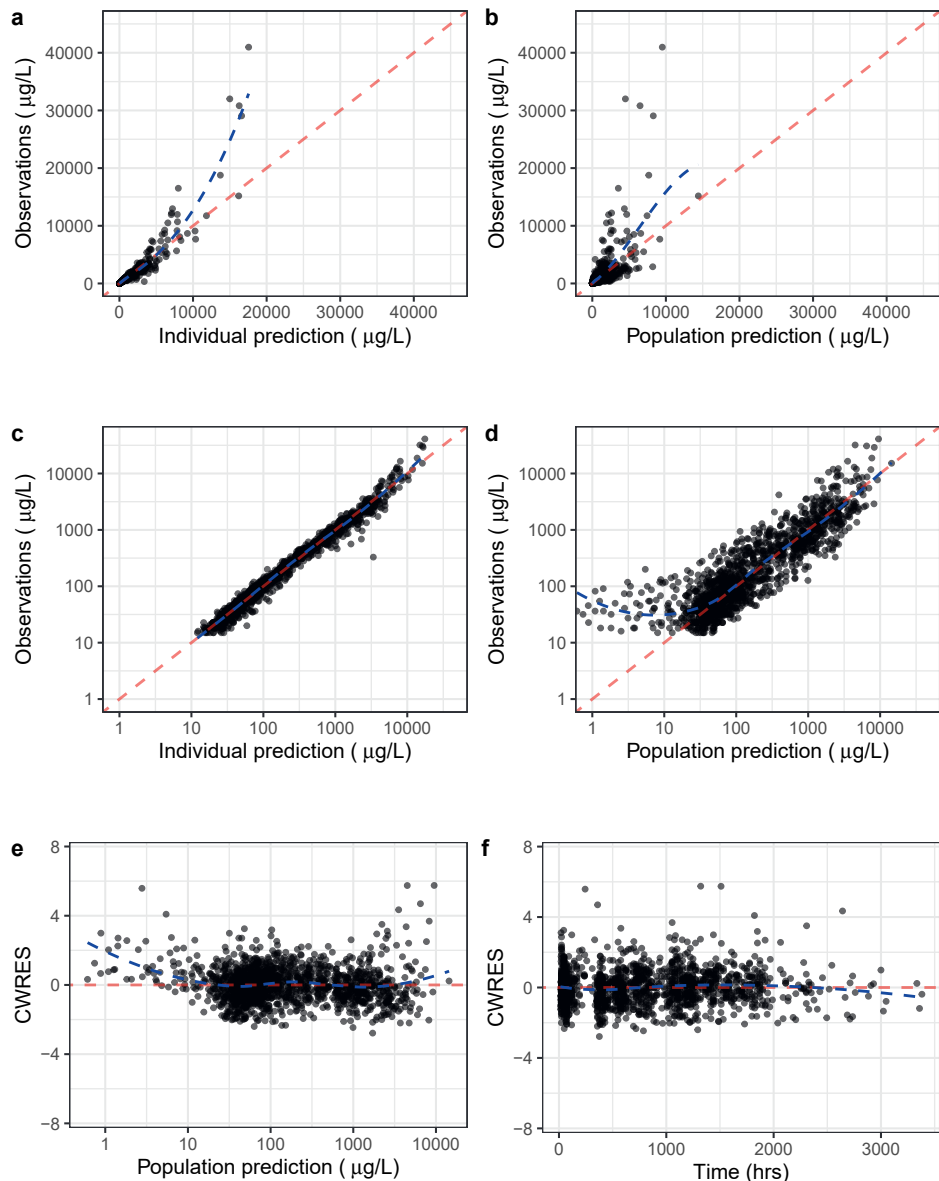


**Figure 7.1:** Goodness-of-fit plots of the developed population PK model, including observations versus individual predictions in both normal (a) and logarithmic scale (c), observations versus population predictions in both normal (b) and logarithmic scale (d), and conditional weighted residual errors (CWRES) versus populations predictions (e) and time after last dose (f). The red dashed lines represent  $y = x$  (a, b, c, d) and  $y = 0$  (e, f). Black dashed lines represent corresponding loess regressions.

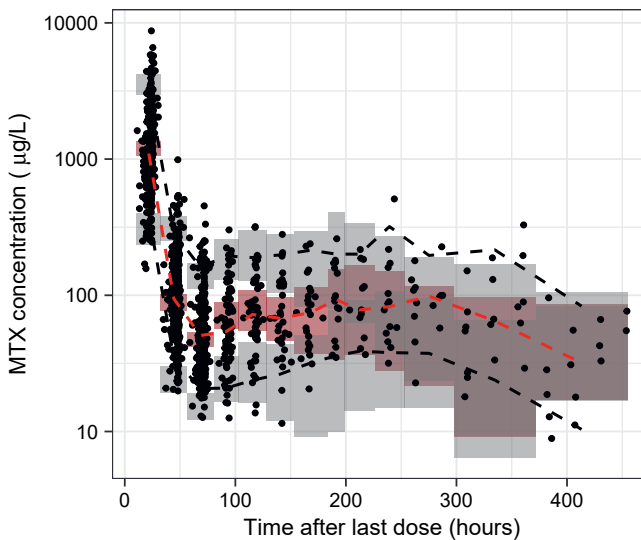


**Figure 7.2:** Prediction-corrected visual predictive check (pcVPC) of the final HD-MTX pharmacokinetic model. Black points represent observations, black dashed lines represent 95<sup>th</sup> and 5<sup>th</sup> percentile of the observations, red dashed line represents the 50<sup>th</sup> percentile of the observations, grey shaded areas represent 95% confidence interval of the 95<sup>th</sup> and 5<sup>th</sup> percentiles of the simulations, and red shaded area represents 95% confidence interval of the 50<sup>th</sup> percentile of the simulations.

### 3.3 Toxicity analysis

Among the 115 subjects, 51 (44.3%) and 76 (66.1%) subjects developed acute renal and hepatotoxicity during at least one administration cycle, respectively. The majority of subjects received  $\leq 4$  courses of treatment (98/115, 85.2%). The observed proportion of patients having each grade of renal or hepatotoxicity during each administration cycle were shown in **Online Resource 7.1, Figure S7.3**. The dose was reduced in 13 subjects after they had either renal or hepatotoxicity or both.

The modelling analysis of renal toxicity showed that among the investigated baseline factors, the inclusion of age, sex, dose in  $\text{mg}/\text{m}^2$ ,  $\text{AUC}_{\text{base}}$ ,  $\text{pC}_{24h}$ ,  $\text{pAUC}_{24-\infty}$ , or eGFR resulted in a significant decrease in OFV in the univariable covariate analysis, among which the baseline eGFR was the most significant predictor ( $\Delta\text{OFV} = -52.8$ ). The inclusion of toxicity status of the previous administration course did not result in a significant decrease in OFV. The treatment regimen itself was also not identified to affect the toxicity probability. The final model of renal toxicity included baseline eGFR (range: 40.2–158.7  $\text{mL}/\text{min}/1.73\text{m}^2$ , maximum predicted probability change ( $\text{max}\Delta\text{P}$ ) = -0.929) and sex (for female,  $\Delta\text{P} = -0.103$ ) as significant covariates.

As for the hepatotoxicity model,  $\text{AUC}_{\text{base}}$ , dose in  $\text{mg}$ , and dose in  $\text{mg}/\text{m}^2$  resulted in significant decreases in OFV in the univariable covariate analysis, among which dose

in  $\text{mg}/\text{m}^2$  showed to be the most significant predictor ( $\Delta\text{OFV} = -14.7$ ). The inclusion of toxicity status of the previous administration cycle did not decrease OFV significantly. No additional covariates were significant after the inclusion of dose in  $\text{mg}/\text{m}^2$ , i.e. the final model of hepatotoxicity only included dose in  $\text{mg}/\text{m}^2$  (range 1500–8000  $\text{mg}/\text{m}^2$ ,  $\text{max}\Delta\text{P} = 0.86$ ) as the most significant covariate.

The parameter estimates of the base and final toxicity models are shown in **Table 7.3**. The RSE of all parameters are < 40% indicating acceptable precision. The inclusion of covariates largely reduced the variance of the random IIV in both models. The VPC plots demonstrated an adequate model predictability for the probability of having renal toxicity, while the decreasing trend of hepatotoxicity over treatment courses was not well captured (**Online Resource 7.1, Figure S7.4**). The wider 90% prediction interval after the 4<sup>th</sup> administration cycle was due to the relatively small sample size at those cycles. **Figure 7.3** demonstrated the change of observed and predicted renal and hepatotoxicity probability as predictor values change. The simulation results showed that the median predicted probability of having renal toxicity decreased to less than 25% when baseline eGFR was higher than 66.6  $\text{mL}/\text{min}/1.73\text{m}^2$ , and the median predicted probability of having hepatotoxicity increased to above 38.5% when dose raised above 3500  $\text{mg}/\text{m}^2$ .

**Table 7.3:** Parameter estimates of the base and final logistic regression model of renal and hepatotoxicity

|                             | Base model |                           | Final model |                           |
|-----------------------------|------------|---------------------------|-------------|---------------------------|
|                             | Estimate   | RSE (%) / [Shrinkage (%)] | Estimate    | RSE (%) / [Shrinkage (%)] |
| <b>Renal toxicity model</b> |            |                           |             |                           |
| $\theta$                    | 0.112      | 29%                       | 0.0595      | 26%                       |
| $\theta_{\text{eGFR}}$      | -          | -                         | -3.06       | 9%                        |
| $\theta_{\text{SEX}}$       |            |                           | -1.32       | 32%                       |
| IIV ( $\omega^2$ )          | 3.29       | 43% [35%]                 | 1.11        | 61% [50%]                 |
| <b>Hepatotoxicity model</b> |            |                           |             |                           |
| $\theta$                    | 0.289      | 11%                       | 0.118       | 15%                       |
| $\theta_{\text{DOSE}}$      | -          | -                         | 2.25        | 38%                       |
| IIV ( $\omega^2$ )          | 0.922      | 48% [41%]                 | 0.708       | 52% [45%]                 |

BSA, body surface area; IIV, inter-individual variability; RSE, relative standard error; eGFR, estimated glomerular filtration rate.

The exposure metrics  $C_{24h}$  and  $\text{AUC}_{24\text{-}\infty}$  were identified to correlate with renal toxicity ( $\Delta\text{OFV} = -75.3$  and  $-85.6$ , respectively) in the univariable covariate analysis but not for hepatotoxicity. The parameter estimates can be found in **Online Resource 7.1, Table S7.2**. The observed proportion of patients with renal toxicity was 61% when  $C_{24h} > 8.64 \mu\text{mol}/\text{L}$  and 68.3% when  $\text{AUC}_{24\text{-}\infty} > 109.5 \mu\text{mol}/\text{L}\cdot\text{h}$ . According to the model simulations, the

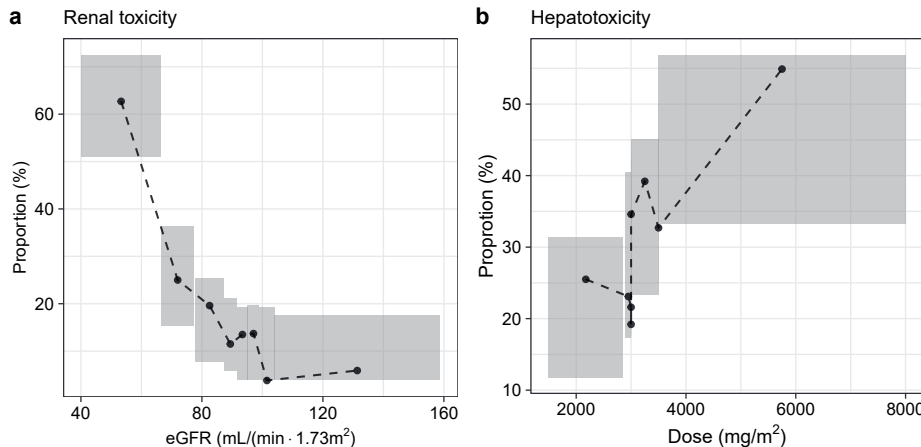


**Figure 7.3:** Visual predictive check of the model for renal toxicity probability over estimated glomerular filtration rate (eGFR) (a) and hepatotoxicity probability over dose (mg/m<sup>2</sup>) (b). Black points represent the observations and shaded areas are the 90% prediction interval of the final models where binning was done based on the number of observations

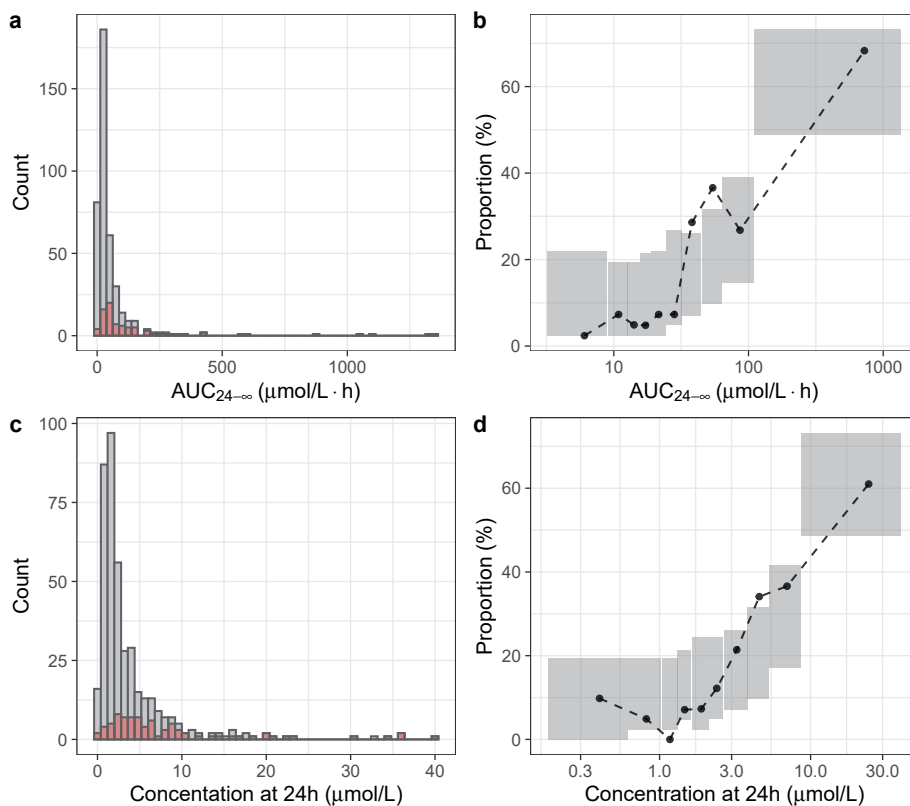


**Figure 7.4:** Distribution of (a) estimated AUC<sub>24-∞</sub> and (c) simulated concentration at 24 hours (C<sub>24h</sub>) of all treatment cycles (grey) and treatment cycles with renal toxicity (red), and observed and predicted probability of renal toxicity over (b) AUC<sub>24-∞</sub> and (d) C<sub>24h</sub>.

predicted median proportions of renal toxicity decreased from 61% to < 29.3% when  $C_{24h}$  decreased to  $\leq 8.64 \mu\text{mol/L}$ , and from 61% to < 26.8% when  $AUC_{24-\infty}$  decreased to  $\leq 109.5 \mu\text{mol/L}^{\text{*}}\text{h}$ , respectively. The distribution of estimated  $AUC_{24-\infty}$  and  $C_{24h}$  of all treatment cycles and observed and predicted probability of renal toxicity over  $AUC_{24-\infty}$  and  $C_{24h}$  were shown in **Figure 7.4**.

## 4. Discussion

In this study, a population PK model was developed for HD-MTX in patients with CNS lymphoma and covariates that explains HD-MTX PK variability were identified. Toxicity analysis identified baseline predictors for renal and hepatotoxicity, and the models allow to estimate the toxicity probability before each administration cycle. Additionally, potential exposure thresholds of  $AUC_{24-\infty}$  and  $C_{24h}$  that indicate a high risk of renal toxicity were suggested to support better HD-MTX treatment.

The identified covariates on CL of MTX in the final model includes albumin and indicators of renal function, which are in accordance with the known PK characteristics of MTX [4, 5]. In addition, the CL of MTX also showed to vary among treatment regimens, which might suggest a need to alter the dose when targeting to the same level of exposure. The possible explanations for this finding could be the differences in infusion duration / rate of HD-MTX, patients' status, and the combined medications among these treatment groups. However, the impact of those factors cannot be distinguished as they highly overlapped with each other. A potential correlation between infusion duration/rate and MTX clearance has been mentioned previously. In those studies, higher CL or lower AUC has been observed in patients receiving HD-MTX with long infusion durations (24 hours) compared to short infusion durations (2–6 hours) [10, 28, 29]. In our study, high CL estimates under 24-hour infusion were also observed. In addition, a 4-hour infusion showed to correlate with low CL estimates compared with 1- or 3.25-hour infusion in our results (**Online Resource 7.1, Figure S7.2**). However, a clear physiological explanation for this observed phenomenon could not be found, and therefore dose alterations based on infusion duration specifically are not recommended.

Currently HD-MTX was dosed per BSA in CNS lymphoma patients. However, our study demonstrated that the influence of BSA on MTX PK is less significant than that of body weight, although these two factors are highly correlated and BSA has been identified as a covariate in previous PK studies [17, 20]. The estimated MTX  $AUC_{24-\infty}$  and  $C_{24h}$  in our study population also showed an increasing trend over BSA (**Online Resource 7.1, Figure S7.5**). A few other studies have also pointed out that BSA is not the most predictive factor

to MTX PK, and BSA-guided dosing should be reconsidered especially for overweight patients [10, 30, 31]. Moreover, a dose reduction for HD-MTX has been suggested for patients with reduced renal function [7, 32]. Taking these facts into account, adjusting the MTX dose with the developed PK model which involves multiple covariates including renal function is considered to be more rational and accurate than BSA-guided dosing, and can help to further reduce PK variability.

The GOF plot of the final PK model showed that the population predictions underpredicted the lower concentrations (data points collected after 200 hours after last drug intake) while the individual predictions fitted well to the observations. These underpredicted concentrations all came from the treatment cycles where delayed elimination was observed. This suggests that the model structure could still be improved to better characterize the concentration-time curves in case of a delayed elimination. For example, an interaction between renal function and MTX PK, which may result in a time dependent MTX elimination, and non-linear elimination at low concentrations can be considered [33, 34]. A three-compartment model could also slightly better capture the delayed elimination. However, a reliable and stable three-compartment model could not be identified based on the current dataset. Since the individual fit of our model is considered to be adequate, a more complicated model was eventually not applied.

The toxicity analysis identified baseline predictors for HD-MTX-induced renal and hepatotoxicity which allow estimation of the toxicity probability before administration cycle. eGFR and sex were identified as significant baseline predictors for renal toxicity probability. Dose ( $\text{mg}/\text{m}^2$ ) and age were also identified as significant predictors in the univariable analysis, which is consistent with previous findings [11, 13]. However, their influence did not remain significant after including eGFR in the model. Our findings suggest that to lower the probability of renal toxicity, the use of HD-MTX for patients with CNS lymphoma is recommended when  $\text{eGFR} > 66.6 \text{ mL}/\text{min}/1.73\text{m}^2$ . This is in accordance with a previous review which indicated that renal function is a key prognostic factor for the tolerance of HD-MTX [32]. Accurately estimating the renal function of the patients before HD-MTX treatment may therefore be key in preventing toxicity during HD-MTX treatment. In patients with relatively low muscle mass, other eGFR measurement techniques such as a iohexol eGFR test could be applied [35]. Patients with a higher risk of toxicity that still need HD-MTX treatment should be carefully monitored and rescue therapy with high dose folate or in severe cases glucarpidase could be considered [36-38].

The dose of HD-MTX ( $\text{mg}/\text{m}^2$ ) was identified to be the strongest predictor of hepatotoxicity. The results suggest that a high risk for hepatotoxicity in patients with CNS lymphoma is

foreseeable if the administrated dose of HD-MTX is higher than 3500 mg/m<sup>2</sup>. In addition, the probability of hepatotoxicity appeared to decrease over treatment cycles which was not fully captured by the model. A possible explanation could be that patients tend to tolerate MTX better when treated for a longer period of time. Drop out due to toxicity is considered to be a less possible reason since less than 50% of subjects who stopped treatment after the first to third treatment courses had hepatotoxicity. Since the information on reason of drop out was not available, it was not considered in the analysis.

MTX exposure metrics was only identified to correlate with renal toxicity in patients with CNS lymphoma. To avoid the impact of possible inaccurate prediction of peak concentrations,  $AUC_{24\text{-}\infty}$  was estimated and included in the analysis instead of  $AUC_{0\text{-}\infty}$ . We also investigated the correlation between  $C_{24h}$  and toxicity as a threshold on  $C_{24h}$  is valuable for early identification of patients at risk and early application of rescue treatment. Our results show that  $AUC_{24\text{-}\infty} > 109.5 \mu\text{mol/L}\cdot\text{h}$  or  $C_{24h} > 8.66 \mu\text{mol/L}$  correlate with high risk of renal toxicity in CNS lymphoma patients (> 60%). The threshold of  $C_{24h}$  is also in line with what was found in a previous study (10  $\mu\text{mol/L}$ ) [7].

Although high MTX exposure can result in toxicity, sufficient exposure is still essential to guarantee the efficacy. To better apply our findings to facilitate the individualization and optimization of HD-MTX therapy in patients with CNS lymphoma, an investigation on exposure-efficacy relationship is still needed. A previous study suggested that  $AUC_{0\text{-}\infty} > 1100 \mu\text{mol/L}\cdot\text{h}$  is associated with a favorable treatment outcome [12]. Due to an identified correlation of  $AUC_{0\text{-}\infty}$  with  $C_{24h}$ , the same group recommend a  $C_{24h}$  target of 4–5  $\mu\text{mol/L}$  [16]. Nonetheless, the direct relationship between  $C_{24h}$  or  $AUC_{24\text{-}\infty}$  and the efficacy has not been reported. Thus, a further investigation on the relationship between  $C_{24h}$  or  $AUC_{24\text{-}\infty}$  and efficacy would be beneficial to establish a therapeutic range for HD-MTX to support the individualization of HD-MTX dosage.

The current study has some limitations. First of all, due to the lack of data sampled in the first 12 hours after the start of MTX infusion, the developed model may not be able to well capture peak concentrations and provide a precise estimate of  $AUC_{0\text{-}\infty}$ . Nevertheless, our study demonstrated that  $AUC_{24\text{-}\infty}$  and  $C_{24h}$  estimated with the model are also predictive to HD-MTX induced renal toxicity. Secondly, since this study was based on real-world data, the possibility of data not being recorded adequately enough may impact our analysis. Nevertheless, our findings may be more representative of real-world patients and are more translatable to clinical practice. Finally, although identified predictors have explained a large proportion of variability in HD-MTX induced toxicities, the unexplained variability remains large. Identifying covariates for the remained variability would be beneficial to

further improve the prediction. Previous studies have reported the influence of ABCC2 on PK of HD-MTX and the potential association of gene MTHFR, SLC19A1 and ABCB1 with MTX-induced hepatic toxicity [8, 21, 39]. Thus, the potential impact of pharmacogenetic polymorphisms would be of interest for future studies.

## 5. Conclusion

A population PK model was developed which adequately characterized the PK profile of HD-MTX in patients with CNS lymphoma. eGFR, treatment regimen, albumin, ALP, and body weight were identified as significant covariates that explain inter- and intra-individual variabilities in PK of HD-MTX. The toxicity analysis identified lower eGFR and male sex, and higher MTX dose ( $\text{mg}/\text{m}^2$ ) as baseline predictors that are associated with higher risk of acute renal and hepatotoxicity, respectively.  $\text{AUC}_{24\text{-}\infty} > 109.5 \text{ }\mu\text{mol}/\text{L}\cdot\text{h}$  and  $\text{C}_{24\text{h}} > 8.64 \text{ }\mu\text{mol}/\text{L}$  were suggested to be potential exposure thresholds that predict a high risk of renal toxicity. These results hold a great potential for further individualizing HD-MTX dosage and preventing acute organ toxicity, which can improve HD-MTX therapy in CNS lymphoma patients.

## Key points

- A population pharmacokinetic (PK) model was developed for high-dose methotrexate (HD-MTX) based on data collected from patients with central nervous system (CNS) lymphoma and subsequently used for exposure-toxicity analysis.
- Lower baseline eGFR and male sex are associated with increased risk of acute renal toxicity (grade  $\geq 1$ ). Higher MTX dose ( $\text{mg}/\text{m}^2$ ) is associated with increased risk of acute hepatotoxicity (grade  $\geq 1$ ).
- The analysis identified that the MTX exposure metrics correlate with renal toxicity only, and area under the concentration-time curve from 24h to infinite ( $\text{AUC}_{24\text{-}\infty} > 109.5 \text{ }\mu\text{mol}/\text{L}\cdot\text{h}$ ) and concentration at 24 hours ( $\text{C}_{24\text{h}} > 8.64 \text{ }\mu\text{mol}/\text{L}$ ) predicted a high risk of renal toxicity.

## References

1. Fallah J, Qunaj L, Olszewski AJ. Therapy and outcomes of primary central nervous system lymphoma in the United States: analysis of the National Cancer Database. *Blood Advances*. 2016;1(2):112-21. doi:10.1182/bloodadvances.2016000927.
2. Calimeri T, Steffanoni S, Gagliardi F, Chiara A, Ferreri AJM. How we treat primary central nervous system lymphoma. *ESMO Open*. 2021;6(4):100213. doi:10.1016/j.esmoop.2021.100213.
3. Jeong SY, Yoon SE, Cho D, Kang ES, Cho J, Kim WS, et al. Real-world experiences of CNS-directed chemotherapy followed by autologous stem cell transplantation for secondary CNS involvement in relapsed or refractory diffuse large B-cell lymphoma. *Front Oncol*. 2022; 12:1071281. doi:10.3389/fonc.2022.1071281.
4. Methotrexate Injection [package insert]. HOSPIRA. U.S. Food and Drug Administration. [https://www.accessdata.fda.gov/drugsatfda\\_docs/label/2018/011719s125lbl.pdf](https://www.accessdata.fda.gov/drugsatfda_docs/label/2018/011719s125lbl.pdf). Revised April 2018. Accessed October 12, 2022.
5. Bannwarth B, Labat L, Moride Y, Schaeverbeke T. Methotrexate in Rheumatoid Arthritis. *Drugs*. 1994;47(1):25-50. doi:10.2165/00003495-199447010-00003.
6. Schmiegelow K. Advances in individual prediction of methotrexate toxicity: a review. *Br J Haematol*. 2009;146(5):489-503. doi:10.1111/j.1365-2141.2009.07765.x.
7. Howard SC, McCormick J, Pui C-H, Buddington RK, Harvey RD. Preventing and Managing Toxicities of High-Dose Methotrexate. *The Oncologist*. 2016;21(12):1471-82. doi:10.1634/theoncologist.2015-0164.
8. Benz-de Bretagne I, Zahr N, Le Gouge A, Hulot JS, Houillier C, Hoang-Xuan K, et al. Urinary coproporphyrin I/(I+III) ratio as a surrogate for MRP2 or other transporter activities involved in methotrexate clearance. *Br J Clin Pharmacol*. 2014;78(2):329-42. doi:10.1111/bcp.12326.
9. Kawakatsu S, Nikanjam M, Lin M, Le S, Saunders I, Kuo DJ, et al. Population pharmacokinetic analysis of high-dose methotrexate in pediatric and adult oncology patients. *Cancer Chemother Pharmacol*. 2019;84(6):1339-48. doi:10.1007/s00280-019-03966-4.
10. Ibarra M, Combs R, Taylor ZL, Ramsey LB, Mikkelsen T, Buddington RK, et al. Insights from a pharmacometric analysis of HD-MTX in adults with cancer: Clinically relevant covariates for application in precision dosing. *Br J Clin Pharmacol*. 2022. doi:10.1111/bcp.15506.
11. Wight J, Ku M, Garwood M, Carradice D, Lasica M, Keamy L, et al. Toxicity associated with high-dose intravenous methotrexate for hematological malignancies. *Leuk Lymphoma*. 2022; 63(10):2375-82. doi:10.1080/10428194.2022.2074987.
12. Joerger M, Huitema AD, Krähenbühl S, Schellens JH, Cerny T, Reni M, et al. Methotrexate area under the curve is an important outcome predictor in patients with primary CNS lymphoma: A pharmacokinetic-pharmacodynamic analysis from the IELSG no. 20 trial. *British journal of cancer*. 2010;102(4):673-7. doi:10.1038/sj.bjc.6605559.
13. Amitai I, Rozovski U, El-Saleh R, Shimony S, Shephelovich D, Rozen-Zvi B, et al. Risk factors for high-dose methotrexate associated acute kidney injury in patients with hematological malignancies. *Hematol Oncol*. 2020;38(4):584-8. doi:10.1002/hon.2759.
14. Lalonde RL, Kowalski KG, Hutmacher MM, Ewy W, Nichols DJ, Milligan PA, et al. Model-based drug development. *Clin Pharmacol Ther*. 2007;82(1):21-32. doi:10.1038/sj.cpt.6100235.
15. Buil-Bruna N, Lopez-Picazo JM, Martin-Algarra S, Troconiz IF. Bringing Model-Based Prediction to Oncology Clinical Practice: A Review of Pharmacometrics Principles and Applications. *Oncologist*. 2016;21(2):220-32. doi:10.1634/theoncologist.2015-0322.

16. Joerger M, Ferreri AJ, Krähenbühl S, Schellens JH, Cerny T, Zucca E, et al. Dosing algorithm to target a predefined AUC in patients with primary central nervous system lymphoma receiving high dose methotrexate. *Br J Clin Pharmacol.* 2012;73(2):240-7. doi:10.1111/j.1365-2125.2011.04084.x.
17. Mei S, Li X, Jiang X, Yu K, Lin S, Zhao Z. Population Pharmacokinetics of High-Dose Methotrexate in Patients With Primary Central Nervous System Lymphoma. *J Pharm Sci.* 2018;107(5):1454-60. doi:10.1016/j.xphs.2018.01.004.
18. Blasco H, Senecal D, Le Gouge A, Pinard E, Benz-de Bretagne I, Colombat P, et al. Influence of methotrexate exposure on outcome in patients treated with MBVP chemotherapy for primary central nervous system lymphoma. *Br J Clin Pharmacol.* 2010;70(3):367-75. doi:10.1111/j.1365-2125.2010.03712.x.
19. Nader A, Zahran N, Alshammaa A, Altawee H, Kassem N, Wilby KJ. Population Pharmacokinetics of Intravenous Methotrexate in Patients with Hematological Malignancies: Utilization of Routine Clinical Monitoring Parameters. *Eur J Drug Metab Pharmacokinet.* 2017;42(2):221-8. doi:10.1007/s13318-016-0338-1.
20. Arshad U, Taubert M, Seeger-Nukpezah T, Ullah S, Spindeldreier KC, Jaehde U, et al. Evaluation of body-surface-area adjusted dosing of high-dose methotrexate by population pharmacokinetics in a large cohort of cancer patients. *BMC Cancer.* 2021;21(1):719. doi:10.1186/s12885-021-08443-x.
21. Simon N, Marsot A, Villard E, Choquet S, Khe HX, Zahr N, et al. Impact of ABCC2 polymorphisms on high-dose methotrexate pharmacokinetics in patients with lymphoid malignancy. *Pharmacogenomics J.* 2013;13(6):507-13. doi:10.1038/tpj.2012.37.
22. ARK™ Methotrexate Assay [package insert]. ARK Diagnostics, Inc.. [https://www.ark-tdm.com/products/cancer/methotrexate/pdfs/ARK\\_Methotrexate\\_Assay\\_Rev07\\_August\\_2017.pdf](https://www.ark-tdm.com/products/cancer/methotrexate/pdfs/ARK_Methotrexate_Assay_Rev07_August_2017.pdf). Revised August 2017. Accessed June 05, 2020.
23. Levey AS, Stevens LA, Schmid CH, Zhang YL, Castro AF, 3rd, Feldman HI, et al. A new equation to estimate glomerular filtration rate. *Ann Intern Med.* 2009;150(9):604-12. doi:10.7326/0003-4819-150-9-200905050-00006.
24. Keizer RJ, Jansen RS, Rosing H, Thijssen B, Beijnen JH, Schellens JH, et al. Incorporation of concentration data below the limit of quantification in population pharmacokinetic analyses. *Pharmacol Res Perspect.* 2015;3(2):e00131. doi:10.1002/prp2.131.
25. Jonsson EN, Karlsson MO. Automated covariate model building within NONMEM. *Pharm Res.* 1998;15(9):1463-8. doi:10.1023/a:1011970125687.
26. NCI Common Terminology Criteria for Adverse Events (CTCAE) version 5.0. November 2017 [cited 2020 October]; Available from: [https://ctep.cancer.gov/protocoldevelopment/electronic\\_applications/docs/CTCAE\\_v5\\_Quick\\_Reference\\_5x7.pdf](https://ctep.cancer.gov/protocoldevelopment/electronic_applications/docs/CTCAE_v5_Quick_Reference_5x7.pdf)
27. Lindblom L, Pihlgren P, Jonsson EN. PsN-Toolkit-a collection of computer intensive statistical methods for non-linear mixed effect modeling using NONMEM. *Comput Methods Programs Biomed.* 2005;79(3):241-57. doi:10.1016/j.cmpb.2005.04.005.
28. Ferreri AJ, Guerra E, Regazzi M, Pasini F, Ambrosetti A, Pivnik A, et al. Area under the curve of methotrexate and creatinine clearance are outcome-determining factors in primary CNS lymphomas. *British journal of cancer.* 2004;90(2):353-8. doi:10.1038/sj.bjc.6601472.
29. Ramsey LB, Panetta JC, Smith C, Yang W, Fan Y, Winick NJ, et al. Genome-wide study of methotrexate clearance replicates SLCO1B1. *Blood.* 2013;121(6):898-904. doi:10.1182/blood-2012-08-452839.
30. Pai MP, Debacker KC, Derstine B, Sullivan J, Su GL, Wang SC. Comparison of Body Size, Morphomics, and Kidney Function as Covariates of High-Dose Methotrexate Clearance in Obese Adults with Primary Central Nervous System Lymphoma. *Pharmacotherapy.* 2020; 40(4):308-19. doi:10.1002/phar.2379.

31. Gallais F, Oberic L, Faguer S, Tavitian S, Lafont T, Marsili S, et al. Body Surface Area Dosing of High-Dose Methotrexate Should Be Reconsidered, Particularly in Overweight, Adult Patients. *Therapeutic Drug Monitoring*. 2021;43(3):408-15. doi:10.1097/Ftd.00000000000000813.
32. Holdhoff M, Mrugala MM, Grommes C, Kaley TJ, Swinnen LJ, Perez-Heydrich C, et al. Challenges in the Treatment of Newly Diagnosed and Recurrent Primary Central Nervous System Lymphoma. *J Natl Compr Canc Netw*. 2020;18(11):1571-8. doi:10.6004/jnccn.2020.7667.
33. Woillard JB, Debord J, Benz-de-Bretagne I, Saint-Marcoux F, Turlure P, Girault S, et al. A Time-Dependent Model Describes Methotrexate Elimination and Supports Dynamic Modification of MRP2/ABCC2 Activity. *Ther Drug Monit*. 2017;39(2):145-56. doi:10.1097/ftd.0000000000000381.
34. Hendel J, Nyfors A. Nonlinear renal elimination kinetics of methotrexate due to saturation of renal tubular reabsorption. *European Journal of Clinical Pharmacology*. 1984;26(1):121-4. doi:10.1007/BF00546719.
35. Zwart TC, de Vries APJ, Engbers AGJ, Dam RE, van der Boog PJM, Swen JJ, et al. Model-Based Estimation of Iohexol Plasma Clearance for Pragmatic Renal Function Determination in the Renal Transplantation Setting. *Clin Pharmacokinet*. 2021;60(9):1201-15. doi:10.1007/s40262-021-00998-z.
36. Ramsey LB, Balis FM, O'Brien MM, Schmiegelow K, Pauley JL, Bleyer A, et al. Consensus Guideline for Use of Glucarpidase in Patients with High-Dose Methotrexate Induced Acute Kidney Injury and Delayed Methotrexate Clearance. *Oncologist*. 2018;23(1):52-61. doi:10.1634/theoncologist.2017-0243.
37. Schaff LR, Lobbous M, Carlow D, Schofield R, Gavrilovic IT, Miller AM, et al. Routine use of low-dose glucarpidase following high-dose methotrexate in adult patients with CNS lymphoma: an open-label, multi-center phase I study. *BMC Cancer*. 2022;22(1):60. doi:10.1186/s12885-021-09164-x.
38. Widemann BC, Balis FM, Kim A, Boron M, Jayaprakash N, Shalabi A, et al. Glucarpidase, leucovorin, and thymidine for high-dose methotrexate-induced renal dysfunction: clinical and pharmacologic factors affecting outcome. *J Clin Oncol*. 2010;28(25):3979-86. doi:10.1200/JCO.2009.25.4540.
39. Suthandiram S, Gan GG, Zain SM, Bee PC, Lian LH, Chang KM, et al. Effect of polymorphisms within methotrexate pathway genes on methotrexate toxicity and plasma levels in adults with hematological malignancies. *Pharmacogenomics*. 2014;15(11):1479-94. doi:10.2217/pgs.14.97.

## Online Resource 7.1: Supplementary figures and tables

### Supplementary Figures

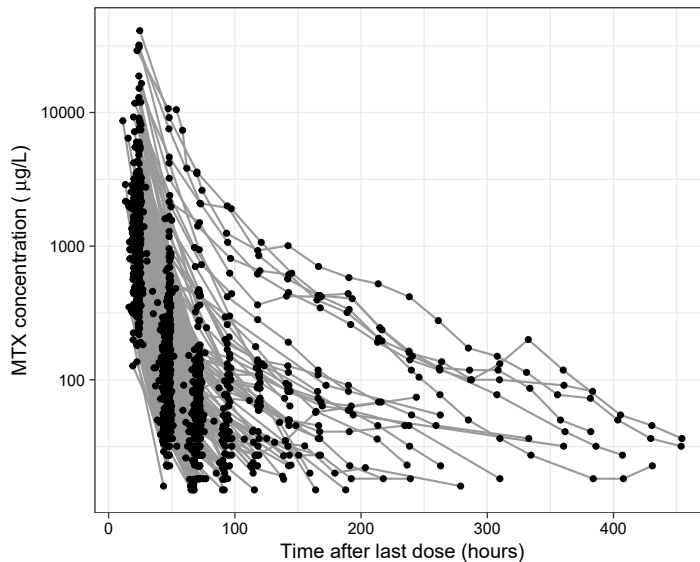


**Figure S7.1:** The collected methotrexate concentration-time curves in patients with CNS lymphoma on semi-logarithmic scale (n = 110 patients).

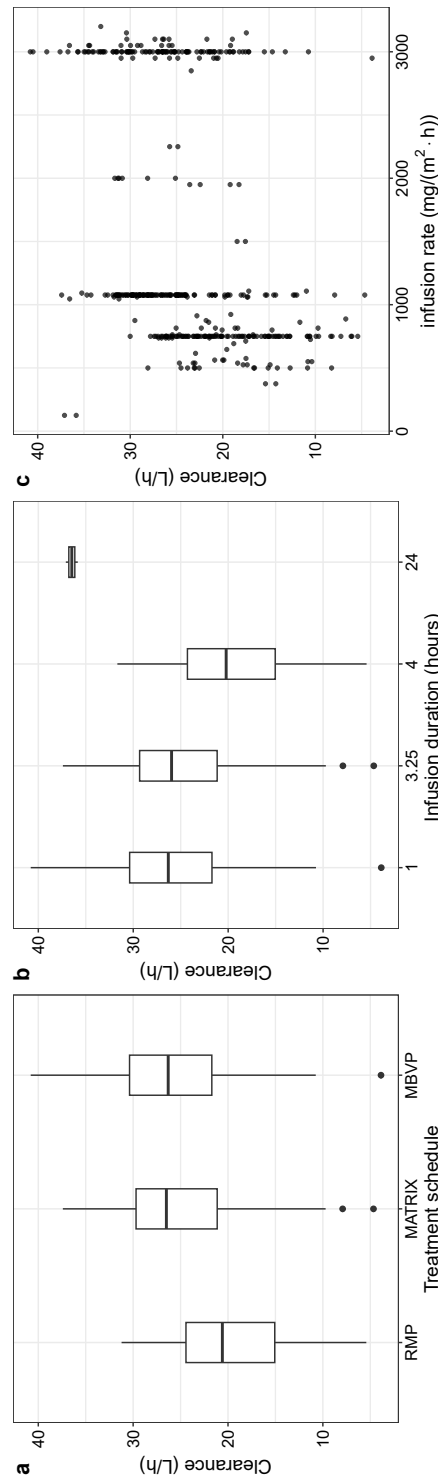


**Figure S7.2:** Estimated MTX clearance versus (a) treatment regimen, (b) infusion duration (hours), and (c) infusion rate.

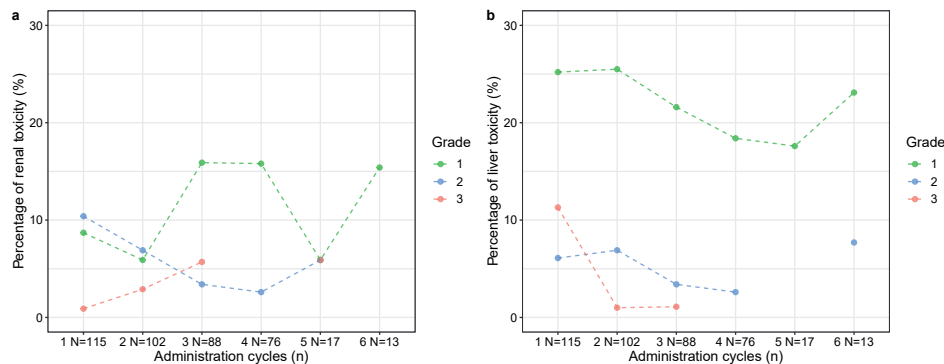


**Figure S7.3:** Observed percentage of renal (a) and liver (b) toxicity under each treatment cycle separated by the toxicity grade.

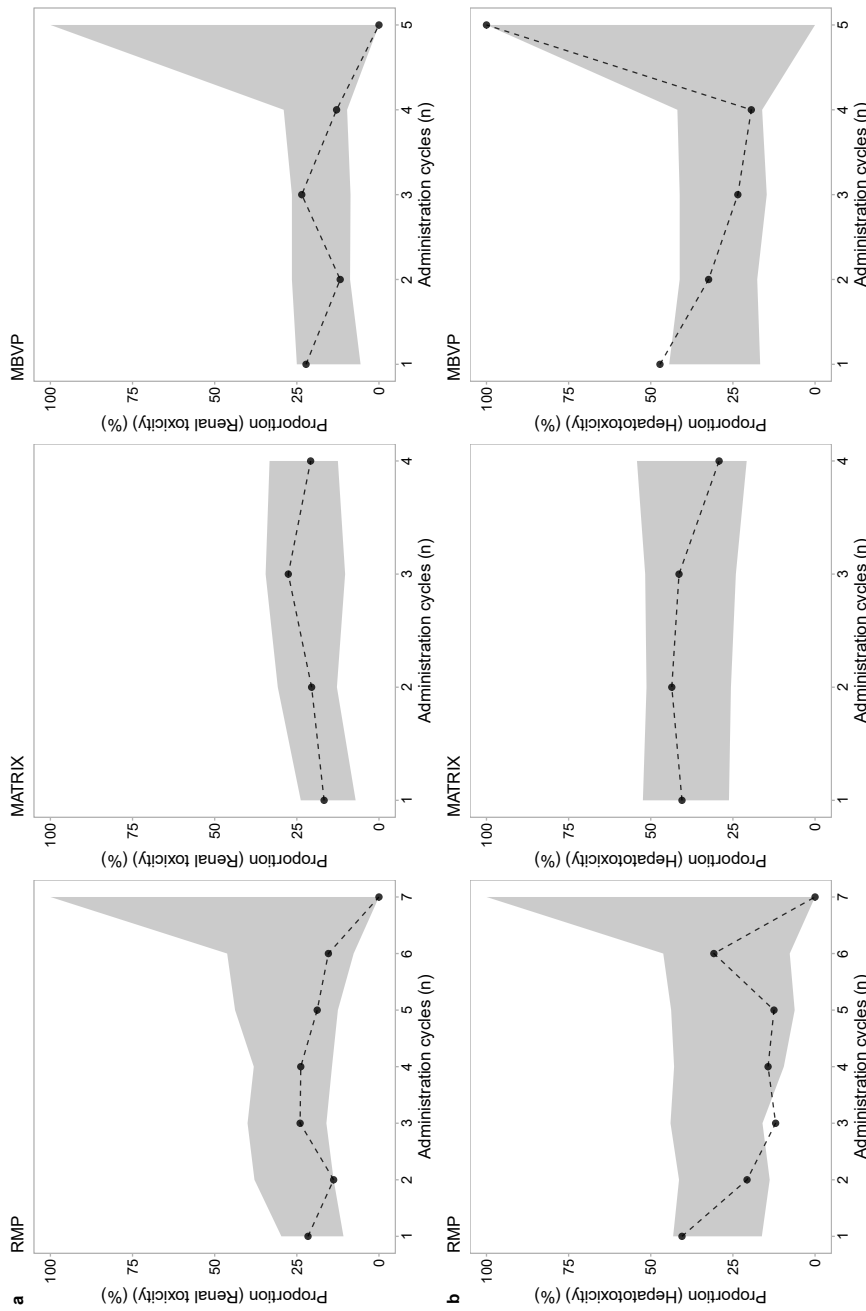


**Figure S7.4:** Visual predictive check of model for renal toxicity probability (a) and hepatotoxicity probability (b) by treatment regimens. Black points represent the observations and shaded areas are the 90% prediction interval of the final model.

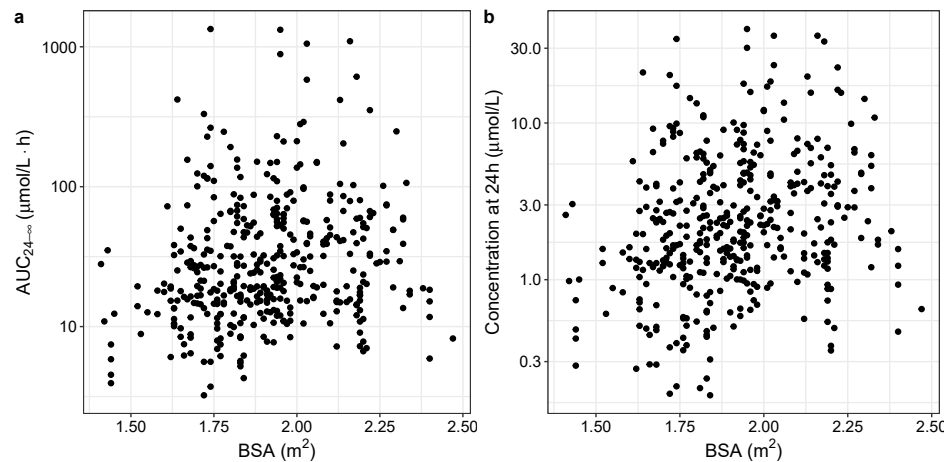


**Figure S7.5:** Estimated area under the concentration-time curve between 24 hours after drug administration to infinity ( $AUC_{24-\infty}$ ) (a) and concentration at 24 hours (b) versus body surface area of the included patients.

## Supplementary Tables

**Table S7.1:** Characteristics of the HD-MTX treatment regimens of the included patients

|  | N of administrations (%) / Median (Range) |  |   |
|--|---|--|---|
| Treatment regimen                            | RMP                                       | MATRIX   | MBVP  |
| Age of patients (years)                      | 72 (28–83)                                | 58.5 (22–67)                                   | 66 (51–76)  |
| Infusion duration                            |   |  |   |
| a. 4 hours                                   | 133 (93.7%)                               | 6 (4.5%)                                       | 0   |
| b. 14–25% dose 15 mins, and the rest 3 hours | 9 (6.3%)                                  | 126 (94.0%)                                    | 0   |
| c. 10% dose 1 hour, and the rest 23 hours    | 0   | 2 (1.5%)                                       | 0   |
| d. 1 hour                                    | 0   | 0  | 136 (100%)  |
| Infusion rate (mg/m <sup>2</sup> /h)         | 750 (375–1077)                            | 1076 (125–2000)                                | 3000 (1500–3200)  |
| Dose of MTX (mg/m <sup>2</sup> )             | 3000 (1500–3650)                          | 3500 (1750–8000)                               | 3000 (1500–3200)  |
| Dose intensity (days)                        | 14.0 (12.9–54.1)                          | 23.0 (11.0–66.9)                               | 15.0 (6–45)   |
| Co-medications                               | rituximab and procarbazine                | high-dose cytarabine, thiotapec, and rituximab | teniposide, carmustine, prednisolone with/without rituximab or high dose cytarabine |

**Table S7.2:** Parameter estimates of the logistic regression model of renal toxicity with exposure metrics included as predictors

|   | Estimate | RSE (%) / [Shrinkage (%)] |
|---|----------|---------------------------|
| Renal toxicity model with AUC <sub>24-∞</sub> |          |                           |
| θ   | 0.0135   | 61%                       |
| θ <sub>AUC<sub>24-∞</sub></sub>               | 0.746    | 11%                       |
| IIIV (ω <sup>2</sup> )                        | 5.69     | 55% [38%]                 |
| Renal toxicity model with C <sub>24h</sub>    |          |                           |
| θ   | 0.0132   | 64%                       |
| θ <sub>C<sub>24h</sub></sub>                  | 0.851    | 10%                       |
| IIIV (ω <sup>2</sup> )                        | 6.04     | 55% [37%]                 |

IIIV, inter-individual variability; RSE, relative standard error; AUC<sub>24-∞</sub>, area under the concentration-time curve between 24 hours after drug administration to infinity; C<sub>24h</sub>, MTX concentration at 24 hours after drug administration.



# Chapter 8

## General discussion





## Introduction

Although anti-cancer treatments have significantly advanced over the past decades, obstacles to accomplishing successful treatment still exist. The occurrence of treatment resistance is one of the major factors that limit the long-lasting efficacy of anti-cancer therapies [1, 2]. Evolutionary mechanisms are increasingly acknowledged as key factors that contribute to the occurrence of treatment resistance [2-5]. A better characterization and understanding of evolutionary tumor progression, and subsequent use of this knowledge to design new treatment regimens would increase the chance to suppress the development of cancer treatment resistance. Another important factor that challenges successful treatment is the substantial variability in pharmacokinetics (PK) / pharmacodynamics (PD) of anti-cancer drugs, which is especially frequently observed in real-world patients. This can result in suboptimal treatment outcomes for part of the patients especially when the therapeutic window is narrow [6, 7]. Moreover, the typically applied maximum tolerated dose (MTD) paradigm in cancer treatment may not be optimal for real-world patients due to high risk of toxicity [8]. These factors highlight the need to gain more insight into the PK/PD profiles and variability of anti-cancer drugs in real-world patients, and to further develop optimized and individualized treatment regimens.

Quantitative modeling with mixed-effect models is widely applied in pharmaceutical research which enables quantitative characterization and prediction of the PK and PD of therapeutic agents. It also allows quantifying inter- and intra-individual variability and identify covariates that explain the variability [9, 10]. With a Bayesian framework, individual parameters can be obtained based on prior knowledge from the model and patient characteristics and data, which can be used to capture and predict individual PK/PD characteristics [7]. In oncology research, the model-based approach is a helpful tool to make use of longitudinal data, such as drug concentrations, tumor burden, and other PD biomarkers, to gain knowledge about the interaction between drug treatment and the human body, as well as cancer progression. This knowledge and developed models can subsequently support the identification of optimal therapeutic regimens and guide individualized treatment rationally (model-informed precision dosing, MIPD) [7, 11, 12].

The studies presented in this thesis applied quantitative modeling approaches to characterize the evolutionary tumor progression and PK/PD of anti-cancer drugs. The developed models were subsequently applied to evaluate and develop optimal and individualized regimens for oncology patients.

## Better understanding of evolutionary tumor progression

### Intra-tumor heterogeneity

Intra-tumor heterogeneity, which suggests distinct cells exist in the same tumor, is considered to be one of the main factors that drive the evolving adaptation of cancer to treatment. Capturing intra-tumor heterogeneity is therefore of importance for a better understanding of evolutionary treatment resistance. As summarized in **chapter 2**, various kinds of quantitative models have been applied to describe and predict tumor dynamics and resistance evolution in cancer patients. Among the reported tumor dynamics models, intra-tumor heterogeneity has been considered when describing tumor regrowth by separating the tumor into components consisting of cells that are sensitive or resistant to therapy. The interaction between sensitive and resistant cells is also the cornerstone for the models that characterize the evolutionary development of drug resistance.

In the studies in **section I**, intra-tumor heterogeneity has served as a key element in the applied models to support the understanding of evolving tumor progression. The presence of pre-existing resistant components (primary resistance) and/or acquired resistance and their interaction have also been frequently discussed. In **chapter 3**, a model that accounted for various clonal populations was developed and it well captured the tumor sizes and mutant *KRAS* levels in circulating tumor DNA (ctDNA) versus time curves from patients with metastatic colorectal cancer (mCRC). In addition to the clonal populations that are sensitive or resistant to the original treatment, a hypothetical third clonal population was also introduced in the model to describe tumor response to multiple treatments. The same structure was also applied to characterize the dynamics of tumor sizes and ctDNA measurements in non-small cell lung cancer (NSCLC) patients. The inclusion of primary or acquired resistance in this study was supported by the detected mutation in ctDNA, which was suggested to be a mediator of acquired resistance [13, 14]. The model therefore included acquired resistance, and primary resistance was only considered for patients with detectable *KRAS* mutation pre-treatment. The developed model allowed us to capture not only the dynamics of total tumor size but also that of sub-clones in the tumor, which reflects the evolutionary progression of the tumor.

The study presented in **chapter 4** further characterized the tumor dynamics in NSCLC patients treated with erlotinib while considering tumor heterogeneity. In this study, we explored models with or without primary resistance while including an acquired resistance for both. The results indicated that the model assuming no primary resistance could adequately fit the obtained data, and estimating primary resistance did not improve the model fit. This might indicate that for NSCLC patients with an activating *EGFR* mutation,

it is mainly the acquired resistance, which was due to the acquisition of *EGFR* p.T790M mutation or other mechanisms, that limits the treatment response. Among previously reported model-based studies on tumor size dynamics in NSCLC patients treated with erlotinib, one study also considered tumor heterogeneity [15]. Their results also showed that the models with or without primary resistance could describe the data equally well even though erlotinib was used as a second-line treatment in their study [15].

In fact, studies on the probability of having resistance at the start of treatment have been performed. They demonstrated that such probability increased as tumor burden increased and it could reach up to  $> 90\%$  [16, 17]. The study that provided the original data for **chapter 3** also suggested that drug resistance is likely to be present prior to the initiation of anti-cancer drug treatment [13]. Yet, the estimated baseline size of the resistance clonal population only accounted for a small part of the total tumor cell population [13]. In **chapter 4**, the estimated baseline size of primary resistance accounted for a small proportion (5.9%) of the baseline tumor size. Therefore, although resistance may be present prior to the treatment, considering the small proportion and the complexity of the model, the primary resistance has been omitted in the models used in our studies. In addition, the data of genetic biomarkers is believed to be viable evidence to support the differentiation of heterogeneous components in the tumor when modeling tumor dynamics considering tumor-heterogeneity [18].

### **Interaction among clonal populations and treatment**

In addition to intra-tumor heterogeneity, capturing the interaction among clonal populations in the tumor and anti-cancer drug treatment is also a cornerstone when describing evolving development of resistance in tumor. We have addressed such interaction by accounting for the differences in proliferation rates of tumor cells, the response of tumor cells to the therapy, and the transition between sensitive and resistant tumor cells in response to treatment.

In order to obtain resistance to treatment, tumor may give up some proliferation capability, which is represented by a fitness cost [19]. Due to this fitness cost, the proliferation rate of the resistant clonal population can be lower than that of the sensitive clonal population [19, 20]. In **chapter 3**, we adopted this concept and assumed that the growth rate of resistant cells was 70% of the sensitive cells. In **chapter 4**, we have also estimated separate growth rates for different cell populations during model development. The estimated growth rate of sensitive cells was 2.19 fold higher than that of the resistant cells. However, the high relative standard error (RES) (104%) indicated a high uncertainty in the estimation.

Therefore, the growth rates of treatment sensitive and resistant clonal populations were eventually set to be the same in this study. This lack of identifiability of separate growth rates is considered to be caused by the limited amount of data.

The response of tumor cells to the therapy has been mainly addressed by adding a regression term on drug susceptible tumor cells. In **chapter 3**, we have included treatment effect with a drug-dependent regression term. This is due to the lack of data on drug exposure or dose in this study. In the meantime, the trough concentrations of the used monoclonal antibody therapy have shown to be able to reach above 90% of the saturation levels at standard treatment regimens, suggesting almost a maximum effect in all patients [21]. However, for other molecules the exposure of which correlates to response, such as tyrosine kinase inhibitors (TKIs), drug levels are important to be included in the analysis. This would be beneficial for the understanding the exposure-response relationship and how drug exposure is driving the evolutionary progression of tumor. Therefore, we explored a model that incorporated exposure-dependent treatment effect in **chapter 4**. However, we did not identify a clear exposure-tumor inhibition relationship within the studied concentration range (the median predicted drug concentrations at the tumor size monitoring time points was 992 ng/ml (range of 284–1554 ng/mL)). A dose-tumor inhibition relationship was also not identified. This lack of relationship between erlotinib exposure and responses, which may be because of the saturated treatment effect, is in line with previous findings [6, 22-24]. Although the influence of drug exposure on the evolving tumor progression could not be investigated in this case, the results may suggest a potential option to decrease the dose of erlotinib to target a lower concentration that still ensures sufficient efficacy but can be better tolerated, especially since a significant proportion of erlotinib-treated patients can have severe toxicity [25].

Because of the selection pressure of anti-cancer drug treatment, our studies in **chapter 3** and **4** assumed that mutations were able to be acquired which resulted in a transition from sensitive to resistant cell population. A back transfer process from drug resistant to sensitive clonal population was also introduced in **chapter 3** during the treatment interruption periods. This assumption allowed capturing the recovery of sensitivity to the treatment upon withdrawal of treatment, which was supported by in vitro observations [26]. This process could also describe the phenomenon that in the absence of the drug, susceptible tumor cells have the benefit of growing back again at the expense of resistant tumor cells. When the back transfer process was removed, the simulation outcomes of evaluated regimens were only slightly affected but the decline of ctDNA upon withdrawal of treatment, which has been observed in mCRC patients [26, 27], could not be captured anymore. It was also observed that under this circumstance, the remaining susceptible

tumor cells had no growth advantage over the resistant tumor cells during the withdrawal of treatment, hence the tumor would not regain susceptibility. Therefore, the introduction of a transition between clonal populations in this study allowed the description of the dynamics of and the competition among different clonal populations based on current available data. More data under intermittent therapy would be valuable to better characterize this dynamic process, and to better estimate parameters.

### Insight provided by ctDNA

Clinically available genetic biomarkers such as ctDNA have been shown to be able to provide insight into tumor heterogeneity and evolution of resistance, and also correlate with tumor burden [18]. Studies have already utilized the available ctDNA data to support the estimation of parameters that are required in the tumor evolution model or to evaluate the simulation results of the models [13, 28, 29]. Thus, we see opportunities to incorporate the ctDNA measurements in model-based tumor dynamics studies to enable better understanding and prediction on the tumor progression and dynamics of tumor sub-clones. Such models would be of help in investigating treatment regimens that increase the chance of overcoming treatment resistance. The model developed in **chapter 3** enabled the characterization of the time-curves of both tumor sizes and ctDNA measurements in patients with mCRC. The link between the generation of genetic variants in ctDNA and tumor burden was accounted by a sub-clonal tumor-size dependent shedding rate which was expressed with Hill equations with tumor size as the independent variable. This model allowed us to describe the delayed emergence of genetic variants in ctDNA indicating treatment resistance as well as the earlier emergence of detectable mutation than disease progression, which was observed in the original studies [13, 30]. The ctDNA measurements also informed the inclusion of primary or acquired resistance.

The study in **chapter 4** demonstrated that in NSCLC patients treated with erlotinib, the baseline ctDNA measurements on variant allele frequency (VAF) of mutant *EGFR* and the presence of a *TP53* mutation have a potential correlation with the estimated parameters related to tumor dynamics (mainly the growth rate constant  $k_g$  and mutation rate constant  $k_m$ ), especially that higher baseline *EGFR* VAF was significantly correlated with increased growth rate constant  $k_g$ . This indicates that patients with higher *EGFR* VAF at baseline may have a worse response to the treatment, which is in line with the clinical findings from an *EGFR* cohort in the START-TKI study, i.e. patients without detectable ctDNA at baseline had a lower rate of radiological progression [25]. An explanation could be the association between ctDNA levels and tumor burden [18, 31]. Our result also supports previous findings suggesting that baseline concomitant *TP53* mutations may relate to

worse clinical outcomes in patients with NSCLC [25]. After incorporating baseline ctDNA measurements, the developed tumor dynamics model could better predict the tumor size dynamics in response to erlotinib treatment in NSCLC patients. This finding also demonstrates the potential to use ctDNA as an early biomarker to support decision making for the treatment of NSCLC patients [32].

## Design treatment to overcome resistance

Designing treatment with gained knowledge on treatment resistance evolution and applying personalized treatment would increase the chance of overcoming cancer treatment resistance [2, 33]. Based on this concept, adaptive treatments where drug selection is guided by the mutation detected in ctDNA, and intermittent treatment which utilizes the fitness advantage of sensitive cells during the withdrawal of treatment to regain sensitivity to treatment have been suggested for better treating cancer patients [18, 33, 34]. This also brings forward opportunities to treat cancer as a chronic disease and has been increasingly studied in the oncology field. Traditional approaches of anti-cancer therapy have not exploited these theoretical advantages. Current protocols typically apply treatment agents at the MTD until evidence of progression [33].

The study presented in **chapter 3** evaluated different designs of adaptive and intermittent treatment regimens with simulations based on the developed model. These regimens aim to prolong the duration of suppressing treatment resistance and thereby overcoming treatment resistance. The adaptive schedules also enabled the personalized design of therapy since the switch of drugs was guided by individual ctDNA measurements. The results of this study showed that the adaptive and intermittent treatment regimens, with appropriate designs, outperformed the conventional continuous treatment. The simulated intermittent regimen which consisted of an 8-week treatment and a 4-week suspension prolonged median progression-free survival (PFS) of the simulated population from 36 weeks to 44 weeks. The simulated adaptive regimens were shown to further prolong median PFS to 56–64 weeks.

Our results are in line with the evolutionary principle, and evidence that supports the feasibility of suggested regimens is present. An example of the adaptive therapy can be seen from the treatments of NSCLC patients. Acquisition of T790M mutation is the main mechanism of acquired resistance upon treatment of erlotinib/gefitinib in NSCLC patients, and osimertinib can be selected for T790M-positive patients [35]. In the study, we introduced a second hypothetical treatment targeting the resistant population that harbors *KRAS*

mutation. Lately, the U.S. Food and Drug Administration (FDA) also granted accelerated approval to the first KRAS-blocking drug [36]. This indicates the potential feasibility of successfully implementing the suggested adaptive treatment.

As for the intermittent treatment, the advantage has been seen from some clinical observations. A study has shown that adaptive intermittent treatment of abiraterone based on prostate-specific antigen (PSA) levels resulted in a better clinical outcome than the typical continuous treatment [34], although the study design may need to be refined [37]. Another retrospective analysis demonstrated that intermittent use of enzalutamide in metastatic castration-resistant prostate cancer patients prolonged the time to PSA failure and improved overall survival [38]. In patients with colorectal cancer, a re-challenge of EGFR blockade has shown to be efficient again [26]. Yet, several clinical studies failed to show improved outcomes in patients undergoing intermittent therapy and the underlined mechanism remains unclear [39-44]. We believe that, in this case, a model-based approach may be helpful for understanding these conflicting results and support identification of the optimal designs. For example, a previous *in silico* study indicated that an intermittent abiraterone followed by a lead-in period was not beneficial for prostate cancer patients, while the adaptive intermittent treatment guided by PSA was the best option [34]. Moreover, the results derived from our study also raised attention to the length of the treatment holiday if improved treatment outcome is desired, as extending the treatment holiday can result in inferior results.

## Model-informed precision dosing (MIPD)

### Quantify variabilities and identify covariates

Our studies in **section II** demonstrated that with the population modeling approach, the variabilities in PK/PD of a therapeutic agent as well as the influence of relevant covariates can be quantified. This would be of great importance to guide dose tailoring for an individual patient prior to the start of treatment to achieve personalized therapy. In **chapter 6**, we have developed a two-compartment population PK model which well described the PK of mitotane in patients with ACC. The covariates that significantly correlate with mitotane PK have been identified, which explained 35.8% and 30.7% of random inter-individual variabilities (IIV) on apparent clearance (CL/F) and central distribution volume (Vc/F), respectively. In this study, we were able to investigate separate effects of lean body weight (LBW) and fat amount (total body weight – LBW) on mitotane distribution volumes, as they are more physiologically plausible covariates [45, 46]. Furthermore, the

inter-occasion variability (IOV) on CL/F was also incorporated to capture the intra-subject variability. The estimates of IOV indicate an overall increasing clearance during the first 500 days followed by a decrease thereafter. This dynamic indicates that a self-induction in mitotane clearance, which has been suggested previously [45], may exist temporarily. This study also for the first time explored and quantified the potential effect of pharmacogenetic variation on mitotane clearance. Eventually, three SNPs, i.e. *CYP2C19\*2* (rs4244285), *SLCO1B3* 699A>G (rs7311358), and *SLCO1B1* 571T>C (rs4149057), were included in the final model. The model estimated that carrying 'A' variant in *CYP2C19\*2* reduced the mitotane CL/F by 44.9%. This is in line with the fact that the 'A' variant of *CYP2C19\*2* is a nonfunctioning variant and has been demonstrated to decrease the activity of *CYP2C19* [47, 48]. The power of pharmacogenetic analysis may be influenced by the small number of included patients and the exploratory characteristic of this analysis. However, as the dataset enabled differentiation between IIV and IOV, the certainty of the possible genotype effect on clearance, which is more likely to be covered by IIV, was increased. Our result suggests that enzyme *CYP2C19* and transporters *SLCO1B3* and *SLCO1B1* for drug uptake in the liver might be involved in mitotane PK pathways, and their polymorphisms should be considered for mitotane dose selection, but further validation is required to translate the findings into an implementable clinical recommendation.

The study in **chapter 7** performed a population PK analysis for high-dose methotrexate (HD-MTX) in patients with central nervous system (CNS) lymphoma based on data from 3 medical centers. In addition to the impact of patients' demographics and physiological condition on HD-MTX PK, the study also enabled an investigation on the variation among patients from different medical centers receiving different treatment regimens. The results show that the identified covariates on clearance (CL) of MTX are in accordance with the known PK characteristics of MTX [49, 50]. Moreover, the CL of MTX also showed to vary among treatment regimens, and the difference in CL was able to be quantified. This might suggest a need to alter the dose when targeting to the same level of exposure. The possible factors that contributed to this result could be the differences in infusion duration / rate of HD-MTX, patients' status, and the combined medications among these treatment groups. However, the impact of those factors cannot be distinguished as they highly overlapped with each other. The included covariates in the final model explained 46.9% of the variability on CL between and within patients. Additionally, body weight was identified as a significant covariate on distribution volume of central compartment which reduced random IIV significantly. Currently, HD-MTX is dosed per body surface area (BSA) in CNS lymphoma patients. However, our study demonstrated that the influence of BSA on MTX PK is less significant, although BSA has been identified as a covariate in

previous PK studies [51, 52]. A few previous studies have also pointed out that BSA is not the most predictive factor to MTX PK, and BSA-guided dosing should be reconsidered especially for overweight patients [53-55]. In our study population, an increasing trend of the estimated MTX area under the concentration-time curve (AUC) from 24 hours after drug administration to infinity ( $AUC_{24-\infty}$ ) and MTX concentration at 24 hours ( $C_{24h}$ ) over BSA has also been observed. Additionally, a dose reduction for HD-MTX has already been suggested for patients with reduced renal function [56, 57]. Taking these facts into account, a potential to dose HD-MTX with a model-based approach that involves multiple covariates including renal function is implied. This is considered to be more rational and accurate than BSA-guided dosing, and can help to further reduce PK variability.

### Better prediction of toxicity

Toxicity can cause unfavorable outcomes in the treatment of cancer patients. Because of this, studies on risk factors and thresholds that predict high toxicity are of great importance. In **chapter 7**, the baseline predictors as well as exposure thresholds that predict a high risk of renal and hepatotoxicity in patients with CNS lymphoma treated with HD-MTX were identified with the model-based approach. Based on the modeling and simulation results, we recommended a baseline eGFR target of  $> 66.6 \text{ mL/min/1.73 m}^2$  for patients with CNS lymphoma to use HD-MTX in order to lower the probability of renal toxicity. This is in accordance with a previous review which indicated that renal function is a key prognostic factor for the tolerance of HD-MTX [57]. Additionally, a higher risk for hepatotoxicity in CNS lymphoma patients is foreseeable if the administrated dose of HD-MTX is higher than  $3500 \text{ mg/m}^2$ . The study also identified correlations between MTX exposure metrics and renal toxicity. In addition to the AUC of MTX,  $C_{24h}$  was also investigated as an exposure metric, as a threshold on  $C_{24h}$  is valuable for early identification of patients at risk and early application of rescue treatment. The modeling results provided potential exposure thresholds that correlate with a high risk of renal toxicity in patients with CNS lymphoma ( $> 60\%$ ). The threshold of  $C_{24h}$  ( $8.66 \mu\text{mol/L}$ ) is also in line with what was found in a previous study ( $10 \mu\text{mol/L}$ ) [56]. For patients with a higher risk of toxicity that still need HD-MTX treatment, they should be carefully monitored and rescue therapy with high dose folate or, in severe cases, glucarpidase could be considered [58-60]. In addition, due to the feature of mixed-effect modeling, once patients' toxicity results of the first cycle are known, the model can also be applied to provide individual threshold that predicts high toxicity. In this circumstance, we believe our study holds great potential for further individualizing HD-MTX dosage and preventing acute organ toxicity, which can improve HD-MTX therapy in CNS lymphoma patients.

### Guide individualized treatment

Based on the identified covariates and pre-defined therapeutic targets, coupled with Bayesian forecasting, MIPD can be applied to guide optimal initial dose selection and dose adaptation for cancer patients. The optimal therapeutic drug monitoring (TDM) strategies can also be explored. The study presented in **chapter 6** designed and evaluated several mitotane dosing strategies, given that TDM was performed, by simulating with the final population PK model. The results indicated that determining the starting dose with the developed model considering included covariates is most beneficial in terms of shortening the time to reach the therapeutic target, compared with starting with the fixed dose for all patients. This design can also limit the risk of toxicity to a relatively low level, together with the designed TDM strategies. Under the setting of individualized starting dose, the regimens with stepwise increasing dose at the start required less time to reach the therapeutic target, while the one with constant starting dose demonstrated the lowest risk of having toxicity. However, due to the fact that a shorter time to reach the therapeutic target is normally paired with a higher probability of toxicity, it is suggested to consider patients' condition on whether the increased risk of having toxicity can be tolerated in order to gain the benefit of reaching the therapeutic target quicker when selecting a dosing regimen. A regimen with a loading dose followed by a maintenance dose would also be desired to allow a fast target attainment. However, we didn't consider this regimen in our study as it requires a high dosage which is not tolerable for most patients. When one (or more) TDM result becomes available, individual parameters could be estimated with the population PK model. The dose amount for subsequent drug administrations can then be determined according. This approach is also demonstrated to be a promising strategy which was predicted to further decrease the risk of toxicity while providing a satisfactory target reaching time. Only that patients' tolerance to the high level of dose increase needs to be considered when applying this strategy. Potentially, with the individual PK parameters, an adequate dose for maintaining a steady drug concentration level after reaching the therapeutic window can be estimated so that the frequency of dose adaptation can be decreased. In **chapter 7**, our findings imply that dosing HD-MTX with a model-based approach would potentially be more rational for further reducing PK variability. In addition, on the basis of our results on toxicity analysis, further investigation on the exposure-response relationship of MTX would be of interest for establishing a therapeutic range for HD-MTX for future model-based personalized dosing.

## Challenges and future perspectives

Addressing treatment resistance considering evolutionary resistance development and applying precision treatment would be beneficial to improve the treatment outcome for oncology patients. The results presented in this thesis show that with the quantitative models, the evolutionary tumor progression and PK/PD of anti-cancer drugs can be characterized and predicted, thereby optimal treatment strategies can be designed and evaluated for oncology patients. However, beyond what has been demonstrated and discussed, challenges still remain regarding data availability, model development, and validation and implementation of the results. Further research and collaborations are needed to overcome the challenges and facilitate better implementation of the findings in the clinic.

### Section I

#### **Knowledge and data availability**

In order to make use of genetic biomarkers to understand the dynamics of tumor sub-clones, previous knowledge of the genetic variants that reflect treatment sensitivity is required. Available data is also essential for developing models to characterize the correlation between anti-cancer treatment responses and biomarkers, and to support decision making. As for ctDNA, although its value in oncology treatment has now been increasingly acknowledged, ctDNA monitoring has not yet been widely applied in routine clinical practice and the availability and collection of longitudinal ctDNA data are limited [31, 32, 61]. Whether patients had metastatic disease and the available sequencing assay and gene panel can also impact the availability of ctDNA data. In **chapter 3**, detectable mutant *KRAS* concentrations were only available from 9 patients out of 25 mCRC patients. In **chapter 4**, detectable mutant *EGFR* VAFs were available in 13 out of 18 NSCLC patients. The limited capability to develop a ctDNA dynamics model and adequately estimate all parameters. The missing data, such as the missing baseline ctDNA measurements in **chapter 4**, may also affect the interpretation of the results. Therefore, more and more detailed data is desired to validate our findings. Since ctDNA is being increasingly studied and the analysis method is improving, together with active collaborations, we see opportunities in the future to gain sufficient knowledge and data on longitudinal ctDNA measurements. This will better support the development of models capturing ctDNA dynamics and the incorporation of ctDNA time curves in the tumor dynamics model, which would benefit the in-depth study on evolutionary resistance development. In addition, once an adequate model is developed, sparsely sampled data can also be well utilized and missing data can be imputed rationally. Currently, effort is being made to establish standards and best practices to better systematize the evaluation

of ctDNA kinetics [31]. Moreover, if sequencing data of multiple variants are available, efforts need to be made to handle these data in a quantitative manner and a selection of variants to be included in the analysis may be required.

### ***Model development for evolutionary tumor progression***

When modeling tumor dynamics in our studies, the sum of the longest diameters (SLD) of all target lesions has been the observation of interest. Nevertheless, the dynamics of each separate lesion would also be suitable for supporting the investigation of the progression of heterogeneous tumors, especially when differences can be observed between primary and metastatic lesions. Thus, further investigation on the dynamics of separate lesions and comparing the findings with what is presented in this thesis can be of interest for future studies.

In addition to what are proposed in this thesis, other modeling strategies that characterize evolutionary tumor dynamics are also available, which can be applied in studies having different focuses. One example would be game theory models which have a stronger focus on the interaction and payoff matrix among different cell populations. The changes in the fitness of cells (fitness cost or benefit) when interacting with therapy and other types of cells are accounted for in game theory models [19, 34]. Another commonly applied modeling strategy is stochastic models which allow describing the stochastic process of proliferation, death, and mutation of tumor cells in the tumor, although the expected outcome can be comparable to those that are derived from ordinary differential equations [62]. In addition, the studies presented in this thesis assumed tumor cells accumulate one mutation that leads to resistance to one drug each time. The possibility of acquiring multiple mutations at a time which leads to multi-drug resistance has not been included in the analysis. This can also be a point of consideration for future studies.

In terms of modelling the time-curves of ctDNA measurements, our study presented in **chapter 3** proposed a concept model for capturing ctDNA dynamics which consists of a sub-clonal tumor-size dependent generation and a first-order elimination. The model considered the correlation between tumor size and ctDNA amount and well characterized the data from mCRC and NSCLC patients. We have also seen recent studies applying models that are classically used to capture tumor size to describe ctDNA time course dynamics. One study characterized the time-curves of mutant *EGFR* in ctDNA in NSCLC patients with a model with zero-order increase, first-order decay, and time-dependent regrowth, and tumor size dynamic was not incorporated [63]. Another study successfully modeled the ctDNA time course using a bi-exponential model (first-order increase and first-order decay) [64]. The correlation between tumor shrinkage and ctDNA drop has been observed

and described by linking the decay rates of tumor sizes and ctDNA data [64]. These studies provide more simple model options with fewer parameters for future pharmacometric studies. However, the underlying biology and tumor heterogeneity were not considered [64]. Moreover, in addition to characterizing the observed data, the prediction of newly acquired mutation which has not yet occurred in the data would also be interesting to be further explored.

### ***Validation and extrapolation of the proposed model and treatment design***

The studies in **section I** illustrated how quantitative models can support the study on evolving tumor progression and treatment optimization so that anti-cancer resistance can be better overcome. However, due to the characteristics of being based on limited data, further validation with external datasets is required to confirm the performance of the model and the added value of the suggested schedules. In addition, prospective clinical studies are warranted before the application of the suggested treatment designs. The validation should concern not only the predictability on the observed time-curves of data, but also on the treatment outcome such as PFS. Regarding clinical trials, several clinical studies on intermittent therapies have been reported, which however failed to show improved outcomes and the underlined mechanism remains unclear [39-44]. The need for clinical trials on adaptive therapy guided by ctDNA is however not met yet [31]. Currently, our group is carrying out a clinical study on intermittent enzalutamide therapy in prostate cancer patients (NCT05393791). The findings would be of great value to evaluate the concept proved in our study.

In addition, our studies were mainly performed in mCRC and NSCLC patients treated with anti-EGFR therapies, and focused explicitly on the use of tumor size measurements and ctDNA data. It would be of interest for future studies to extrapolate the concept models and findings to other targeted treatments and cancer types. Moreover, other oncologic biomarkers would in principle also be valuable to provide insight into the evolutionary dynamics of tumor and guide treatment. A previous study has demonstrated the value of PSA in guiding the intermittent treatment of prostate cancer patients [34].

Furthermore, to support further research and enable the achievement of the ultimate goal of optimizing and personalizing anti-cancer treatment, a multidisciplinary collaboration is essential. This is due to the requirement of in-depth knowledge about tumor and clonal dynamics as well as skills needed for complex modeling and simulation.

***Implementation of proposed treatment design***

Challenges also remain to apply the proposed novel treatment strategies in **chapter 3** that could better overcome resistance in clinical practice. First of all, our study indicated that intermittent therapy may only work for the responders to certain targeted treatment. Thus, for patients who had detectable resistance mutation pre-treatment, a better option would be to choose another treatment from start. Moreover, despite that the intermittent regimens were predicted to provide better treatment outcome than the continuous regimen in a population level, opposite results can be seen when looking at simulated subjects individually, same as when comparing adaptive and intermittent regimens. This indicates that variability between individuals can affect the choice of regimen. Thus, the idea of individual intermittent treatment, the concept of which has been proposed in the treatment of prostate cancer patients [34], could be further investigated.

Furthermore, in order to apply adaptive treatment guided by ctDNA measurements, the mutations indicating sensitivity to treatment need to be acknowledged beforehand. If multiple mutations have been reported, a selection may be required based on the strength of evidence and capability of the quantification technique, such as the gene panel in the assay and the number of mutations that can be detected simultaneously. To strengthen clinical implementation of ctDNA in the future, the turnaround times of the sequencing assays should also be short. In **chapter 3**, the study focused on the most representative mutation that is associated with resistance. However, not all patients developed detectable KRAS mutation during the course of treatment. This indicates that in order to better implement adaptive treatment, multiple relevant mutations may need to be considered. In addition, our study demonstrated that the frequency of monitoring ctDNA and the thresholds of adjusting treatment also matters when implementing adaptive treatment to improve treatment outcome. We have evaluated frequencies of once every 4–12 weeks which has been shown to be feasible [13, 65], but there is no clear validated optimal time point for ctDNA analysis [31]. The sampling frequency can also depend on the disease, therapy, sequencing assays, financial burden, and burden on the patients. After validation, the proposed computational model can be of help to inform the best practice on monitoring ctDNA and guide optimized treatment accordingly [31].

## Section II

### ***Implementation of MIPD***

As discussed in **chapter 5**, to facilitate the implementation of MIPD in clinical practice, efforts are still required to overcome several challenges, such as to evaluate the model and to translate the research findings into user-friendly MIPD software [7]. Currently, multiple programs have been developed and are already in use for model-informed TDM [7, 66]. In **chapter 6**, we have also developed a Shiny app to elucidate how precision dosing advice of mitotane for ACC patients can be informed by the developed population PK model. We have implemented the final PK model and an optimized individualized dosing regimen into this app. With this program, based on the input of the characteristics of a certain patient, an individualized starting dose can be determined by the model and be visualized together with the predicted mitotane concentration-time curves for this patient. Currently, the build-in algorithm only allows the determination of the starting dose according to the input information corresponding to the included covariates. As a R package that supports empirical Bayesian estimation is now available [67], we see a potential to implement the regimen where a more precise dose amount can be determined according to individual parameters estimated based on available TDM results. Nevertheless, this app is currently intended for research purpose only. Validation in hospital settings is still needed for its application in clinic or transferring the model to a commercial platform.

Moreover, given that programs are available for model-informed TDM, the developed models in our studies are believed to be able to be further applied to support model-based TDM of mitotane and high-dose MTX.

### ***Further PK/PD analysis for precision dosing***

In addition to PK, variabilities in PD should also be taken into consideration when implementing precision treatment. FDA recently proposed the Project Optimus which encourages improving dose selection and optimization for oncology drugs by accounting for both efficacy and tolerability rather than automatically selecting the MTD [8, 68]. In **chapter 7**, we have developed a toxicity model which allows quantifying the probability of having renal or hepatotoxicity in patients with CNS lymphoma treated with HD-MTX given the value of risk factors. The identified exposure thresholds on  $C_{24h}$  can also be applied to guide the early use of rescue therapy. Nevertheless, in order to better guide personalized treatment, further PK/PD analyses are still warranted. Firstly, in addition to already investigated factors, the impact of pharmacogenetic polymorphisms on the PK and toxicity probability in patients with CNS lymphoma treated with HD-MTX would

be of interest to future studies. Previous studies have demonstrated the influence of ABCC2 polymorphisms on the PK of HD-MTX in patients with lymphoid malignancy [69, 70]. Gene *MTHFR*, *SLC19A1*, and *ABCB1* were reported to potentially associate with an increased risk for hepatic toxicity [71]. Exploring the impact of pharmacogenetic polymorphisms has the potential to better explain inter-patient variability. Additionally, studies on the penetration of MTX to the CNS would also be of interest as CNS is the target site of MTX and neurotoxicity is also a major problem for patients receiving HD-MTX treatment. This goal can be achieved by applying physiologically based pharmacokinetic modelling (PBPK) approach [72]. Furthermore, although high drug exposure can result in toxicity, sufficient exposure is still essential to guarantee the efficacy. In our study, an exposure-efficacy relationship was not investigated. A previous study suggested that  $AUC_{0-\infty} > 1100 \mu\text{mol/L} \cdot \text{h}$  is associated with a favorable treatment outcome [73]. Due to an identified correlation of  $AUC_{0-\infty}$  with  $C_{24h}$ , the same group recommended a  $C_{24h}$  target of 4–5  $\mu\text{mol/L}$  [74]. Nonetheless, the direct relationship between  $C_{24h}$  and the efficacy has not been reported. Therefore, further investigation is warranted to explore the possibility of establishing a therapeutic range for HD-MTX, which could better facilitate future personalized dosing.

## Conclusion

Addressing treatment resistance considering evolutionary resistance development and applying personalized drug treatment would be beneficial to improve the treatment outcome for oncology patients. This thesis has applied the quantitative modeling approach to characterize the evolutionary tumor dynamics and ctDNA dynamics and quantify PK/PD variabilities for anti-cancer drugs. The developed model can facilitate the identification of optimal treatment designs and guide individualized treatment rationally, although challenges remain for the results implementation and further research and more data is warranted to validate the findings and support better practice of personalized treatment.

## References

1. Sun X, Hu B. Mathematical modeling and computational prediction of cancer drug resistance. *Brief Bioinform.* 2018;19(6):1382-99. doi:10.1093/bib/bbx065.
2. Vasan N, Baselga J, Hyman DM. A view on drug resistance in cancer. *Nature.* 2019;575(7782):299-309. doi:10.1038/s41586-019-1730-1.
3. Zhao B, Hemann MT, Lauffenburger DA. Modeling Tumor Clonal Evolution for Drug Combinations Design. *Trends Cancer.* 2016;2(3):144-58. doi:10.1016/j.trecan.2016.02.001.
4. Beksac AT, Paulucci DJ, Blum KA, Yadav SS, Sfakianos JP, Badani KK. Heterogeneity in renal cell carcinoma. *Urol Oncol.* 2017;35(8):507-15. doi:10.1016/j.urolonc.2017.05.006.
5. Kim C, Gao R, Sei E, Brandt R, Hartman J, Hatschek T, et al. Chemoresistance Evolution in Triple-Negative Breast Cancer Delineated by Single-Cell Sequencing. *Cell.* 2018;173(4):879-93 e13. doi:10.1016/j.cell.2018.03.041.
6. Verheijen RB, Yu H, Schellens JHM, Beijnen JH, Steeghs N, Huitema ADR. Practical Recommendations for Therapeutic Drug Monitoring of Kinase Inhibitors in Oncology. *Clin Pharmacol Ther.* 2017;102(5):765-76. doi:10.1002/cpt.787.
7. Kluwe F, Michelet R, Mueller-Schoell A, Maier C, Klopp-Schulze L, van Dyk M, et al. Perspectives on Model-Informed Precision Dosing in the Digital Health Era: Challenges, Opportunities, and Recommendations. *Clin Pharmacol Ther.* 2021;109(1):29-36. doi:10.1002/cpt.2049.
8. Fourie Zirkelbach J, Shah M, Vallejo J, Cheng J, Ayyoub A, Liu J, et al. Improving Dose-Optimization Processes Used in Oncology Drug Development to Minimize Toxicity and Maximize Benefit to Patients. *J Clin Oncol.* 2022;40(30):3489-500. doi:10.1200/JCO.22.00371.
9. Buil-Bruna N, Lopez-Picazo JM, Martin-Algarra S, Troconiz IF. Bringing Model-Based Prediction to Oncology Clinical Practice: A Review of Pharmacometrics Principles and Applications. *Oncologist.* 2016;21(2):220-32. doi:10.1634/theoncologist.2015-0322.
10. Lalonde RL, Kowalski KG, Huttmacher MM, Ewy W, Nichols DJ, Milligan PA, et al. Model-based drug development. *Clin Pharmacol Ther.* 2007;82(1):21-32. doi:10.1038/sj.cpt.6100235.
11. Barbolosi D, Ciccolini J, Lacarelle B, Barlesi F, Andre N. Computational oncology--mathematical modelling of drug regimens for precision medicine. *Nature Reviews Clinical Oncology.* 2016;13(4):242-54. doi:10.1038/nrclinonc.2015.204.
12. Agur Z, Elishmereni M, Kheifetz Y. Personalizing oncology treatments by predicting drug efficacy, side-effects, and improved therapy: mathematics, statistics, and their integration. *Wiley interdisciplinary reviews Systems biology and medicine.* 2014;6(3):239-53. doi:10.1002/wsbm.1263.
13. Diaz LA, Jr., Williams RT, Wu J, Kinde I, Hecht JR, Berlin J, et al. The molecular evolution of acquired resistance to targeted EGFR blockade in colorectal cancers. *Nature.* 2012; 486(7404):537-40. doi:10.1038/nature11219.
14. Xie H, Kim RD. The Application of Circulating Tumor DNA in the Screening, Surveillance, and Treatment Monitoring of Colorectal Cancer. *Ann Surg Oncol.* 2020. doi:10.1245/s10434-020-09002-7.
15. Mistry HB, Helmlinger G, Al-Huniti N, Vishwanathan K, Yates J. Resistance models to EGFR inhibition and chemotherapy in non-small cell lung cancer via analysis of tumour size dynamics. *Cancer Chemother Pharmacol.* 2019;84(1):51-60. doi:10.1007/s00280-019-03840-3.
16. Iwasa Y, Nowak MA, Michor F. Evolution of resistance during clonal expansion. *Genetics.* 2006;172(4):2557-66. doi:10.1534/genetics.105.049791.
17. Komarova NL, Burger JA, Wodarz D. Evolution of ibrutinib resistance in chronic lymphocytic leukemia (CLL). *Proceedings of the National Academy of Sciences of the United States of America.* 2014;111(38):13906-11. doi:10.1073/pnas.1409362111.

18. Wan JCM, Massie C, Garcia-Corbacho J, Mouliere F, Brenton JD, Caldas C, et al. Liquid biopsies come of age: towards implementation of circulating tumour DNA. *Nat Rev Cancer*. 2017;17(4):223-38. doi:10.1038/nrc.2017.7.
19. Basanta D, Gatenby RA, Anderson AR. Exploiting evolution to treat drug resistance: combination therapy and the double bind. *Molecular pharmaceutics*. 2012;9(4):914-21. doi:10.1021/mp200458e.
20. Terranova N, Girard P, Klinkhardt U, Munafò A. Resistance Development: A Major Piece in the Jigsaw Puzzle of Tumor Size Modeling. *CPT Pharmacometrics Syst Pharmacol*. 2015;4(6):320-3. doi:10.1002/psp4.45.
21. Yang BB, Lum P, Chen A, Arends R, Roskos L, Smith B, et al. Pharmacokinetic and pharmacodynamic perspectives on the clinical drug development of panitumumab. *Clin Pharmacokinet*. 2010;49(11):729-40. doi:10.2165/11535970-00000000-00000.
22. Yu H, Steeghs N, Nijenhuis CM, Schellens JH, Beijnen JH, Huitema AD. Practical guidelines for therapeutic drug monitoring of anticancer tyrosine kinase inhibitors: focus on the pharmacokinetic targets. *Clin Pharmacokinet*. 2014;53(4):305-25. doi:10.1007/s40262-014-0137-2.
23. Kenmotsu H, Imamura CK, Kawamura T, Oyakawa T, Omori S, Nakashima K, et al. Prospective evaluation of the relationship between response and exposure of total and unbound erlotinib in non-small cell lung cancer patients. *Cancer Chemother Pharmacol*. 2022;90(2):115-23. doi:10.1007/s00280-022-04452-0.
24. Fukudo M, Ikemi Y, Togashi Y, Masago K, Kim YH, Mio T, et al. Population pharmacokinetics/pharmacodynamics of erlotinib and pharmacogenomic analysis of plasma and cerebrospinal fluid drug concentrations in Japanese patients with non-small cell lung cancer. *Clin Pharmacokinet*. 2013;52(7):593-609. doi:10.1007/s40262-013-0058-5.
25. Steendam CMJ, Veerman GDM, Pruis MA, Atmodimedjo P, Paats MS, van der Leest C, et al. Plasma Predictive Features in Treating EGFR-Mutated Non-Small Cell Lung Cancer. *Cancers (Basel)*. 2020;12(11):3179. doi:10.3390/cancers12113179.
26. Siravegna G, Mussolin B, Buscarino M, Corti G, Cassingena A, Crisafulli G, et al. Clonal evolution and resistance to EGFR blockade in the blood of colorectal cancer patients. *Nat Med*. 2015;21(7):795-801. doi:10.1038/nm.3870.
27. Parseghian CM, Loree JM, Morris VK, Liu X, Clifton KK, Napolitano S, et al. Anti-EGFR-resistant clones decay exponentially after progression: implications for anti-EGFR rechallenge. *Ann Oncol*. 2019;30(2):243-9. doi:10.1093/annonc/mdy509.
28. Bozic I, Nowak MA. Timing and heterogeneity of mutations associated with drug resistance in metastatic cancers. *Proceedings of the National Academy of Sciences of the United States of America*. 2014;111(45):15964-8. doi:10.1073/pnas.1412075111.
29. Sun X, Bao J, Shao Y. Mathematical Modeling of Therapy-induced Cancer Drug Resistance: Connecting Cancer Mechanisms to Population Survival Rates. *Sci Rep*. 2016;6:22498. doi:10.1038/srep22498.
30. Xiong L, Cui S, Ding J, Sun Y, Zhang L, Zhao Y, et al. Dynamics of EGFR mutations in plasma recapitulates the clinical response to EGFR-TKIs in NSCLC patients. *Oncotarget*. 2017;8(38):63846-56. doi:10.18632/oncotarget.19139.
31. Sanz-Garcia E, Zhao E, Bratman SV, Siu LL. Monitoring and adapting cancer treatment using circulating tumor DNA kinetics: Current research, opportunities, and challenges. *Sci Adv*. 2022;8(4):eabi8618. doi:10.1126/sciadv.abi8618.
32. Bruno R, Chanu P, Kagedal M, Mercier F, Yoshida K, Guedj J, et al. Support to early clinical decisions in drug development and personalised medicine with checkpoint inhibitors using dynamic biomarker-overall survival models. *British journal of cancer*. 2023. doi:10.1038/s41416-023-02190-5.

33. Gatenby RA, Brown JS. Integrating evolutionary dynamics into cancer therapy. *Nature Reviews Clinical Oncology*. 2020;17(11):675-86. doi:10.1038/s41571-020-0411-1.

34. Zhang J, Cunningham JJ, Brown JS, Gatenby RA. Integrating evolutionary dynamics into treatment of metastatic castrate-resistant prostate cancer. *Nature Communications*. 2017;8(1). doi:10.1038/s41467-017-01968-5.

35. Nagano T, Tachihara M, Nishimura Y. Mechanism of Resistance to Epidermal Growth Factor Receptor-Tyrosine Kinase Inhibitors and a Potential Treatment Strategy. *Cells*. 2018;7(11):212. doi:10.3390/cells7110212.

36. FDA Approval of KRAS Inhibitor Sotorasib for Lung Cancer Hailed as Milestone. 2021 June 25 [cited 2021 July12th]; Available from: <https://www.cancer.gov/news-events/cancer-currents-blog/2021/fda-sotorasib-lung-cancer-kras>

37. Mistry HB. On the reporting and analysis of a cancer evolutionary adaptive dosing trial. *Nat Commun*. 2021;12(1):316. doi:10.1038/s41467-020-20174-4.

38. Rowe M, Hidayat A, Walter S, Pollard A, Norris T, Victor D, et al. The use of intermittent enzalutamide dosing in the treatment of metastatic castrate-resistant prostate cancer. *Journal of Clinical Oncology*. 2020;38(6\_suppl):81-. doi:10.1200/JCO.2020.38.6\_suppl.81.

39. Algazi AP, Othus M, Daud AI, Lo RS, Mehnert JM, Truong TG, et al. Continuous versus intermittent BRAF and MEK inhibition in patients with BRAF-mutated melanoma: a randomized phase 2 trial. *Nat Med*. 2020;26(10):1564-8. doi:10.1038/s41591-020-1060-8.

40. Alva A, Hussain M. Optimal pharmacotherapeutic management of hormone-sensitive metastatic prostate cancer. *Drugs*. 2013;73(14):1517-24. doi:10.1007/s40265-013-0106-3.

41. Cella D, Jensen SE, Hahn EA, Beaumont JL, Korytowsky B, Bhattacharyya H, et al. Fatigue in patients with advanced renal cell carcinoma receiving sunitinib on an intermittent versus continuous dosing schedule in a randomized phase II trial. *Cancer Med*. 2014;3(5):1353-8. doi:10.1002/cam4.286.

42. Colleoni M, Luo W, Karlsson P, Chirgwin J, Aebi S, Jerusalem G, et al. Extended adjuvant intermittent letrozole versus continuous letrozole in postmenopausal women with breast cancer (SOLE): a multicentre, open-label, randomised, phase 3 trial. *Lancet Oncol*. 2018;19(1):127-38. doi:10.1016/s1470-2045(17)30715-5.

43. Jerusalem G, Farah S, Courtois A, Chirgwin J, Aebi S, Karlsson P, et al. Continuous versus intermittent extended adjuvant letrozole for breast cancer: final results of randomized phase III SOLE (Study of Letrozole Extension) and SOLE Estrogen Substudy. *Ann Oncol*. 2021;32(10):1256-66. doi:10.1016/j.annonc.2021.07.017.

44. Sofen H, Gross KG, Goldberg LH, Sharata H, Hamilton TK, Egbert B, et al. A phase II, multicenter, open-label, 3-cohort trial evaluating the efficacy and safety of vismodegib in operable basal cell carcinoma. *J Am Acad Dermatol*. 2015;73(1):99-105.e1. doi:10.1016/j.jaad.2015.03.013.

45. Arshad U, Taubert M, Kurlbaum M, Frechen S, Herterich S, Megerle F, et al. Enzyme autoinduction by mitotane supported by population pharmacokinetic modelling in a large cohort of adrenocortical carcinoma patients. *Eur J Endocrinol*. 2018;179(5):287-97. doi:10.1530/EJE-18-0342.

46. Vanslooten H, Vanseters AP, Smeenk D, Moolenaar AJ. O,P'-Ddd (Mitotane) Levels in Plasma and Tissues during Chemotherapy and at Autopsy. *Cancer Chemoth Pharm*. 1982;9(2):85-8. doi:10.1007/bf00265384.

47. Whirl-Carrillo M, McDonagh EM, Hebert JM, Gong L, Sangkuhl K, Thorn CF, et al. Pharmacogenomics knowledge for personalized medicine. *Clin Pharmacol Ther*. 2012;92(4):414-7. doi:10.1038/clpt.2012.96.

48. PharmGKB. rs4244285, Variant annotation. [cited 2019 28 Aug]; Available from: <https://www.pharmgkb.org/variant/PA166154053/variantAnnotation>

49. Methotrexate Injection [package insert]. HOSPIRA. U.S. Food and Drug Administration. [https://www.accessdata.fda.gov/drugsatfda\\_docs/label/2018/011719s125lbl.pdf](https://www.accessdata.fda.gov/drugsatfda_docs/label/2018/011719s125lbl.pdf). Revised April 2018. Accessed October 12, 2022.
50. Bannwarth B, Labat L, Moride Y, Schaeverbeke T. Methotrexate in Rheumatoid Arthritis. *Drugs*. 1994;47(1):25-50. doi:10.2165/00003495-199447010-00003.
51. Arshad U, Taubert M, Seeger-Nukpezah T, Ullah S, Spindeldreier KC, Jaehde U, et al. Evaluation of body-surface-area adjusted dosing of high-dose methotrexate by population pharmacokinetics in a large cohort of cancer patients. *BMC Cancer*. 2021;21(1):719. doi:10.1186/s12885-021-08443-x.
52. Mei S, Li X, Jiang X, Yu K, Lin S, Zhao Z. Population Pharmacokinetics of High-Dose Methotrexate in Patients With Primary Central Nervous System Lymphoma. *J Pharm Sci*. 2018;107(5):1454-60. doi:10.1016/j.xphs.2018.01.004.
53. Pai MP, Debacker KC, Derstine B, Sullivan J, Su GL, Wang SC. Comparison of Body Size, Morphomics, and Kidney Function as Covariates of High-Dose Methotrexate Clearance in Obese Adults with Primary Central Nervous System Lymphoma. *Pharmacotherapy*. 2020;40(4):308-19. doi:10.1002/phar.2379.
54. Ibarra M, Combs R, Taylor ZL, Ramsey LB, Mikkelsen T, Buddington RK, et al. Insights from a pharmacometric analysis of HDMTX in adults with cancer: Clinically relevant covariates for application in precision dosing. *Br J Clin Pharmacol*. 2022. doi:10.1111/bcp.15506.
55. Gallais F, Oberic L, Faguer S, Tavitian S, Lafont T, Marsili S, et al. Body Surface Area Dosing of High-Dose Methotrexate Should Be Reconsidered, Particularly in Overweight, Adult Patients. *Therapeutic Drug Monitoring*. 2021;43(3):408-15. doi:10.1097/Ftd.0000000000000813.
56. Howard SC, McCormick J, Pui C-H, Buddington RK, Harvey RD. Preventing and Managing Toxicities of High-Dose Methotrexate. *The Oncologist*. 2016;21(12):1471-82. doi:10.1634/theoncologist.2015-0164.
57. Holdhoff M, Mrugala MM, Grommes C, Kaley TJ, Swinnen LJ, Perez-Heydrich C, et al. Challenges in the Treatment of Newly Diagnosed and Recurrent Primary Central Nervous System Lymphoma. *J Natl Compr Canc Netw*. 2020;18(11):1571-8. doi:10.6004/jnccn.2020.7667.
58. Ramsey LB, Balis FM, O'Brien MM, Schmiegelow K, Pauley JL, Bleyer A, et al. Consensus Guideline for Use of Glucarpidase in Patients with High-Dose Methotrexate Induced Acute Kidney Injury and Delayed Methotrexate Clearance. *Oncologist*. 2018;23(1):52-61. doi:10.1634/theoncologist.2017-0243.
59. Schaff LR, Lobbous M, Carlow D, Schofield R, Gavrilovic IT, Miller AM, et al. Routine use of low-dose glucarpidase following high-dose methotrexate in adult patients with CNS lymphoma: an open-label, multi-center phase I study. *BMC Cancer*. 2022;22(1):60. doi:10.1186/s12885-021-09164-x.
60. Widemann BC, Balis FM, Kim A, Boron M, Jayaprakash N, Shalabi A, et al. Glucarpidase, leucovorin, and thymidine for high-dose methotrexate-induced renal dysfunction: clinical and pharmacologic factors affecting outcome. *J Clin Oncol*. 2010;28(25):3979-86. doi:10.1200/JCO.2009.25.4540.
61. Herbreteau G, Vallee A, Charpentier S, Normanno N, Hofman P, Denis MG. Circulating free tumor DNA in non-small cell lung cancer (NSCLC): clinical application and future perspectives. *J Thorac Dis*. 2019;11(Suppl 1):S113-S26. doi:10.21037/jtd.2018.12.18.
62. Tomasetti C, Levy D. An elementary approach to modeling drug resistance in cancer. *Mathematical biosciences and engineering : MBE*. 2010;7(4):905-18. doi:10.3934/mbe.2010.7.905.

63. Janssen JM, Verheijen RB, van Duijl TT, Lin L, van den Heuvel MM, Beijnen JH, et al. Longitudinal nonlinear mixed effects modeling of EGFR mutations in ctDNA as predictor of disease progression in treatment of EGFR-mutant non-small cell lung cancer. *Clin Transl Sci.* 2022;15(8):1916-25. doi:10.1111/cts.13300.
64. Ribba B, Roller A, Helms HJ, Stern M, Bleul C. Circulating tumor DNA: Opportunities and challenges for pharmacometric approaches. *Front Pharmacol.* 2022;13:1058220. doi:10.3389/fphar.2022.1058220.
65. Sorensen BS, Wu L, Wei W, Tsai J, Weber B, Nexo E, et al. Monitoring of epidermal growth factor receptor tyrosine kinase inhibitor-sensitizing and resistance mutations in the plasma DNA of patients with advanced non-small cell lung cancer during treatment with erlotinib. *Cancer.* 2014;120(24):3896-901. doi:10.1002/cncr.28964.
66. Jager NGL, Chai MG, van Hest RM, Lipman J, Roberts JA, Cotta MO. Precision dosing software to optimize antimicrobial dosing: a systematic search and follow-up survey of available programs. *Clin Microbiol Infect.* 2022;28(9):1211-24. doi:10.1016/j.cmi.2022.03.041.
67. Fidler M, Wilkins JJ, Hooijmaijers R, Post TM, Schoemaker R, Trame MN, et al. Nonlinear Mixed-Effects Model Development and Simulation Using nlmixr and Related R Open-Source Packages. *CPT Pharmacometrics Syst Pharmacol.* 2019;8(9):621-33. doi:10.1002/psp4.12445.
68. Shah M, Rahman A, Theoret MR, Pazdur R. The Drug-Dosing Conundrum in Oncology - When Less Is More. *N Engl J Med.* 2021;385(16):1445-7. doi:10.1056/NEJMp2109826.
69. Simon N, Marsot A, Villard E, Choquet S, Khe HX, Zahr N, et al. Impact of ABCC2 polymorphisms on high-dose methotrexate pharmacokinetics in patients with lymphoid malignancy. *Pharmacogenomics J.* 2013;13(6):507-13. doi:10.1038/tpj.2012.37.
70. Benz-de Bretagne I, Zahr N, Le Gouge A, Hulot JS, Houillier C, Hoang-Xuan K, et al. Urinary coproporphyrin I/(I + III) ratio as a surrogate for MRP2 or other transporter activities involved in methotrexate clearance. *Br J Clin Pharmacol.* 2014;78(2):329-42. doi:10.1111/bcp.12326.
71. Suthandiram S, Gan GG, Zain SM, Bee PC, Lian LH, Chang KM, et al. Effect of polymorphisms within methotrexate pathway genes on methotrexate toxicity and plasma levels in adults with hematological malignancies. *Pharmacogenomics.* 2014;15(11):1479-94. doi:10.2217/pgs.14.97.
72. Perkins RS, Davis A, Campagne O, Owens TS, Stewart CF. CNS penetration of methotrexate and its metabolite 7-hydroxymethotrexate in mice bearing orthotopic Group 3 medulloblastoma tumors and model-based simulations for children. *Drug Metab Pharmacokinet.* 2023;48:100471. doi:10.1016/j.dmpk.2022.100471.
73. Joerger M, Huitema AD, Krähenbühl S, Schellens JH, Cerny T, Reni M, et al. Methotrexate area under the curve is an important outcome predictor in patients with primary CNS lymphoma: A pharmacokinetic-pharmacodynamic analysis from the IELSG no. 20 trial. *British journal of cancer.* 2010;102(4):673-7. doi:10.1038/sj.bjc.6605559.
74. Joerger M, Ferreri AJ, Krähenbühl S, Schellens JH, Cerny T, Zucca E, et al. Dosing algorithm to target a predefined AUC in patients with primary central nervous system lymphoma receiving high dose methotrexate. *Br J Clin Pharmacol.* 2012;73(2):240-7. doi:10.1111/j.1365-2125.2011.04084.x.



# Chapter 9

## Summary **Nederlandse samenvatting**





## Summary

Quantitative modeling with mixed-effect models has been increasingly applied in pharmaceutical research. It allows quantitative description and prediction of pharmacokinetics (PK) and pharmacodynamics (PD) of therapeutic agents, as well as to quantify and explain inter- and intra- individual variability. In oncology research, the model-based approach can be applied to make use of longitudinal data to learn about the interaction between drug treatment and the human body, as well as cancer progression. The developed model can subsequently support the identification of the optimal regimen and facilitate individualized treatment.

In cancer treatment, the occurrence of treatment resistance is one of the major causes of treatment failure in patients. An insight into the inter- and intra-tumor heterogeneity and evolutionary dynamics of tumors, and subsequent use of this knowledge for designing treatment strategies would be beneficial for optimizing targeted anti-cancer treatment. In **Section I** of this thesis, we applied the model-based approach to specifically interpret tumor size dynamics and evolutionary resistance development during treatment, and explored optimal regimens that can better suppress the development of resistance.

In order to identify opportunities and challenges of quantitatively characterizing anti-cancer treatment response accounting for tumor dynamics and evolutionary resistance development, an overview of currently available model structures is needed. In **chapter 2**, we performed a systematic search and comprehensively summarized the mathematical models that have been used to describe and predict tumor growth (inhibition) dynamics and evolutionary resistance development. We particularly focused on models that are applicable to clinical data. In this review, tumor dynamic models displayed by ordinary differential equations, algebraic equations, and partial differential equations were identified and summarized. Tumor proliferation, regression due to treatment, tumor heterogeneity and treatment resistance are key elements that are commonly considered in those models. The dynamics of biomarkers can also be incorporated which enables better understanding and prediction of tumor progression. As for models for evolutionary tumor resistance, stochastic and deterministic models were identified and summarized. The required data and knowledge as well as the applicability of the models to different cancer types and treatment options were also summarized. The results of this review may facilitate a novel model-based analysis of anti-cancer treatment response and the occurrence of resistance, which incorporates both tumor dynamics and evolutionary resistance development.

Among the studies included in this review, detailed data regarding evolutionary resistance has not yet been incorporated in tumor size-based modeling of anti-cancer treatment

response. Given that genetic biomarkers, such as circulating tumor DNA (ctDNA), become increasingly available, there is an opportunity to make use of such data to support the development of a tumor dynamics model that accounts for evolutionary resistance for cancer patients. The developed model could subsequently support the optimization and personalization of anti-cancer therapy with simulations.

In order to test this concept, in **chapter 3**, a mathematical model incorporating various clonal populations and evolving cancer resistance was developed to characterize tumor size dynamics and resistance development under treatment. With parameter values fitted to the data or informed by literature data, the model well captured previously reported tumor sizes and mutant *KRAS* levels in ctDNA of patients with metastatic colorectal cancer (mCRC) treated with panitumumab. Subsequently, we evaluated anti-cancer treatment schedules the design of which considered the evolving progression of tumor and demonstrated the use of ctDNA as a marker to guide adaptive treatment. The simulation results indicated that compared with a conventional continuous treatment schedule, intermittent schedules with treatment holidays and adaptive schedules guided by ctDNA could better suppress the evolving cancer resistance. Intermittent and adaptive schedules were also predicted to result in improved clinical outcomes, i.e. the predicted median progression-free survival (PFS) and time period in which the tumor size stayed below the baseline level were prolonged. With the sensitivity analysis, we identified parameters of which the accurate estimation is important for the model to capture the observed dynamics of tumor sizes and mutation concentrations. Nevertheless, the intermittent and adaptive treatment still provided better treatment outcomes when parameter values varied.

In **chapter 4**, we further characterized the tumor dynamics considering intra-tumor heterogeneity and explored the correlation between ctDNA measurements and tumor dynamics parameters based on data from non-small cell lung cancer (NSCLC) patients treated with erlotinib. The study included intensively sampled erlotinib PK curves from 29 patients, and tumor sizes, ctDNA measurements, and sparsely sampled erlotinib concentrations from 18 patients from the START-TKI study. A population PK model of erlotinib was first developed and subsequently applied to investigate the exposure-tumor dynamics relationship. To characterize the tumor dynamics, models accounting for intra-tumor heterogeneity and acquired resistance with or without a pre-existing resistance component were investigated. Eventually, a model with acquired resistance only resulted in an adequate fit to the data. Additionally, no significant exposure-response relationship for erlotinib was identified within the observed exposure range. Subsequently, the correlation of baseline ctDNA measurements on *EGFR* and *TP53* variants with tumor dynamics parameters was explored. The analysis indicated that higher baseline plasma *EGFR* mutation levels correlated with

increased tumor growth rates, and the inclusion of ctDNA data improved model fit. This result suggests that quantitative ctDNA measurements have the potential to be a predictor of anti-cancer treatment response, which encouraged to use ctDNA as an early biomarker.

Since high PK/PD variabilities of anti-cancer drugs are present in real-world patients which may result in unfavorable treatment outcomes, a better understanding of such variabilities would be beneficial to improve anti-cancer therapy for individual patients. In **Section II** of this thesis, we demonstrated the application of pharmacometric modeling in characterizing the PK/PD profiles and variabilities of anti-cancer drugs, and in supporting precision treatment for real-world patients. We first introduced model-informed precision dosing (MIPD) and the current application and benefit of MIPD in supporting optimal and precision anti-cancer treatment in **chapter 5**. MIPD adopts pharmacometric models to guide precision dose selection aiming for improved therapeutic target attainment and optimal treatment outcome. MIPD can be applied to rationally guide initial dose selection and dose adaptation during anti-cancer treatment, as well as therapeutic drug monitoring (TDM). The advantage of MIPD over conventional strategies in cancer treatment has been demonstrated in many research and clinical trials. However, challenges still have to be overcome to implement MIPD of cancer therapies in clinical practice. We highlighted a few challenges and provided future perspectives regarding optimal target identification, suitable model selection, available programs, and the necessity of prospective clinical trials.

In **chapter 6**, we performed a population PK analysis to characterize and predict mitotane PK in patients with adrenocortical carcinoma (ACC). Additionally, we explored and quantified the potential effect of pharmacogenetic variations on mitotane clearance for the first time to better explain the PK variability of mitotane. A two-compartment PK model was developed based on retrospectively collected data from 48 patients. For each patient, the genotyping results of 172 SNPs from the DMET<sup>TM</sup> platform were included in the analysis. The exploratory analysis identified 11 SNPs that were potentially related to mitotane clearance. The final stepwise covariate analysis identified the lean body weight (LBW), genotypes of *CYP2C19*\*2 (rs4244285), *SLCO1B3* 699A>G (rs7311358), and *SLCO1B1* 571T>C (rs4149057) as significant covariates on mitotane clearance (CL/F). This suggests that enzyme CYP2C19 and transporter SLCO1B1 and SLCO1B3 may play roles in mitotane disposition but further external or in vitro evaluation is warranted to confirm the results. Based on the developed model, various dosing regimens and the TDM process were simulated to investigate optimal and individualized mitotane regimens for patients with ACC. The results indicated that determining the starting dose individually with the developed model is beneficial to shorten the period for mitotane to reach the therapeutic target and limit the risk of toxicity. Regimens that can effectively maintain

mitotane concentration within its therapeutic range, i.e., 14–20 mg/L, were established. One optimal regimen was then built in a Shiny app to elucidate an option of providing treatment advice for a new patient based on the model.

In **chapter 7**, we performed a population PK analysis on high-dose methotrexate (HD-MTX) in patients with central nervous system (CNS) lymphoma. Data from 110 patients from 3 medical centers were available in this study. A two-compartment population PK model was developed and shown to adequately describe the PK data. Estimated glomerular filtration rate (eGFR), treatment schedule, albumin, alkaline phosphatase, and body weight were identified as significant covariates. The results suggest that adjusting the HD-MTX dose with a model-based approach may be more rational to further reduce PK variability than dosing only based on body surface area (BSA). Subsequently, a (exposure-)toxicity analysis was performed to identify predictive factors for acute renal and liver toxicity. eGFR and sex were identified to be significant baseline predictors for renal toxicity, and HD-MTX dose ( $\text{mg}/\text{m}^2$ ) was the strongest baseline predictor of liver toxicity. Simulation results suggest that starting HD-MTX when  $\text{eGFR} > 66.6 \text{ mL}/\text{min}/1.73\text{m}^2$  is recommended for patients with CNS lymphoma, and a dose higher than  $3500 \text{ mg}/\text{m}^2$  predicted a high risk of liver toxicity. The exposure metrics of methotrexate (MTX) including the area under the concentration-time curve ( $\text{AUC}_{24\text{-}\infty}$ ) and concentration at 24 hours ( $\text{C}_{24\text{h}}$ ) were identified to correlate with renal toxicity but not with liver toxicity.  $\text{AUC}_{24\text{-}\infty} > 109.5 \mu\text{mol}/\text{L}\cdot\text{h}$  and  $\text{C}_{24\text{h}} > 8.64 \mu\text{mol}/\text{L}$  were suggested to be potential exposure thresholds that predict a high risk of toxicity. These findings would be beneficial for further individualizing HD-MTX dosage and preventing acute organ toxicity, which can improve HD-MTX therapy in CNS lymphoma patients.

Finally, in **chapter 8**, we discussed the results of this thesis and potential challenges and perspectives for future studies. We have shown that with the quantitative models, the evolutionary progression of tumor can be characterized and predicted, accounting for interactions among heterogeneous tumor cells and supported by mutant gene variants detected in ctDNA. In addition, population PK/PD modeling allows for a quantitative description of the PK and PD of anti-cancer drugs at both population and individual levels. The developed model can further facilitate the identification of optimal treatment designs and guide individualized treatment rationally for oncology patients. However, challenges still remain for data collection (especially for ctDNA data), model development and validation, and results implementation (including suggested regimens and the models). Further research is warranted to validate the findings and support better practice of personalized treatment.

## Nederlandse samenvatting

Kwantitatieve modellering met zogenaamde gemengde-effect modellen wordt vaker toegepast in farmaceutisch onderzoek. Het maakt het mogelijk om de farmacokinetiek (PK) en farmacodynamiek (PD) van geneesmiddelen kwantitatief te beschrijven en te voorspellen. Daarnaast kan met deze methode de inter- en intra-individuele variabiliteit gekwantificeerd en verklaard worden. In oncologisch onderzoek kan de op modellen gebaseerde benadering worden toegepast om longitudinale gegevens te benutten om meer te weten te komen over de interactie tussen medicamenteuze behandeling en het menselijk lichaam, evenals de progressie van kanker. Het ontwikkelde model kan vervolgens de identificatie van het optimale behandelingsregime ondersteunen en individuele behandeling vergemakkelijken.

Bij kankerbehandeling is de opkomst van behandelingsresistentie één van de belangrijkste oorzaken van therapiefalen bij patiënten. Inzicht in de inter- en intra-tumor heterogeniteit en evolutionaire dynamiek van tumoren, en het daaropvolgende gebruik van deze kennis voor het ontwerpen van behandelstrategieën, zou zeer gunstig zijn voor het optimaliseren van gerichte antikankerbehandeling. In **Sectie I** van dit proefschrift hebben we deze op modellen gebaseerde benadering specifiek toegepast om de dynamiek van tumorgrootte en evolutionaire resistantieontwikkeling tijdens de behandeling te interpreteren, en optimale behandelregimes te verkennen die de ontwikkeling van resistantie beter kunnen onderdrukken.

Om kansen en uitdagingen te identificeren bij het kwantitatief karakteriseren van de reactie op antikankerbehandeling rekening houdend met tumordynamiek en evolutionaire resistantieontwikkeling, is een overzicht van momenteel beschikbare modelstructuren nodig. In **hoofdstuk 2** hebben we een systematische zoektocht uitgevoerd en de wiskundige modellen die zijn gebruikt om de dynamiek van tumor(groei) en evolutionaire resistantieontwikkeling te beschrijven en voorspellen, uitgebreid samengevat. We richtten ons met name op modellen die toepasbaar zijn op klinische data. In deze review werden tumordynamische modellen weergegeven door gewone differentiaalvergelijkingen, algebraïsche vergelijkingen en partiële differentiaalvergelijkingen geïdentificeerd en vervolgens samengevat. Tumorproliferatie en regressie als gevolg van behandeling, tumorheterogeniteit en behandelingsresistentie zijn belangrijke elementen die doorgaans in die modellen worden meegenomen. De dynamiek van biomarkers kan ook worden opgenomen in de modellen, wat een beter begrip en voor-spelling van de tumorontwikkeling mogelijk maakt. Wat betreft modellen voor evolutionaire tumorresistentie, werden stochastische en deterministische modellen geïdentificeerd en samengevat. De benodigde gegevens en kennis, evenals de toepasbaarheid van de modellen

op verschillende kancersoorten en behandelingsmogelijkheden, werden ook samengevat. De resultaten van deze review kunnen een nieuwe op modellen gebaseerde analyse van de reactie op antikankerbehandeling en het optreden van resistentie vergemakkelijken, waarbij zowel tumordynamiek als evolutionaire resistentieontwikkeling worden meegenomen.

Onder de studies die in deze review zijn opgenomen, is gedetailleerde informatie over evolutionaire resistentie nog niet opgenomen in de op tumoromvang gebaseerde modellering van de reactie op antikankerbehandeling. Gezien het feit dat genetische biomarkers, zoals circulerend tumor-DNA (ctDNA), steeds meer beschikbaar worden, is er een mogelijkheid om dergelijke gegevens te gebruiken ter ondersteuning van de ontwikkeling van een tumordynamisch model dat rekening houdt met evolutionaire resistentie bij kankerpatiënten. Het ontwikkelde model kan vervolgens de optimalisatie en personalisatie van antikankertherapie ondersteunen met behulp van simulaties.

Om dit concept te testen, is in **hoofdstuk 3** een wiskundig model ontwikkeld dat verschillende klonale populaties en evoluerende kankerresistentie meeneemt om de dynamiek van tumorgrootte en resistentieontwikkeling onder behandeling te karakteriseren. Met parameterwaarden afgestemd op de beschikbare data of geïnformeerd door literatuurgegevens, beschreef het model eerder gerapporteerde tumorgroottes en mutante KRAS-niveaus in ctDNA van patiënten met gemitastaseerde dikkedarmkanker (mCRC) die met panitumumab waren behandeld redelijk goed. Vervolgens evaluateerden we behandelingsschema's die rekening hielden met de voortschrijdende progressie van tumoren en toonden we aan dat het gebruik van ctDNA als marker om adaptieve behandeling te begeleiden in potentie kan worden gebruikt. De simulatieresultaten gaven aan dat vergeleken met een conventioneel continu behandelingsschema, onderbroken schema's met behandelingspauzes en adaptieve schema's begeleid door monitoring van ctDNA de evoluerende kankerresistentie beter konden onderdrukken. Er werd ook voorspeld dat onderbroken en adaptieve schema's zouden resulteren in verbeterde klinische resultaten, d.w.z. de voorspelde mediane progressievrije overleving (PFS) en de periode waarin de tumorgrootte onder het basale niveau bleef, werden verlengd. Met de gevoelighedenanalyse identificeerden we parameters waarvan de nauwkeurige schatting belangrijk is voor het model om de waargenomen dynamiek van tumorgroottes en mutatieconcentraties vast te leggen. Desalniettemin boden de onderbroken en adaptieve behandeling betere behandelingsresultaten wanneer de parameterwaarden varieerden.

In **hoofdstuk 4** karakteriseerden we de tumordynamiek verder, waarbij rekening werd gehouden met intra-tumor heterogeniteit, en onderzochten we de correlatie tussen ctDNA-metingen en tumordynamiekparameters op basis van gegevens van patiënten met niet-

kleincellige longkanker (NSCLC) die met erlotinib werden behandeld. De studie omvatte intensief gesamplede erlotinib PK-curves van 29 patiënten, en tumorgrootte meetwaarden, ctDNA-metingen en spaarzaam gesamplede erlotinib-concentraties van 18 patiënten uit de START-TKI-studie. Een populatie-PK-model van erlotinib werd eerst ontwikkeld en vervolgens toegepast om de relatie tussen blootstelling en tumordynamiek te onderzoeken. Om de tumordynamiek te karakteriseren, werden modellen onderzocht die rekening houden met intra-tumor heterogeniteit en verworven resistantie met of zonder een vooraf bestaand resistantiecomponent. Uiteindelijk resulteerde een model met alleen verworven resistantie in een adequate overeenkomst met de beschikbare gegevens. Bovendien werd geen significante blootstellings-responsrelatie voor erlotinib geïdentificeerd binnen het waargenomen blootstellingsbereik. Vervolgens werd de correlatie van baseline ctDNA-metingen van *EGFR*- en *TP53*-varianten met tumordynamiekparameters onderzocht. De analyse gaf aan dat hogere plasma-*EGFR*-mutatienniveaus bij aanvang correleerden met verhoogde tumorgroeisnelheden, en de opname van ctDNA-gegevens verbeterde de modelaanpassing. Dit resultaat suggereert dat kwantitatieve ctDNA-metingen het potentieel hebben om een vroege voorspeller te zijn van de reactie op antikankerbehandeling, wat stimuleert om ctDNA te gebruiken als een vroege biomarker in de klinische praktijk.

Aangezien er in de praktijk hoge PK/PD-variabiliteit van antikankermedicijnen aanwezig is bij patiënten, wat kan leiden tot ongunstige behandelingsresultaten, zou een beter begrip van dergelijke variabiliteit gunstig zijn om de antikankertherapie voor individuele patiënten te verbeteren. In **Sectie II** van dit proefschrift hebben we de toepassing van farmacometrische modellering laten zien bij het karakteriseren van de PK/PD-profielen en variabiliteit van antikankermedicijnen, en bij het ondersteunen van precisiebehandeling voor patiënten in de klinische praktijk. We hebben eerst model-geïnformeerde precisiedosering (MIPD) geïntroduceerd en de huidige toepassing en voordelen van MIPD in het ondersteunen van optimale en precieze antikankerbehandeling besproken in **hoofdstuk 5**. MIPD maakt gebruik van farmacometrische modellen om precisiedosering te begeleiden met als doel een verbeterde therapeutische blootstelling en daaropvolgende optimale behandelingsresultaten. MIPD kan worden toegepast om rationeel de initiële dosiskeuze en dosisaanpassing tijdens antikankerbehandeling vast te stellen, net als therapeutic drug monitoring (TDM). Het voordeel van MIPD ten opzichte van conventionele strategieën in de behandeling van kanker is aangetoond in veel onderzoeken en klinische trials. Er moeten echter nog obstakels worden overwonnen om MIPD van kankertherapieën in de klinische praktijk te implementeren. We hebben een aantal uitdagingen benadrukt en toekomstperspectieven geboden met betrekking tot optimale doelidentificatie, geschikte modelselectie, beschikbare programma's en de noodzaak van prospectieve klinische onderzoeken.

In **hoofdstuk 6** hebben we een populatie-PK-analyse uitgevoerd om de PK van mitotaan te karakteriseren en voorspellen bij patiënten met bijnierschorscarcinoom (ACC). Bovendien hebben we voor de eerste keer het potentiële effect van farmacogenetische variaties op mitotaanklaring kwantitatief onderzocht om de PK-variabiliteit van mitotaan beter te verklaren. Er werd een tweecompartimenten-PK-model ontwikkeld op basis van retrospectief verzamelde gegevens van 48 patiënten. Voor elke patiënt werden de genotyperesultaten van 172 SNPs van het DMET™-platform opgenomen in de analyse. De verkennende analyse identificeerde 11 SNPs die potentieel gerelateerd waren aan mitotaanklaring. De uiteindelijke stapsgewijze covariaatanalyse identificeerde het lichaamsgewicht zonder vet (LBW), genotypen van *CYP2C19\*2* (rs4244285), *SLCO1B3* 699A>G (rs7311358) en *SLCO1B1* 571T>C (rs4149057) als significante covariaten voor schijnbare mitotaanklaring (CL/F). Dit suggereert dat het enzym CYP2C19 en de transporters SLCO1B1 en SLCO1B3 mogelijk een rol spelen in de verdeling van mitotaan, maar verdere externe of in vitro-evaluatie is nodig om de resultaten te bevestigen. Op basis van het ontwikkelde model werden verschillende doseringsschema's en het TDM-proces gesimuleerd om optimale en geïndividualiseerde mitotaanregimes voor patiënten met ACC te onderzoeken. De resultaten gaven aan dat het individueel bepalen van de startdosis met het ontwikkelde model gunstig is om de periode voor mitotaan om het therapeutische doel te bereiken te verkorten en het risico op toxiciteit te beperken. Regimes die effectief mitotaan concentratie binnen het therapeutische bereik kunnen handhaven (14–20 mg/L) werden vastgesteld. Eén optimaal regime werd vervolgens gebouwd in een Shiny-app om een optimaal behandelingsadvies voor een nieuwe patiënt op basis van het model te genereren en te visualiseren.

In **hoofdstuk 7** hebben we een populatie PK-analyse uitgevoerd op hoge doses methotrexaat (HD-MTX) bij patiënten met lymfoom van het centrale zenuwstelsel (CZS). Gegevens van 110 patiënten uit drie academische medische centra waren beschikbaar in deze studie. Er werd een tweecompartimenten populatie PK-model ontwikkeld en getoond om de PK-gegevens adequaat te beschrijven. Geschatte glomerulaire filtratiesnelheid (eGFR), behandel schema, albumine, alkalische fosfatase en lichaamsgewicht werden geïdentificeerd als significante covariaten. De resultaten suggereren dat het aanpassen van de HD-MTX-dosering met een op modellen gebaseerde benadering mogelijk rationeler is om de PK-variabiliteit verder te verminderen dan dosering alleen op basis van lichaamsoppervlak (BSA). Vervolgens werd een (blootstellings-)toxiciteitsanalyse uitgevoerd om voorspellende factoren voor acute nier- en leverotoxiciteit te identificeren. eGFR bij start behandeling en geslacht werden geïdentificeerd als significante basale voorspellers voor niertoxiciteit, en de HD-MTX-dosering ( $\text{mg}/\text{m}^2$ ) was de sterkste basale voorspeller van leverotoxiciteit. Simulatieresultaten suggereren dat om niertoxiciteit te voorkomen het

aanbevolen is om alleen te starten met een volledig dosis van HD-MTX wanneer patiënten met CZS-lymfoom een eGFR  $> 66,6 \text{ mL/min}/1,73\text{m}^2$  hebben. Een dosis hoger dan 3500 mg/m<sup>2</sup> voorspelde een verhoogd risico op levertoxiciteit. De blootstellingsmetingen van methotrexaat (MTX), waaronder de oppervlakte onder de concentratie-tijdcurve (AUC<sub>24-∞</sub>) en de concentratie na 24 uur (C<sub>24h</sub>), werden geïdentificeerd als correlerend met niertoxiciteit, maar niet met levertoxiciteit. AUC<sub>24-∞</sub>  $> 109,5 \mu\text{mol/L} \cdot \text{uur}$  en C<sub>24h</sub>  $> 8,64 \mu\text{mol/L}$  werden voorgesteld als mogelijke blootstellingsdrempels die een hoog risico op toxiciteit voorspellen. Deze bevindingen zouden nuttig kunnen zijn voor verdere individualisering van de HD-MTX-dosering en het voorkomen van acute orgaantoxiciteit, wat de HD-MTX-therapie bij patiënten met CZS-lymfoom kan verbeteren.

Tenslotte, in **hoofdstuk 8**, hebben we de resultaten van deze scriptie en potentiële uitdagingen en perspectieven voor toekomstige studies besproken. We hebben aangetoond dat met kwantitatieve modellen de evolutionaire progressie van tumoren kan worden gekarakteriseerd en voorspeld, rekening houdend met interacties tussen heterogene tumorcellen en ondersteund door gemuteerde genvarianten die zijn gedetecteerd in ctDNA. Bovendien maakt populatie PK/PD-modellering een kwantitatieve beschrijving mogelijk van de PK en PD van antikankergeneesmiddelen op zowel populatie- als individueel niveau. Het ontwikkelde model kan verder bijdragen aan de identificatie van optimale behandelingontwerpen en het rationeel begeleiden van geïndividualiseerde behandeling voor oncologiepatiënten. Er blijven echter uitdagingen bestaan voor gegevensverzameling (vooral voor ctDNA-gegevens), modelontwikkeling en validatie, en de implementatie van resultaten (inclusief voorgestelde behandelingsregimes en modellen). Verder onderzoek is nodig om de bevindingen te valideren en een betere praktijk van gepersonaliseerde behandeling te ondersteunen.



# Appendices

**Curriculum Vitae**  
**List of publications**  
**Acknowledgement**





## Curriculum Vitae

Anyue Yin was born on February 24<sup>th</sup> 1992 in Beijing, China.

In 2010, she started her bachelor study in Pharmaceutical Sciences at Peking University, Beijing, China, and received her BSc degree in 2014. She then started her master's study in the field of Pharmacometrics at Peking University under the supervision of Prof. dr. Wei Lu. During this period, she performed research on population pharmacokinetic analysis of olanzapine based on clinical data with the assistance of model-based meta-analysis. She obtained her MSc degree in 2016.

In March 2017, she started a research internship at the Leiden Academic Centre for Drug Research (LACDR) at Leiden University, the Netherlands, under the supervision of Prof. dr. P.H. van der Graaf and Dr. J.G.C. van Hasselt. During her internship, she performed a quantitative systems pharmacology analysis to characterize the interaction between noradrenaline and vasopressin in vasoconstriction.

In September 2017, she started her PhD at the Leiden University Medical Center (LUMC) under the supervision of Prof. dr. H.J. Guchelaar and Dr. D.J.A.R. Moes. Her PhD projects focused on using pharmacometric modeling and simulation approaches to better guide anti-cancer treatment individualization and overcome treatment resistance. During her time at LUMC, she also provided help to other projects.

Since October 2023, she works as an Associate Consultant at Pharmetheus.

## List of publications

### Publications related to this thesis

**Yin A**, de Groot FA, et al. Population pharmacokinetic and toxicity analysis of high-dose methotrexate in patients with central nervous system lymphoma. *In preparation*

**Yin A\***, Veerman GDM\*, et al. Quantitative modeling of tumor dynamics and development of drug resistance in non-small cell lung cancer patients treated with erlotinib. *Submitted*

**Yin A**, van Hasselt JGC, Guchelaar HJ, Friberg LE#, Moes DJAR#. Anti-cancer treatment schedule optimization based on tumor dynamics modelling incorporating evolving resistance. *Sci Rep.* 2022 Mar 10;12(1):4206.

**Yin A\***, Ettaieb MHT\*, et al. Population Pharmacokinetic and Pharmacogenetic Analysis of Mitotane in Patients with Adrenocortical Carcinoma: Towards Individualized Dosing. *Clin Pharmacokinet.* 2021 Jan;60(1):89-102.

**Yin A**, Moes DJAR, van Hasselt JGC, Swen JJ, Guchelaar HJ. A Review of Mathematical Models for Tumor Dynamics and Treatment Resistance Evolution of Solid Tumors. *CPT Pharmacometrics Syst Pharmacol.* 2019 Oct;8(10):720-737.

### Publications not related to this thesis

**Yin A**, Yamada A, Stam WB, van Hasselt JGC, van der Graaf PH. Quantitative systems pharmacology analysis of drug combination and scaling to humans: the interaction between noradrenaline and vasopressin in vasoconstriction. *Br J Pharmacol.* 2018 Aug;175(16):3394-3406.

**Yin A\***, Shang D\*, Wen Y, Li L, Zhou T, Lu W. Population pharmacokinetics analysis of olanzapine for Chinese psychotic patients based on clinical therapeutic drug monitoring data with assistance of meta-analysis. *Eur J Clin Pharmacol.* 2016 Aug;72(8):933-944.

\* Shared first authorship

# Shared last authorship

## Acknowledgement

This book is now reaching its end. In this last part of the book, I would like to express my heartfelt gratitude to those who have played an important role in my studies and life, and have been supporting me over the past years.

I would like to first thank my promoter Henk-Jan and co-promoter Dirk Jan. I am extremely grateful to have had the opportunity to work on such appealing and challenging projects under your supervision. Henk-Jan, thank you for your trust, guidance, and encouragement. Your valuable suggestions and knowledge in clinical pharmacology and pharmacogenetics have broadened my view and have always been helpful for my study design. Dirk Jan, your expertise in pharmacometrics and clinical pharmacology has been a great source of inspiration. Thank you for always being available when needed, and I am also truly grateful for your patience and trust, as well as your support in my growth as a professional and my future career choices.

The completion of my studies is also inseparable from the outstanding contribution of all the collaborators. Thank you all for your expertise and support, and for sharing the data. Coen and Lena, it was a great pleasure to be able to collaborate with you on more than one project. I am deeply grateful for the knowledge you have shared and the constructive input you have provided.

I am also delighted to be able to work with such wonderful colleagues. Jesse, thank you for your input on my projects and your patience in explaining genotyping methods and results. My PhD colleagues and roommates: Xiaoyan, Frank, Carin, Catherijne, Anabel, Tom, Sylvia vL, Lisanne, Sylvia K, Emma, Rineke, Iris, Clair, Qinglian, Henok, Amy, Amar, Wisse, Henieh, Romy, Sofia and Rozita, thank you for helping me in adapting myself to the PhD life as well as to the Dutch society. I feel so fortunate to get to work with and learn from such talented and warm-hearted people. Maaike and Michel, my postdoc-mates, we have been colleagues for so many years. I appreciate our great teamwork and the care and support you have offered. I am grateful that you could be my paranympths. Wendy, Maria, Stephanie, and Kyra, thank you for your assistance with both administrative and daily matters. Without doubt, I also want to express my thankfulness to all my other colleagues in the department. Thank you for being interested in my study and offering me help in my work and life. I have had a wonderful time in KFT.

A special thanks to Dirk Jan for helping with the Dutch Summary translation.

My master and bachelor intern students, Mike, Max, Alma, and Aarushi, thank you for your contribution and for helping me to grow into a better mentor.

I am also thankful for having a group of lovely friends: Lifeng Sun, Minglong Liu, Yu Fu, Hong Su, Tan Zhang, Feiyan Liu, Yuchen Guo, and many others I have not listed. I feel grateful that we support each other in life as well as in research. Thank you for enriching my PhD life.

我也要感谢我的父母和家人。这些年聚少离多，让您们挂心了。感谢您的包容和理解，以及对我始终如一的支持和鼓励。

(I would also like to thank my parents and family members. Over the past years, we have been apart more than been gathered. I can feel your concern and worries. I appreciate your understanding, and thank you for your consistent support and encouragement.)

Last but not least, my love Tingjie, I am truly grateful that you are always by my side. You always help me to pull myself together whenever needed, and make me feel more confident when facing challenges. I also appreciate the fact that I could ask you for scientific advice. We have experienced so many together, and I can't wait to start a new chapter of life with you!



